

Single-particle cryo-EM structures of oligomeric membrane protein complexes

Dissertation
zur Erlangung des Doktorgrades
der Naturwissenschaften

vorgelegt beim Fachbereich 14
Biochemie, Chemie, Pharmazie
der Johann Wolfgang Goethe-Universität
in Frankfurt am Main

von
Martin Wilkes
aus Siegen, Deutschland

Frankfurt am Main, 2016 (D30)

Diese Arbeit wurde in der Arbeitsgruppe von Prof. Dr. Christine Ziegler der Abteilung Strukturbiologie des Max-Planck-Institutes für Biophysik in Frankfurt am Main durchgeführt und vom Fachbereich 14 Biochemie, Chemie und Pharmazie der Goethe-Universität als Dissertation angenommen.

This work was performed in the department of Structural Biology at the Max-Planck-Institute of Biophysics in Frankfurt am Main and accepted as a dissertation in the department of Biochemistry, Chemistry and Pharmacy from the Goethe-University Frankfurt.

Dekan: Prof. Dr. Michael Karas

1. Gutachter: Prof. Dr. Clemens Glaubitz
2. Gutachter: Prof. Dr. Christine Ziegler

Datum der Disputation: 04.11.2016

Parts of this thesis are in preparation for publication:

Wilkes M, de Sanctis S, Gläsner M, Witzgall R, Kühlbrandt W, Ziegler C (2016) Cryo-EM structure of the human TRP channel polycystin-2. (Manuscript in preparation)

Wilkes M, Koshy C, Madej G, Kühlbrandt W, Ziegler C (2016) The activation cycle of BetP. (Manuscript in preparation)

Wilkes M^{*}, Schulz S^{*}, Kühlbrandt W, Meier T (2016) Cryo-EM structure of the rotor ring from a novel type of rotary ATPase. (Manuscript in preparation)

*Shared authorship

Table of contents

Table of contents	VII
List of figures.....	XI
List of tables.....	XIV
List of abbreviations	XV
Zusammenfassung.....	XVIII
Abstract.....	XXIV
1 Introduction	1
1.1 Transient receptor potential (TRP) channel family.....	1
1.1.1 Architecture of TRP channels	2
1.1.1.1 Structure of TRPV1	3
1.1.2 TRP channel polycystin-2	5
1.1.3 Function of polycystin-2	7
1.1.4 Subcellular localization of polycystin-2	8
1.1.4.1 Localization of PC-2 in the endoplasmatic reticulum	8
1.1.4.2 Localization of PC-2 at the plasma membrane.....	9
1.1.4.3 Localization of PC-2 in the primary cilium of kidney cells	9
1.1.5 Polycystin-2 in autosomal dominant polycystic kidney disease.....	10
1.2 Secondary-active transporters	11
1.2.1 Osmotic stress in bacteria	11
1.2.2 Secondary-active transporter BetP from <i>Corynebacterium glutamicum</i>	12
1.2.2.1 Atomic structure of BetP from <i>C. glutamicum</i>	12
1.2.2.2 Transport mechanism of BetP from <i>C. glutamicum</i>	15
1.2.2.3 Regulation of BetP from <i>C. glutamicum</i>	19
1.3 Rotary ATPases	23
1.3.1 Classification of rotary ATPases	23
1.3.2 Architecture of rotary ATPases	23
1.3.2.1 Structure and function of the soluble F ₁ domain	25
1.3.2.2 Structure and function of the membrane-embedded Fo domain	26
1.3.3 N-Type ATPase	31
1.4 Single-particle cryo-EM structure determination.....	32
1.5 Aim of this work.....	35
2 Materials and Methods	36
2.1 Materials	36
2.1.1 Instruments	36

2.1.2	Kits	36
2.1.3	Enzymes	37
2.1.4	Chemicals	37
2.1.5	Media and Antibiotics	37
2.1.5.1	Media for <i>E.coli</i>	37
2.1.5.2	Media for eukaryotic cells	37
2.1.5.3	Antibiotics	37
2.1.6	Plasmids and Oligonucleotids	38
2.1.7	Organisms	41
2.2	Molecular biological methods	43
2.2.1	Polymerase chain reaction	43
2.2.2	Purification of PCR products	44
2.2.3	Agarose gel electrophoresis	44
2.2.4	Gelextraction of DNA	44
2.2.5	DNA cleavage by restriction enzymes	44
2.2.6	Ligation of DNA fragments	44
2.2.7	Primer synthesis and sequencing of manufactured DNA	45
2.2.8	Isolation of vector DNA	45
2.2.9	Preparation of competent <i>E. coli</i> cells	45
2.2.10	Transformation of competent <i>E. coli</i> cells	46
2.2.11	Preparation of glycerol-stocks	46
2.2.12	Transfection of eukaryotic cells and selection of a stable cell line	46
2.2.13	Freezing of cell lines	47
2.3	Biochemical methods	47
2.3.1	Protein production in <i>E. coli</i>	47
2.3.2	Protein production in eukaryotic cells	47
2.3.3	Protein purification	48
2.3.3.1	Disruption of cells	48
2.3.3.2	Preparation of HEK293S GnT ^I endoplasmatic reticulum membranes	49
2.3.3.3	Preparation of <i>E.coli</i> and HEK293S GnT ^I membranes	49
2.3.3.4	Solubilisation of membrane proteins	49
2.3.3.5	Immobilized nickel-nitrilotriacetic acid (Ni-NTA) chromatography	49
2.3.3.6	Immobilized strep-tactin affinity chromatography	50
2.3.3.7	Immobilized amylose affinity chromatography	50
2.3.3.8	Immobilized lentil lectin chromatography	50
2.3.3.9	Anion exchange (AEX) chromatography	50
2.3.3.10	Size exclusion chromatography (SEC).....	51
2.3.3.11	Sucrose density gradient centrifugation	51
2.3.3.12	Concentration of protein samples	51
2.3.3.13	Exchange of detergent to amphipol A8-35.....	51

2.3.4 Protein analysis	52
2.3.4.1 Photometrical determination of protein concentration	52
2.3.4.2 Bradford assay	52
2.3.4.3 Bicinchoninic acid (BCA) assay	52
2.3.4.4 Sodium dodecyl sulphate polyacrylamid gel electrophoresis (SDS-PAGE).....	52
2.3.4.5 Blue-native polyacrylamide gel electrophoresis (BN-PAGE)	53
2.3.4.6 Electro-elution of proteins after BN-PAGE	54
2.3.4.7 Western blot analysis.....	54
2.3.4.8 Protein reconstitution into liposomes	55
2.4 Biophysical methods	56
2.4.1 3D crystallization	56
2.4.2 Laser confocal scanning microscopy	56
2.4.3 Electron microscopy methods	57
2.4.3.1 Negative-stain electron microscopy	57
2.4.3.2 Freeze-fracture electron microscopy	57
2.4.3.3 Freeze-fracture labelling.....	57
2.4.3.4 Fixation and sectioning of eukaryotic cells	58
2.4.3.5 Quantum dot labelling	60
2.4.3.6 Electron cryomicroscopy (cryo-EM).....	60
2.4.4 Image-processing	60
2.4.5 Map visualization and analysis	61
3 Structural investigations and cellular localization of the human TRP channel polycystin-2	62
3.1 Results of the structural investigations and cellular localization of polycystin-2	62
3.1.1 Expression and purification of different PC-2 truncation mutants for 3D crystallization	62
3.1.2 Expression and cellular localization of PC-2 wild type and different PC-2 truncation mutants in GnTII cells for structural investigation	65
3.1.3 Purification, oligomeric state and structure determination of PC-2 expressed in GnTII cells	75
3.1.3.1 Purification and oligomeric state of PC-2(His ₆).....	75
3.1.3.2 Purification of PC-2(StrepII).....	78
3.1.3.3 Structure determination of PC-2(StrepII).....	84
3.1.3.4 Cryo-EM structure of PC-2(StrepII)	85
3.2 Discussion	92
3.2.1 Expression of PC-2 and different PC-2 truncation mutants in GnTII cells	92
3.2.2 Activity measurements of PC-2 in GnTII cells	93
3.2.3 Crystalloid formation during PC-2 expression in GnTII cells	94
3.2.4 Subcellular localization of PC-2 and truncation mutants in GnTII cells	95
3.2.5 Purification and oligomeric state of PC-2	96
3.2.6 4.6 Å cryo-EM structure of PC-2	97

3.2.7	Summary	100
4	Cryo-EM structure of BetP from <i>C. glutamicum</i>.....	101
4.1	Results of the cryo-EM structure determination of BetP	101
4.1.1	Purification of BetP in amphipol A8-35	101
4.1.2	Single-particle cryo-EM of BetP in amphipol A8-35.....	103
4.1.2.1	Cryo-EM of BetP in amphipol A8-35	103
4.1.2.2	Cryo-EM structure determination of BetP in amphipol A8-35	104
4.1.2.3	Cryo-EM structure of BetP in amphipol A8-35	105
4.1.3	Comparison of the cryo-EM and X-ray structure of BetP	106
4.2	Discussion	109
4.2.1	Inward-open state of BetP	109
4.2.2	Mechanism of BetP activation	110
4.2.3	Summary	111
5	Structural investigation of the N-type ATPase c-ring from <i>B. pseudomallei</i>	113
5.1	Single-particle cryo-EM of the <i>B. pseudomallei</i> N-type ATPase c-ring	113
5.1.1	2D classification of the rotor ring.....	113
5.1.2	3D structure determination of the <i>B. pseudomallei</i> N-type ATPase rotor ring in different amphiphatic molecules by single-particle cryo-EM	115
5.1.2.1	Analysis of the rotor ring in amphipol A8-35	116
5.1.2.2	Analysis of the rotor ring in DDM	117
5.1.2.3	Analysis of the rotor ring in C ₁₂ E ₈	118
5.1.2.4	Analysis of the rotor ring in LDAO	118
5.1.3	Cryo-EM map of the <i>B. pseudomallei</i> N-type ATPase c ₁₇ ring.....	122
5.2	Discussion.....	125
5.2.1	Impact of the detergent on cryo-EM structure determination of the N-type ATPase c-ring....	125
5.2.2	Impact of the particle number on cryo-EM structure determination of the N-type ATPase rotor ring	129
5.2.3	Rotor ring stoichiometry and biological consequences for the N-type ATPase.....	130
5.2.4	Summary	133
6	Conclusions and perspectives	134
7	Appendix.....	137
8	References.....	138
9	Acknowledgement.....	157
10	Curriculum vitae.....	159

List of figures

Figure 1: The TRP channel family.....	1
Figure 2: Structure of TRPV1 and TRPA1	5
Figure 3: Cartoon model of human PC-2.....	6
Figure 4: PC-2 expression causes whorl and karmellae ER in HEK293, CHO, COS-7 and MDCK cells	8
Figure 5: The different transporter types	11
Figure 6: Known compounds transported by carriers of the BCCT family.....	12
Figure 7: Crystal structure and topological organization of BetP.....	13
Figure 8: Coordination of glycine betaine in the occluded state of BetP	14
Figure 9: Topology model of the LeuT fold	15
Figure 10: Comparison of the LeuT X-ray structure and the inward-facing LeuT model.....	16
Figure 11: Scheme of the gating mechanism in LeuT	17
Figure 12: Overview of BetP conformations occurring during the alternating access	18
Figure 13: Opening and closing of the periplasmic and cytoplasmic gate in BetP	19
Figure 14: Activation of BetP by osmotic stress in <i>C. glutamicum</i> and in <i>E. coli</i>	21
Figure 15: Interaction of POPG molecules in the central cavity of BetP	21
Figure 16: Model for osmoregulatory interactions within a BetP trimer.....	22
Figure 17: General architecture of F-, A- and V-type rotary ATPases.....	24
Figure 18: Nucleotide-binding and rotary catalysis model of ATP synthesis in rotary ATPases	26
Figure 19: X-ray structures of different ATPase rotor rings.....	28
Figure 20: Different models of the ion translocation through the F _o domain.....	30
Figure 21: Scheme of single-particle data processing	32
Figure 22: Projection matching procedure.....	33
Figure 23: Purification of PC-2c.....	64
Figure 24: Cartoon of different PC-2 constructs, which were successfully inserted into the genome of GnTII cells.....	66
Figure 25: Western blot of PC-2(His ₆) and C-terminal truncation mutants	66
Figure 26: Laser confocal scanning microscopy of GnTII cells	67
Figure 27: Gold-labeled thin section of GnTII cells expressing PC-2	68
Figure 28: Labelling of purified membrane stacks after freeze-fracture and thin sectioning.....	69
Figure 29: Thin sections of PC-2 expressing GnTII cells at different time points.....	71
Figure 30: Cellular morphology and localization of PC-2Δ143 in GnTII cells	72

Figure 31: Cellular morphology and localization of PC-2Δ182 in GnTI ⁻ cells	73
Figure 32: Cellular morphology and localization of PC-2Δ273 in GnTI ⁻ cells	74
Figure 33: Solubilisation of PC-2(His ₆) from GnTI ⁻ membranes	75
Figure 34: Purification and oligomeric state of PC-2(His ₆).....	77
Figure 35: Negative-stain EM of purified PC 2(His6) in DDM	78
Figure 36: Purification of PC-2(StrepII) in fos-choline 14.....	79
Figure 37: Native-PAGE and negative-stain EM of purified PC-2 in fos-choline 14	80
Figure 38: SDS-, native-PAGE and negative-stain EM of PC-2(StrepII) in amphipol A8-35.....	81
Figure 39: SDS-PAGE after electro-elution of PC-2(StrepII) in amphipol A8-35.....	82
Figure 40: Size exclusion chromatograms and electron cryomicrographs of PC-2(StrepII) in LMNG/CHS and amphipol A8-35	84
Figure 41: 2D class averages of PC-2.....	85
Figure 42: 4.6 Å cryo-EM structure of PC-2	86
Figure 43: Comparison of cryo-EM structures of PC-2, TRPV1 and TRPA1	87
Figure 44: Overlay of the membrane domains of TRPV1, TRPA1 and PC-2.....	87
Figure 45: Local resolution of the PC-2 structure.....	88
Figure 46: Comparison of the pore region of PC-2 with the opened and closed TRPV1 structure	89
Figure 47: Secondary structure prediction of the extracellular domain.....	90
Figure 48: Structural elements of the extracellular domain.....	91
Figure 49: Location of ADPKD related mutations in PC-2	93
Figure 50: Structure of TRPV1 in complex with the vanilloid ligand resiniferatoxin (RTX) and the spider double-knot toxin (DkTx)	94
Figure 51: Resolved structural elements of the extracellular domain.....	99
Figure 52: Purification of BetP in amphipol A8-35.....	102
Figure 53: Negative-stain electron micrograph of purified BetP in amphipol A8-35	102
Figure 54: Electron cryomicrograph of purified BetP in amphipol A8-35	103
Figure 55: 2D class averages of BetP in amphipol A8-35.....	104
Figure 56: Cryo EM structure of BetP in amphipol A8 35.....	105
Figure 57: Residues essential for BetP trimerization are visible in the cryo-EM map.....	105
Figure 58: Comparison between the X-ray (grey) and the cryo-EM (red) structure of BetP	106
Figure 59: Orientation of the C-terminal α-helix in the cryo-EM structure of BetP	107
Figure 60: Possible interactions between the C-terminal domain of BetP and POPG molecules	107

Figure 61: Movement of the C-terminal domain upon K⁺ binding..... 110

Figure 62: Two possible K⁺ binding sites changing the C-terminal interaction network..... 111

Figure 63: Two-dimensional class averages of the N-type ATPase rotor ring using different software packages (EMAN2, XMIPP and IMAGIC)..... 114

Figure 64: Schematic representation of the processing pathway for each amphiphatic molecule 116

Figure 65: 3D refinements and classifications of the rotor ring in ampipol A8-35, DDM, C₁₂E₈ and LDAO with the corresponding FSC curves 120

Figure 66: Electron cryomicroscopy map of the N-type ATPase rotor ring..... 123

Figure 67: Model of the N-type ATPase rotor ring fitted in the cryo-EM map..... 124

Figure 68: Structure of the N-type ATPase rotor ring 124

Figure 69: 2D class averages of the N-type ATPase rotor ring in different amphiphatic molecules 127

Figure 70: Cryo-EM maps of the rotor ring in different amphiphatic molecules..... 128

Figure 71: Putative proton binding site of the N-type ATPase rotor ring..... 131

Figure 72: Chemical structures of amphiphatic molecules used in this work for single-particle cryo-EM..... 137

List of tables

Table 1: Structures of TRP channels and TRP channel domains (ARD, ankyrin repeat domain; CaM, calmodulin; PC 1, polycystin-1; PC 2, polycystin 2).....	2
Table 2: Plasmids.....	38
Table 3: Oligonucleotids.....	40
Table 4: Bacterial strains.....	41
Table 5: Eukaryotic cells.....	42
Table 6: Thermocycler program of the three step PCR.....	43
Table 7: Thermocycler program of the two step PCR.....	43
Table 8: PCR mixture.....	43
Table 9: SDS-PAGE separation gel.....	53
Table 10: SDS-PAGE stacking gel.....	53
Table 11: Buffer BN-PAGE.....	54
Table 12: List of antibodies for Western blot analysis.....	55
Table 13: List of antibodies for immuno labelling.....	56
Table 14: List of antibodies for freeze-fracture labelling.....	58
Table 15: List of antibodies for immunology.....	59
Table 16: Expression and purification of different PC-2 constructs in <i>E.coli</i>	62
Table 17: Densities and micelle sizes of amphiphatic molecules compared to the densities of amorphous ice and protein.....	121
Table 18: Summary of single-particle cryo-EM structure determination of the N-type ATPase rotor ring.....	121
Table 19: Applied b-factors in cryo-EM structure determination.....	137

List of abbreviations

2D	two dimensional
3D	three dimensional
Å	Angstrom(s)
aa	amino acids
ADP	adenosin-5'-diphosphate
ADPKD	autosomal dominant polycystic kidney disease
AEX	anion exchange
ALPS	amphipathic lipid packing sensor
APC	amino acid/polyamine/organocation
APS	ammonium persulfate
ARD	ankyrin repeat domain
ATP	adenosine-5'-triphosphate
a. u.	arbitrary units
BCA	bicinchoninic acid
BCC	betaine-choline-carnitine
BCCT	betaine-choline-carnitine-transporter
BN	blue native
bp	base pairs
<i>B. pseudomallei</i>	<i>Burkholderia pseudomallei</i>
BSA	bovine serum albumin
C ₁₂ E ₈	octaethylene glycol monododecyl ether
CaM	calmodulin
CHS	cholesteryl hemisuccinate
<i>C. glutamicum</i>	<i>Corynebacterium glutamicum</i>
cryo-EM	electron cryomicroscopy
CV	column volume
DCCD	N,N'-dicyclohexylcarbodiimide
dd	double distilled
DDM	n-dodecyl-β-D-maltoside
DMSO	dimethyl-sulfoxide
DNA	deoxyribonucleic acid
dNTP	deoxyribonucleotide triphosphate

<i>E. coli</i>	<i>Escherichia coli</i>
EDTA	ethylenediaminetetraacetic acid
EM	electron microscopy
EMAN	Electron micrograph analysis
ER	endoplasmatic reticulum
<i>et al.</i>	<i>et alii</i>
FBS	fetal bovine serum
HEK	human embryonic kidney
His ₆	hexameric histidin tag
IMAGIC	Image analysis in the computer
IP ₃	inositol trisphosphate
kb	kilobase
LB	Luria Bertani
LDAO	lauryldimethylamide-N-oxide
LMNG	lauryl maltose neopentyl glycol
MBP	maltose binding protein
MD	molecular dynamic
MPD	2-methyl-2,4-pentadiol
NCS1	nucleobase/cation symporter-1
NMR	nuclear magnetic resonance
NSS	neurotransmitter/sodium symporter
NTA	nitrilotriacetic acid
OD	optical density
p	pico
P _i	inorganic phosphate
PACS	phosphofurin acidic cluster sorting protein
PAGE	polyacrylamide gel electrophoresis
PC	polycystin
PCR	polymerase chain reaction
pdb	protein database
PBS	phosphate buffer saline
PEG	polyethylene glycol
<i>pmf</i>	<i>proton motive force</i>
POPC	1-palmitoyl-2-oleoyl- <i>sn</i> -glycero-3-phosphocholine

POPG	1-palmitoyl-2-oleoyl-sn-glycero-3-phosphoglycerol
PVDF	polyvinylidene fluoride
Relion	Regularized likelihood optimization
rpm	revolutions per minute
SEC	size exclusion chromatography
SDS	sodium dodecyl sulphate
SIMPLE	Single-particle image processing linux engine
<i>smf</i>	<i>sodium motif force</i>
SSS	solute/sodium symporter
StrepII	Streptactin tag
TAE	Tris-acetate-EDTA
TBS	Tris buffered saline
TEMED	tetramethylethylenediamine
TEV	tobacco etch virus
TMH	transmembrane helix
TRP	transient receptor potential
U	units
UV	ultra violet
v/v	volume per volume
w/v	weight per volume
w/w	weight per weight
XMIPP	X-Windows-based microscopy image processing package

Zusammenfassung

Mit Hilfe von Einzelpartikel Kryo-EM ist es möglich, mit wenigen µg an reinem Protein hoch aufgelöste Strukturen zu bestimmen. In dieser Arbeit wurden die Strukturen des humanen TRP Kanals Polycystin-2, des sekundär aktiven Transporters BetP von *Corynebacterium glutamicum* und des Rotor-Rings der N-Typ ATPase von *Burkholderia pseudomallei* mittels Einzelpartikel Kryo-Elektronenmikroskopie (Kryo-EM) bestimmt.

TRP (transient receptor potential) Kanäle kommen ausschließlich in Eukaryoten vor und sind anhand von DNA Sequenzvergleichen identifiziert worden. Sie wurden in 6 Unterfamilien, TRPC (canonical), TRPA (ankyrin), TRPM (melastatin), TRPML (mucoipin), TRPV (vanilloid) und TRPP (polycystin), eingeteilt. Alle TRP Kanäle sind nicht-selektive Kationenkanäle, die eine Vielzahl von zellulären Antworten auslösen, indem sie die intrazelluläre Kalziumkonzentration ändern. Sie bestehen aus sechs membrandurchspannenden Helices sowie zytoplasmatischen N- und C-Termini. Die Sequenzhomologie innerhalb der TRP Kanalfamilie liegt bei ~20 %. Dabei beschränken sich die homologen Regionen auf die membrandurchspannenden Helices, während die zytoplasmatischen Domänen sehr divers sind. Letztere sind für die unterschiedlichen Funktionen der TRP Kanäle wichtig, da sie unter anderem Bindestellen für aktivierende oder inhibierende Substanzen darstellen. Es wird angenommen, dass sich alle TRP Kanäle zu Tetrameren zusammenlagern, um einen aktiven Kanal zu bilden. Die Struktur von TRP Kanälen war lange Zeit unbekannt, bis es 2013 gelang, die Struktur von TRPV1 mittels Einzelpartikel Kryo-Elektronenmikroskopie zu lösen. Die Struktur zeigt, dass die Organisation der membrandurchspannenden Helices sehr ähnlich zu spannungsabhängigen Ionenkanälen wie z.B. Kv1.2 ist. Polycystin-2 gehört zu der Unterfamilie TRPP. Patienten mit der autosomal dominanten Erbkrankheit „polyzystische Nierenerkrankung“ tragen Mutationen in den Genen *PKD1* oder *PKD2*. Das Gen *PKD1* kodiert für das Protein Polycystin-1 und *PKD2* für den TRP Kanal Polycystin-2 (PC-2). PC-2 weist Signalsequenzen auf, die dafür verantwortlich sind, dass PC-2 einerseits im endoplasmatischen Retikulum (ER) verweilt, andererseits in Anwesenheit von Interaktionspartnern zur Plasmamembran oder in das Primäre Zilium von Nierenepithelzellen transportiert wird. Die Funktion von PC-2 ist damit abhängig von der zellulären Lokalisierung. Im ER funktioniert PC-2 als ein Kalzium-abhängiger Kalzium freisetzender Kanal, während es im primären Zilium einen Komplex mit Polycystin-1 bildet und auf mechanosensitive Stimuli reagiert.

In dieser Arbeit wurden verschiedene Deletionsmutanten von PC-2 hergestellt und erfolgreich in das Genom menschlicher HEK293 GnTI Zellen inseriert. Diese Zellen tragen eine Mutation in dem Gen, das für die N-Acetyl-Glycosyl-Transferase I codiert, wodurch alle Proteine, die posttranslational glykosyliert werden, das gleiche Glykosylierungsmuster aufweisen. Zellen mit der höchsten Expressionsrate von PC-2 sowie den Deletionskonstrukten wurden selektioniert und weiter kultiviert. 48 Stunden nach Induktion der Genexpression wurde die zelluläre Lokalisation von PC-2 mittels konfokaler Laser-Scanning-Mikroskopie und Elektronenmikroskopie bestimmt. Dabei stellte sich heraus, dass die Akkumulation von PC-2 in den Zellen zu einer Veränderung der ER Morphologie führt. Es konnte durch Mutationsanalysen gezeigt werden, dass diese Veränderung einerseits durch das hohe Aufkommen von PC-2 im ER und andererseits durch die C-terminale coiled-coil Domäne von PC-2 verursacht wird. So führte die Deletion der C-terminalen coiled-coil Domäne zu einer ausschließlichen Lokalisation von PC-2 Δ 143 an der Plasmamembran. Die Deletion aller funktionellen C-terminalen Domänen (PC-2 Δ 182) resultierte dagegen wieder in der ER Lokalisierung und in einer Veränderung der ER Morphologie. Diese Art von ER Morphologie wird als kristalloides ER bezeichnet und konnte *in vitro* bislang nur infolge einer Überexpression der HMG-CoA Reduktase in UT-1 Zellen beobachtet werden. Es wird angenommen, dass kristalloides ER entsteht, wenn Proteine, die an der Lipidbiosynthese beteiligt sind, im ER angehäuft werden. Eine *in vivo* Studie an Mäusen hat gezeigt, dass PC-2 an dem Reparaturmechanismus von Membranen beteiligt ist. Somit besteht eine Verbindung zwischen PC-2 und der Lipidbiosynthese. Die Bestimmung des Oligomierzustandes von PC-2 mittels nativer Polyacrylamid-Gelelektrophorese bestätigte, dass PC-2 ein stabiles Tetramer bildet. Die Reinigung von PC-2 wurde während dieser Arbeit optimiert. Durch die Verwendung von 2,2-Didecylpropan-1,3-bis- β -D-Maltopyranosid (LMNG) in Verbindung mit 5-Cholesten-3 β -ol-3 hemisuccinat (CHS) als Detergenz konnte PC-2 schließlich in hoher Qualität gereinigt werden. Einzelpartikel Kryo-EM Strukturen von bereits gelösten kleinen Membranproteinen zeigten, dass es von Vorteil sein kann, das Membranprotein nicht in klassischen Detergenzien zu frieren, sondern in Amphipol A8-35. Amphipol A8-35 ist ein amphiphatisches Molekül, das sich so fest um den hydrophoben Teil des Proteins lagert, dass es weiterhin in Lösung bleibt, auch wenn überschüssiges Amphipol A8-35 und Detergenz entfernt wird. Durch den Austausch von LMNG/CHS mit Amphipol A8-35 konnte die Struktur mittels Einzelpartikel Kryo-Elektronenmikroskopie (Kryo-EM) gelöst werden. Die Struktur von PC-2 mit einer Auflösung von 4.6 Å zeigt, dass die Anordnung der membrandurchspannenden Helices große Ähnlichkeit zu den bekannten TRP Kanal Strukturen von TRPV1, TRPV2 und TRPA1 aufweist. Ein Vergleich von PC-2 mit der offenen und geschlossenen Struktur von

TRPV1 lässt den Schluss zu, dass PC-2 in der offenen Konformation vorliegt. Im Gegensatz zu TRPV1, TRPV2 und TRPA1 besitzt PC-2 eine ~25 kDa große extrazelluläre Domäne. Diese Domäne zeigte eine stabile Faltung und konnte in der EM Struktur aufgelöst werden. Damit ist PC-2 der erste TRP Kanal, der mit extrazellulärer Domäne strukturell gelöst wurde. Man kann davon ausgehen, dass die Struktur von PC-2 durch die Erweiterung des Kryo-EM Datensatzes verfeinert werden kann, bis eine Auflösung erreicht ist, die es erlaubt Seitenketten zuzuordnen.

Sekundär-aktive Transporter nutzen die Energie, die in einem Substratgradienten liegt, um ein zweites Substrat gegen das Konzentrationsgefälle zu transportieren. Dabei können die gekoppelten Substrate entweder in die gleiche oder in die entgegengesetzte Richtung transportiert werden. Entsprechend wird dann von einem Co- oder Antiport gesprochen. Der sekundär-aktive Symporter BetP von *Corynebacterium glutamicum* gehört zu der Familie der BCC-Transporter und wird bei einem osmotischen Schock aktiviert. Die Änderung der externen Osmolalität wird von BetP auf zwei verschiedene Arten wahrgenommen. Einerseits erkennt BetP Änderungen im physikalischen Zustand der Membran, andererseits misst die C-terminale Domäne von BetP die interne Kaliumkonzentration. Im aktivierten Zustand transportiert BetP zwei Natriumionen entlang und ein Glycinbetain Molekül gegen das Konzentrationsgefälle. Dieses System erlaubt es der Zelle, bis zu 2 M Glycinbetain im Zytoplasma zu akkumulieren, wodurch der Wasserausstrom aus der Zelle zum Erliegen kommt. Das sichert der Zelle das Überleben unter extremen osmotischen Bedingungen. Glycinbetain erhöht nicht nur das osmotische Potential des Zytoplasmas, sondern wirkt zusätzlich als Faltungshelfer und Chaperon. Die Struktur einer N-terminalen Deletionsmutante von BetP wurde erstmals im Jahr 2009 mittels Röntgenkristallographie gelöst. BetP bildet ein Trimer, indem jedes Monomer eine funktionelle transportierende Einheit darstellt. Weitere Strukturen von BetP zeigen verschiedene Zustände, die das Protein während des Transportes von Glycinbetain einnimmt. Bis heute ist BetP das einzige Protein, das in nahezu allen möglichen Transportzuständen des "Alternating-Access-Cycle" kristallisiert wurde. Dadurch kann der Transportmechanismus von BetP detailliert beschrieben werden. Allerdings gibt es bisher wenig strukturelle Informationen, an Hand deren der Regulationsmechanismus von BetP und die Rolle der N-terminalen Domäne aufgeklärt werden kann. Ein Grund dafür ist, dass die C-terminale Domäne in allen Kristallstrukturen an einem wichtigen Kristallkontakt beteiligt ist, sodass dieser unabhängig von den (in)aktivierenden Bedingungen in einem künstlichen Zustand gehalten wird. Es wird angenommen, dass die C-terminalen Domänen von BetP ihre Konformationen in Anwesenheit von Kaliumionen ändern, was zu einer Aktivierung von BetP führt. Aus biochemischen und strukturellen Daten ist bekannt,

dass die C-terminale Domäne mit Lipiden in der Plasmamembran wechselwirkt. Eine weitere Hypothese ist, dass die amphiphatische Helix (h7) den Sensor für Veränderungen im physikalischen Zustand der Membran bildet. Um mehr strukturelle Informationen über die N- und C-terminale Domäne von BetP zu bekommen, wurde die Struktur von BetP mittels Einzelpartikel Kryo-EM bestimmt.

Die Einzelpartikel Kryo-EM Struktur von BetP mit einer Auflösung von 6.8 Å zeigt deutliche Unterschiede zu den bisher gelösten Röntgenkristallstrukturen. Der größte Unterschied liegt in der C-terminalen Domäne, die eine neue Orientierung aufweist. In der EM Struktur liegt die C-terminale Domäne dicht am Protein und ist im Vergleich zu den Kristallstrukturen um $\sim 30^\circ$ rotiert. Die neue Lokalisierung ermöglicht Interaktionen zwischen positiv geladenen Resten des C-terminalen Domäne und negativ geladenen Phospholipidkopfgruppen, die in der zentralen Kammer von BetP binden. Der zweite Unterschied ist, dass h7 im Vergleich zu den Röntgenkristallstrukturen in Richtung Periplasma verschoben ist. Damit kommt sie auf der Höhe der Phospholipidkopfgruppen der Plasmamembran zu liegen. Diese Orientierung unterstützt die Annahme, dass h7 Änderungen im physikalischen Zustand der Membran erkennen kann. Die Kryo-EM Struktur zeigt BetP in einem nach innen geöffneten Zustand, der im Vergleich zu den Kristallstrukturen weiter geöffnet ist. Da die Kryo-EM Struktur von BetP nur in Anwesenheit von Natrium-, nicht aber von Kaliumionen und Glycinbetain bestimmt wurde, wird angenommen, dass es sich bei der Struktur um den inaktiven Zustand von BetP handelt. Es wird vermutet, dass sich die Orientierung der C-terminalen Domäne bei Aktivierung ändert und eine Position wie in den Kristallstrukturen einnimmt. Das hat eine Neuorientierung von h7 zur Folge, die ebenfalls an der Regulation von BetP beteiligt ist. Die Kombination von Kristall- und EM-Struktur erlaubt eine strukturelle Beschreibung des Regulationsmechanismus von BetP. Eine Untersuchung des aktiven Zustandes von BetP mittels Einzelpartikel Kryo-EM könnte den aktiven Zustand von BetP, wie er in der Röntgenkristallstruktur zu sehen ist, bestätigen.

Rotierende ATPasen sind membrangebundene Enzymkomplexe, die eine essentielle Rolle bei der zellulären Energieumwandlung spielen. Je nach Typ der ATPase und der zellulären Umgebung nutzen diese entweder die Energie, die bei der Hydrolyse von Adenosintriphosphat (ATP) entsteht um einen Ionengradienten über einer Membran aufzubauen oder sie nutzen diesen Gradienten um den zellulären Energieträger ATP zu generieren. Es gibt drei Arten von rotierenden ATPasen, die als F-, A- und V-Typ ATPasen bezeichnet werden. Die F-Typ ATPasen kommen in allen Domänen des Lebens vor und sind die am besten untersuchte Gruppe. Sie sind hauptsächlich für die Synthese von ATP verantwortlich. A-Typ ATPasen sind

vorwiegend in Archaeen zu finden und können sowohl ATP synthetisieren als auch hydrolysieren. V-Typ ATPasen nutzen ausschließlich die Energie der ATP Hydrolyse um einen Ionengradienten aufzubauen. Sie kommen in Zellorganellen von Eukaryoten vor, z.B. den Vakuolen. Eine bioinformatische Studie aus dem Jahr 2010 zeigte, dass in einigen prokaryotischen Zellen neben der F-Typ noch eine weitere rotierende ATPase, die N-Typ ATPase, in dem Genom codiert ist und deswegen in der Zelle existieren könnte. Aus Sequenzvergleichen ging hervor, dass diese ATPasen den F-Typ ATPasen vermutlich sehr ähnlich sind. Alle rotierenden ATPasen haben einen vergleichbaren Aufbau: Sie bestehen aus einem löslichen (F_1) und einem membrangebundenen (F_0) Teil. In der löslichen Domäne befinden sich die katalytischen Bereiche, in denen ATP Moleküle entweder synthetisiert oder hydrolysiert werden. Zu den membrangebundenen Untereinheiten gehört unter anderem der Rotor- oder c-Ring. Dieser Ring transportiert entweder Natriumionen oder Protonen über die Membran. Dabei bindet er die Ionen von einer und entlässt diese auf der anderen Membranseite, nachdem er einmal um fast 360° rotiert ist. Eine zum Membranstator gehörige Untereinheit dieses Enzymkomplexes verhindert dabei, dass die Ionen ohne Rotation über die Membran gelangen. Die Energie, die bei der Rotation oder der ATP Hydrolyse entsteht, wird durch einen zentralen Schaft zwischen dem Rotor-Ring und den katalytischen Bereichen übertragen. Unter ATP hydrolysierenden Bedingungen wird eine Rotation des Rotor-Rings in die Richtung erzwungen, welche zur Bildung eines Protonen- oder Natriumionengradienten führt, während unter ATP bildenden Bedingungen ein Protonen- oder Natriumionengradient die Rotation des Rotor-Rings in die gegenläufige Richtung erzeugt. Die Rotor-Ringe der F-Typ ATPasen sind am Besten untersucht und bestehen je nach Spezies aus 8 - 15 identischen Untereinheiten. Dabei transportieren sie ein Ion pro Untereinheit und da während einer Rotation von 360° drei ATP Moleküle gebildet werden, kann aus der Anzahl der Untereinheiten auf das Ionen-zu-ATP Verhältnis geschlossen werden. In dieser Arbeit wurde gezeigt, dass der Rotor-Ring der N-Typ ATPase von *Burkholderia pseudomallei* aus 17 identischen Untereinheiten aufgebaut ist. Damit hat dieser Rotor-Ring das größte bisher bekannte Ionen-zu-ATP Verhältnis und ermöglicht es der N-Typ ATPase theoretisch auch bei sehr geringer protonenmotorischer Kraft noch ATP zu generieren.

In diesem Teil der Doktorarbeit lag der Fokus auf der Strukturbestimmung des Rotor-Rings der N-Typ ATPase von *B. pseudomallei* mit Hilfe von Einzelpartikel Kryo-EM. Der Proteinkomplex zeigte eine hohe Stabilität in vielen verschiedenen amphiphatischen Molekülen, was es ermöglichte den Effekt dieser Moleküle auf die Strukturbestimmung zu untersuchen. Dazu wurden Einzelpartikel Kryo-EM Analysen des Rotor-Rings in Amphipol A8-35, n-Dodecyl- β -D-

Maltosid (DDM), Octaethylen Glycol Monododecyl Ether (C₁₂E₈) and Lauryldimethylamin-N-oxid (LDAO) durchgeführt. Es konnte gezeigt werden, dass bei diesem sehr kleinen Membranprotein die Wahl des Detergenzes für den Erfolg der Strukturbestimmung ausschlaggebend war. Entscheidend waren dabei die Dichte und die Mizellengröße des Detergenz. Die Struktur des Rotor-Rings konnte mit Hilfe von Einzelpartikel Kryo-EM gelöst werden, wenn dieser durch LDAO, einem Detergenz mit sehr geringer Dichte und kleiner Mizelle, in Lösung gehalten wurde. Die 6.1 Å Struktur zeigt sehr große Ähnlichkeiten zu bereits bekannten Strukturen von F-Typ ATPase Rotor-Ringen. Die Kryo-EM Dichte bestätigte die 17-fache Symmetrie des Rotor-Rings und zeigte, dass er eine Höhe von ~65 Å und einen Durchmesser von ~65 Å auf der zytoplasmatischen und von ~70 Å auf der periplasmatischen Seite aufweist.

Abstract

Electron microscopy covers a wide range of resolutions and object sizes. The technique was used in this work to answer cell biological questions about the human TRP channel polycystin-2 (PC-2) and to solve the structures of PC-2, the secondary-active transporter BetP from *C. glutamicum*, as well as the N-type ATPase rotor ring from *B. pseudomallei*.

TRP channels exclusively found in eukaryotes were identified and grouped into subfamilies by sequence homology. To date six subfamilies, namely TRPC (“canonical”), TRPA (“ankyrin”), TRPM (“melastatin”), TRPV (“vanilloid”), TRPML (“mucolipin”) and TRPP (“polycystin”) are known. In general, TRP channels are tetrameric, non-selective cation channels that initiate several cellular responses after activation by changing the intracellular Ca^{2+} concentration. The first structures of TRP channels were obtained by single-particle cryo-EM showing that TRP channels consist of six transmembrane helices with a cytoplasmic N- and C-terminal domain. Sequence homology within the TRP channel family is predominantly found in the transmembrane region whereas the cytoplasmic N- and C-terminal domains are very diverse. That is why the total sequence homology of the TRP channel family is only ~20 %. To date the structures of the TRPV1, TRPV2 and TRPA1 channels are known. This study focused on the structural and functional investigation of the human TRP channel polycystin-2 (PC-2). PC-2 is involved in the human inheritable autosomal dominant polycystic kidney disease. The function of PC-2 depends on its cellular localization. On the one hand it is proposed to be an intracellular calcium dependent calcium release channel remaining in the endoplasmatic reticulum, on the other hand it forms a non-selective cation channel at the plasma membrane, while in complex with polycystin-1 it is proposed to act as a mechanosensitive channel.

The genes of PC-2 and different C-terminal truncation mutants were successfully cloned into the genome of GnTI⁻ cells and laser confocal scanning and electron microscopy were used to investigate the cellular localization. Surprisingly, the expression of PC-2 causes the formation of crystalloid ER, which has already been observed before after an overexpression of HMG-CoA reductase in UT-1 cells. The formation of crystalloid ER was connected to ER proteins involved in lipid biogenesis. Although PC-2 is not directly involved in lipid biogenesis, it plays a regulatory function for the repair mechanism of the lipid bilayer. Truncation of the second C-terminal coiled-coil domain inhibited crystalloid ER formation and led to exclusive plasma membrane localization. Further truncation of the C-terminal domain to PC-2 Δ 273 increased the amount of protein remaining in the ER causing the formation of small crystalloid patches. PC-2

was expressed in sufficient amounts for further biochemical and structural studies. The oligomeric state of PC-2 was investigated by native-PAGE and confirmed that PC-2 forms a tetramer. During the purification of PC-2 negative-stain electron microscopy was used to test sample quality. After several steps of optimization a pure PC-2 sample was obtained by using a mixture of lauryl maltose neopentyl glycol (LMNG) and cholesteryl hemisuccinate (CHS) as detergents. For single-particle cryo-EM studies LMNG/CHS was exchanged by amphipol A8-35 that resulted in a 4.6 Å structure. The structure of PC-2 revealed that the membrane domain is similarly organised to the previously determined TRP channels TRPV1, TRPV2 and TRPA1. In contrast to these channels PC-2 has an extracellular domain of ~25 kDa, which is highly ordered and was resolved in the EM density.

Secondary-active transporters are ubiquitous membrane proteins that facilitate the transport of their substrate against its concentration gradient. BetP from *Corynebacterium glutamicum* transports the osmolyte glycine betaine together with two sodium ions. The protein assembles as a stable trimer, in which each monomer forms a transporting subunit. BetP is activated during an osmotic downshift in which water flows out of the cell. On the one hand the accumulation of glycine betaine prevents water efflux while on the other hand it stabilizes cytoplasmatic proteins. BetP recognizes the osmotic downshift by an increase of the intracellular K⁺ concentration combined with a stimulus that is perceived via the membrane. For the activation of BetP the N- and C-terminal domains of the protein are essential. Whereas the function of the N-terminal domain is still not known in detail, the C-terminal domain is crucial for K⁺ sensing. To date many different X-ray structures of N-terminally truncated, surface-engineered BetP mutants were solved showing BetP in almost every state of the alternating access cycle. Therefore the alternating access mechanism can be described in detail for this transporter. However, the molecular mechanism of activation in BetP is still under investigation especially because structural information about the N- and C-terminal domains is sparse.

Single-particle electron cryomicroscopy was used to determine the structure of full-length BetP. The obtained 6.8 Å structure shows a different state of BetP compared to all known X-ray structures. For the first time all C-terminal domains of BetP were completely resolved indicating a new orientation of this domain. In contrast to the X-ray structures, the C-terminal domains are located closer to BetP and rotated by ~30°. The proximity of the C-terminal α -helix to the cytoplasmic side of BetP allows the interaction of C-terminal arginines with POPG molecules bound in the central cavity of BetP. The second difference between the EM and X-ray structures is the position of the amphiphatic helix (h7). In the EM structure h7 is shifted towards the

periplasm close to the headgroups of the lipid bilayer. Such a positioning supports the hypothesis that h7 is important for membrane curvature sensing. The cryo-EM density reveals a new inward-open state of BetP in which the cytoplasmic gate is more open compared to all known X-ray structures. It is proposed in this work that the cryo-EM structure of BetP represents an inactive state. This is supported by the fact that no K^+ and glycine betaine were added during sample preparation and the fact that the C-terminal domain undergoes conformational changes during activation. Although the cryo-EM structure revealed new details about BetP, the N-terminal domain was not visible, indicating that this domain is flexible.

Rotary ATPases are ubiquitous macromolecular machines involved in energy conversion and are classified as F-, A- and V-type ATPases. All rotary ATPases have a similar architecture with a soluble and a membrane-embedded domain. The soluble domain contains the catalytic sites for ATP generation/hydrolysis. The membrane domain transports H^+ or Na^+ across the membrane. Both domains contain stator and rotor subunits. In the membrane domain the rotor is formed by a rotor or c-ring, which is connected via a central stalk to the soluble catalytic domain for ATP generation/hydrolysis. Under ATP synthesizing conditions, ions are transported along their concentration gradient resulting in a rotation of the c-ring. The energy of the c-ring rotation is transmitted via the central stalk to the catalytically active nucleotide-binding sites resulting in ATP generation. Under ATP hydrolysing conditions, the central stalk transmits energy from ATP hydrolysis to the c-ring, which then rotates and transports ions against their concentration gradient. The number of ion-binding sites in the c-ring defines how many ions are transported during the synthesis/hydrolysis of three ATP molecules. Several X-ray structures of F-type ATPase rotor rings revealed that they are composed of 8 - 15 identical copies. In 2010, a bioinformatics study reported that next to the F-, V- and A-type ATPases a novel type of rotary ATPases presumably exists which was hence named N-type ATPase. N-type ATPases were proposed to be closely-related to F-type ATPases, although the corresponding *N-atp* operon has a different gene organization. N-type ATPases might be either proton or sodium ion selective or they could also appear with a promiscuous ion selectivity.

To investigate the structure of the N-type ATPase rotor ring from *Burkholderia pseudomallei* a single-particle cryo-EM study was performed in collaboration with Sarah Schulz (group of Dr. Thomas Meier, Department of Structural Biology, MPI of Biophysics Frankfurt; now Prof. and Chair of Structural Biology, Imperial College London, UK). This study revealed that the protein complex is composed of 17 identical c-subunits forming a ring with the highest number of subunits known so far. Consequently, the rotor ring has the highest ion-to-ATP ratio of all so far

known rotary ATPases. In this work, the c_{17} ring was confirmed by a 6.1 Å cryo-EM structure. Based on the cryo-EM density and a homology model calculated on the *B. pseudomallei* c-subunit sequence a model of the c_{17} ring was built. The N-type ATPase c-ring has a height of ~65 Å, a diameter of ~65 Å at the cytoplasm and of ~70 Å at the periplasm. Like other membrane proteins, the c-ring has to be embedded in an amphiphatic molecule to keep the protein in aqueous solutions. Strikingly, the rotor ring was stable in the presence of many different detergents, allowing the analysis of their impact on single-particle cryo-EM structure determination. Four different cryo-EM datasets of the rotor ring in the surfactant amphipol A8-35 and the detergents n-dodecyl-β-D-maltoside (DDM), octaethylene glycol monododecyl ether (C₁₂E₈) and lauryldimethylamine-N-oxide (LDAO) were recorded and analyzed. These amphiphatic molecules differ in their density and their micelle size. With lower detergent density more details of the rotor ring became visible in the 3D volume. However, only the reduction of both, the density and the micelle size, finally allowed structure determination of the rotor ring. This indicates that for single-particle cryo-EM of this small membrane protein the detergent used for analysis is a decisive factor in structure determination. The structure of the N-type ATPase rotor ring from *B. pseudomallei* is the first structural information of an N-type ATPase enlarging the known rotor ring stoichiometries from 15 to 17.

1 Introduction

1.1 Transient receptor potential (TRP) channel family

Transient receptor potential (TRP) channel family members were identified and grouped by sequence homology instead by ligand function or ion selectivity as it was done for other ion channels (Huang, 2004). More than 30 mammalian TRP channels have been identified and grouped into six subfamilies, namely TRPC (“canonical”), TRPA (“ankyrin”), TRPM (“melastatin”), TRPV (“vanilloid”), TRPML (“mucolipin”) and TRPP (“polycystin”) (figure 1) (Clapham *et al*, 2005).

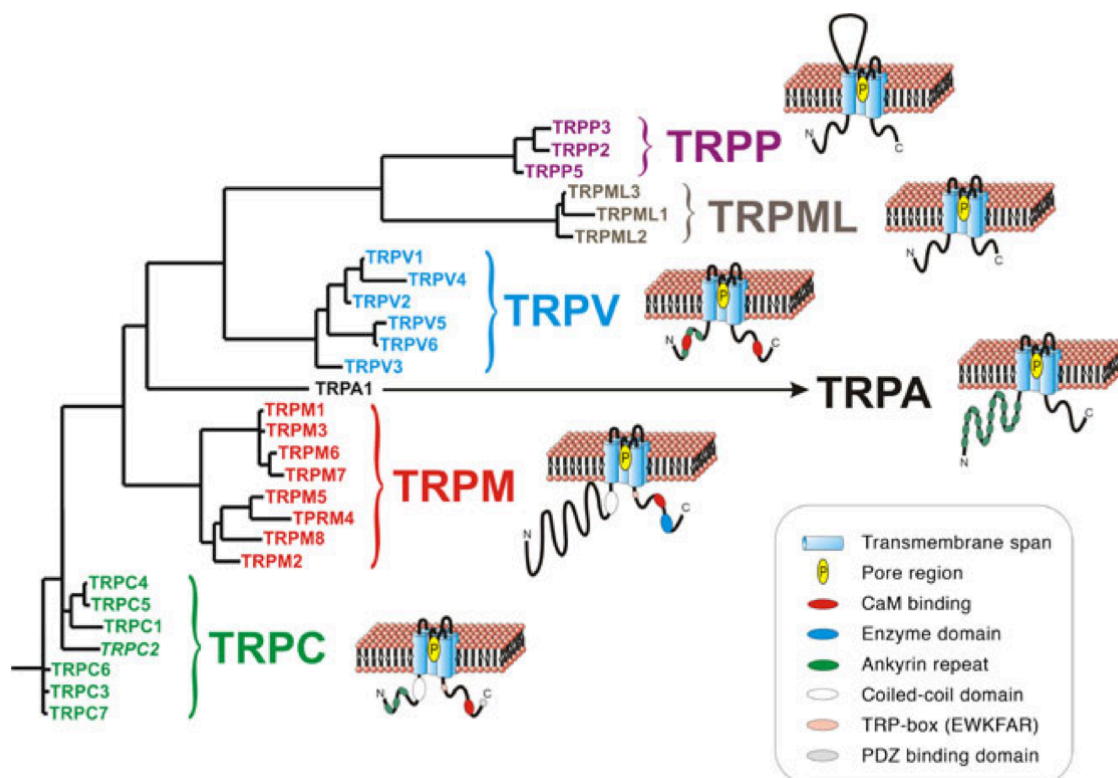


Figure 1: The TRP channel family

The TRP channel family is divided into six subfamilies named TRPC, TRPM, TRPA, TRPV, TRPML and TRPP. The membrane domain is conserved within the TRP channel family, whereas the cytoplasmic soluble domains are diverse. A soluble extracellular domain is only found in the TRPP subfamily. The figure was taken from (Nilius *et al*, 2005).

TRP channels are tetrameric, non-selective cation channels that initiate several cellular responses by mediating a change of the intracellular Ca^{2+} concentration after their activation (Wu *et al*,

2010). They consist of six transmembrane spanning domains with a pore domain between the fifth and sixth transmembrane segment and intracellular N- and C-termini (Liao *et al*, 2013; Paulsen *et al*, 2015). TRP channels are commonly found in epithelial cells but due to their variety of activation stimuli they are also widely spread in almost all other cell types (Wu *et al*, 2010).

1.1.1 Architecture of TRP channels

High-resolution structural information of TRP channels was limited for a long time to their soluble domains due to the difficulty of producing sufficient quantities of full-length protein for 3D crystallization (table 1) (Hellmich *et al*, 2014). In the last few years dramatic technical improvements in electron cryomicroscopy (cryo-EM) allowed determination of high-resolution structures of proteins ≤ 200 kDa (Bai *et al*, 2015b; Kühlbrandt, 2014; Li *et al*, 2013). Single-particle cryo-EM is a method that requires only small amounts of pure protein compared to X-ray crystallography and will be an important tool for future TRP channel structural biology. Using this method three TRP channels, TRPV1, TRPV2 and TRPA1 have been solved to 3.4 Å, 3.8 Å and 4.0 Å resolution, respectively (Liao *et al*, 2013; Paulsen *et al*, 2015; Zubcevic *et al*, 2016). These structures provide striking insights into the architecture of the TRP channel family. High-resolution structures of other TRP channel family members will further help to understand their function and mechanism. The first TRP channel structure, the one of TRPV1, is briefly reviewed in the next chapter.

Table 1: Structures of TRP channels and TRP channel domains (ARD, ankyrin repeat domain; CaM, calmodulin; PC 1, polycystin-1; PC 2, polycystin 2)

	Organism	Protein	Fragment	Resolution	PDB / reference
EM	Rat	TRPV1	Full-length	3.4-4.2 Å	3J5Q / 3J5Q / 3J5R (Cao <i>et al</i> , 2013; Liao <i>et al</i> , 2013)
	Human	TRPA1	Full-length	4.0 Å	3JPQ (Paulsen <i>et al</i> , 2015)
	Rabbit	TRPV2	Full-length	3.8 Å	5AN8 (Zubcevic <i>et al</i> , 2016)
	Mouse	TRPC3	Full-length	15 Å	(Mio <i>et al</i> , 2007)
	Mouse	TRPA1	Full-length	16 Å	(Cvetkov <i>et al</i> , 2011)
	Rat	TRPV1	Full-length	19 Å	(Moiseenkova-Bell <i>et al</i> , 2008)

	Human	TRPM2	Full-length	28 Å	(Maruyama <i>et al</i> , 2007)	
	Rat	TRPV4	Full-length	35 Å	(Shigematsu <i>et al</i> , 2010)	
X-ray crystallography	Human	TRPV2	ARD+ATP	1.7 Å	2F37 (McCleverty <i>et al</i> , 2006)	
	Mouse	TRPV6	ARD	1.7 Å	2RFA (Phelps <i>et al</i> , 2008)	
	Human	PC-2	Coiled-coil	1.9 Å	3HRO / 3HRN (Yu <i>et al</i> , 2009)	
	Mouse	TRPV3	ARD	1.95 Å	4N5Q (Shi <i>et al</i> , 2013)	
	Rat	TRPV1	C-terminus + CaM	1.95 Å	3SUI (Lau <i>et al</i> , 2012)	
	Rat	TRPM7	Coiled-coil	2.01 Å	3E7K (Fujiwara <i>et al</i> , 2008)	
	Rat	TRPV2	ARD	2.2 Å	2ETA (Jin <i>et al</i> , 2006)	
	Chicken	TRPV4	ARD	2.3 Å	3JXI (Landouere <i>et al</i> , 2010)	
	Human	PC-2L1	Coiled-coil	2.69 Å	3TE3 (Molland <i>et al</i> , 2012)	
	Rat	TRPV1	ARD+ATP	2.7 Å	2PNN (Lishko <i>et al</i> , 2007)	
	Human	PC-2L1	Coiled-coil	2.8 Å	4GIF (Yu <i>et al</i> , 2012)	
	Mouse	TRPM7	A-Kinase	2.8 Å	1IAJ (Yamaguchi <i>et al</i> , 2001)	
	Human	TRPV4	ARD	2.85 Å	4DX1 (Inada <i>et al</i> , 2012)	
	NMR	Human	PC-2	EF hand		2KLD (Schumann <i>et al</i> , 2009)
		Human	PC-2	EF hand		2KQ6 (Petri <i>et al</i> , 2010)
Human		PC-1	PKD domain		1B4R (Bycroft <i>et al</i> , 1999)	

1.1.1.1 Structure of TRPV1

TRPV1 activation is connected to sensing pain caused by hot temperature and vanilloid compounds such as capsaicin, making TRPV1 an important therapeutic target (Szallasi *et al*, 2012). The homotetrameric TRPV1 channel contains an N-terminal cytoplasmic region with six ankyrin repeats, followed by a linker region that is connected to the transmembrane domain formed by six membrane-spanning helices. The pore is formed by a loop between the fifth and sixth transmembrane helix ending in a ~150 amino acids (aa) long cytoplasmic C-terminal stretch. For structure determination flexible domains were removed which did not alter channel

activity (Liao *et al*, 2013). The membrane domain of the tetrameric structure is similar to the corresponding domain of voltage-gated ion channels such as Kv1.2 (Long *et al*, 2005). The transmembrane helices (TMH) 1 - 4 are located on the periphery of the channel, while TMH 5 and 6 tetramerize forming the central ion pore. The high sequence similarity of the membrane domain within the TRP channel family as well as the fact that the same helical arrangement was also observed in the later determined TRPA1 and TRPV2 channel indicate that all TRP channels differ mainly in the architecture of their soluble domains (figure 2) (Paulsen *et al*, 2015; Zubcevic *et al*, 2016).

A special feature of non-selective cation channels, such as TRPV1, TRPV2 and TRPA1, is their short selectivity filter compared to filters of selective cation channels like KcsA (Doyle *et al*, 1998). In the related voltage-gated channels the sensor domain is formed by four conserved arginines in TMH 1 - 4 (Catterall, 2010). These arginines are missing in TRP channels, resulting in much lower voltage sensitivity (Cao *et al*, 2013).

The N-terminal domain of TRPV1 forms ankyrin repeat domains (ARDs) that are involved in the interaction with regulatory molecules and proteins like calmodulin. In the cryo-EM structure, parts of the N-terminal domain were not resolved but could be complemented by high-resolution X-ray structures of the ARDs (Phelps *et al*, 2008; Szallasi *et al*, 2007).

The structures of TRPV1, TRPV2 and TRPA1 gave insights into their activation and regulation and show structural similarities and differences within the TRP channel family (figure 2). TRP channels are activated and inactivated by different stimuli that are sensed in different ways. The soluble domains play an important role in channel regulation and contain the main structural differences within the TRP channel family.

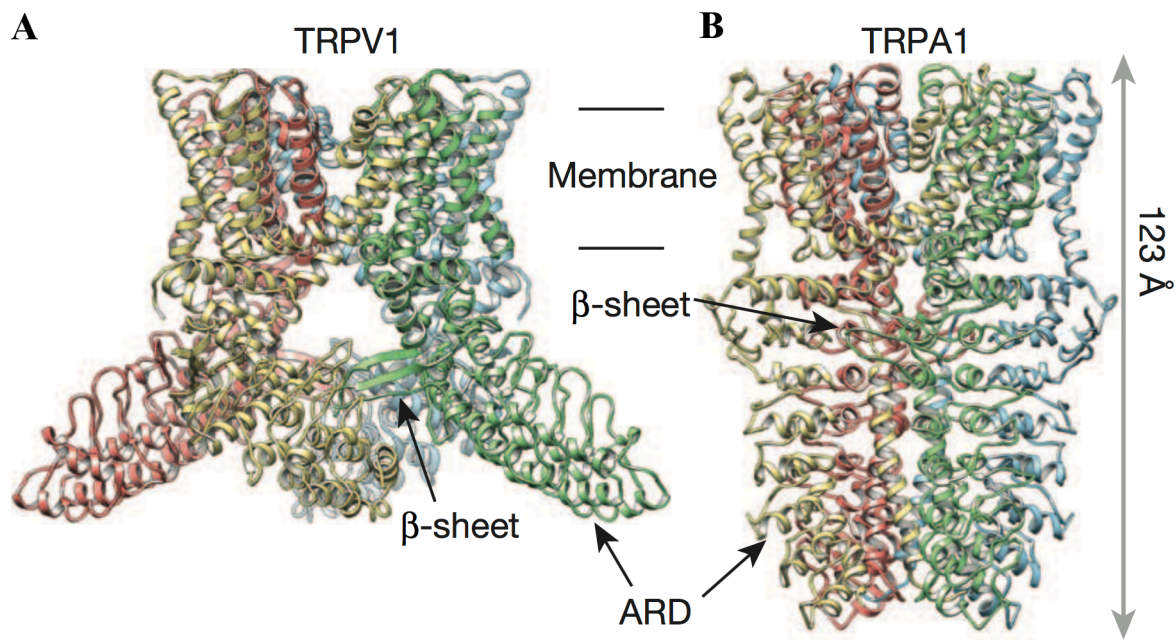


Figure 2: Structure of TRPV1 and TRPA1

The structural comparison between (A) the TRPV1 and (B) the TRPA1 channel reveals that the membrane domain has the same fold whereas the cytoplasmic domains are different. The figure was taken from (Paulsen *et al*, 2015).

1.1.2 TRP channel polycystin-2

The human *PKD2* gene encoding for PC-2 was identified in 1996 (Mochizuki *et al*, 1996). It is located on chromosome 4q21-23, divided into 15 exons and comprises over 68 kb of genomic DNA (Hayashi *et al*, 1997). The final transcript encodes for 968 amino acids forming the 110 kDa PC-2 that is post-translationally glycosylated (Cai *et al*, 1999). Mutation studies revealed that PC-2 contains six transmembrane helices, cytoplasmic N- and C-termini and a ~25 kDa extracellular domain formed by loop 1 (Hoffmeister *et al*, 2011b). Regulatory elements have been identified in the soluble N- and C-terminal domains as well as in the intracellular loop 4 (figure 3). The first 15 N-terminal amino acids of PC-2 contain the RVxP-motif that is important for the transport of PC-2 to the primary cilium in renal epithelial cells (Geng *et al*, 2006). During this transport PC-2 has to pass the Golgi apparatus for which the KxxxF-motif found in loop 4 is essential (Hoffmeister *et al*, 2011a). The C-terminal domain contains a calcium-binding EF-hand (aa 754-782) that influences the activity of PC-2 (Cantiello, 2004; Mochizuki *et al*, 1996). The following endoplasmic reticulum (ER) retention sequence (aa 787-820) is involved in channel trafficking. Between the Ca²⁺ binding motif and the ER retention signal, a coiled-coil domain is predicted as secondary structure (aa 763-796) (Tsiokas *et al*,

1997). However, a functional role of this domain could not be identified so far. A second coiled-coil domain responsible for homodimerization is formed by the amino acid stretch 839 to 873 (Giamarchi *et al*, 2010). Based on the NetGlycate Server 1.0 five glycosylation sites were predicted to be located in the first extracellular loop (Johansen *et al*, 2006).

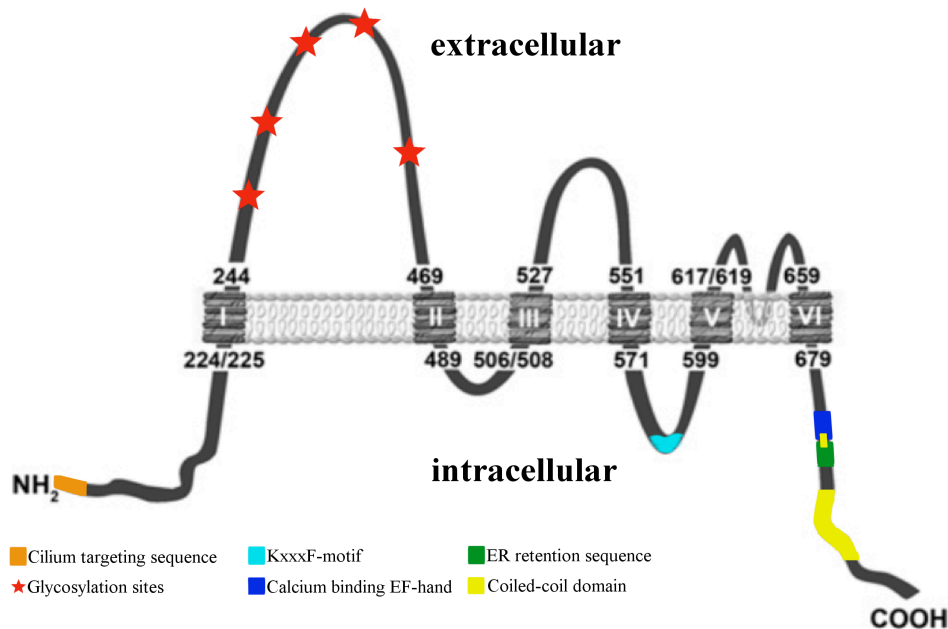


Figure 3: Cartoon model of human PC-2

Functional domains are highlighted in the corresponding colours. The figure was modified from (Hoffmeister *et al*, 2011b).

Like all TRP channels, PC-2 is expected to assemble into tetramers. In addition to the formation of homotetramers, PC-2 seems to be able to interact with other TRP channels assembling into heterotetramers (Tsiokas *et al*, 1997). Increasing evidence points to the fact that PC-2 associates with polycystin-1, a protein with eleven predicted transmembrane helices that is also included in the TRPP channel family (Qian *et al*, 1997a; Tsiokas *et al*, 1997). The second C-terminal coiled-coil domain of PC-2 could be crystallized by the addition of the C-terminal coiled-coil domain of PC-1. In the crystal structure only the C-terminal domain of PC-2 was solved forming a trimer which lead to the conclusion that PC-2 and PC-1 form a heterotetramer with a stoichiometry of 3:1 (Yu *et al*, 2009). It has to be considered that only a trimeric C-terminal coiled-coil domain of PC-2 formed by the amino acid stretch 833 to 895 (62 amino acids) was resolved in the X-ray structure and not the complete C-terminal domain composed of 289 amino acids. However, it is

widely accepted that PC-1 influences the intracellular transport of PC-2 from the ER to the plasma membrane and the primary cilium (Hanaoka *et al*, 2000; Nauli *et al*, 2003).

1.1.3 Function of polycystin-2

PC-2 and homologous proteins as PC-2L1 (PC-2 like protein 1) and PC-2L2 (PC-2 like protein 2) were grouped into the TRPP channel subfamily forming non-selective cation channels (Witzgall, 2005). First functional studies were performed on PC2-L1, indicating 50 % sequence identity and 71 % sequence similarity to PC-2, showing that PC-2L1 is permeable to Na⁺, K⁺, Ba²⁺ and Ca²⁺ (Chen *et al*, 1999). The highest conductance of ~370 pS was measured in the presence of 110 mM KCl (Liu *et al*, 2002). Strikingly, the C-terminal calcium-binding domain of PC-2L1 has no influence on channel activity (Li *et al*, 2002).

Subsequent functional studies on PC-2 revealed that it is permeable for Ca²⁺, Mg²⁺ (Koulen *et al*, 2002), Na⁺, K⁺, NH₄⁺, Li⁺, Rb⁺ (Luo *et al*, 2003; Vassilev *et al*, 2001), Cs⁺ and Ba²⁺ and inhibited by La³⁺ and Gd³⁺ (Gonzalez-Perrett *et al*, 2001). Like other calcium channels, PC-2 is sensitive against the drug amiloride and inhibited by an extracellular calcium concentration of 90 mM (Luo *et al*, 2003; Vassilev *et al*, 2001). The inhibition by extracellular calcium was also described for other Ca²⁺ permeable TRP channels and is suggested to be important to protect the cell against excessive Ca²⁺ influx (Hoenderop *et al*, 1999; Nilius *et al*, 2002). Contrary to other calcium channels, PC-2 is insensitive against the drug nifedipine as well as the intracellular calcium channel regulators inositol trisphosphate (IP₃) and ryanodine revealing that PC-2 is a new type of Ca²⁺ channel (Koulen *et al*, 2002). In addition, it was shown that different to PC-2L1 the intracellular calcium-binding domain of PC-2 is involved in channel regulation by stabilizing the open conformation revealing functional differences between PC-2 and PC-2L1 (Vassilev *et al*, 2001).

Taken together, the precise cellular function of PC-2 is still not known. On the one hand it is suggested that PC-2 remains in the ER forming an intracellular calcium release channel (Koulen *et al*, 2002) and on the other hand it was demonstrated that PC-2 together with PC-1 form a mechanosensor in the primary cilium of kidney cells (Nauli *et al*, 2003). Moreover, whole-cell patch-clamp experiments identified PC-2 as non-selective cation channel in the absence of PC-1 (Luo *et al*, 2003).

However, the consensus of all these studies is that PC-2 activates and deactivates cellular signalling pathways by the second messenger Ca²⁺ independent of its cellular localization.

1.1.4 Subcellular localization of polycystin-2

1.1.4.1 Localization of PC-2 in the endoplasmatic reticulum

The impact of subcellular localization on PC-2 activity is still under investigation. Early studies revealed that PC-2 expressed in HEK293 cells is sensitive against endoglycosidase H (Cai *et al*, 1999) indicating an ER localization, as proteins transported through the Golgi apparatus are resistant against this enzyme (Rothman *et al*, 1980). Other studies, in which PC-2 was expressed in LLC-PK₁ and HeLa cells, confirmed this result by immunofluorescence microscopy revealing a co-localization of PC-2 and the ER protein disulfide isomerase (Gallagher *et al*, 2000; Hidaka *et al*, 2004). The localization of PC-2 in ER membranes in CHO cells was shown by density gradient centrifugation (Hanaoka *et al*, 2000; Koulen *et al*, 2002). These results were supported by an immunofluorescence and electron microscopy study, revealing a morphology change to karmellae and whorl ER during PC-2 expression in HEK293, CHO, COS-7 and MDCK cells (figure 4). Moreover, the second C-terminal coiled-coil domain of PC-2 (aa 839-873) that is important for homodimerization was found to be essential for morphology changes (Giamarchi *et al*, 2010). Deletion of this domain inhibited changes in ER morphology but not the ER localization of PC-2. Previous studies showed that a membrane protein expressed in different cell lines could initiate different ER morphologies. It was suggested that the different lipid composition in these cells is the decisive factor for ER morphology changes (Wright *et al*, 1990).

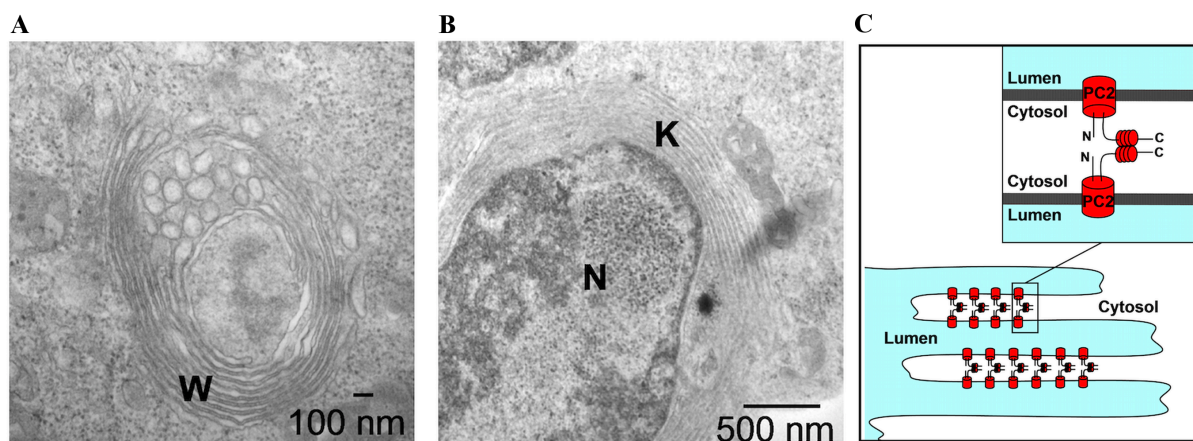


Figure 4: PC-2 expression causes whorl and karmellae ER in HEK293, CHO, COS-7 and MDCK cells

Expression of PC-2 in different cell lines causes a morphology change of the endoplasmatic reticulum into (A) whorl and (B) karmellae ER. (C) The second C-terminal coiled-coil domain of PC-2 was identified to be involved in the ER morphology change pointing to a homotypic interaction of PC-2. The figures were taken from (Giamarchi *et al*, 2010).

1.1.4.2 Localization of PC-2 at the plasma membrane

A study in LCC-PK₁ cells revealed that trafficking of PC-2 from the ER to the plasma membrane is regulated by phosphorylation of S812 by the casein kinase 2. The localization of PC-2 in the ER is mediated by phosphofurin acidic cluster sorting protein-1 and -2 (PACS-1 and PACS-2), which are important to retain proteins in the ER (Kottgen *et al*, 2005). In contrast to these findings PC-2 was detected at the plasma membrane independent of S812 phosphorylation in MDCK and mIMCD cells. In these cells it was possible to measure the function of PC-2 by patch-clamp analysis (Luo *et al*, 2003). The localization of PC-2 at the plasma membrane was also shown in Sf9 (Gonzalez-Perrett *et al*, 2001), EpH4 and HCT8/E8 cells (Scheffers *et al*, 2002).

The inconsistency of the subcellular localization of PC-2 in cell culture studies was also observed *in vivo*. While in adult human and mice PC-2 is located inside the ER of kidney cells (Cai *et al*, 1999; Koulen *et al*, 2002), it was found to be located additionally at the plasma membrane in foetal kidney cells (Ong *et al*, 1999). Besides, in kidney cells PC-2 was found at apical membranes in cells of other organs like the placenta (Gonzalez-Perrett *et al*, 2001), the parotid gland and the submandibular gland (Obermuller *et al*, 1999).

1.1.4.3 Localization of PC-2 in the primary cilium of kidney cells

The localization of PC-2 in the primary cilium of kidney cells was shown *in vivo* (Gallagher *et al*, 2006; Yoder *et al*, 2002) and *in vitro* (Cai *et al*, 1999; Kottgen *et al*, 2005; Streets *et al*, 2006). The N-terminal RVxP-motif was identified to initiate the transport of PC-2 into the cilium independent of C-terminal interaction partners (Geng *et al*, 2006). In addition, the phosphorylation of PC-2 at S812 did not influence the cilium localization (Kottgen *et al*, 2005; Streets *et al*, 2006). The consistency of the PC-2 localization in the primary cilium *in vivo* and *in vitro* within different studies indicates that PC-2 fulfils an important role in this cellular organelle.

Different cellular protein pools might cause the variable subcellular localization of PC-2 in different tissues during growth. However, it has to be considered that the precise cellular function of PC-2 is still unknown. More research is required to understand how PC-2 is activated, regulated and how mutations in this protein can cause autosomal dominant polycystic kidney disease (ADPKD).

1.1.5 Polycystin-2 in autosomal dominant polycystic kidney disease

With a prevalence of at least 0.1 % ADPKD is one of the most common inherited human diseases (Gallagher *et al*, 2002). The main symptom of ADPKD is the formation of fluid-filled cysts within the kidney parenchyma, often accompanied by liver and pancreatic cysts, heart valve defects and aneurysms (Peters *et al*, 1992; Roscoe *et al*, 1993; Torra *et al*, 1996). The fluid-filled cysts in the kidney develop in nephrons, which are the basic structural and functional unit of the kidney. As the disease progresses the cysts expand until they have replaced almost the entire kidney parenchyma that surrounds the nephrons (Harris, 1999). As a consequence of the expanding cysts, the kidney increases 10 - 14 fold in size resulting in a mass of up to 4 kg per kidney. In comparison a healthy kidney has a mass of just 150 g (Martinez *et al*, 1995). In 50 % of all cases ADPKD causes kidney failure at the age of 60.

ADPKD is caused by mutations in two genes, namely *PKD1* and *PKD2* encoding for polycystin-1 and polycystin-2, respectively. In 85 % of all cases mutations in *PKD1* and in 15 % mutations in *PKD2* lead to ADPKD (Peters *et al*, 1992; Roscoe *et al*, 1993; Torra *et al*, 1996). A few patients suffering from ADPKD did not have mutations in *PKD1* or *PKD2*, suggesting that a third gene locus (*PKD3*) is involved. However, this gene locus has not yet been identified (Sutters, 2006). Although patients with mutations in either *PKD1* or *PKD2* show similar phenotypes, the disease progression is slower for patients with mutations in *PKD2* (Veldhuisen *et al*, 1997).

Remarkably, only 5 % of all nephrons of patients suffering from ADPKD develop fluid-filled cysts, which is a low fraction for an autosomal dominant inherited disease. Therefore the two-hit hypothesis was proposed stating that in addition to the germ line mutations somatic mutations are essential for cyst formation (Qian *et al*, 1997b; Wu *et al*, 1998). So far dialysis and kidney transplantations are the only available treatments against ADPKD.

To understand the molecular mechanism of ADPKD, the precise cellular functions of PC-1 and PC-2 as well as the impact of the different subcellular localizations of PC-2 have to be known. Structural information of PC-1 and PC-2 would extend the knowledge of ADPKD tremendously in order to develop a drug-based treatment. These drugs could bind specifically to PC-2 to control channel activity by stabilizing either the closed or opened state.

1.2 Secondary-active transporters

Transporters are membrane proteins that facilitate the specific uptake and release of their substrate(s). They supply the cell with essential nutrients or protect it against toxic substances. Thereby they transport their substrate either along (in the case of uniporters) or against (in case of active transporters) the concentration gradient. Movement against the concentration gradient is energetically unfavoured and requires energy. Depending on the energy source, active transporters are divided into two types: primary- and secondary-active transporters. While the transport of primary active-carriers is directly coupled to ATP hydrolysis, secondary-active transporters commonly require a proton or sodium ion gradient. Secondary-active transporters can further be classified into symporters performing a co-transport of ion(s) and substrate(s) and antiporters transporting substrate(s) and ion(s) in different directions (figure 5). Secondary-active transporters are spread throughout all kingdoms of life and are probably found for every low-molecular weight compound in nature (Saier, 2000).

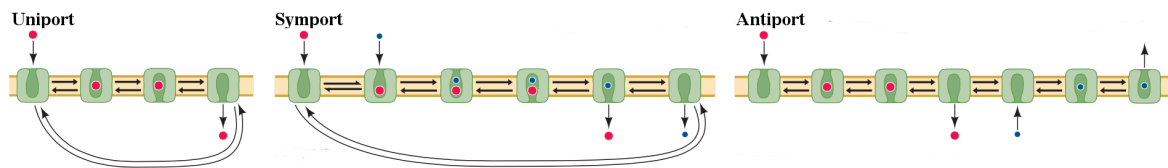


Figure 5: The different transporter types

Uniporters translocate their substrate (red circle) along the concentration gradient. Symporters and antiporters transport two substrates (red and blue circle). The figure was taken from (Forrest *et al*, 2009).

1.2.1 Osmotic stress in bacteria

Osmotic stress in bacteria will occur immediately if the cell is exposed to either a hypo- or hyper-osmotic surrounding, triggering a rapid water flux across the semipermeable plasma membrane (Wood, 1999). Under hypo-osmotic conditions water flows into the cell, driving the turgor to such a magnitude that the cell is threatened to burst. To protect the cell against lysis mechanosensitive channels open thereby releasing ions and solutes (Booth *et al*, 2007). Hyper-osmotic environments lead to a rapid efflux of water resulting in turgor collapse (Record *et al*, 1998). Under this condition the cell growth slows down until it finally stops (Cayley *et al*, 2003). To counteract water efflux, the cell raises the osmotic potential of its interior by the accumulation of either ions or organic osmolytes (Altendorf *et al*, 2009; Wood, 1999). Organic

osmolytes can be accumulated up to two molar inside the cell without affecting the cell's vital functions (Empadinhas *et al*, 2008; Kempf *et al*, 1998; Peter *et al*, 1996). Moreover, these osmolytes stabilize the proper conformation of proteins as well as the formation of protein assemblies thereby maintaining their biological function (Arakawa *et al*, 1985; Bolen *et al*, 2001; Street *et al*, 2010). The best-investigated secondary-active transporter is BetP from *Corynebacterium glutamicum*, which is involved in the accumulation of the osmolyte glycine betaine (Kramer, 2009; Perez *et al*, 2012; Ziegler *et al*, 2010).

1.2.2 Secondary-active transporter BetP from *Corynebacterium glutamicum*

BetP is part of the betaine-choline-carnitine-transporter (BCCT) family that plays a key role in prokaryotic osmotic stress response and comprises about 2200 representatives, predominantly found in bacteria (Saier, 2000). Increasing knowledge on the BCCT family revealed that members of this family can also transport other osmolytes next to betaine, carnitine and choline (figure 6). BCCT transporters are secondary-active transporters. Most transporters of this family share a common hydrophathy profile with twelve predicted transmembrane α -helices connected to a cytoplasmatic N- and C-terminal domain of different length which are important for BCCT regulation (Peter *et al*, 1998).

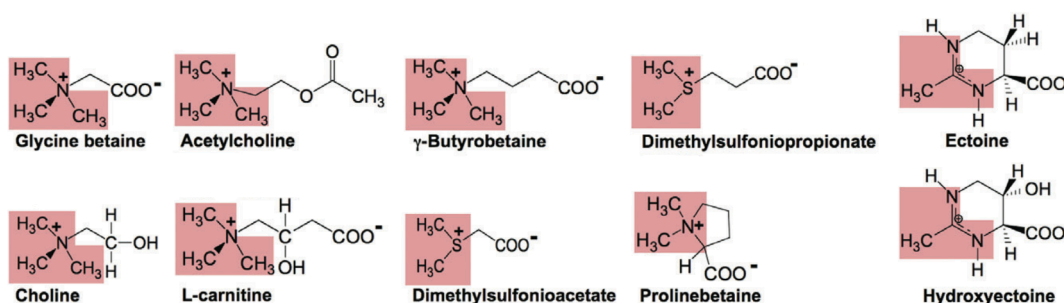


Figure 6: Known compounds transported by carriers of the BCCT family

The positively charged nitrogen and sulphur groups, as well as the delocalized positive charge in ectoine and hydroxyectoine are highlighted in red. The figure was taken from (Ziegler *et al*, 2010).

1.2.2.1 Atomic structure of BetP from *C. glutamicum*

The first X-ray structure of an N-terminally truncated, charged-engineered BetP mutant was determined in 2009 and revealed first structural insights into the BCCT family. BetP crystallized as an asymmetric trimer in which each monomer consists of twelve transmembrane helices (TMH) and an amphiphatic α -helix (called h7) that runs parallel to the cytoplasmic membrane

surface (figure 7). The curved h7 and the long bent TMH 2 provide a hydrophobic scaffold for the transporter centre (figure 7 B) (Ressl *et al*, 2009). This fold was confirmed by a subsequent structure of CaiT, another member of the BCCT family (Schulze *et al*, 2010). CaiT is a sodium and proton-independent antiporter transporting γ -butyrobetaine and carnitine. Sequence alignments revealed that h7 has a conserved length within the BCCT family and that in all cases this helix is capable of hydrophobic and ionic interactions. Therefore it was assumed that all BCCT family members form a stable trimer (Ziegler *et al*, 2010). For BetP all essential residues for trimerization were shown to be located in h7 and TMH 2 (Perez *et al*, 2011).

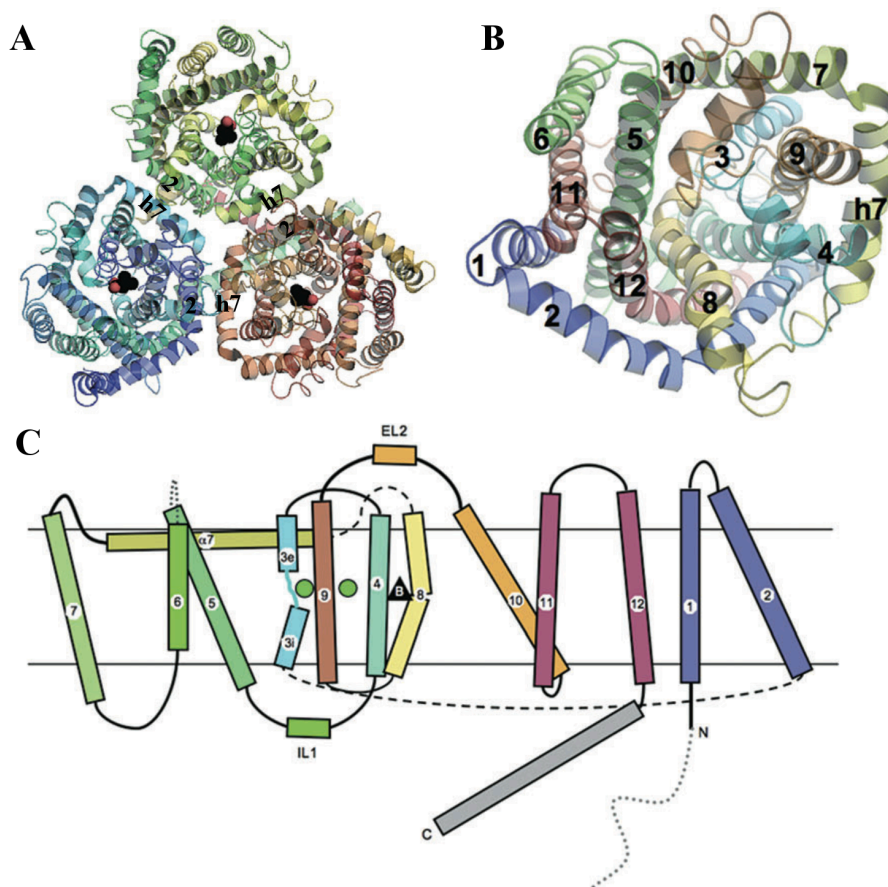


Figure 7: Crystal structure and topological organization of BetP

(A) Crystal structure of BetP from *C. glutamicum* (pdb 2WIT). The view from the periplasm (top view) reveals the trimeric assembly of BetP. TMH 2 and h7 that provide a hydrophobic scaffold for the transporter centre are highlighted. (B) Top view on a BetP monomer. (C) Topological organization of BetP with the two sodium ions indicated as green circles and the substrate glycine betaine as black triangle. TMH 1 - 12 as well as h7 are highlighted in the same colour in B and C. The figures were taken from (Ziegler *et al*, 2010).

In the first X-ray structure of BetP, all protomers are in the substrate-bound, inward-occluded state. Hydrophobic residues in TMH 4 and TMH 8 that are highly conserved within the BCCT family form the substrate-binding site. The substrate is stabilized by cation- π interactions. In BetP glycine betaine is coordinated by W189, W194 and Y197 of TMH 4 and W374 of TMH 8 (figure 8) (Ressl *et al*, 2009).

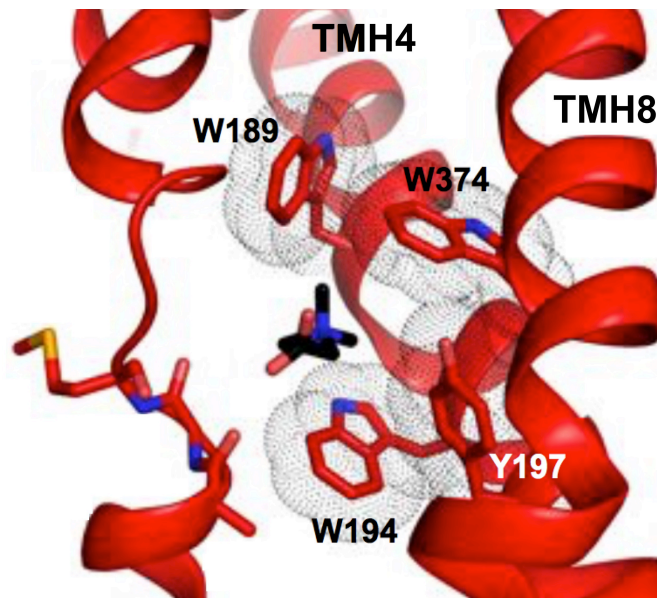


Figure 8: Coordination of glycine betaine in the occluded state of BetP

The aromatic box in BetP is formed by W189, W194 and Y197 of TMH 4 and W374 of TMH 8 stabilizing the substrate glycine betaine by cation- π interactions. The figure was modified from (Perez, 2012).

The ten core transmembrane helices TMH 3 - 12 of BetP adopt a characteristic fold that is found in many other transporters as well. This structural fold comprises an internal two-fold pseudosymmetry with its axis running parallel to the membrane plane through the centre of the transporter. The topology of the first five transmembrane helices (TMH 3 - 7 in BetP) is inverted with respect to the last five transmembrane helices (TMH 8 - 12 in BetP) (figure 9). This fold was initially described for the leucine transporter LeuT from *Aquifex aeolicus* and therefore named the LeuT fold (Yamashita *et al*, 2005). To date the LeuT fold is found in five different transporter families: the neurotransmitter/sodium symporter (NSS) family (Yamashita *et al*, 2005), the solute/sodium symporter (SSS) family (Faham *et al*, 2008), the nucleobase/cation symporter-1 (NCS1) family (Shimamura *et al*, 2010), the amino acid/polyamine/organocation (APC) family (Fang *et al*, 2009) and the BCCT family (Ressl *et al*, 2009).

Next to the pseudosymmetry the LeuT fold is additionally characterized by discontinuous helices where the unwound segments are located in the middle of the helix. These unwound regions allow main-chain oxygens and amino groups to stabilize substrate coordination instead of being involved in helix-stabilizing interactions (Khafizov *et al*, 2010).

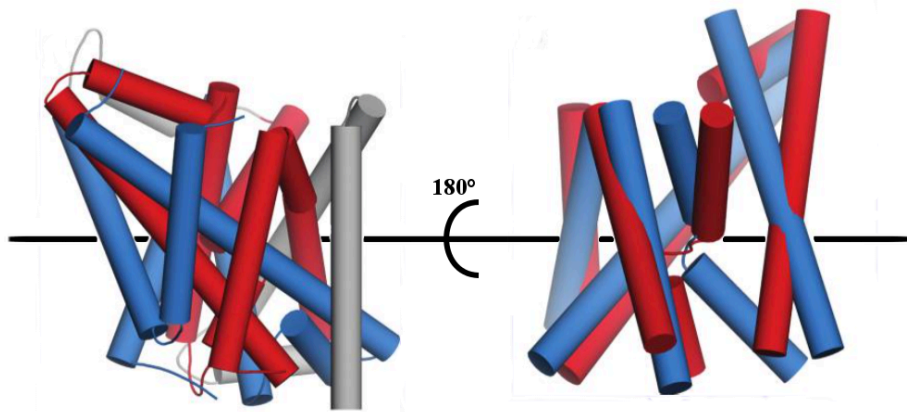


Figure 9: Topology model of the LeuT fold

The two inverted repeats of the LeuT structure (pdb 2A65) are depicted in red and blue, respectively. The two sets of five transmembrane helices can be superimposed by a 180° inversion around an axis parallel to the membrane (black line). The figure was modified from (Khafizov *et al*, 2010).

1.2.2.2 Transport mechanism of BetP from *C. glutamicum*

Many structures of LeuT fold transporters in different conformations are known today. Based on these conformations the “rocking bundle model” (Forrest *et al*, 2009) and the “gating model” (Krishnamurthy *et al*, 2009) for the alternating access mechanism (Jardetzky, 1966) of LeuT fold transporters were proposed.

For the “rocking bundle model” the inward-facing LeuT structure was compared with an outward-facing LeuT model, which was generated by swapping the conformations of the inverted repeats (Forrest *et al*, 2008). Remarkably the threading of TMH 1 - 5 onto the structure of TMH 6 - 10 changes the accessibility of the substrate and ion-binding pocket to the opposite membrane site. This observation was consistent with the alternating access mechanism (Jardetzky, 1966). The changes between the inward- and outward-facing states were proposed to result from a rocking of the bundle formed by TMH 1, 2, 6 and 7. Thereby the TMH 3, 4, 5, 8, 9 and 10 built a stationary scaffold. According to the rocking bundle mechanism the substrate and ion-binding sites would be located at the interface between the moving bundle and the stationary

scaffold. Depending on the bundle position they are alternately accessible from the cytoplasm or periplasm (figure 10) (Forrest *et al.*, 2009). A comparison of the structures of LeuT fold transporters crystallized in the inward- and outward-open state, e.g. Mhp1 and BetP, revealed that the simplification of the rocking bundle model is not consistent with the X-ray structures. X-ray structures revealed that TMH 1 does not move as a rigid body and that there is some degree of independent movement within the helix bundle.

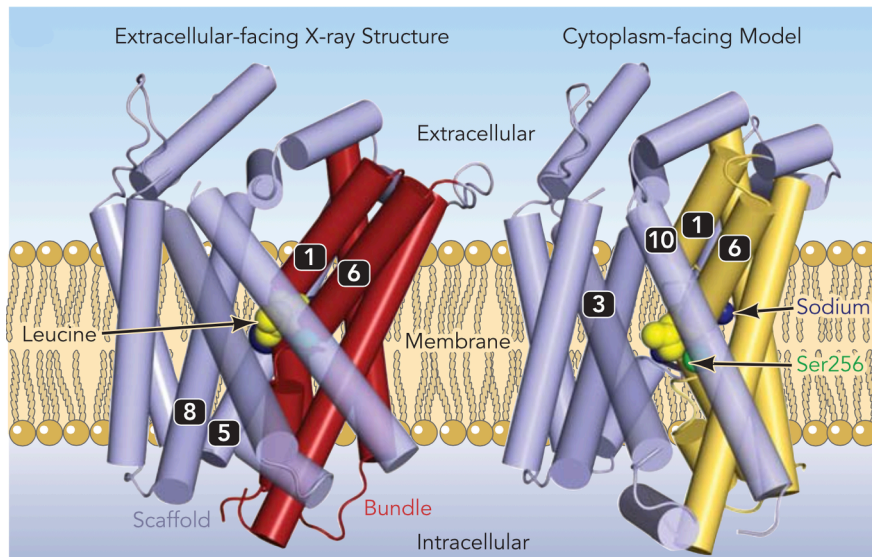


Figure 10: Comparison of the LeuT X-ray structure and the inward-facing LeuT model

The inward-facing model of LeuT was generated by swapping the conformations of the two inverted repeats. The bundle (red or yellow) pivots around the central binding site viewed from the membrane plane approximately at the position of S256. The substrate is highlighted in yellow and the sodium ions in blue. The figure was taken from (Forrest *et al.*, 2009).

The “gating model” for alternating access is based on the X-ray structures of LeuT transporters in the inward- and outward-facing state and assumes that the primary substrate- and ion-binding sites are flanked by two gates controlling the accessibility to these sites (Krishnamurthy *et al.*, 2009). Accordingly, only one gate can open at a time inhibiting the formation of a continuous transmembrane pore (figure 11). One of the gates is formed by side chain residues and called “periplasmic gate” whereas the other gate, called “cytoplasmic gate”, is formed by transmembrane helices. The periplasmic gate opens and closes by relatively small conformational changes whereas the cytoplasmic gate opens and closes by re-orientation of the first helices of each repeat (TMH 1 and TMH 6 or TMH 3 and TMH 8 in LeuT or BetP, respectively) (Shimamura *et al.*, 2010).

Although both, the “rocking bundle” and “gating” models of the alternating access make use of the inherent symmetry of LeuT-fold transporters, it appears that the extent to which each model is valid varies for different LeuT-fold transporters.

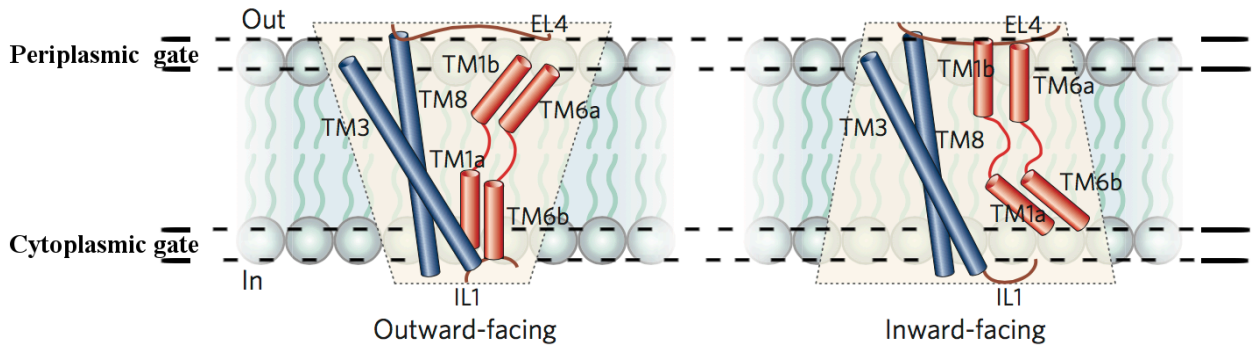


Figure 11: Scheme of the gating mechanism in LeuT

In the outward-facing state the periplasmic gate is open while the cytoplasmic gate is closed. During the movement from the outward- to the inward-facing state the periplasmic gate closes first followed by the opening of the cytoplasmic gate. The figure was modified from (Krishnamurthy *et al*, 2009).

In recent years, further X-ray structures of BetP were solved revealing BetP in different conformational states in addition to the substrate-bound inward-occluded state. As BetP crystallizes as an asymmetric trimer all three protomers can have a different conformation within the crystal. Up to date eight distinct conformations of BetP occurring during the alternating access have been solved (figure 12) (Perez *et al*, 2014; Perez *et al*, 2012; Ressler *et al*, 2009).

Based on the different conformations the alternating access mechanism for BetP has been described in detail revealing that BetP undergoes a hybrid of rocking bundle and gating mechanism that is influenced by sodium binding (Perez *et al*, 2012). In the outward-open state two sodium ions bind weakly to the transporter, first occupying the Na2 site close to the cytoplasm and then the Na1 site at the periplasm (Perez *et al*, 2014). The binding of glycine betaine initiates the closing of the periplasmic gate, which is connected to a tight binding of the sodium ion in the Na1 site by TMH 5, TMH 8 and TMH 11 (corresponding to TMH 3, TMH 6 and TMH 9 in LeuT). Thereby these helices move closely together, resulting in the substrate-bound closed state of BetP.

The release of the sodium ion in the Na2 site triggers the movement of TMH 3 (TMH 1 in LeuT), which is involved in sodium coordination and results in a detachment of TMH 3 from TMH 7 (TMH 1 and TMH 5 in LeuT). This leads to the opening of the cytoplasmic gate and the release

of glycine betaine and the second sodium ion. During the alternating access mechanism the intracellular gates undergo uncoupled hinge movements. It was suggested that the differences in the sodium binding sites in LeuT-fold transporters are responsible for the relative contribution of rigid body rotation versus gating hinge movements in each transporter (Perez *et al*, 2012).

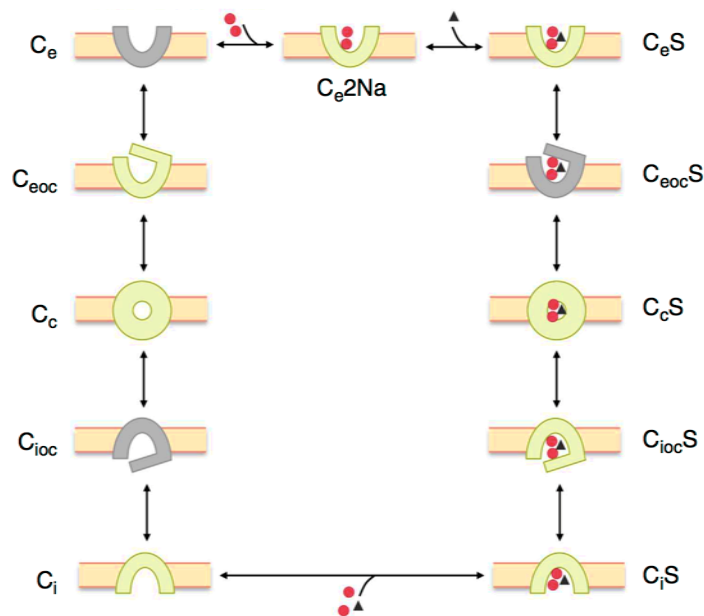


Figure 12: Overview of BetP conformations occurring during the alternating access

Conformations in green were solved by X-ray crystallography whereas no X-ray structure is available for the grey conformations (C_e2Na , substrate-free outward-open sodium bound (pdb 4DOJ); C_eS , substrate-bound outward-open (pdb 4LLH); $C_{eoc}S$, substrate-bound outward-occluded; C_cS , substrate-bound closed (pdb 4AIN); $C_{ioc}S$, substrate-bound inward-occluded (pdb 2WIT); C_iS , substrate-bound inward-open (pdb 4DOJ/3P03/4AIN/4LLH); C_i , substrate-free inward-open (pdb 4AMR); C_{ioc} , substrate-free inward-occluded; C_c , substrate-free closed (pdb 4AIN); C_{eoc} , substrate-free outward-occluded (pdb 4DOJ); C_e , substrate-free outward-open state). The figure was taken from (Perez *et al*, 2014).

A new feature observed in BetP is a spring-like movement of the unfolded region in TMH 3 (TMH 1 in LeuT). Such a movement provides structural flexibility to couple an electrochemically favoured binding and release of ions to an alternating opening and closing of gates (Hunte *et al*, 2005).

Taken together, all structural elements performing the conformational change from an outward- to an inward-facing state of BetP are involved in the formation of the sodium binding sites (figure 13).

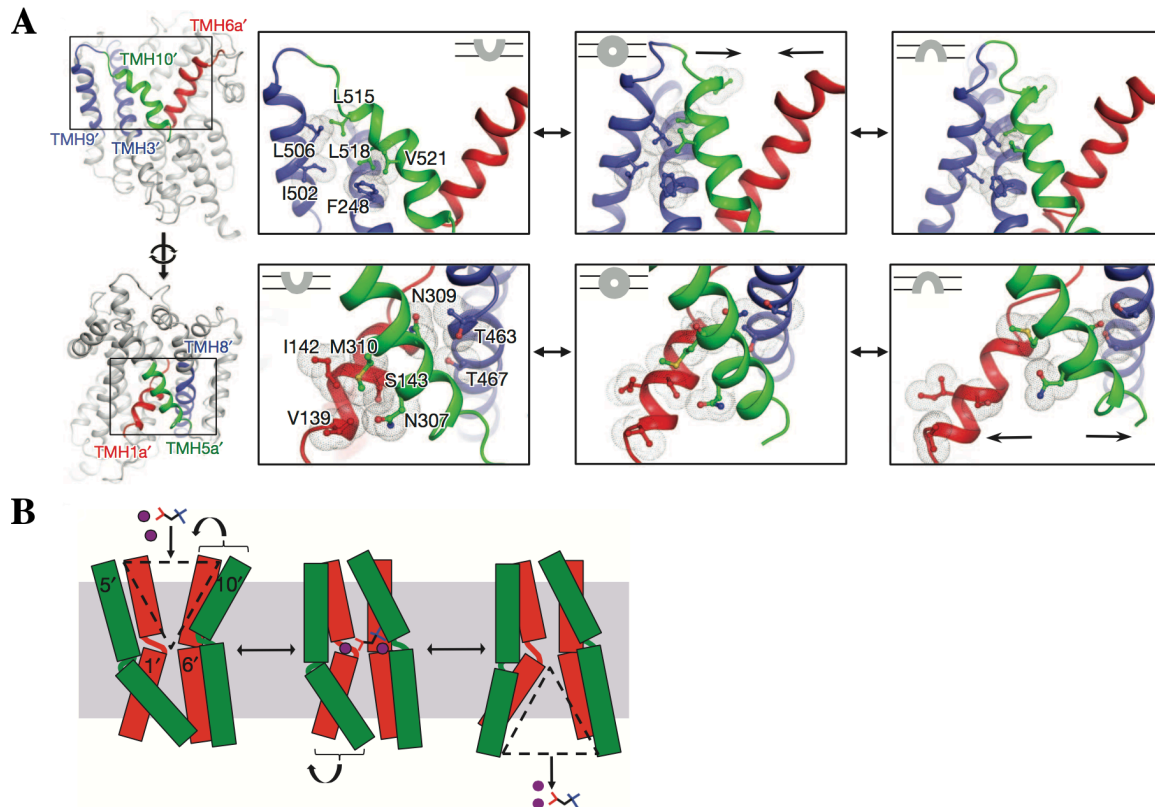


Figure 13: Opening and closing of the periplasmic and cytoplasmic gate in BetP

(A) Sequence of opening and closing of gating main-chains on both sides of the membrane. The Na1 site is connected to the periplasmic gate and formed by T246, T250, F380, A472 and T499 whereas the Na2 site is connected to the cytoplasmic gate formed by A147, N308, F464, T467 and S468. (B) Model of alternating access gating mechanism in BetP. From left to right C_e , C_c and C_i states are shown, glycine betaine is black, blue and red and sodium ions are in purple. Arrows indicate the closing of the periplasmic and the opening of the cytoplasmic gate. Helices are numbered corresponding to the LeuT structure. In BetP TMH 1' is TMH 3, TMH 3' is TMH 5, TMH 5' is TMH 7, TMH 6' is TMH 8, TMH 8' is TMH 10, TMH 9' is TMH 11 and TMH 10' is TMH 12. The figure was taken from (Perez *et al*, 2012).

1.2.2.3 Regulation of BetP from *C. glutamicum*

The multiplicity of potential physical stimuli related to osmotic stress makes it difficult to analyze the sensory input into a transporter protein (Wood, 1999). However, studies of BetP reconstituted in proteoliposomes showed that BetP is capable of responding to osmotic stress in an artificial proteoliposome system (Rubenhagen *et al*, 2000). This allows the analysis of individual physical stimuli on BetP activation. The stimuli important for BetP activation can be distinguished into two classes. The first stimulus is an increase in the intracellular K^+ (Rb^+ or

Cs⁺) concentration (Rubenhagen *et al*, 2001) whereas the second stimulus originates from the membrane (Steger *et al*, 2004).

The increase of intracellular K⁺ concentration as response to a hyper-osmotic shock was found to occur *in vivo* in *E. coli*, *Bacillus subtilis* and *C. glutamicum* (Dinnibier *et al*, 1988; Whatmore *et al*, 1990; Wolf *et al*, 2003). This supports that K⁺ is a signal for osmotic stress (Morbach *et al*, 2005). Mutagenesis studies of the C-terminal domain of BetP revealed that this domain is involved in K⁺ sensing. Interestingly, these studies also show an interaction between the C- and N-terminal domain, suggesting that this interaction plays a role in BetP activation (Ott *et al*, 2008). An X-ray structure of BetP in the presence of RbCl revealed possible K⁺ binding sites clustered around the C-terminal α -helix (Perez, 2012). The C-terminal domains are resolved to different extent in the X-ray structure. While the C-terminal α -helices of chain A and C are oriented to TMH 1 of chain C and B respectively, the C-terminal α -helix of chain B is oriented differently. The asymmetrical C-terminal α -helices may reflect functionally different conformations in the activation cycle revealing that transport regulation is a collective effect of intra-protomer interactions (Ressl *et al*, 2009). It was shown that monomeric BetP is functionally active but not effectively regulated, indicating the importance of the trimeric interaction for transport regulation (Perez *et al*, 2011).

However, the intracellular K⁺ concentration is not the only factor that triggers BetP activation. The second factor is a stimulus perceived via the membrane in which BetP is incorporated (Schiller *et al*, 2006). The influence of the lipid composition was shown *in vitro* and *in vivo*. Whereas BetP reaches the activity maximum in *C. glutamicum* at 1.250 Osm/kg, the activity maximum of heterologously expressed BetP in *E. coli* is already accomplished at lower osmolalities (figure 14). In both cases the activation of BetP is attained in less than a second (Peter *et al*, 1996; Rubenhagen *et al*, 2000). Another aspect supporting the influence of lipids on BetP activation is the fact that BetP is activated by chill stress independent of K⁺ (Ozcan *et al*, 2005). A comparison between the sequences of the amphipathic helix (h7) with the general motif for sensing changes in the lipid bilayer curvature, called amphipathic lipid packing sensor (ALPS or ArfGAP1 lipid packing sensor) motif, revealed some consistent characteristics. Amphipathic helices lack charged residues on their polar surface and therefore associate with the membrane only by their hydrophobic face. This makes them highly sensitive to changes in membrane curvature (Mesmin *et al*, 2007).

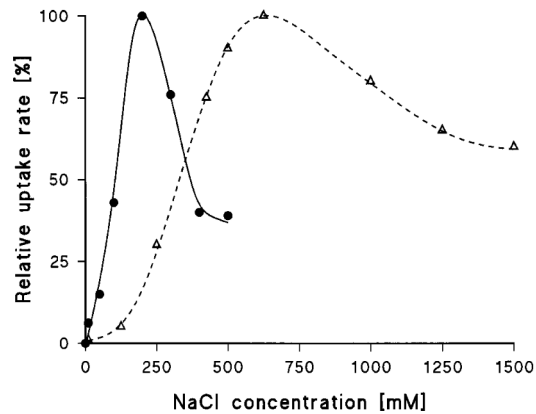


Figure 14: Activation of BetP by osmotic stress in *C. glutamicum* and in *E. coli*

In *C. glutamicum* BetP is completely active at 625 mM NaCl (dashed line) whereas the activation maximum is shifted to lower osmolarity if BetP is expressed heterologously in *E. coli* where it is active at 200 mM NaCl (black line). The figure was taken from (Peter *et al*, 1996).

An X-ray structure of BetP at a resolution of 2.7 Å revealed five 1-palmitoyl-2-oleoyl-sn-glycero-3-phosphoglycerol (POPG) lipids bound in the central cavity of BetP (figure 15) (Koshy *et al*, 2013).

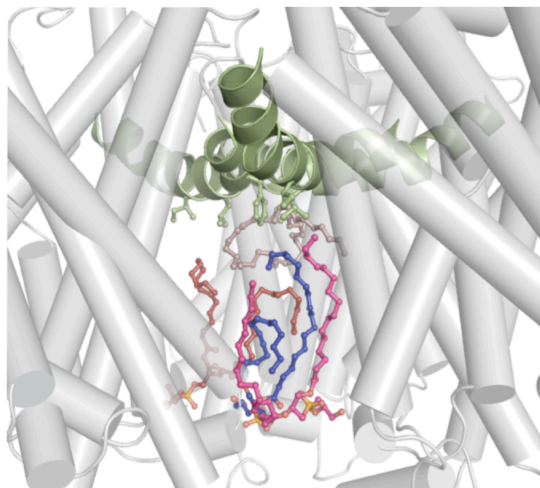


Figure 15: Interaction of POPG molecules in the central cavity of BetP

Five POPG molecules were solved in the X-ray structure of BetP at 2.7 Å interacting with the amphiphatic h7 of each monomer on the periplasmic side and with the C-terminal α -helix of BetP on the cytoplasmic side. The figure was taken from (Koshy, 2014).

These POPG molecules interact with the amphiphatic helix (h7) of the BetP trimer via their hydrophobic tail on the periplasmic side as well as with the C-terminal α -helix via their polar head groups on the cytoplasmic side (figure 15) forming a transducing link between these two sensors (Koshy, 2014).

The current model for BetP activation assumes that under normal physiological conditions positively charged residues of the C-terminal domain of one monomer interact with the negatively charged residues in loop 2 and loop 8 of the adjacent subunit as well as with negatively charged head groups of bound lipids (figure 16 A). Under hyper-osmotic stress the increase of the intracellular K^+ concentration combined with a stimulus sensed at the membrane, which is recognized by h7, initiates a conformational change which alters the interaction network and allows BetP to import glycine betaine. It is assumed that in the activated form the C-terminal domain of one monomer is bound to the N-terminal domain of another monomer stabilizing the activated state (figure 16 B) (Waclawska *et al*, 2015; Ziegler *et al*, 2010).

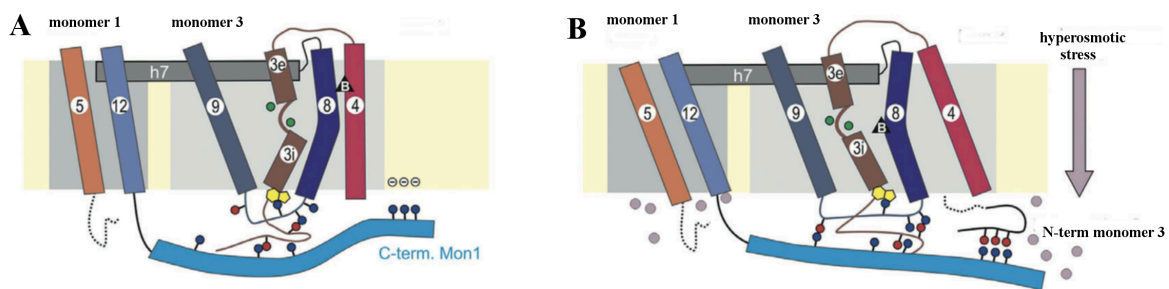


Figure 16: Model for osmoregulatory interactions within a BetP trimer

(A) In the inactive state the C-terminus of monomer 1 interacts with loop 2 and loop 8 of monomer 3 as well as with negatively charged lipids. (B) Under hyper-osmotic stress the increase in the intracellular K^+ concentration (grey circles) in conjunction with a stimulus perceived via the membrane initiates a conformational change activating BetP. As a result the C-terminus of monomer 1 interacts with the N-terminus of monomer 3. The figure was taken from (Ziegler *et al*, 2010).

1.3 Rotary ATPases

Rotary ATPases are ubiquitous macromolecular machines involved in biological energy conversion. They either synthesize or hydrolyze the cellular energy carrier adenosine-5'-triphosphate (ATP). The synthesis of ATP from adenosine-5'-diphosphate (ADP) and inorganic phosphate (P_i) is an energetically unfavourable phosphorylation reaction in cells. To perform this reaction rotary ATPases use either a proton (H^+) or sodium ion (Na^+) gradient. A proton gradient is commonly generated across a membrane by either respiration or photosynthesis (Muench *et al*, 2011; von Ballmoos *et al*, 2009) whereas a sodium ion gradient can be generated during the fermentation of organic compounds like glutamate (Beatrix *et al*, 1990; Boiangiu *et al*, 2005). Rotary ATPases are not only important for ATP generation. In the presence of ATP they can use the energy from ATP hydrolysis to set up a H^+ or Na^+ gradient. This gradient formation is important, for example, for the acidification of intracellular compartments in eukaryotes or to provide a transmembrane electrochemical gradient for the active transport of molecules and ions (Forgac, 2007). The direction in which a rotary ATPase works depends on the kind of enzyme and its inherent possibility to perform ATP hydrolysis/synthesis as well as the ATP concentration inside the cell and the available chemical gradient (Cross *et al*, 2004).

1.3.1 Classification of rotary ATPases

Rotary ATPases can be distinguished according to their different structures and their physiological functions. Up to now three different types of rotary ATPases are characterized and named F-, A- and V-type ATPases. F-type ATPases are ATP synthesizing machines and are found in mitochondria and chloroplasts of eukaryotes and in the plasma membrane of bacteria. The rotary ATPases of archaea (and some bacteria) reside in the plasma membrane and can work either in ATP synthesis or hydrolysis direction. These rotary ATPases are classified as A-type ATP (synth)ases. In the membrane of intracellular eukaryotic organelles, like vacuoles and lysosomes, V-type ATPases are located. These enzymes function exclusively as ATP-driven ion-pumps for intracellular acidification (Muench *et al*, 2011).

1.3.2 Architecture of rotary ATPases

Independent of their physiological function, all rotary ATPases share a similar overall architecture with a soluble and a membrane-embedded domain. The F-type ATP (synth)ase is the most intensively studied rotary ATPase and used to describe the general ATPase architecture (figure 17 A) as well as the structure and function of the soluble and membrane-embedded

domain in more detail (1.3.2.1 and 1.3.2.2). The soluble domain where ATP is either synthesized or hydrolyzed is called F_1 (A_1 or V_1) domain and consists of three alternating α - and β -subunits as well as of one γ -, δ - and ϵ -subunit (Conover *et al*, 1963; Penefsky *et al*, 1960; Pullman *et al*, 1960). While in eukaryotes, the F-type ATP synthase is more complex the basic architecture of the membrane-embedded domain is found in bacteria and formed by the a-, b- and c-subunits and called F_0 (A_0 or V_0) domain in which the c-subunits form the so called c- or rotor ring (Kagawa *et al*, 1966; Stock *et al*, 1999). The F_0 domain facilitates the H^+ or Na^+ transport across the membrane. Both domains are connected via two different types of stalks: a central stalk (formed by the γ - and ϵ -subunits) important for torque transmission and one to three outer stalks (formed by the b- and δ -subunits) for counteracting the rotation, stabilization and regulation (Stewart *et al*, 2013). The number of outer stalks can also be used to identify a rotary ATPase as F-, A- or V-type ATPase. An F-type ATPase has just one, an A-type ATPase two and a V-type ATPase has three outer stalks (figure 17) (Muench *et al*, 2011).

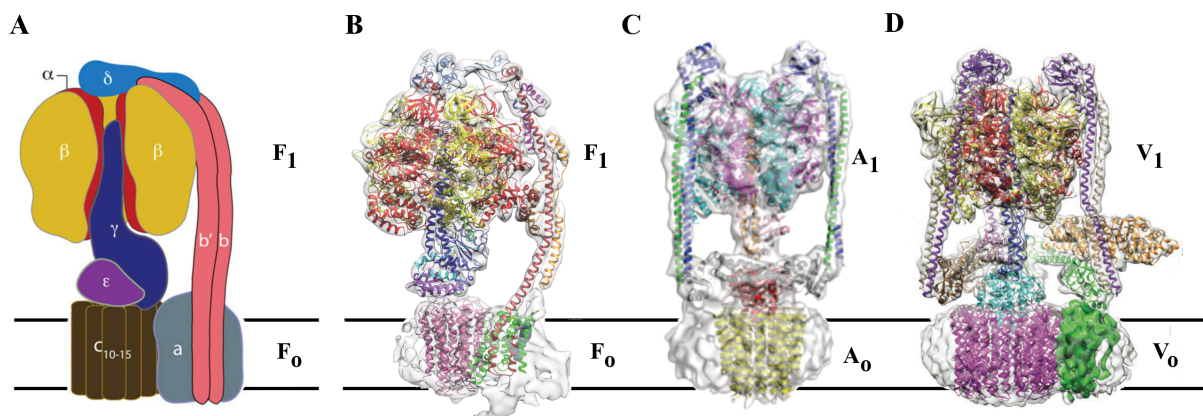


Figure 17: General architecture of F-, A- and V-type rotary ATPases

(A) A schematic model of a bacterial F-type ATPase showing all subunits of the entire complex. Electron cryo-microscopy maps of (B) the bovine mitochondrial F-type ATPase at a resolution of 6.5 Å, (C) the A-type ATPase from *Thermus thermophilus* at a resolution of 9.7 Å and (D) the V-type ATPase from *Saccharomyces cerevisiae* at 7.6 Å. Different subunits of rotary ATPases were solved by X-ray crystallography and fitted into the subnanometre cryo-EM densities revealing the structure of the entire complex. The black lines indicate the membrane. The figures were taken from (Stewart *et al*, 2013; Walker, 2013; Zhao *et al*, 2015; Zhou *et al*, 2015).

1.3.2.1 Structure and function of the soluble F₁ domain

High-resolution X-ray structures of the F₁ domain from several organisms and in several nucleotide-bound states show different steps occurring during the catalysis or hydrolysis of ATP (Abrahams *et al*, 1994; Okazaki *et al*, 2011; Rees *et al*, 2012). The F₁ domain consists of three pairs of nucleotide-binding catalytic (β) and nucleotide-binding, but non-catalytic (α) subunits. These subunits are arranged around the central stalk (γ -subunit) with the catalytic sites at the $\alpha\beta$ interface. All three pairs are in different conformations within an ATPase at a given time point. While one pair is in the open (O) conformation, the other pairs are in the loose (L) and in the tight (T) conformation. During ATP synthesis the nucleotide-binding subunits undergo conformational changes. Thereby the O conformation switches into the L, L into T and T into O conformation. In the O conformation the freshly synthesized ATP is released. Meanwhile ADP + P_i are bound in the L and ATP is synthesized during the change from the O to the T conformation. Each conformational change is driven by a rotation of approximately 120° of the central stalk (figure 18). The initial state of all subunits is reached after a rotation of 360° in which three ATP molecules are generated (Adachi *et al*, 2007; Itoh *et al*, 2004). This nucleotide-binding and rotary catalysis of ATP is known as the binding change mechanism (Boyer, 1993).

Describing the binding change mechanism backwards displays the situation that occurs in the F₁ domain in the case of ATP hydrolysis. Upon ATP hydrolysis the enzyme turns counterclockwise (viewed from the cytoplasm) inducing a rotation of approximately 120° in the central stalk. The binding change mechanism is ubiquitous for rotary ATPases and occurs also in A₁ and V₁ domains (Stewart *et al*, 2013).

In the bacterial F-type ATPase the δ - and the ϵ -subunit of the F₁ domain connect the F₁ to the F₀ domain. The δ -subunit is placed on top of the $\alpha\beta$ hexamer forming a connection to the b-subunits of F₀ while the ϵ -subunit is part of the central stalk connecting F₁ to the c-ring (Wilkins *et al*, 1997). In addition the ϵ -subunit is supposed to have a regulatory function by sensing either the ATP or the proton (sodium) concentration inhibiting ATP hydrolysis by performing a conformational change (Cingolani *et al*, 2011; Feniouk *et al*, 2006; Yagi *et al*, 2007).

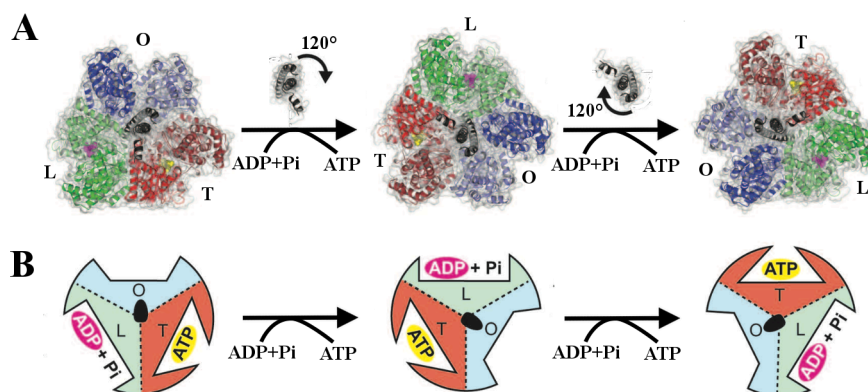


Figure 18: Nucleotide-binding and rotary catalysis model of ATP synthesis in rotary ATPases

Following the binding change mechanism the $\alpha\beta$ pairs alternately undergo three different conformational states (Boyer, 1993). In the loose (L) state ADP + P_i are bound which react to ATP in the tight (T) state driven by a clockwise 120° rotation of the central stalk (black). Another clockwise rotation by 120° changes the conformation of the T into the open (O) state thereby releasing ATP. The initial state of all $\alpha\beta$ pairs is reached by a third 120° rotation. (A) Three states of the rotary catalytic cycle are captured in the bovine mitochondrial F_1 -ATPase depicted from the membrane site (Abrahams *et al*, 1994). The three $\alpha\beta$ pairs are highlighted in light and dark red, green and blue, respectively. (B) Draft of the binding change mechanism. The subunits and nucleotide-binding modes are coloured in the same way as in the X-ray structures. The figure was modified from (Stewart *et al*, 2013).

1.3.2.2 Structure and function of the membrane-embedded F_o domain

Structure of the rotor ring

The first structural investigation of an *E. coli* F-type ATPase c-subunit was done by NMR spectroscopy (Girvin *et al*, 1998). This study showed that a single c-subunit consists of a hairpin. The loop that connects the two α -helices is usually formed by the amino acids RQPE and interacts with the central stalk (Stock *et al*, 1999). Subsequently, several high-resolution structures of F-type ATPase c-rings were solved showing the overall architecture and the ion-binding site of the rotor ring in different conformations. The first rotor ring structure was solved from the *Ilyobacter tartaricus* F-type ATP synthase revealing an hour-glass shaped, oligomeric complex of eleven identical c-subunits (figure 19 A). In each subunit a Na^+ was bound approximately at the middle of the membrane (Meier *et al*, 2005). A subsequent structure of the same rotor ring at higher-resolution and additional molecular dynamic (MD) simulations revealed the precise Na^+ -coordination in which a water molecule is involved next to side chain and backbone interactions (figure 19 B) (Meier *et al*, 2009). The key residue is thereby a

conserved glutamate (or aspartate) residue that is present in every rotor ring, independent of the c-ring ion specificity.

Most of today's known X-ray structures of F-type ATPase c-rings show that the rotor rings of these enzymes are composed of several identical c-subunits, each consisting of two helices forming a hairpin. In F-type ATPases the number of c-subunits corresponds to the number of ions that are translocated during a 360° rotation. The smallest F-type ATPase c-ring is formed by 8 subunits in *Bos taurus* (Watt *et al*, 2010), followed by the c₉ ring in *Mycobacterium phlei* (Preiss *et al*, 2015) and the c₁₀ ring in *Saccharomyces cerevisiae* (Stock *et al*, 1999). An F-type ATPase rotor ring consisting of 12, 13 or 14 c-subunits was found in *Thermus thermophilus* (Toei *et al*, 2007), *Bacillus pseudofirmus* OF4 (Preiss *et al*, 2010) (figure 19 C) and *Spinacia oleracea* (Vollmar *et al*, 2009) (figure 19 D) respectively. The largest F-type ATPase rotor ring known to date is from the cyanobacterium *Spirulina platensis* and has 15 c-subunits (Pogoryelov *et al*, 2007) (figure 19 E).

Most of the X-ray structures of F-type ATPase c-rings were solved in the ion-locked conformation, meaning that the H⁺ or Na⁺ is tightly bound in every c-subunit. Next to a conserved glutamate or aspartate, different residues are involved in the ion coordination in different rotor rings (Meier *et al*, 2009; Pogoryelov *et al*, 2009; Preiss *et al*, 2010; Symersky *et al*, 2012). The ion-locked conformation is energetically the most favoured state within the hydrophobic environment of the lipid bilayer. However, the X-ray structure of the *S. cerevisiae* F-type ATP synthase c-ring crystallized in a 2-methyl-2,4-pentadiol (MPD)/propylene glycol mixture revealed the open conformation of the ion-binding site (Symersky *et al*, 2012). In this conformation the conserved glutamate faces a more hydrophilic environment. The open conformation could also be obtained when an F- or V-type ATPase rotor ring was crystallized in the presence of the ATP synthase inhibitor N,N'-dicyclohexylcarbodiimide (DCCD) which covalently binds to the protonated ion-binding glutamate (Mizutani *et al*, 2011; Pogoryelov *et al*, 2010). Based on these results it was suggested that the open conformation is found at the a/c-interface allowing the ion uptake or release (Pogoryelov *et al*, 2010).

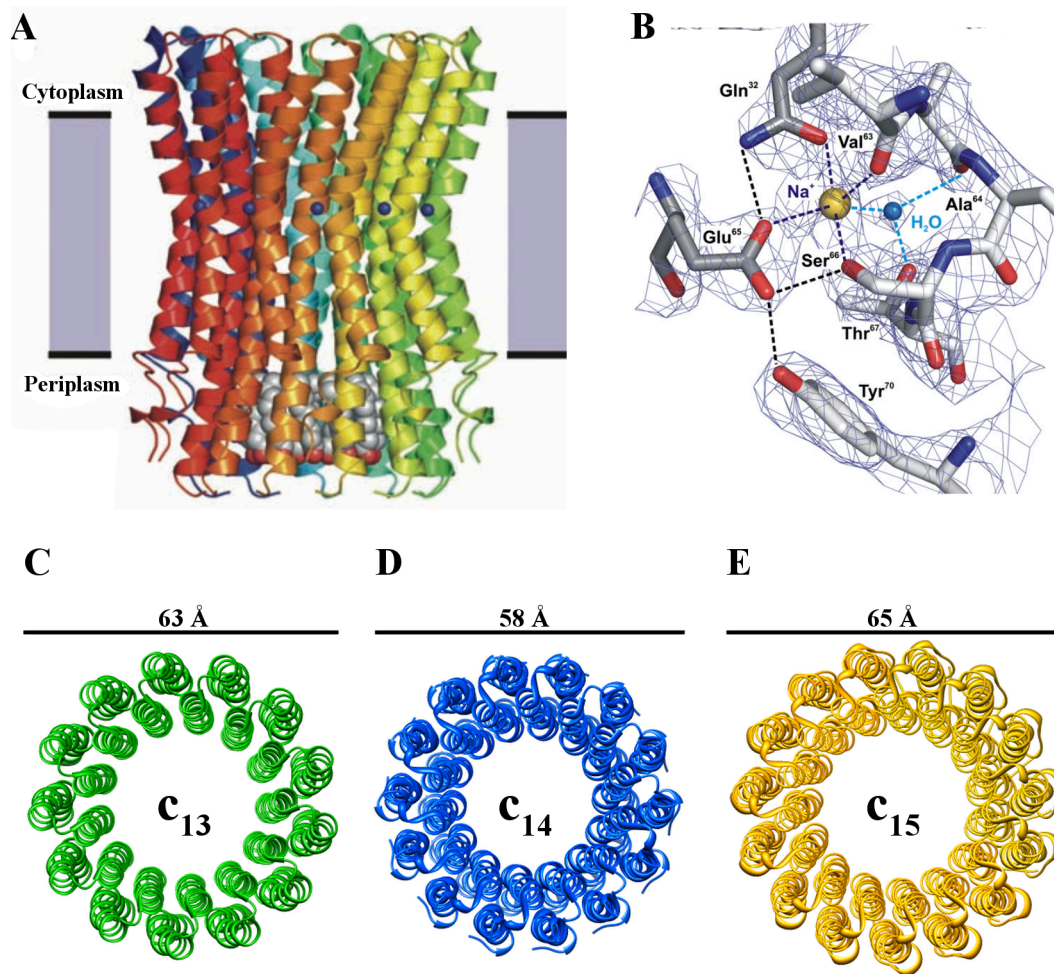


Figure 19: X-ray structures of different ATPase rotor rings

(A) The rotor ring of the *Ilyobacter tartaricus* F-type ATP synthase (pdb 1YCE) is shown from the membrane plane and reveals an hour-glass shape. Sodium ions are highlighted as blue dots. (B) A close-up of the Na^+ binding site in the subsequent *I. tartaricus* rotor ring structure (pdb 2WGM) shows the fivefold Na^+ coordination. Four coordination sites are formed by the side chain oxygens of E65 and Q32 of one c-subunit and the hydroxyl oxygen of S66 and the backbone carbonyl hydrogen of V63 of the adjacent c-subunit. The fifth coordination site is built by a water molecule present in the ion-binding pocket. The figures were taken from (Meier *et al.*, 2005) and (Meier *et al.*, 2009), respectively. (C) The rotor rings of *Bacillus pseudofirmus* OF4 (pdb 2X2V) (Preiss *et al.*, 2010), (D) *Spinacia oleracea* (pdb 2W5J) (Vollmar *et al.*, 2009) and (E) *Spirulina platensis* (pdb 2WIE) (Pogoryelov *et al.*, 2009) are seen from the cytoplasm showing their different stoichiometries and diameters.

Mechanism of ion translocation

During ATP synthesis the central stalk rotates with a step size of about 120° . This movement is caused by a rotation of the membrane-embedded c-ring and is connected to a transmembrane H^+

or Na⁺ ion transport. However, the exact mechanism how H⁺ or Na⁺ ions are transported through F_o is still unknown due to lacking high-resolution structures of this domain. Two models for the ion translocation mechanism called “push-and-pull” and “ratchet” mechanism were proposed (Dimroth *et al.*, 2006; Junge *et al.*, 1997; Vik *et al.*, 1994). Both have in common that the conserved glutamate or aspartate of the rotor ring ion-binding site interacts with a conserved arginine residue of the stator a-subunit.

In the “push-and-pull” mechanism a conserved arginine residue of the a-subunit regulates the access to the ion-binding sites in the rotor ring (figure 20 A). After a H⁺ or Na⁺ has bound to the rotor ring it remains in the ion-binding site while the c-ring rotates almost 360°. After this rotation the ion-binding site enters again the a/c-interface where the ion is repelled by the conserved arginine of the a-subunit leaving the binding site towards the cytoplasm. Thereby the ion exit pathway is localized in the c-ring. The negatively charged glutamate then interacts with the arginine. Driven by the membrane potential the glutamate moves towards the periplasm passing the arginine. Another ion flows through a channel in the a-subunit and binds to the glutamate which points to the periplasmic side. In the ion-locked conformation the ion is transported into the lipid environment (Dimroth *et al.*, 2006; Meier *et al.*, 2002).

The “ratchet” mechanism is characterized by two half channels that are localized in the a-subunit (figure 20 B). The ions travel through the first half channel in the a-subunit on one side of the membrane, bind to the c-ring and are released via the second half channel on the other side of the membrane after the c-ring performed a rotation of almost 360° (Vik *et al.*, 1994). Thereby the conserved, negatively charged glutamate or aspartate in the c-ring ion-binding site interacts with the arginine of the a-subunit after the ion is released. The rotation direction is mediated by the proton or sodium ion concentration gradient and the arginine in the a-subunit acts as a ratchet, inhibiting the energetically unfavourable backwards movement of the rotor ring (Aksimentiev *et al.*, 2004; Feniouk *et al.*, 2008; Junge *et al.*, 1997).

Recent electron cryomicroscopy studies on *Polytomella* ATP synthase dimers revealed first structural insights into the stator a-subunit although the resolution does not allow the precise determination of the proton translocation mechanism (Allegretti *et al.*, 2015). Two half-channels could be identified and placed at the a-subunit and c-ring (a/c-)interface (figure 20 C). This location was further supported by subsequent cryo-EM studies on a V-type ATPase from *Saccharomyces cerevisiae* and a bovine mitochondrial F-type ATPase (Zhao *et al.*, 2015; Zhou *et*

al, 2015). The three cryo-EM structures of ATPases revealed that the a-subunit is formed by horizontal membrane-intrinsic α -helices. The horizontal positioning of the helices inhibits the direct flow of protons through the membrane. The positively charged arginine residue of the a-subunit in the a/c-interface inhibits the backwards rotation of the rotor ring (figure 20 C) (Allegretti *et al*, 2015; Mitome *et al*, 2010; Zhao *et al*, 2015; Zhou *et al*, 2015).

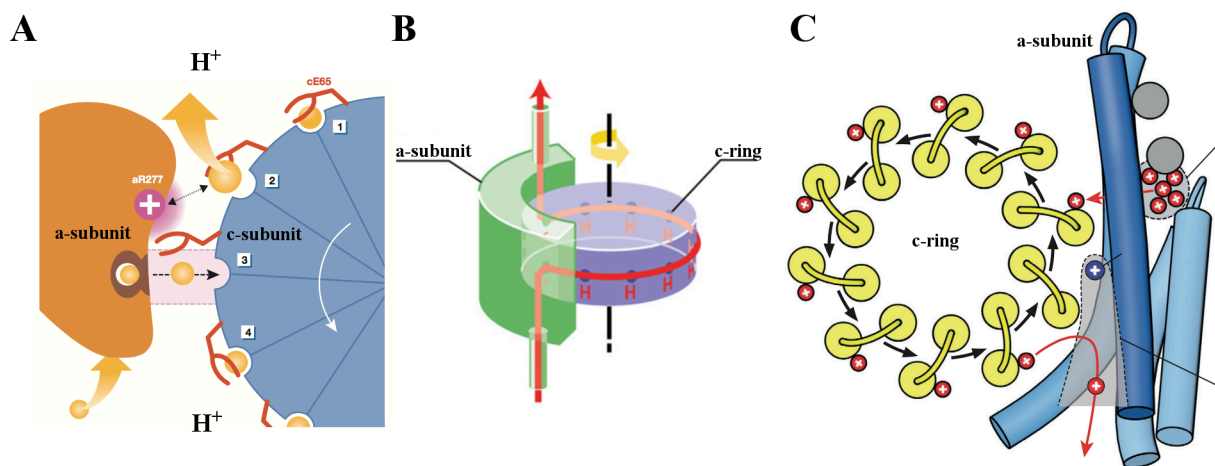


Figure 20: Different models of the ion translocation through the F_0 domain

(A) In the “push-and-pull” mechanism a conserved arginine in the a-subunit regulates the access to the ion-binding site in the rotor ring. The positively charged ion is repelled by the arginine and released. The negatively charged glutamate or aspartate interacts with the arginine and moves towards the periplasm driven by the membrane potential. It passes the arginine binding a new ion (Dimroth *et al*, 2006). (B) In the “ratchet” model, the ions passage the membrane by travelling through one half channel in the a-subunit on one side of the membrane where they bind to the c-ring. The ions are released via the other half channel after the c-ring performed a rotation of almost 360° (Junge *et al*, 1997; Vik *et al*, 1994). (C) Based on the cryo-EM structure of *Polytomella* ATPase dimers the two half-channels are located at the a/c-interface. The positively charged arginine residue at the a-subunit (highlighted as blue circle with a white plus) inhibits the backwards rotation. The figures were taken from (Dimroth *et al*, 2006; Walker, 2013) and (Allegretti *et al*, 2015), respectively.

The ion to ATP ratio

The different c-ring stoichiometries have a major impact on the bioenergetic cost of making ATP (Watt *et al*, 2010). Whereas in *S. platensis* 15 protons are required, in bovine mitochondria only 8 protons are necessary to synthesize three ATP molecules. Nevertheless, a rotor ring with a high number of c-subunits allows the synthesis of ATP at smaller membrane potentials or substrate concentrations than a rotor ring with a small number of c-subunits (Stewart *et al*, 2013). The

differences in the rotor ring stoichiometries probably reflect physiological adaptations to the various cell internal and cell external environments (Meier *et al.*, 2011; Preiss *et al.*, 2014).

In comparison to F-type ATPase c-subunits, the rotor ring subunits of V-type ATPases are composed of four helices, formed by covalently connected hairpins. Only one ion per subunit is transported in these enzymes due to a loss of the ion-binding carboxylate in one of the hairpins. Accordingly, the c_{10} ring of *Enterococcus hirae* V-type ATPase is composed of 20 hairpins but transports only 10 protons during a rotation of 360° (Murata *et al.*, 2004). In A-ATPases the rotor ring stoichiometry seems to be very diverse. A single subunit can be composed of 1 to 13 helical hairpins. Consequently, some rotor rings of A-type ATPases can translocate more ions per subunit during a rotation of 360° (Hilario *et al.*, 1998; Muller, 2004).

1.3.3 N-Type ATPase

In addition to F-, A- and V-type ATPases a novel (N-)type of rotary ATPase was proposed in a bioinformatics study in 2010 (Dibrova *et al.*, 2010). These N-type ATPases seem to be always present next to an F-type ATPase in various phylogenetically independent species. The proposal as a classification of this enzyme as a new type of rotary ATPase originates from the fact that the N-*atp* operon organization differs from that of other *atp* operons (Dibrova *et al.*, 2010). A recent study revealed that the N-type ATPase from *Burkholderia pseudomallei* is H^+ dependent while sequence alignments indicate that N-type ATPases in general could either be H^+ or Na^+ dependent. These sequence alignments together with biochemical data indicate that N-type and F-type ATPase c-subunits are very similar, suggesting that one ion is transported per N-type ATPase c-subunit (Schulz, 2015). In 2011 a study of the cyanobacterium *Aphanothece halophytica* showed that this bacterium expresses a Na^+ -coupled rotary N-type ATPase that allows the organism to grow under high salt conditions (Soontharapirakkul *et al.*, 2011). Since no structural information of this kind of rotary ATPase is available so far, it is still under debate if N-type ATPases really exist in bacteria and if they synthesize or hydrolyze ATP under physiological conditions.

1.4 Single-particle cryo-EM structure determination

Single-particle cryo-EM is a technique that starts with a purified protein that is plunge-frozen in liquid ethane to obtain protein in random orientations in amorphous ice. In a next step hundred to thousands of cryomicrographs of the protein in vitrified ice are taken which allow the selection of thousands to hundred of thousands single protein particle images. In a two-dimensional (2D) classification the selected particles are sorted according to their orientation in ice (figure 21). Particles that do not display the correctly folded protein are removed during this classification. The cleaned particle set is then applied for three-dimensional (3D) structure determination.

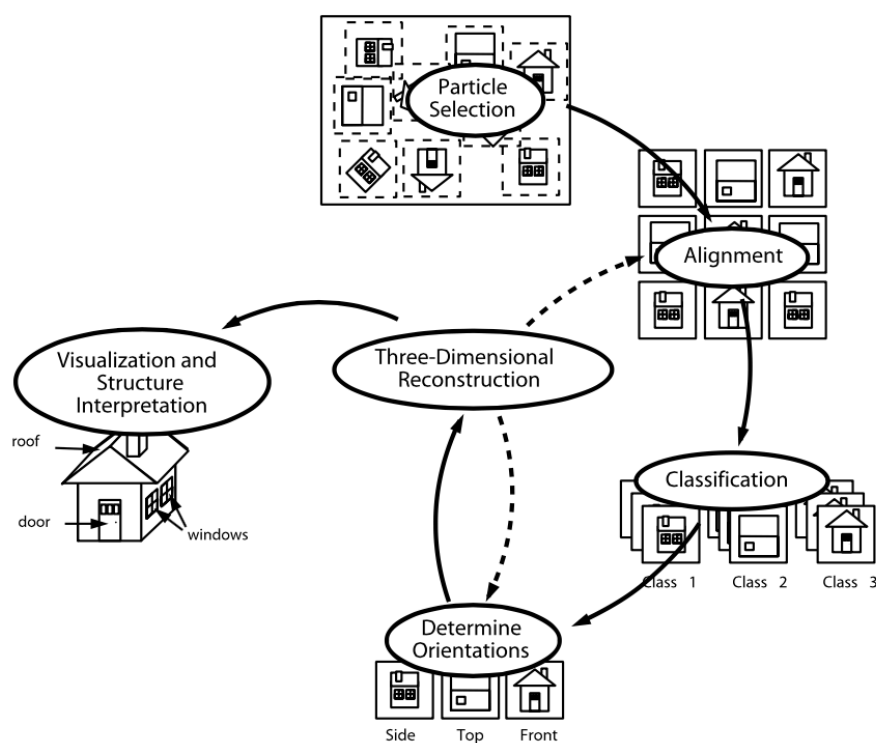


Figure 21: Scheme of single-particle data processing

After particle selection the particles are aligned according to their orientation in ice resulting in 2D class-averages. Class averages that display the protein in different orientations are selected and subjected to a 3D reconstruction. The figure was taken from (Thuman-Commike, 2001).

The software that was used for single-particle 3D structure determination in this work is Relion-1.3. The method for 3D structure determination that is implemented in the software is the projection matching (figure 22) (Scheres, 2012). In this method 2D projections are calculated of an initial model to which the single particles are aligned (Penczek *et al*, 1994). Parameters that display how well an alignment of the picked particles against the 2D projections of a reference

worked are the accuracy angles of translation and rotation (Scheres, 2012). The software derives the Euler angles of each projection and calculates a 3D structure of the aligned particles after one iteration step. The new structure is then used as model for the next iteration step. This means that 2D projections of the new model are calculated to which all particles are aligned again. The process continues until the particles cannot be aligned more accurately to new projections. After the last iteration step the accuracy angles of translation and rotation should be below 10 degrees (Scheres, 2012). Structure determination by single-particle cryo-EM strongly depends on the applied starting model. In other words an appropriate structure can only be obtained by using the correct initial model.

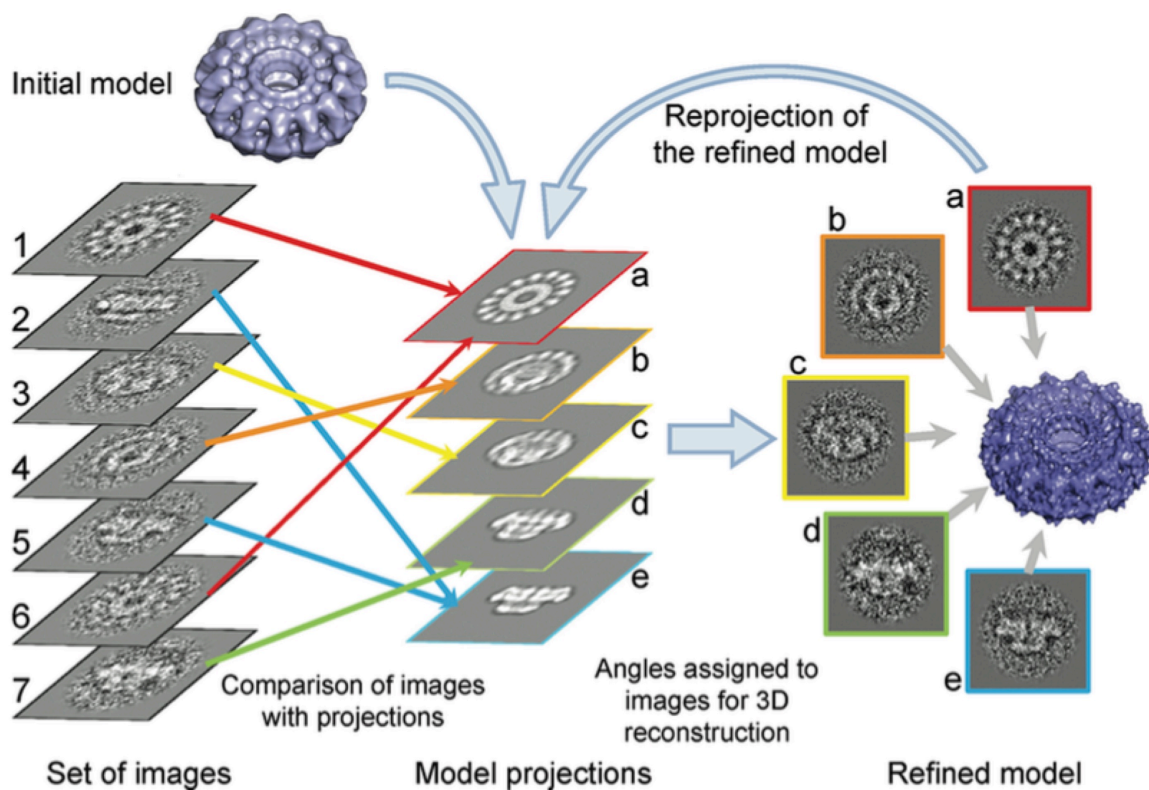


Figure 22: Projection matching procedure

Selected particles are aligned against projections of an initial model. After alignment the Euler angles of the reference images are transferred to the selected particles and a 3D structure is calculated. This structure is then used as model for the next iteration step. The figure was taken from (Orlova *et al.*, 2011).

In Relion-1.3 the user can choose between a 3D classification and a 3D refinement algorithm. The main difference between the two is that in a 3D classification the user can decide how many iterations the program should do and how many 3D references are applied. This way particles

can be separated that appear similar in 2D class averages but represent a different conformation of the protein, for example. In addition, the user can tune the impact of higher frequencies, which means that the program will consider also higher-resolution features during the particle alignment.

In a 3D refinement the user has no influence on this. Here the particles are separated randomly into two independent half datasets. These half datasets are then aligned against the same starting model but do not interfere with each other. This way overfitting of the data is precluded as two 3D refinements run in parallel. After the last iteration step, which is reached when the particles cannot be aligned more accurately to the projections, the two 3D maps are compared by a Fourier shell correlation (FSC) and merged. The FSC is a function that plots the correlation coefficients between the Fourier transform of two volumes as a function of the spatial frequency (resolution) over shells of approximately equal resolution (Penczek, 2010). The threshold to declare the resolution is 0.143 and called gold standard (Henderson *et al*, 2012). This value is based on the theoretical correlation between the best 3D structure calculated from a full dataset of selected particles and a perfect reference, e.g. an X-ray structure of the same protein (Rosenthal *et al*, 2003).

The gold standard is not implemented in the 3D classification algorithm implying the risk that the user can calculate overfitted 3D maps. Therefore the calculated structures obtained from a 3D classification have to be judged carefully.

1.5 Aim of this work

The aim of the first study was the structural and functional investigation of the human TRP channel polycystin-2. Therefore an expression system for PC-2 had to be established as well as a purification protocol. Since structural information of PC-2 was limiting, truncation mutants of PC-2 were also considered next to the full-length PC-2. The structure of soluble truncation mutants should be investigated by X-ray crystallography, while full-length PC-2 should be analysed by single-particle cryo-EM. The homogeneity of the sample is essential for structure determination and thus the cell line GnT1⁻ should be used for expression because in these cells all membrane proteins are glycosylated in the same way. Laser confocal scanning and electron microscopy should be used to determine the cellular localization of PC-2 and the truncation mutants because the function of PC-2 seems to be different depending on the organelle where it is transported.

In the second study the goal was to investigate the structure of the secondary-active transporter BetP from *C. glutamicum* by single-particle cryo-EM. BetP was already crystallized in many different states that occur during the alternating access (Perez *et al*, 2012). However, in each X-ray structure the N-terminal domain was truncated and only the C-terminal domain of one protomer, which is involved in crystallization contacts, could be completely solved. To gain more information about the C- and N-terminal domains the structure of the protein should be examined in solution. For single-particle cryo-EM BetP should be incorporated and purified in amphipol A8-35, an amphiphatic molecule that seems to support cryo-EM structure investigation.

In a parallel study to this work, the rotor ring of the *B. pseudomallei* N-type ATPase has been purified via a heterologous (*E. coli*) expression system and biochemically characterized. The c-ring was shown to use a H⁺ as a physiological coupling ion and seemed to have an unusual high molecular mass, which would result in a high c-ring stoichiometry (Schulz, 2015). The aim of the third study of my PhD thesis was to determine the *B. pseudomallei* N-type ATPase rotor ring stoichiometry and structure by single-particle cryo-EM.

2 Materials and Methods

2.1 Materials

2.1.1 Instruments

5415 C centrifuge (Beckman, Fullerton)
Äkta Purifier System (GE Healthcare, Freiburg)
Äkta Explorer System (GE Healthcare, Freiburg)
Avanti J-30 I centrifuge (Beckman, Fullerton)
Axiovert 200 microscope (Zeiss, Germany)
EM208S electron microscope (FEI, Oregon, USA)
Ettan (GE Healthcare, Freiburg)
Biophotometer (Eppendorf, Hamburg)
Cary 50 UV-Vis Spectrometer (Hoefer, San Francisco)
Cell disruptor (Constant Systems, Northants)
CellSpin (Integra Biosciences, Biebertal)
Hereaus TypB6 incubator (Heraeus, Hanau)
J6-MI centrifuge (Beckman, Fullerton)
JEOL F3200 electron microscope (Jeol, Eching)
Microplate reader (MWG Eurofins Genomics, Ebersberg)
Mighty Small SE250/SE260 SDS-PAGE (Hoefer, San Francisco)
Mosquito crystallization robot (TTP Labtech LTD)
Multitron AS120 shaker (Infors AG, Bottingen)
Optima L-70K ultracentrifuge (Beckman Coulter, Krefeld)
Philips CM120 electron microscope (Philips, Aachen)
Vitrobot III (FEI, Hillsboro, USA)

2.1.2 Kits

QIAprep Spin Miniprep Kit (Qiagen, Hilden)
QIAquick PCR Purification Kit (Qiagen, Hilden)
QIAquick Gel Extraction Kit (Qiagen, Hilden)
PCR Mycoplasma Test (PromoKine, Heidelberg)
Solution Master Detergent Kit (Anatrace, Maumee, USA)

2.1.3 Enzymes

Phusion High-Fidelity DNA Polymerase (Thermo Fisher Scientific, Dreieich)

Restriction Endonucleases (Thermo Fisher Scientific, Dreieich)

T4 DNA-Ligase (Thermo Fisher Scientific, Dreieich)

Alkaline Phosphatase (Roche, Mannheim)

N-Glycosidase F (Roche, Mannheim)

2.1.4 Chemicals

All chemicals used in this work were purchased from Addgene (Cambridge, USA), Anatrace (Maumee, USA), Avanti Polar Lipids (Alabaster, USA), Bio-Rad (Hercules, USA), GE Healthcare (Freiburg), Glycon (Luckenwalde), Hampton research (Aliso Viejo, USA), Merck (Darmstadt), New England Biolabs (Frankfurt), Qiagen (Hilden), Roche (Mannheim), Roth (Karlsruhe), Serva (Heidelberg), Sigma-Aldrich (St. Louis, USA) and Thermo Fisher Scientific (Dreieich). Media for eukaryotic cells were purchased from Thermo Fisher Scientific (Dreieich) and Sigma-Aldrich (St. Louis, USA).

2.1.5 Media and Antibiotics

2.1.5.1 Media for *E.coli*

Luria Bertani (LB) Medium:

10 g/l Bacto-tryptone; 5 g/l Bacto-yeast extract; 10 g/l NaCl

2.1.5.2 Media for eukaryotic cells

Tissue culture of HEK293, HEK293S GnTII⁻, LtTA-2,22 cells

500 ml DMEM/HAM F12; 10 % Fetal bovine serum (FBS); 50 U/ml Pen/Strep

Solution culture of HEK293S GnTII⁻ cells,

1000 ml Freestyle media, 5 % FBS, 50 U/ml Pen/Strep

2.1.5.3 Antibiotics

Ampicillin 500 µg/ml

Blasticidin 5 µg/ml

Carbenicillin 50 µg/ml

Chloramphenicol 34 µg/ml

Kanamycin	50 µg/ml
Gentamycin	350 µg/ml
Penicillin/Streptomycin	50 µg/ml

2.1.6 Plasmids and Oligonucleotids

All plasmids used in this work are listed in table 2.

Table 2: Plasmids

Plasmid	Features	Reference
pACMV-tetO	The vector was originally designed by Reeves <i>et al.</i> for inducible overexpression of the opsin gen in GnT1 ⁻ cells.	(Reeves <i>et al.</i> , 1996)
pACMV-tetO-PKD2-StrepII	A StrepII tag was added to the sequence of PKD2 and cloned into the vector via the restriction sites <i>KpnI</i> and <i>XhoI</i> .	This work
pACMV-tetO-PKD2-His ₆	A His ₆ tag was added to the sequence of PKD2 and cloned into the vector via the restriction sites <i>KpnI</i> and <i>XhoI</i> .	This work
pACMV-tetO-PKD2-ΔC143-His ₆	A His ₆ tag was added to the sequence coding the first 825 aa of PC-2, removing the second C-terminal coiled-coil region and cloned into the vector via the restriction sites <i>KpnI</i> and <i>XhoI</i> .	This work
pACMV-tetO-PKD2-ΔC182-His ₆	A His ₆ tag was added to the sequence coding the first 786 aa of PC-2, removing the second C-terminal coiled-coil region and the ER retention signal and cloned into the vector via the restriction sites <i>KpnI</i> and <i>XhoI</i> .	This work
pACMV-tetO-PKD2-ΔC273-His ₆	A His ₆ tag was added to the sequence coding the first 713 aa of PC-2, removing the first and second C-terminal coiled-coil region, the ER retention signal and the Ca ²⁺ binding domain and cloned into the vector via the restriction sites <i>KpnI</i> and <i>XhoI</i> .	This work

pACMV-tetO-ΔN581-PKD2-His ₆	A His ₆ tag was added to the sequence coding for the aa 582-968, the proposed pore region of PC-2 with the complete C-terminus and cloned into the vector via the restriction sites <i>KpnI</i> and <i>XhoI</i> .	This work
pACMV-tetO-ΔN205-PKD2-ΔC273-His ₆	A His ₆ tag was added to the sequence coding for the aa 206-695, including all predicted transmembrane domains of PC-2 and cloned into the vector via the restriction sites <i>KpnI</i> and <i>XhoI</i> .	This work
pcDNA3-PKD2-HA	<i>PKD2</i> gene cloned into a pcDNA3 vector from Invitrogen.	Prof. Dr. Witzgall, Uni Regensburg
pMAL-c2/TEV-PKD2c	The aa 678-968 of the human <i>PKD2</i> gene were cloned into the pMAL-c2 vector from NEB (Frankfurt).	Prof. Dr. Witzgall, Uni Regensburg
pMAL-c2/TEV-PKD1c	The C-terminal cytoplasmic domain of the human <i>PKD1</i> gene cloned into the pMAL-c2 vector from Invitrogen (Carlsbad, USA).	Prof. Dr. Witzgall, Uni Regensburg
pMAL-c2/TEV-PIGEA14	The gene of PIGEA-14 was cloned into the pMAL-c2 vector from Invitrogen	Prof. Dr. Witzgall, Uni Regensburg
pet-26b (+)	Plasmid for bacterial expression with kanamycin resistance.	Novagen (Schwalbach)
pet-26b(+)-ΔN581-PKD2-StrepII	A StrepII tag was added to the sequence coding for the aa 582-968 of PC-2, the proposed pore region of PC-2 with the complete C-terminus and cloned into the vector via the restriction sites <i>NdeI</i> and <i>XhoI</i> .	This work
pet-26b(+)-His ₆ -ΔN581-PKD2-StrepII	A His ₆ tag was added in front of ΔN581-PKD2-StrepII	This work
pet-26b(+)-ΔN581-PKD2-ΔC143-StrepII	A StrepII tag was added to the sequence coding for the aa 582-825, the proposed pore region of PC-2 with the cytoplasmic Ca ²⁺ binding domain and the ER retention signal and cloned into the vector via the	This work

	restriction sites <i>NdeI</i> and <i>XhoI</i> .	
pet-26b(+)-ΔN695-PKD2-ΔC143-StrepII	A StrepII tag was added to the sequence coding for the aa 695-825, containing the Ca ²⁺ binding domain and the ER retention signal of PC-2 and cloned into the vector via the restriction sites <i>NdeI</i> and <i>XhoI</i> .	This work
pet-26b(+)-ΔN581-PKD2-ΔC291-StrepII	A StrepII tag was added to the sequence coding for the aa 581-695, the proposed pore region of PC-2 and cloned into the vector via the restriction sites <i>NdeI</i> and <i>XhoI</i> .	This work
pASK-IBA5 betP	pASK-IBA5 with <i>BETP</i> cloned over the <i>BsaI/HindIII</i> restriction site	(Rubenhagen <i>et al</i> , 2000)

All oligonucleotids purchased and used in this work are listed in table 3.

Table 3: Oligonucleotids

Label	Sequence 5'-3'	Description
PKD2_for_KpnI	CGCCGGGGTACCGTGACCGCG ATGGTGAAC	Sense primer with <i>KpnI</i> restriction site for all PC-2 constructs starting at the N-terminus of the wild type gen.
PKD2_rev_his_XhoI	GATCTGGTGTCTCGAGTCAGTGA TGATGATGATGATGTACGTGGA CATTAGAACT	Anti-sense primer for PC-2(His ₆) with <i>XhoI</i> restriction site.
PKD2_rev_strep_XhoI	ATCAAGCTCGAGTCACTTTTCA AATTGTGGATGAGACCATAACGT GGACATTAGAACT	Anti-sense primer for PC-2(StrepII) with <i>XhoI</i> restriction site.
PKD2_rev1_Δcoil_XhoI	ACTTGAAACTCTTCGTAATACT CGAGTCAATGATGATGATGATG ATGTCTGGAGCTATGTCCGC	Anti-sense primer for PC-2ΔC143(His ₆) with <i>XhoI</i> restriction site.
PKD2_rev2_Δcoil_XhoI	ACTAGAACCTCTTCCTCGAGTC ACTTTTCAAATTGTGGATGAGA CCATCTGGAGCTATGTCCGC	Anti-sense primer for PC-2ΔC143(StrepII) with <i>XhoI</i> restriction site
PKD2_rev_ΔER_XhoI	GGACGTGGTAACTCGAGTCAAT GATGATGATGATGATGCCTCTC	Anti-sense primer for PC-2ΔC182(His ₆) with <i>XhoI</i> restriction site

	TTTCTCCAAGTC	
PKD2_rev_ΔCa_XhoI	AATGTTCTCCTCGAGTCAATGA TGATGATGATGATGGACCAAA GCTTTATGG	Anti-sense primer for PC-2ΔC273(His ₆) with <i>XhoI</i> restriction site
ΔN_PKD2_for_KpnI	ATGAGCGGTACCTCGACAACC ATGTCTCGATGTG	Sense primer with <i>KpnI</i> restriction site for ΔN581-PC-2
M-PC2-for	GGGGAACAGGTACCATGGAGG AAAGCAGCACTAACCGAGAGA AATA	Sense primer with <i>KpnI</i> restriction site for ΔN205-PC-2ΔC273(His ₆)
M-PC2-rev	ATCTTTATGATACTCGAGTCAC TTTTCAAATTGTGGATGAGACC AAGCTTTCTGCTGTGCCAAG	Anti-sense primer with <i>XhoI</i> restriction site for ΔN205-PC-2ΔC273(His ₆)
ΔN_PKD2_for_NdeI	AGCTCTCTACAACATATGTCTC GATGTGCCA	Sense primer with <i>NdeI</i> restrictions side starting at aa 582

2.1.7 Organisms

Table 4 contains all bacterial strains that were used for experiments in this work.

Table 4: Bacterial strains

Strain	Genotype	Reference
DH5α TM	F ⁻ Φ80 <i>lacZ</i> ΔM15Δ (<i>lacZYA-argF</i>) U169 <i>recA1 endA1 hsdR17</i> (rk ⁻ , mk ⁺) <i>phoA supE44</i> <i>λ thi1 gyrA96 relA1</i>	Invitrogen, (D-Karlsruhe);
BL21(DE3)	F ⁻ <i>ompT hsdSB</i> (rB ⁻ , mB ⁻) <i>gal dcm</i> (DE3) pLysS (CamR)	Novagen (Schwalbach)
Rosetta (DE3)pLysS	F ⁻ <i>ompT hsdSB</i> (rB ⁻ , mB ⁻) <i>gal dcm</i> (DE3) pLysSRARE (CamR)	Novagen (Schwalbach)
XL1 Blue	<i>B F- hsdSB</i> (rB ⁻ , mB ⁻) <i>gal dcm ompT</i> (DE3)	Novagen (Schwalbach)

All eukaryotic cell lines purchased or generated in this work are listed in table 5.

Table 5: Eukaryotic cells

Strain	Genotype	Reference
HEK-293	<i>human embryonic kidney</i>	ATC (Rockville, MD)
LtTA-2,22 / PC-2 fl- HA	pig kidney cell Inducible expression of PKD2-HA gene in LLC-PK ₁ cells.	(Cai <i>et al</i> , 1999)
HEK293S GnT1 ⁻	<i>human embryonic kidney</i> Mutation in the N-acetylglucosaminyltransferase I (GnT1) gene leads to lack of complex N-glycans.	(Reeves <i>et al</i> , 1996)
HEK293S GnT1 ⁻ / PC-2-StrepII	GnT1 ⁻ cells stable transfected with pACMV-tetO-PKD2-StrepII. Inducible expression of PC-2(StrepII) by tetracycline.	This work
HEK293S GnT1 ⁻ / PC-2-His ₆	GnT1 ⁻ cells stable transfected with pACMV-tetO-PKD2-His ₆ . Inducible expression of PC-2(His ₆) by tetracycline.	This work
HEK293S GnT1 ⁻ / PC-2-ΔC143-His ₆	GnT1 ⁻ cells stable transfected with pACMV-tetO-PKD2-ΔC143-His ₆ . Inducible expression of PC-2-ΔC143(His ₆) by tetracycline.	This work
HEK293S GnT1 ⁻ / PC-2-ΔC182-His ₆	GnT1 ⁻ cells stable transfected with pACMV-tetO-PKD2-ΔC182-His ₆ . Inducible expression of PC-2ΔC182(His ₆) by tetracycline.	This work
HEK293S GnT1 ⁻ / PC-2-ΔC273-His ₆	GnT1 ⁻ cells stable transfected with pACMV-tetO-PKD2-ΔC273-His ₆ . Inducible expression of PC-2ΔC273(His ₆) by tetracycline.	This work
HEK293S GnT1 ⁻ / ΔN581-PC-2-His ₆	GnT1 ⁻ cells stable transfected with pACMV-tetO-ΔN581-PKD2-His ₆ . Inducible expression of ΔN581-PC-2(His ₆) by tetracycline.	This work
HEK293S GnT1 ⁻ / ΔN205-PC-2-ΔC273 His ₆	GnT1 ⁻ cells stable transfected with pACMV-tetO-ΔN205-PKD2-ΔC273-His ₆ . Inducible expression of ΔN205-PC-2(His ₆) by tetracycline.	This work

2.2 Molecular biological methods

2.2.1 Polymerase chain reaction

For the *in vitro* amplification of specific DNA fragments the polymerase chain reaction (PCR) was performed (Mullis *et al*, 1987). Depending on the primer length a two step PCR was used instead of the classical three step PCR, skipping the annealing step. The PCR mixture as well as the thermocycler settings are listed in the tables 6 - 8.

Table 6: Thermocycler program of the three step PCR

Step	Temperature (°C)	Time (s)	cycle
Initial denaturation	98	60	1x
Denaturation	98	50	30x
Annealing	58	50	30x
Elongation	72	30	30x
Final elongation	72	300	1x

Table 7: Thermocycler program of the two step PCR

Step	Temperature (°C)	Time (s)	cycle
Initial denaturation	98	60	1x
Denaturation	98	50	30x
Annealing/Elongation	72	107	30x
Final elongation	72	300	1x

Table 8: PCR mixture

Component	Volume (µl)
Phusion High-Fidelity (HF) DNA Polymerase	0.5
Phusion HF DNA Polymerase buffer (5x)	10
Template: plasmid DNA (100 ng/µl)	1
Sense primer (10 pmol/µl)	2.5
Anti-sense primer (10 pmol/µl)	2.5
dNTP mix (10 mM each)	1
DMSO (100 % (v/v))	4.5
ddH ₂ O	28

2.2.2 Purification of PCR products

QIAquick PCR Purification Kit (Qiagen, Hilden) was used according to manufacturer's instruction to purify the amplified DNA. The DNA concentration and quality was determined with a Nanodrop 1000 spectrophotometer (Peqlab).

2.2.3 Agarose gel electrophoresis

DNA products were analysed by agarose gel electrophoresis. Therefore 0.7 - 1.0 % agarose was dissolved in 1x Tris-acetate-EDTA (TAE-) buffer (40 mM Tris-HCl, 4 mM EDTA, 40 mM acetic acid), DNA samples were mixed with 6x DNA loading dye (Thermo Fisher Scientific, Dreieich) and loaded onto the agarose gel next to 1 kb DNA ladder (Thermo Fisher Scientific, Dreieich) used as molecular weight standard. To visualize the separated DNA fragments by UV-light ethidium bromide was added to the agarose gel. Separation of DNA samples was carried out for 45 min at 100 V.

2.2.4 Gelextraction of DNA

To extract DNA samples after gel electrophoresis QIAquick Gel Extraction Kit (Qiagen, Hilden) was used according to manufacture's instruction. Quality and concentration of the DNA was determined after extraction using a Nanodrop 1000 spectrophotometer (Peqlab).

2.2.5 DNA cleavage by restriction enzymes

DNA was cut by different restriction enzymes from Thermo Fisher Scientific (Dreieich) according to manufacturer's instruction. Digested PCR products were purified with QIAquick PCR Purification Kit (Qiagen, Hilden) whereas digested vectors designed for ligation were purified with an agarose gel electrophoreses.

2.2.6 Ligation of DNA fragments

Ligation of purified and digested PCR products (inserts) and plasmid DNA (vector) was carried out at room temperature for 4 h. The ratio of insert to vector DNA depended on the size of both. Following formula was used to calculate the amount of insert DNA given to 50 ng vector DNA:

$$125ng \cdot \frac{size_of_insert(bp)}{size_of_vector(bp)} = insert(ng)$$

1 μ l of T4 ligase (Thermo Fisher Scientific, Dreieich) and 2 μ l of T4 ligase buffer (Thermo Fisher Scientific, Dreieich) was added to the reaction mix and filled with ddH₂O to a final volume of 20 μ l.

2.2.7 Primer synthesis and sequencing of manufactured DNA

Oligonucleotide primers used for PCR and DNA sequencing were purchased from MWG Eurofins Genomics (Ebersberg). Sequencing of cloned products was performed by SRD (Bad Homburg).

2.2.8 Isolation of vector DNA

A single colony of transformed *E. coli* cells was transferred in 5 ml LB medium with the respective antibiotic and incubated over night at 37°C and 220 rpm. Cells were harvest 4°C by centrifugation for 10 min at 4.500 g. Vector DNA was isolated with QIAprep Spin Miniprep Kit (Qiagen, Hilden) according to manufacture's instruction.

2.2.9 Preparation of competent *E. coli* cells

A preculture of XL1 blue, DH5 α TM or BL21(DE3) was grown in 5 ml LB medium at 37°C and 200 rpm over night. Next morning 4 ml of the preculture were used to inoculate 200 ml LB medium and cells were grown until an OD₆₀₀ of 0.6 was reached. The culture was incubated on ice for 10 min and centrifuged for 10 min at 2.200 g and 4°C. The sedimented cells were resuspended in 10 ml ice cooled 100 mM MgCl₂ and centrifuged for 10 min at 2200 g and 4°C afterwards. The cell pellet was carefully resuspended in 10 ml ice cold 100 mM CaCl₂ with 10 % glycerol (v/v) and incubated on ice for 30 min. Again cells were centrifuged for 10 min at 2.200 g and 4°C, resuspended in 2 ml of ice cold 100 mM CaCl₂ with 10 % glycerol (v/v), aliquoted in 0.2 ml and immediately frozen in liquid nitrogen. Competent cells were stored at - 80°C.

To prepare competent Rosetta (DE3)pLysS cells 35 ml LB media was inoculated with 350 μ l of corresponding competent cells (purchased from Novagen). Cells were grown at 37°C at 220 rpm until an OD₆₀₀ of 0.4 - 0.5 was reached. Cells were centrifuged for 10 min at 4°C and 1100 g and resuspended in 3.5 ml of LB media containing 10 % PEG 3350, 5 % DMSO and 25 mM MgSO₄ • 7 H₂O. Cells were aliquoted in 0.35 ml, frozen in liquid nitrogen and stored at - 80°C.

2.2.10 Transformation of competent *E. coli* cells

For transformation 0.2 ml (XL1 blue or DH5 α TM) or 0.35 ml (Rosetta (DE3)pLysS or BL21(DE3)) of competent cells were thawed on ice before 10 μ l of ligation reaction or 100 ng of vector DNA was added. Cells were incubated for 30 min on ice followed by a heat shock at 42°C for 35 s (XL1 blue or DH5 α TM) or 90 s (Rosetta (DE3)pLysS or BL21(DE3)). After incubation on ice for 1 - 2 min cells were supplemented with 0.8 ml LB media and incubated at 37°C, 250 rpm for 60 min. For selection 200 μ l of the solution was plated directly, whereas the remaining cells were centrifuged for 5 minutes at 5.000 g, resuspended in 100 μ l of LB media and then plated on a LB-agar containing the corresponding antibiotic.

2.2.11 Preparation of glycerol-stocks

A single colony from a transformation plate was transferred into 5 ml LB media containing the corresponding antibiotic and incubated at 37°C and 220 rpm over night. Cells were harvest by centrifugation (10 min, 4.500 g, 4°C), resuspended in 0.5 ml 50 % glycerol, frozen in liquid nitrogen and stored at - 80°C.

2.2.12 Transfection of eukaryotic cells and selection of a stable cell line

Eukaryotic cells were grown in a 6-well plate in DMEM/HAM F12 media with 10 % FBS and 50 U/ml Pen/Strep (for GnTI⁻ additionally 5 μ g/ml blasticidin was added) at 37°C and 5 % CO₂ until a confluence of 80 % was reached. The medium was replaced by fresh medium and cells were incubated for 60 min at 37°C and 5 % CO₂. Per well 5 μ g DNA was mixed with 10 μ g polyethylenimine (PEI) (stock solution 1 mg/ml PEI in ddH₂O) and incubated at room temperature for 10 min before 100 μ l DMEM/HAM F12 media with 10 % FBS and 50 U/ml Pen/Strep was added. The media of the cells was removed, DNA/PEI solution was added and cells were incubated for 24 h at 37°C and 5 % CO₂.

For transient expression DNA/PEI solution was removed and DMEM/HAM F12 media with 10 % FBS and 50 U/ml Pen/Strep was added.

For selection of a stable GnTI⁻ cell line 350 μ g gentamycin was added to DMEM/HAM F12 media with 10 % FBS, 50 U/ml Pen/Strep and 5 μ g/ml blasticidin. After 72 h dead cells were washed away using PBS buffer. Survived cells were detached from the surface and isolated with trypsin. Single cells were transferred into 96-well tissue culture plates and supplemented with DMEM/HAM F12 media containing 20 % conditioned media (sterile filtered media harvested from cultured cells), 10 % FBS, 50 U/ml Pen/Strep, 5 μ g/ml blasticidin and 350 μ g/ml

gentamycin. Cell growth was checked by light microscopy every day and growing cells were passaged into larger cell flasks, tested for protein expression before the cell line was frozen for long-term storage or discarded in case no expression was detected.

2.2.13 Freezing of cell lines

Cells were harvested and isolated from a confluent T175 tissue culture flask using 10 ml trypsin. After isolation 15 ml DMEM/HAM F12 media with 10 % FBS, 50 U/ml Pen/Strep were added, cells were counted with a Neubauer chamber and softly centrifuged at 200 g for 5 min at room temperature. Cell pellet was resuspended in 10 % DMSO and 90 % FBS to a total cell amount of $3 \cdot 10^6$ cells/ml. 1 ml aliquots were slowly frozen in isopropanol at - 80°C for 24 h before they were transferred in liquid nitrogen.

2.3 Biochemical methods

2.3.1 Protein production in *E. coli*

A colony from a transformation plate or 10 µl of a glycerol stock was transferred into 100 ml LB medium containing the corresponding antibiotic and cells were grown over night at 37°C and 220 rpm. The preculture was used to inoculate 1 l to 12 l of LB medium with the corresponding antibiotic to an OD₆₀₀ of 0.1 and cells were grown at 37°C and 200 rpm. At an OD₆₀₀ of 0.5 - 1.0 expression was induced by the addition of 1.0 mM IPTG or 200 µg/L anhydrotetracycline. After 4 h of protein production cells were harvested by centrifugation (25 min, 3.600 g at 4°C). Cells were resuspended in buffer (25 mM HEPES pH 7.5, 150 mM NaCl and 1 mM Pefabloc for soluble PC-2 constructs, 10 % glycerol was added for PC-2 constructs containing a membrane domain and 50 mM Tris pH 7.5, 150 mM NaCl, 10 % glycerol and 1 mM Pefabloc was used for BetP), frozen in liquid nitrogen and stored at - 80°C.

2.3.2 Protein production in eukaryotic cells

Testexpressions and transient expressions were performed in 6-well plates, whereas expression for protein purification was performed with stable cell lines cultured in either EasyFill Cell Factories (culture area 2.528 cm²) or suspension of up to 4 l. Stable cell lines were grown continuously in T175 tissue culture flasks until they reached confluence. Cells were detached and isolated from the surface using 1 mM EDTA in PBS buffer and transferred into an EasyFill

Cell Factory or into a 250 ml spinner flask. A small amount of cells was kept in the T175 tissue culture flasks for permanent cell growth.

The EasyFill Cell Factory was filled with 800 ml DMEM/HAM F12 media with 10 % FBS, 50 U/ml Pen/Strep, 5 µg/ml blasticidin and 350 µg/ml gentamycin. Expression was induced as soon as cells were confluent by replacing the media with 500 ml DMEM/HAM F12 media containing 10 % FBS, 50 U/ml Pen/Strep, 3 µg/ml tetracycline and 5 mM sodium butyrate. Cells were harvest 48 hours later by 1 mM EDTA in PBS, transferred into 50 ml falcons and centrifuged for 10 min at 4.500 g and 4°C. Cells were resuspended in PBS buffer and centrifuged again. The cell pellet was frozen in liquid nitrogen and stored at - 80°C.

The 250 ml spinner flask was filled with 125 ml Freestyle media supplemented with 5 % FBS, 25 U/ml Pen/Strep and sterile phenol red and continuously stirred at 50 rpm. Everyday the cell number was checked using a Neubauer chamber and fresh media was added in a way that the cell number did not fall below 500.000 cells/ml. Expression was induced by addition of media containing a final concentration of 3 µg/ml tetracycline and 5 mM sodium butyrate. 48 h after induction cells were harvest by centrifugation (25 min, 3.600 g at 4°C). Cells were resuspended in PBS buffer and centrifuged again for 10 min at 4.500 g and 4°C. The cell pellet was resuspended in buffer (25 mM HEPES pH 7.5, 10 % glycerol, 150 mM NaCl, 2 mM EDTA, 2 mM EGTA, complete protease inhibitor) for cell disruption.

2.3.3 Protein purification

2.3.3.1 Disruption of cells

E. coli cells and large amounts of eukaryotic cells were thawed in a water bath at room temperature and lysed using a cell disruptor (Constant Systems) at 2.0 kbar and 4°C. Cell debris was removed by centrifugation for 15 min at 10.000 g and 4°C.

Small amounts of eukaryotic cells used for testexpressions or transient expression were centrifuged for 10 min at 4.500 g and 4°C and resuspended in 50 mM Tris pH 7.5, 150 mM NaCl, 1 % Triton X-100, 10 % glycerol and complete protease inhibitor. Cell lysis was performed for 15 min in a sonicator water bath at room temperature. Cell debris was removed by centrifugation for 2 min at 10.000 g and 4°C. Supernatant was immediately used for further analysis on SDS-PAGE and Western blot.

2.3.3.2 Preparation of HEK293S GnTI⁻ endoplasmatic reticulum membranes

Cells were harvest by centrifugation for 10 min at 4.500 g and 4°C and resuspended in 3 ml of ice cold 40 mM HEPES pH 7.2, 5 mM MgCl₂, 5 mM EGTA, complete protease inhibitor and DNase. Cells were passaged 35 times through a 27-gauge needle in 1 ml batches on ice. Cell debris was sedimented at 1.000 g, 4°C for 10 min. Cell pellets were resuspended in buffer without DNase and centrifuged again. The cell pellet was then resuspended in buffer containing 2.2 M sucrose and immediately applied on a sucrose density gradient.

2.3.3.3 Preparation of *E.coli* and HEK293S GnTI⁻ membranes

The separation of membrane and soluble proteins was performed using an ultracentrifuge. Membranes were sedimented at 150.000 g, 4°C for 60 min, resuspended and homogenized with a dounce homogenizer in 10 - 50 ml buffer (same buffers as used for cell disruption without protease inhibitor) afterwards. The supernatant was used for the purification of soluble proteins or discarded.

2.3.3.4 Solubilisation of membrane proteins

The total protein concentration was adjusted to 10 mg/ml for *E.coli* membranes and 2.5 mg/ml for HEK293S GnTI⁻ membranes by addition of the corresponding buffer. Membrane solution was stirred while detergent was slowly added to a final detergent concentration of 1 %. The mixture was stirred for 60 min before unsolubilised material was removed by centrifugation at 150.000 g, 4°C for 60 min. The supernatant contained solubilised membrane proteins and was used for further purification.

2.3.3.5 Immobilized nickel-nitrilotriacetic acid (Ni-NTA) chromatography

For purification of His-tagged proteins by gravity-flow chromatography preloaded Ni-NTA from Quiagen (Hilden) was used. The column was equilibrated with 5 column volumes of buffer before protein solution was added to the material. To remove unspecifically bound proteins the material was first washed with 10 column volumes of buffer, followed by buffer with increasing imidazole concentration (5 mM, 10 mM, 25 mM, 50 mM) and finally 5 column volumes of buffer with 150 mM imidazole to elute the specific bound proteins. All fractions were collected for further analysis by SDS-PAGE and Western blot.

2.3.3.6 Immobilized strep-tactin affinity chromatography

Proteins expressed with a StrepII-tag were purified using the strep-tactin sepharose from IBA (Göttingen). The column material was washed with 5 column volumes of ddH₂O before it was equilibrated with the same volume of buffer. The protein sample was loaded on the column and unspecifically bound proteins were washed away with 10 column volumes of buffer and another 10 column volumes of buffer containing 500 mM NaCl. Bound proteins were eluted with buffer supplemented with 5 mM desthiobiotin.

2.3.3.7 Immobilized amylose affinity chromatography

Proteins fused to a maltose binding protein (MBP) via a TEV cleavage site were purified using an amylose resin (NEB, Frankfurt am Main). The resin was first washed with 3 column volumes of ddH₂O before it was equilibrated with buffer. The protein solution was loaded on the column using gravity flow and unbound proteins were washed away using 12 column volumes of buffer. The target protein was either eluted together with the fusion protein using buffer containing 10 mM maltose or eluted alone by the cut-off of MBP using 10 - 50 µg TEV-protease.

2.3.3.8 Immobilized lentil lectin chromatography

Proteins expressed in HEK293S GnTI⁻ cells containing glycosylated extracellular domains were purified using Lentil Lectin Sepharose 4B (GE Healthcare, Freiburg). The column material was equilibrated with buffer before protein solution was added and incubated with the material over night at 4°C. The day after the column was washed with 5 column volumes of buffer containing 500 mM NaCl followed by buffer with increasing α -D-methylglucoside concentration (5 mM, 10 mM, 25 mM, and 50 mM). Glycosylated proteins were eluted with buffer containing 150 mM α -D-methylglucoside. All fractions containing the target protein were combined and used for further purification.

2.3.3.9 Anion exchange (AEX) chromatography

Before loading on an AEX chromatography column, the protein sample was dialyzed against buffer without salt and concentrated to a final volume of 5 ml if necessary. For anion exchange chromatography a Mono Q 5/50 GL column (GE Healthcare, Freiburg) was used on an Ettan system. The column was equilibrated with 50 mM HEPES pH 7.5 and the sample was loaded using a flow rate of 0.25 ml/min. The protein was eluted over 10 column volumes with a continuous NaCl gradient using 50 mM HEPES pH 7.5 and 1.000 mM NaCl as second buffer.

2.3.3.10 Size exclusion chromatography (SEC)

For size exclusion chromatography an Äkta explorer, Äkta purifier or an Ettan system (GE Healthcare, Freiburg) was used. Depending on the size and amount of the construct either a Superose 6 10/300, Superose 6 PC 3.2/30, Superose 6 3.2/300, Superdex 200 10/300, Superdex 200 5/150 or Superdex 75 10/300 was used. All buffers used in a SEC were filtered and degassed before they were connected to the system. Columns were washed with ddH₂O before they were equilibrated with buffer. Protein samples were concentrated to 50 - 100 µl for the Ettan system or to 500 µl for the Äkta systems and commonly centrifuged at 5.000 g for 60 s through a Spin-X filter with 0.22 µm membrane pore size (Sigma-Aldrich, Taufkirchen). The protein sample was loaded with a flow rate of either 0.03 ml/min or 0.4 ml/min depending on the column and system used for the SEC.

2.3.3.11 Sucrose density gradient centrifugation

Sucrose density gradients were used for further protein purification or for the purification of endoplasmatic reticulum (ER) membranes. Protein solution was added on top of a continuous sucrose gradient (1.0 M - 0.7 M sucrose in the corresponding buffer) and centrifuged in a swing-out rotor (SW 40 Ti or SW 60 Ti) at 200.000 g for 17 h. The gradient was separated in 25 fractions of equal size and analysed by SDS-PAGE.

A continuous sucrose gradient (1.5 M - 0.7 M sucrose in 40 mM HEPES pH 7.2, 5 mM MgCl, 5 mM EGTA and complete protease inhibitor) was added on top of disrupted cells resuspended in buffer containing 2.2 M sucrose. Membranes were separated by centrifugation for 20 h at 40.000 g at 4°C.

2.3.3.12 Concentration of protein samples

Protein samples were concentrated using Vivaspin 4 or Vivaspin 500 (Sartorius, Göttingen) centrifugal filter units with a molecular weight cut-off of 10 - 100 kDa. The samples were concentrated according to manufacture's instruction. The centrifugation speed was set to 3.500 g.

2.3.3.13 Exchange of detergent to amphipol A8-35

Amphipol A8-35 was added to a membrane protein solution at a 3-fold excess (w/w) and the mixture was incubated at 4°C for 4 h under rocking or rotation. 15 mg of activated biobeads were added per 1 ml protein-detergent-amphipol mixture and incubated over night at 4°C. Biobeads were removed over a plastic column. To separate single proteins in amphipol A8-35 from protein aggregates the solution was centrifuged through a Spin-X filter for 60 s at 5.000 g.

2.3.4 Protein analysis

2.3.4.1 Photometrical determination of protein concentration

The protein concentration of soluble proteins was determined using a Nanodrop 1000 spectrophotometer (Peylab). The absorption was measured at 220 nm and 280 nm and the theoretical extinction coefficient was calculated with the ProtParam tool on the expasy server (<http://web.expasy.org/protparam>). The protein concentration was calculated according to Beer-Lambert.

2.3.4.2 Bradford assay

To determine the protein concentration of proteins in detergent or in a lipid environment the Bradford assay was used (Bradford, 1976). The interaction between the dye Coomassie Brilliant Blue G-250 with cationic and hydrophobic side chains of the protein results in a bathochromic shift in the absorption of Coomassie from 465 nm to 595 nm. Based on a BSA standard curve and the absorption at 595 nm the protein concentration was calculated.

2.3.4.3 Bicinchoninic acid (BCA) assay

The concentration of protein solution containing fos-choline detergents was determined using the BCA assay. Cu^{2+} ions are reduced by the protein backbone to Cu^+ that is complexed by bicinchoninic acid leading to an absorption shift to 592 nm. To start the reaction 1 ml of BCA solution was mixed with 50 μl sample and 20 μl 4 % (w/v) CuSO_4 and incubated for 30 min at 60°C. The sample was cooled to room temperature (15 min), the absorption was measured at 592 nm and the protein concentration was calculated based on a BSA standard curve.

2.3.4.4 Sodium dodecyl sulphate polyacrylamid gel electrophoresis (SDS-PAGE)

The composition and purity of a protein under denaturing conditions was determined by SDS-PAGE (Laemmli, 1970). The protein sample was diluted with SDS loading dye and analysed with a 7.5 %, 10 % or 12 % separation gel (table 9) depending on the size of the investigated protein. On top of the separation gel a 4 % stacking gel (table 10) was polymerized. 4 - 15 % Mini-PROTEAN TGX gradient gels (Biorad, München) were used to separate larger protein aggregations. The electrophoresis was started at 80 V and set to 120 V after the protein sample entered the separation gel. For SDS-PAGE a Mighty Small II electrophoresis unit (Hoefer US-Holliston) or a Mini-PROTEAN Tetra Cell (Biorad, München) was used with 25 mM Tris, 200 mM glycine and 0.1 % (w/v) SDS as electrophoresis buffer. Gels were stained either with

Coomassie Brilliant Blue by a protocol of Studier (Studier, 2005) or with silver according to Nesterenko *et al.* (Nesterenko *et al.*, 1994). Prestained Protein Ladder (Thermo Fisher Scientific, Dreieich) was used as a molecular weight marker.

Table 9: SDS-PAGE separation gel

Buffer	12 % separating gel	10 % separating gel	7.5 % separating gel
1.5 M Tris-HCl, pH 8.8	1.5 ml	1.5 ml	1.5 ml
40 % (v/v) acrylamide	1.8 ml	1.5 ml	1.125 ml
10 % (w/v) SDS	60 μ l	60 μ l	60 μ l
ddH ₂ O	2.64 ml	2.94 ml	2.565 ml
TEMED	5 μ l	5 μ l	5 μ l
10 % (w/v) APS	20 μ l	20 μ l	20 μ l

Table 10: SDS-PAGE stacking gel

Buffer	4 % stacking gel
0.5 M Tris-HCl, pH 6.8	1.0 ml
40 % (v/v) acrylamide	0.4 ml
10 % (w/v) SDS	60 μ l
ddH ₂ O	2.56 ml
TEMED	4 μ l
10 % (w/v) APS	20 μ l

2.3.4.5 Blue-native polyacrylamide gel electrophoresis (BN-PAGE)

Proteins were analysed by gel electrophoresis under non-denaturing conditions according to the protocol of Schagger *et al.* (Schagger, 1991). Protein samples were diluted with NativePAGE sample buffer and subjected to a NativePAGE Novex® 4 – 16 % or a NativePAGE Novex® 3 - 12 % Bis-Tris gel (Thermo Fisher Scientific, Dreieich). NativeMark unstained protein standard (Thermo Fisher Scientific, Dreieich) was applied to determine the size of the proteins. Electrophoresis was performed in a XCell SureLock electrophoresis unit (Thermo Fisher Scientific, Dreieich) at 4°C, started at 100 V, 15 mA and increased to 400 V, 15 mA after 60 min. Gels were destained using 10 % (v/v) methanol and 10 % (v/v) glacial acetic acid (table 11).

In the case a Western blot of a BN-PAGE was performed the protocol of Schagger *et al.* was modified as described in Wittig *et al.* (Wittig *et al.*, 2006).

Table 11: Buffer BN-PAGE

Buffer	Composition
Anode buffer	50 mM Bis-Tris pH 7.0
Cathode buffer	15 mM Bis-Tris pH 7.0, 50 mM Tricine, 0.02 % (w/v) Coomassie Brilliant Blue G-250

2.3.4.6 Electro-elution of proteins after BN-PAGE

For preparative elution of membrane proteins in amphipol A8-35 out of a BN-PAGE a 422 Electro-Eluter (Biorad, München) was used. The protein bands were cut out of the BN-gel using a scalpel and transferred into the elution chamber. Electro-elution was performed according to manufacture's instruction.

2.3.4.7 Western blot analysis

Gels from a SDS- or BN-PAGE were placed on top of three filter papers (Whatman 3MM filter paper) that were soaked in transfer buffer (100 mM Tris pH 8.3, 192 mM glycine, 0.2 % (w/v) SDS, 10 % (v/v) methanol) and a PVDF membrane activated in methanol. On top of the gel additional three filter papers soaked in transfer buffer were placed. Proteins were blotted for 35 min at 15 V onto the PVDF membrane. After a BN-PAGE was blotted the membrane was washed first in 25 % methanol and 10 % acetic acid until marker bands were clearly visible. Marker bands were drawn on the membrane with a pencil before the membrane was shortly soaked in methanol to remove residual dye. To block unspecific binding sites the membrane was incubated in 3 % (w/v) BSA in TBS buffer (20 mM Tris/HCl, 150 mM NaCl, pH 7.5) for 60 min at room temperature. The membrane was washed once with TBS buffer for 10 s and placed in a primary antibody solution (1/100 - 1/4000 primary antibody, 1x TBS, 3 % BSA) for at least 60 min. To remove free primary antibodies the membrane was washed at least three times with TBS buffer and placed in a secondary antibody solution (1/4000 antibody, 1x TBS, 3 % BSA) for another 60 min. The membrane was washed again three times with 1x TBS before protein bands were detected using SigmaFast BCIP/NBT. The reaction was stopped by the addition of ddH₂O. All antibodies used for Western blots used in this work are listed in table 12.

Table 12: List of antibodies for Western blot analysis

Antibody	Manufacturer
Anti-polyHistidine	Sigma-Aldrich (Taufkirchen)
StrepMAB-Classic	IBA (Göttingen)
Anti-PC-2 [YCE2]	Santa Cruz Biotechnology (Heidelberg)
Anti-PC-2 [D-3]	Santa Cruz Biotechnology (Heidelberg)
Anti-PC-2 [G-20]	Santa Cruz Biotechnology (Heidelberg)
Anti-PKD2	Thermo Fisher Scientific (Dreieich)
Anti-PC-1 [7E12]	Santa Cruz Biotechnology (Heidelberg)
Anti-PC-1 [H-260]	Santa Cruz Biotechnology (Heidelberg)
Anti-HMG CoA reductase	Merck Millipore (Schwalbach)
Anti-DP-1 (K-20)	Santa Cruz Biotechnology (Heidelberg)
Anti-REEP5 (E-13)	Santa Cruz Biotechnology (Heidelberg)
Anti-mouse (whole molecule-Alkaline Phosphatase)	Sigma-Aldrich (Taufkirchen)
Anti-rabbit (whole molecule-Alkaline Phosphatase)	Sigma-Aldrich (Taufkirchen)
Anti-goat (whole molecule-Alkaline Phosphatase)	Sigma-Aldrich (Taufkirchen)

2.3.4.8 Protein reconstitution into liposomes

For reconstitution of membrane proteins into liposomes 50 mg 1-palmitoyl-2-oleoyl-*sn*-glycero-3-phosphocholine (POPC) in chloroform were used. Chloroform was removed under a nitrogen stream and dry lipids were resuspended in 25 mM HEPES pH 7.5, 10 % glycerol and 150 mM NaCl to a final concentration of 20 mg/ml. Aliquots of 500 μ l were frozen in liquid nitrogen and stored at - 80°C. Reconstitution was performed as described in Ott *et al.* (Ott *et al.*, 2008). Briefly, the lipid solution was thawed and extruded through 400 nm pore size polycarbonate filters (Avestin, Mannheim). Homogenised liposomes were treated with Triton-X100 until solubilisation started which was detected by measuring the absorbance at 540 nm. Liposomes were mixed with the purified protein solution at a lipid/protein ratio of 30:1 and incubated for 30 min at room temperature. Biobeads were added in 6 steps to remove the detergent by incubation over night. Next morning proteoliposomes were collected by centrifugation (435.000 g, 45 min, 4°C). Proteoliposomes were resuspended in 100 μ l 25 mM HEPES pH 7.5, 10 % glycerol and 150 mM NaCl and then used for either freeze-fracture analysis or quantum dot labelling.

2.4 Biophysical methods

2.4.1 3D crystallization

3D crystallization was performed by vapour diffusion in hanging drops. To find the best crystallization conditions different commercially available crystal screens (Hampton Research, Aliso Viejo, USA and Jena Bioscience, Jena) were tested in 96-well plates using a Mosquito crystallization robot. For each well 300 nl protein solution was mixed with 300 nl of crystallization buffer and incubated at 18°C or 4°C. Crystals were fished with nylon loops, flash-frozen in liquid nitrogen and tested for diffraction at the European Synchrotron Radiation Facility (ESRF, Grenoble, France).

2.4.2 Laser confocal scanning microscopy

GnT1⁺ cells were cultured on coverslips until they reached 60 % confluence. Protein expression was induced by the addition of 3 µg/ml tetracycline and 5 mM sodium butyrate and cells were cultivated for another 48 h. Medium was replaced by 4 % paraformaldehyde in PBS buffer and cells were fixed at room temperature for 40 min. Cells were washed twice with PBS buffer before they were incubated for 45 min with 2 % BSA, 0.2 % Triton X-100 in PBS buffer. The solution was replaced by the first antibody (table 13) diluted 1/100 in 2 % BSA in PBS buffer. After 2 h at room temperature unbound antibody was removed by washing steps (1x 5 min 350 mM NaCl in PBS buffer, 2x 5 min PBS buffer) before the second antibody diluted 1/10000 in 2 % BSA in PBS buffer (table 13) was added for 1 h at room temperature. The cells were washed twice with PBS buffer before they were sealed airtight on a stage in 40 % glycerol in PBS buffer. Images were recorded with a Zeiss laser confocal scanning microscope and then analysed with Adobe Photoshop. Confocal microscopy was performed in the laboratory of Ralph Witzgall (University Regensburg).

Table 13: List of antibodies for immuno labelling

Antibody	Manufacturer
Anti-PC2 [YCE2]	Santa Cruz Biotechnology (Heidelberg)
Anti-mouse Alexa 488	VWR (Darmstadt)

2.4.3 Electron microscopy methods

2.4.3.1 Negative-stain electron microscopy

For negative-stain EM 3 μ l of protein solution in detergent or in amphipol A8-35 (0.05 - 0.1 mg/ml) were applied to a glow-discharged EM grid covered with a thin layer of continuous carbon film. The grid was washed twice with water and stained with 1 % uranyl acetate. Negatively stained EM grids were imaged with a Philips CM120 operating at 120 kV. Images were recorded at a nominal magnification of 59,000x using a 2k x 2k charged coupled device (CCD) camera, corresponding to a pixel size of 2.37 Å per pixel on the specimen.

2.4.3.2 Freeze-fracture electron microscopy

A sample of purified ER or proteoliposomes was placed between two copper plates and subsequently frozen in liquid ethane. Freeze-fracture was performed with a BAF 060 machine (Bal-Tec) at a temperature of - 130°C and a pressure of 2×10^{-7} mbar. The sample was shadowed with platinum/carbon followed by pure carbon to reinforce the replica. Organic material was washed away with 45 % (v/v) chromosulfuric acid for 10 h. Samples were washed 6 times in ddH₂O, transferred on a 400 mesh copper grid with Pioloform N65 (Wacker Polymer Systems, München) and analysed with an EM208S electron microscope (FEI, Oregon, USA). All freeze-fracture steps were performed by Friederike Joos (Department of Structural Biology, Max-Planck-Institute of Biophysics, Frankfurt).

2.4.3.3 Freeze-fracture labelling

The initial steps were as described for the standard freeze-fracture protocol, except that the replica was not cleaned with chromosulfuric acid. To preserve protein features the replica was washed for 20 h with 2.5 % SDS, 30 mM sucrose in 10 mM Tris pH 8.3. The sample was washed with PBS buffer for 5 min and blocked twice with 0.1 % BSA in PBS buffer for 5 min before the first antibody (table 14) in PBS buffer with 0.1 % BSA was added. After 1 h the first antibody was removed by four washing steps using 0.1 % BSA in PBS buffer for 15 min. The second antibody (table 14) in PBS buffer with 0.1 % BSA was added to the sample and incubated for 30 min. Free antibody was washed off with PBS buffer (3 x 10 min) and the sample was fixed with 0.5 % glutaraldehyde in PBS buffer. Samples were washed three times with ddH₂O, transferred on 100 mesh copper grids coated with Pioloform N65 (Wacker Polymer Systems, München) and analysed in an EM208S electron microscope (FEI, Oregon, USA). All

freeze-fracture and labelling steps were performed by Friederike Joos (Department of Structural Biology, Max-Planck-Institute of Biophysics, Frankfurt).

Table 14: List of antibodies for freeze-fracture labelling

Antibody	Manufacturer
Anti-PC2 [YCE2]	Santa Cruz Biotechnology (Heidelberg)
Anti-mouse coupled to 18 nm gold	Life technologies, Darmstadt

2.4.3.4 Fixation and sectioning of eukaryotic cells

For morphology and immunology studies stable cell lines were used. Cells were cultured as described in section 2.3.2. Briefly, cells were cultured in 6-well plates until 70 % confluence and protein production was induced by the addition of 3 µg/ml tetracycline and 5 mM sodium butyrate.

Fixation of cells for morphology studies

Medium was removed and replaced by 2.5 % (v/v) glutaraldehyde in 100 mM sodium cacodylate pH 7.4 and cells were incubated for 2 h at room temperature. Prefixed cells were washed three times with 100 mM sodium cacodylate pH 7.2 for 15 min, scraped out and subsequently embedded in 4 % Bacto Agar (BD, New Jersey, USA). Samples were dehydrated using an ethanol gradient series (1x 20 min 30 %, 2x 20 min 50 %, 2x 30 min 70 %, 2x 30 min 90 %, 2x 30 min 100 %) and infiltrated with Low Viscosity Premix Kit-Medium (2x 20 min 30 %, 2x 30 min 50 %, 2x 30 min 75 %, overnight 100 %, 2x 2 h 100 %) (Agar Scientific, Stansted, UK). Polymerization was for 16 h at 60°C and 80 - 120 nm thin sections were prepared with an Ultracut S Microtome (Leica, Wetzlar).

For post-fixation 1 % (v/v) osmium tetroxide in 100 mM sodium cacodylate pH 7.4 was added to thin sections and incubated for 1 h at room temperature. Samples were washed four times with ddH₂O and twice with 50 mM sodium acetate pH 5.2 before 1 % (w/v) uranyl acetate was added and samples were stored at 4°C over night. Next morning uranyl acetate was removed and the samples were washed three times with ddH₂O. The samples were analysed in an EM208S electron microscope (FEI, Oregon, USA). All fixation steps were performed by Friederike Joos (Department of Structural Biology, Max-Planck-Institute of Biophysics, Frankfurt).

Fixation of cells for immunology studies

Medium was removed and cells were fixed in the culture plate for 2 h at room temperature with 2 % (v/v) paraformaldehyde in PBS buffer. Cells were washed three times with PBS buffer for 10 min and incubated with 2 % glycine in PBS buffer for 2.5 h at room temperature. The sample was washed again three times with PBS buffer before cells were scraped out carefully and immediately embedded in 4 % Bacto Agar (BD, New Jersey, USA). Samples were dehydrated using an ethanol gradient series (1x 20 min 30 %, 2x 20 min 50 %, 2x 30 min 70 %, 2x 30 min 90 %, 2x 30 min 100 %) and infiltrated with LR White Resin, medium grade Acrylic Resin (Resin Company, London, UK). Polymerization was carried out at 55°C for 36 h and 80 - 120 nm thin sections were prepared with an Ultracut S Microtome (Leica, Wetzlar). Thin sections were incubated with saturated sodium periodate for 1 h at room temperature. The sample was washed five times (1x 10 min with 2 % glycine in PBS buffer, 1x 10 min with PBS buffer, 1x 10 min with 1 % BSA in PBS buffer containing 0.1 % Tween 20, 2x 10 min with 0.1 % BSA in PBS buffer and 0.1 % Tween 20) before the first antibody in PBS buffer with 0.1 % BSA was added for 1 h. The first antibody was removed, followed by four washing steps with PBS for 5 min each, before the second antibody coupled to 18 nm gold in PBS buffer with 0.1 % BSA was added for 1 h. Free antibody was removed by washing the sample three times for 5 min with PBS buffer. 1 % (v/v) glutaraldehyde in PBS was added for 10 min before the sample was washed three times with ddH₂O and stained with 1 % (w/v) uranyl acetate and lead citrate. Samples were analysed using an EM208S electron microscope (FEI, Oregon, USA). All fixation and labelling steps were performed by Friederike Joos (Department of Structural Biology, Max-Planck-Institute of Biophysics, Frankfurt). Table 15 contains all antibodies used for immunology.

Table 15: List of antibodies for immunology

Antibody	Manufacturer
Anti-PC2 [YCE2]	Santa Cruz Biotechnology (Heidelberg)
Anti-PKD2	Thermo Fisher Scientific (Dreieich)
Anti-HMG CoA reductase	Merck Millipore (Schwalbach)
Anti-mouse coupled to 18 nm gold	VWR (Darmstadt)
Anti-rabbit coupled to 18 nm gold	VWR (Darmstadt)

2.4.3.5 Quantum dot labelling

For quantum dot labelling, disrupted GnTI cells or proteoliposomes were used. The sample was incubated with 1 μ l Qdot® 605 Streptavidin Conjugate (Life technologies, Darmstadt) for 60 min at 4°C. Free quantum dots were either removed during further purification of intact ER membranes or by centrifugation (250.000 g, 4°C, 45 min). The labelling of a sample was tested under UV light before it was frozen on Quantifoil R2/2 grids.

2.4.3.6 Electron cryomicroscopy (cryo-EM)

For cryo-EM, aliquots of 3 μ l of purified protein (in amphipol A8-35, DDM, C₁₂E₈, LDAO and LMNG/CHS) with a concentration of 0.6 - 5 mg/ml were placed on glow-discharged holey carbon grids (Quantifoil R2/2) and plunge-frozen in a Vitrobot III (FEI) at 70 % humidity, 10°C with 7 - 11 s blotting time. Cryo-EM images were collected at liquid nitrogen temperature on a JEOL 3200 FSC electron microscope operating at 300 kV with an in-column energy filter equipped with a K2 Summit direct electron detector camera (Gatan). The slit width was adjusted to 20 eV and images were recorded in counting mode at a nominal magnification of 30,000x corresponding to a pixel size of 1.14 Å on the specimen. The total exposure time was 5 s or 7 s leading to an accumulated dose of 40 - 80 electrons per Å². Each image was fractionated into 25 - 35 sub frames with an accumulation time of 0.2 s. Defocus values in the final datasets ranged from 0.5 - 4.0 μ m.

2.4.4 Image-processing

Global beam induced motion of images was corrected (Li *et al*, 2013) and the contrast transfer function for each image was determined using CTFFIND3 (Mindell *et al*, 2003). Micrographs were 3 x 3 binned and initial particles were selected using the program Boxer implemented in EMAN2 (Ludtke *et al*, 1999). First 2D class averages were performed using Relion-1.3 (Scheres, 2012). Best class averages were selected as reference for automatic picking using Relion-1.3. Each micrograph was manually tested to delete false-positive and select false-negative particles. Further 2D and 3D classification as well as 3D refinements were performed within the Relion-1.3 workflow (Scheres, 2012; Wong *et al*, 2014). Particle-based beam-induced movement correction and polishing was performed in Relion-1.3 (Bai *et al*. 2013, Scheres 2014) using a running average of seven movie frames and a standard deviation of one pixel for the translational alignments.

In addition to Relion-1.3 XMIPP (Marabini *et al*, 1996) or EMAN2 (Ludtke *et al*, 1999) were used for 2D classification and IMAGIC (van Heel *et al*, 2000; van Heel *et al*, 1996) for

symmetrisation. EMAN2 and SIMPLE (Elmlund *et al*, 2012) were used to generate initial models as well as for band-pass-filtering of references applied in 3D refinements.

2.4.5 Map visualization and analysis

Densities were visualized and atomic models were fitted into cryo-EM densities in Chimera (Pettersen *et al*, 2004). PDBs were refined against EM densities using phenix real-space-refinement (Afonine *et al*, 2012). Local resolution of cryo-EM structures was determined by ResMap (Kucukelbir *et al*, 2014).

3 Structural investigations and cellular localization of the human TRP channel polycystin-2

3.1 Results of the structural investigations and cellular localization of polycystin-2

3.1.1 Expression and purification of different PC-2 truncation mutants for 3D crystallization

To gain high-resolution structural information of important PC-2 regions, truncation mutants of PC-2 were cloned into a pet26b vector. The C-terminal domain of PC-2 (PC-2c) as well as the PC-2 interaction partners PC-1c (the cytoplasmic C-terminal domain of polycystin-1) and PIGEA14 (a 14 kDa soluble protein with a predicted coiled-coil domain) were cloned into a pMAL-c2 vector. Using this vector, a maltose binding protein was added to the C-terminus of each construct separated by a TEV cleavage site. Constructs cloned into a pMAL-c2 vector were kindly provided by Prof. Dr. Witzgall (University Regensburg, Germany). Rosetta (DE3)pLysS cells are codon-optimized *E. coli* cells used to produce large amounts of soluble eukaryotic proteins. However, only a few PC-2 truncation mutants could be produced in suitable amounts and only one was stable during purification and suitable for 3D crystallization setups (table 16).

Table 16: Expression and purification of different PC-2 constructs in *E. coli*

Construct	Features of the Construct	Expression	Purification
PC-2c	complete C-terminal domain of PC-2	✓	✓
PC-1c	C-terminal coiled-coil domain of PC-1 that interacts with PC-2c	✓	Aggregated as soon as MBP was cut off
PIGEA14	Protein that binds to PC-2c	✓	Aggregated as soon as MBP was cut off
ΔN581-PC-2(StrepII)	Proposed pore region of PC-2 with the complete C-terminal domain	Degraded during expression	Not possible to remove degradation products

(His ₆)ΔN581-PC-2(StrepII)	Proposed pore region of PC-2 with the complete C-terminal domain	Degraded during expression	Not possible to remove degradation products
ΔN581-PC-2ΔC143(StrepII)	Proposed pore region of PC-2 with the Ca ²⁺ binding and ER retention domain	✓	Degraded during purification
ΔN695-PC-2ΔC143(StrepII)	Proposed pore region of PC-2 with the Ca ²⁺ binding domain	✓	Degraded during purification
ΔN581-PC-2ΔC291(StrepII)	Proposed pore region of PC-2	No protein production	

The full-length C-terminal domain of PC-2 was the only PC-2 truncation mutant that was stable during expression and purification and could be subjected to 3D crystallization trials. PC-2c consists of 289 amino acids with a calculated molecular weight of 32.6 kDa. The C-terminal domain has a coiled-coil domain that forms the anchoring point for interaction partners. Previous studies on the isolated C-terminal domain claimed that it assembles into a tetramer with a total molecular mass of 130.6 kDa (Ferreira *et al*, 2011).

PC-2c was purified on an amylose column before the MBP tag was cut off using a TEV-protease. The MBP-tag as well as the TEV-protease were separated from PC-2c by Ni-NTA chromatography. As the final purification step, size exclusion chromatography was performed, resulting in a monodisperse protein sample (figure 23 A). The purity of the sample was analysed by SDS-PAGE (figure 23 B). The protein appeared at a slightly higher molecular weight (between 35 - 40 kDa) in the SDS-PAGE compared to the calculated theoretical mass of 32.6 kDa. In the native-PAGE the protein was detected around 242 kDa (figure 23 C). This molecular weight could correspond to an octameric (260.8 kDa) complex, which could result from the interaction of two tetramers. This would support the theory that PC-2 forms a homotetramer like other TRP channels do (Ferreira *et al*, 2011; Liao *et al*, 2013).

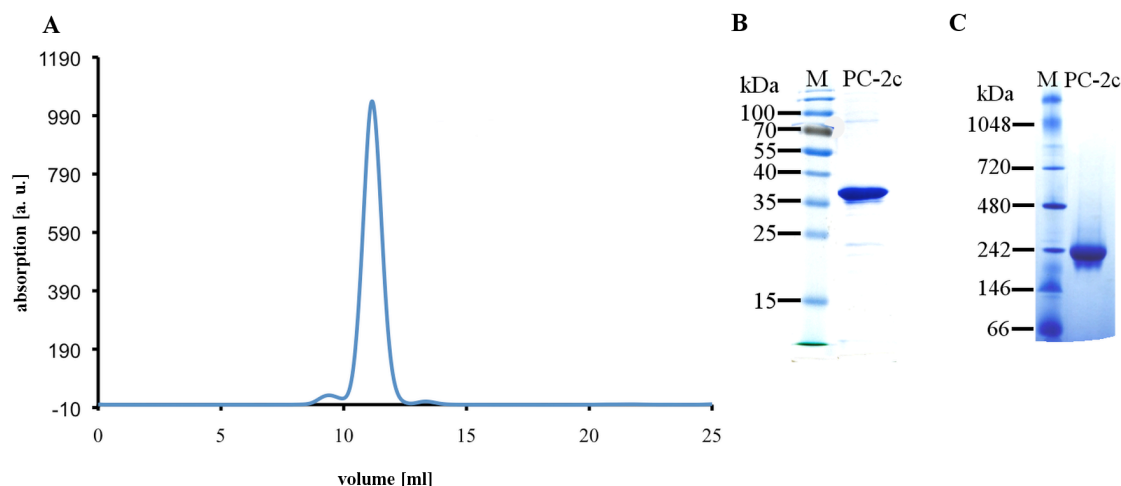


Figure 23: Purification of PC-2c

(A) Size exclusion chromatography of purified PC-2c (Superose 6 PC 10/300). PC-2c elutes with a retention volume of 12.4 ml. The absorption was monitored at 280 nm (B) The purified protein was analysed by SDS-PAGE; **M** marker (PageRuler, Thermo Fisher Scientific, Dreieich) and (C) native-PAGE; **M** marker (NativeMark, Thermo Fisher Scientific, Dreieich).

For 3D crystallization the purified PC-2c was concentrated to 10 - 30 mg/ml and different commercially available crystal screens (JBScreen Classic 1-10, JBScreen Membrane 1-3, Hampton Index, Hampton Crystal screen 1+2 and Hampton MemGold) were used. Since PC-2c contains a Ca^{2+} binding domain, all conditions were also tested in the presence of 5 mM CaCl_2 . Initial screening did not yield crystals.

A prior crystal structure of the second coiled-coil domain of PC-2 as well as structures of the PC-2L1 coiled-coil domain show that these domains crystallize only in the presence of an interaction partner, although this partner was not resolved in the structure (Molland *et al*, 2012; Yu *et al*, 2009; Yu *et al*, 2012). To take advantage of the stabilizing effect of ions and proteins that bind to the C-terminal domain of PC-2, PC-2c was co-purified with PIGEA14 and the coiled-coil domain of PC-1. In contrast to a stabilizing effect these interaction partners aggregated during the co-purification preventing crystallization, although the coiled-coil domain of PC-1 was successfully used in a previous study (Yu *et al*, 2009). A reason could be that all tested interaction partners were cloned to a maltose binding protein (MBP). On the one hand this increased the protein yield dramatically and allowed purification via an amylose resin, on the other hand the MBP, which is about twice the size of the interaction partner, might interfere with correct folding. Therefore the expressed interaction partner was unfolded but kept soluble as

long as it was connected to the MBP. The expression of the interaction partners without MBP was performed by Prof. Dr. Witzgall and did not lead to a sufficient protein production.

The addition of CaCl₂ to PC-2c neither improved the purification nor resulted in protein crystal formation. Another approach to stabilize PC-2c could be the incubation and co-crystallization of PC-2c with a specific Fab fragment. This technique was already successful in X-ray crystallography (Frey *et al*, 2010).

3.1.2 Expression and cellular localization of PC-2 wild type and different PC-2 truncation mutants in GnTI⁻ cells for structural investigation

GnTI⁻ cells are modified HEK293 cells with a loss of function mutation in the N-acetylglucosaminyltransferase-I gene. This leads to a homogenous glycosylation of proteins with two N-acetylglucosamine and five mannose residues (Reeves *et al*, 2002a). Moreover these cells can be grown in solution to a high cell density and were shown to produce enough protein for 3D crystallization (Standfuss *et al*, 2011).

PC-2 and truncation mutants were cloned into a special vector designed for inducible protein production in these cells (pACMV-tetO) (Reeves *et al*, 2002a; Reeves *et al*, 2002b). After transfection the cultivation of the cells was continued in the presence of gentamycin. For PC-2 and all truncation mutants a single cell dilution was performed to isolate cells that inserted the gene of interest as well as the operon coding for the gentamycin resistance. The single cell dilution was transferred into 96 well plates. Wells that contained only one cell were manually selected by light microscopy. Single cells were grown and first transferred into 24 well plates before expression tests were performed in 6 well plates. The amount of produced protein was monitored by Western blot analysis. The cell lines that produced the highest amount of PC-2(His₆), PC-2(StrepII), PC-2ΔC143, PC-2ΔC182, PC-2ΔC273, ΔN581-PC-2 and ΔN205-PC-2ΔC273, respectively, were frozen for long-time storage.

The N- and C-terminal domains of PC-2 were truncated removing functional cytoplasmatic domains. The expression of all constructs with a truncated N-terminus was not detectable in Western blots, suggesting that these mutants were not stable, whereas C-terminal truncation mutants could be used for further studies (figure 24).

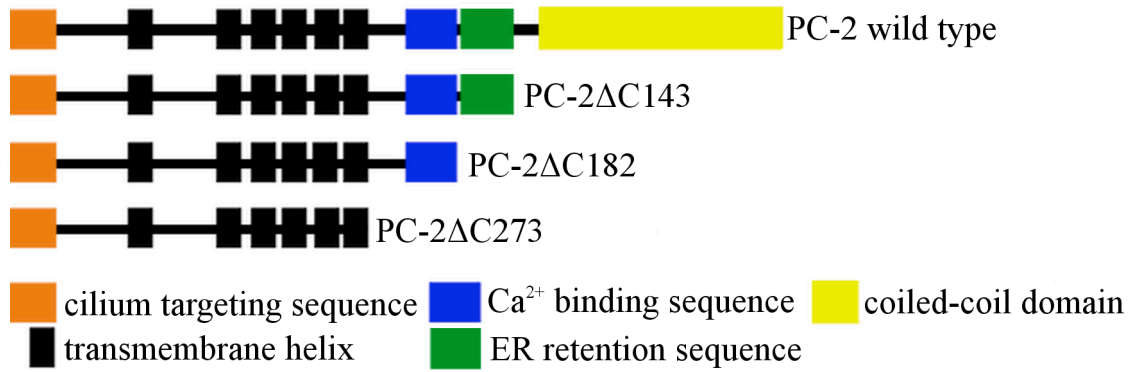


Figure 24: Cartoon of different PC-2 constructs, which were successfully inserted into the genome of GnTI cells

The C-terminal domain of PC-2 was truncated by stepwise deleting of the coiled-coil, the ER retention sequence and the Ca²⁺ binding EF-hand. All constructs have either a C-terminal StrepII- or His₆-tag.

The expression of PC-2 was compared with the C-terminal truncation mutants by applying the same amount of disrupted cells on a SDS-PAGE 48 h after expression was induced. To test whether the constructs were glycosylated or not, disrupted cells were incubated with N-glycosidase F and loaded on the SDS-PAGE. Western blot analysis revealed that all constructs were glycosylated and expressed in comparable amounts (figure 25).

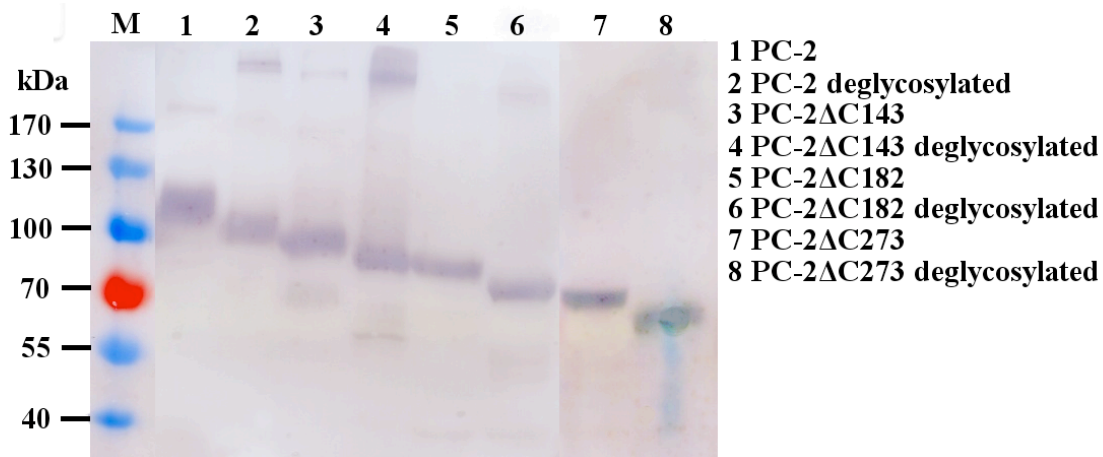


Figure 25: Western blot of PC-2(His₆) and C-terminal truncation mutants

PC-2(His₆) and C-terminal truncation mutants were expressed in GnTI cells. Cells were disrupted and either loaded directly or after incubation with N-glycosidase F for 15 min on a SDS-PAGE. A Western blot was performed using an anti-PC-2 antibody and a second antibody coupled to an alkaline phosphatase. Due to deglycosylation a shift of about 10 kDa to lower molecular weight was observed indicating that all constructs were glycosylated. **M** marker (PageRuler, Thermo Fisher Scientific, Dreieich)

To functionally characterize PC-2 by whole-cell patch-clamp studies, the protein has to be present at the plasma membrane. Previous studies revealed that the C-terminal coiled-coil domain is responsible for the formation of stacked ER (Giamarchi *et al*, 2010) and that the protein has to be truncated from its C-terminus to E787 before the protein is transported to the plasma membrane (Cai *et al*, 1999). To confirm these results GnTI⁺ cells expressing PC-2(His₆) for 48 h were analysed with a laser confocal scanning microscope kindly provided by Prof. Dr. Witzgall (University of Regensburg). Areas of accumulated protein were visualized with the fluorophore Alexa 488 coupled to an antibody. The protein was found either in round arrays (arrows, figure 26 A) or very close to the plasma membrane (arrowheads, figure 26 A). A MOCK control using the same cells without inducing PC-2 expression confirmed that PC-2(His₆) was specifically labelled (figure 26 B).

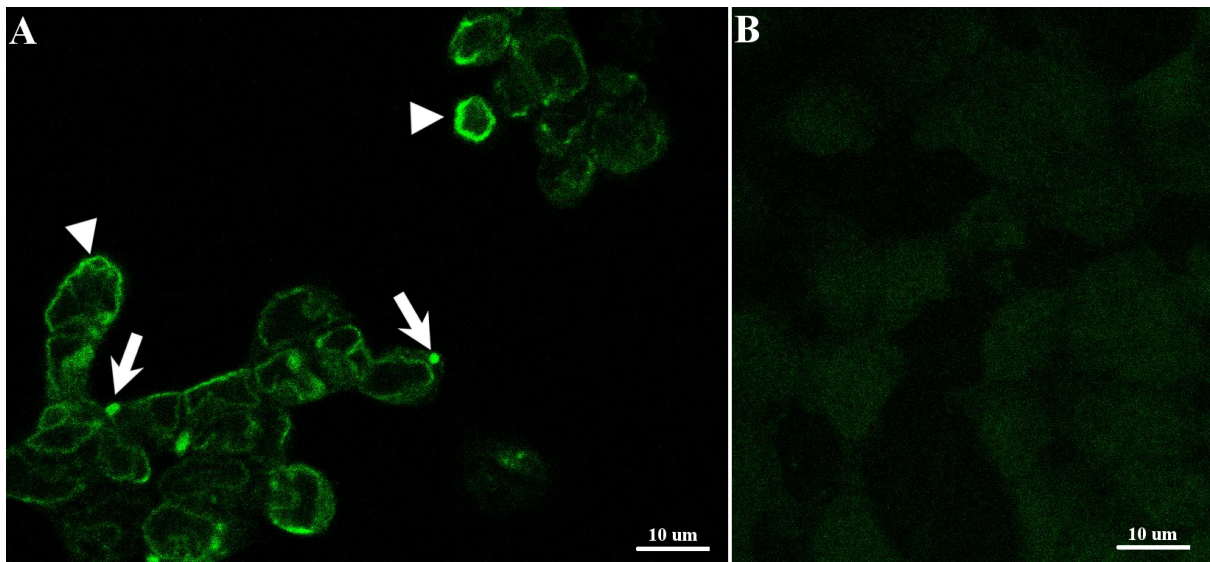


Figure 26: Laser confocal scanning microscopy of GnTI⁺ cells

(A) Expression of PC-2(His₆) was induced 48 h before cells were analysed by laser confocal scanning microscopy. Accumulation of PC-2 was observed in either round arrays (arrows) or close to the plasma membrane (arrowheads). (B) PC-2 was not detected in a MOCK control of GnTI⁺ cells where PC-2 expression was not induced.

According to the resolution limit of the confocal microscope it was not certain that PC-2(His₆) is in the plasma membrane of GnTI⁺ cells. To answer this question the localization of PC-2(His₆) as well as PC-2(StrepII) was investigated by electron microscopy. For this, cells expressing PC-2(His₆/StrepII) for 48 h were harvested using PBS with 1 mM EDTA and fixed with

formaldehyde. The immunogold labelling was performed in collaboration with Friederike Joos (Department of Structural Biology, Max-Planck-Institute of Biophysics, Frankfurt).

In the immunogold labelled thin sections, gold labels were found mainly at membrane stacks inside the cell, which appeared as round arrays in the laser confocal scanning microscope. In addition, gold labels were clearly found at the plasma membrane (figure 27). Remarkably, control cells in which either PC-2 expression was not induced before labelling or in which GFP was labelled instead of PC-2 did not show any comparable signal. A different affinity tag did not alter the localization of PC-2. This clearly points to the fact that PC-2 is transported to the plasma membrane in GnT1⁻ cells.

The localization of PC-2 at the plasma membrane enabled patch-clamp measurements on the whole-cell which were performed in collaboration with Dr. Christian Bamann (group of Prof. Ernst Bamberg, Department of Structural Biology, Max-Planck-Institute of Biophysics, Frankfurt). However, none of the measurements show PC-2 activity.

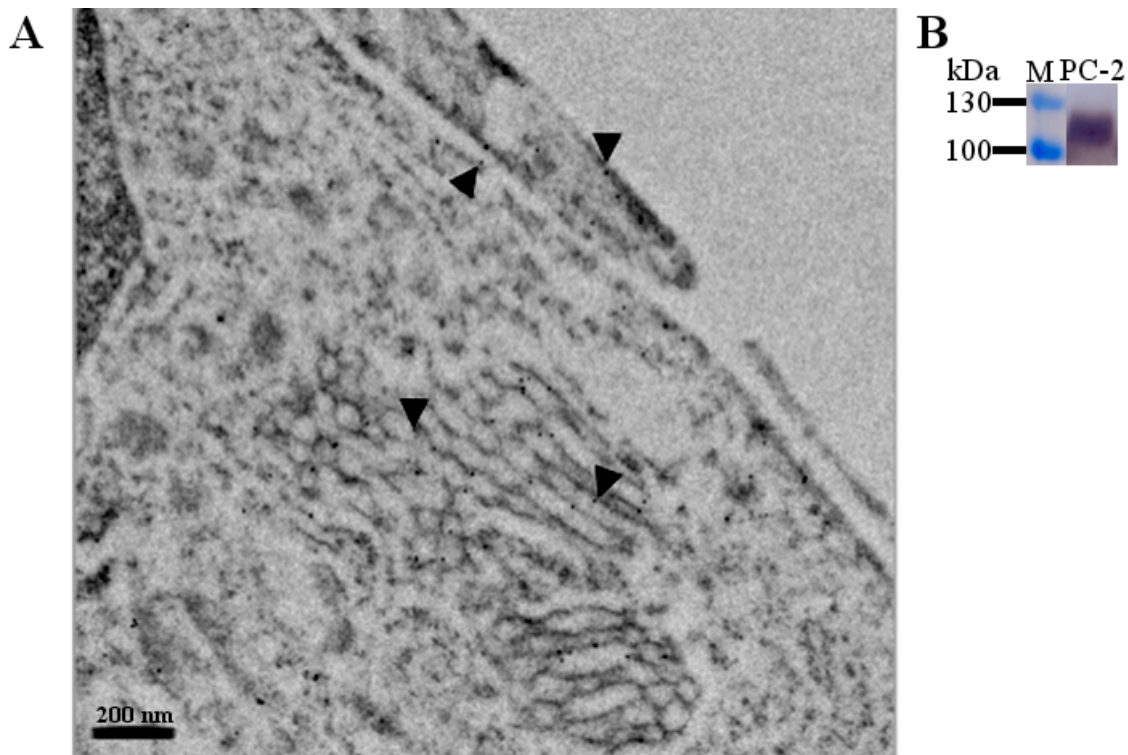


Figure 27: Gold-labelled thin section of GnT1⁻ cells expressing PC-2

(A) Expression of PC-2 was induced 48 h before PC-2 was labelled using an anti-PC-2 antibody against the C-terminal domain of PC-2. Gold labels were visible as small black dots (arrowheads). (B) Western blot analysis of the cells used for immunogold labelling; M marker (PageRuler, Thermo Fisher Scientific, Dreieich).

To investigate whether PC-2 is uniformly distributed inside the internal membrane stacks, these stacks were purified and analysed by freeze-fracture electron microscopy and immunogold labelling. To preserve the morphology of the purified membrane stacks PC-2 was labelled by immunogold before the membranes were fixed with osmium tetroxide, which inhibits antibody binding. The drawback of this approach was that C-terminal domains of PC-2 molecules located between two adjacent membranes were not accessible for antibody binding. However proteins in these regions were accessible by freeze-fracture labelling. Remarkably, the huge membrane stacks were not separated during purification and could be analysed in their original shape. Freeze-fracture of immunogold labelled PC-2 revealed an accumulation of gold labels when two membranes were in close proximity (figure 28 A, arrowheads). These results were confirmed by immunogold labelling of thin sections where labels were observed between membranes (figure 28 B, arrowheads).

This indicated that the cytoplasmatic domains of opposite PC-2 molecules interact with each other. The observed membrane formation inside GnT1⁻ cells after PC-2 expression was different from the previously described karmellae and whorl ER that were observed in HEK293T, CHO, COS-7 and MDCK after PC-2 expression (Giamarchi *et al*, 2010).

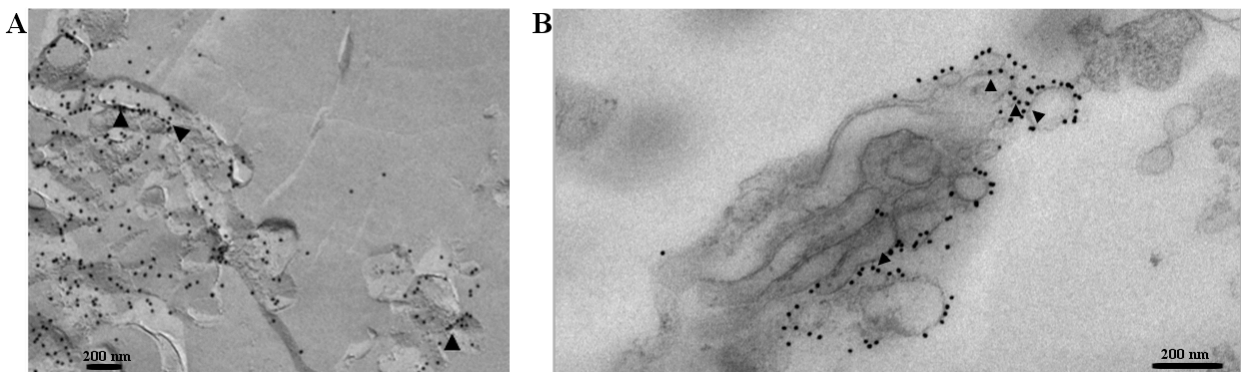


Figure 28: Labelling of purified membrane stacks after freeze-fracture and thin sectioning

Cells expressed PC-2 for 48 h before intracellular membrane stacks were purified. (A) Freeze-fracture labelling of purified membrane stacks showed an accumulation of gold where two membranes were in close proximity (arrowheads). (B) Immunogold labelling confirmed these results. Although PC-2 could not be labelled inside the membrane stacks, labels could be found between membranes at the outer side of the stacks (arrowheads).

To investigate how the intracellular membrane stacks were formed during the expression of PC-2, GnT1⁻ cells were analysed by thin sectioning at different time points. Therefore the cells

were fixed with osmium tetroxide to maintain the cellular morphology. The expression of PC-2 at different time points was monitored by Western blot analysis.

Before the expression of PC-2 was induced, the typical cell morphology was observed. The cell nucleus filled almost half of the cell and mitochondria were visible in the cytoplasm (figure 29 A). After induction, the cell morphology changed. After 6 h of PC-2 expression new membranes were formed around the cell nucleus building karmellae-like structures after 12 h (figure 29 B - C). After 24 h the membrane stacks started to expand and grew continuously until they filled almost the entire cytoplasm after 72 h. During the whole time a connection to the cell nucleus was observed (figure 29 D - F). Expression times above 72 h led to cell death. A correlation between the growth of the intracellular membrane stacks and an increasing production of PC-2 was monitored by Western blot analysis (figure 29 G). By comparing the observed membrane formation with previous described membrane morphologies, it was identified as crystalloid ER (Anderson *et al*, 1983; Pathak *et al*, 1986; Yamamoto *et al*, 1996).

It is still unknown what causes the formation of crystalloid ER. A study of Anderson *et al*. linked crystalloid formation to an overexpression of HMG-CoA reductase, an enzyme involved in the cholesterol biogenesis. However, neither an overexpression of HMG-CoA reductase nor of other proteins involved in ER formation like DP-1 and REEP5 (Park *et al*, 2010; Shibata *et al*, 2008) was observed in PC-2 expressing GnT1⁻ cells.

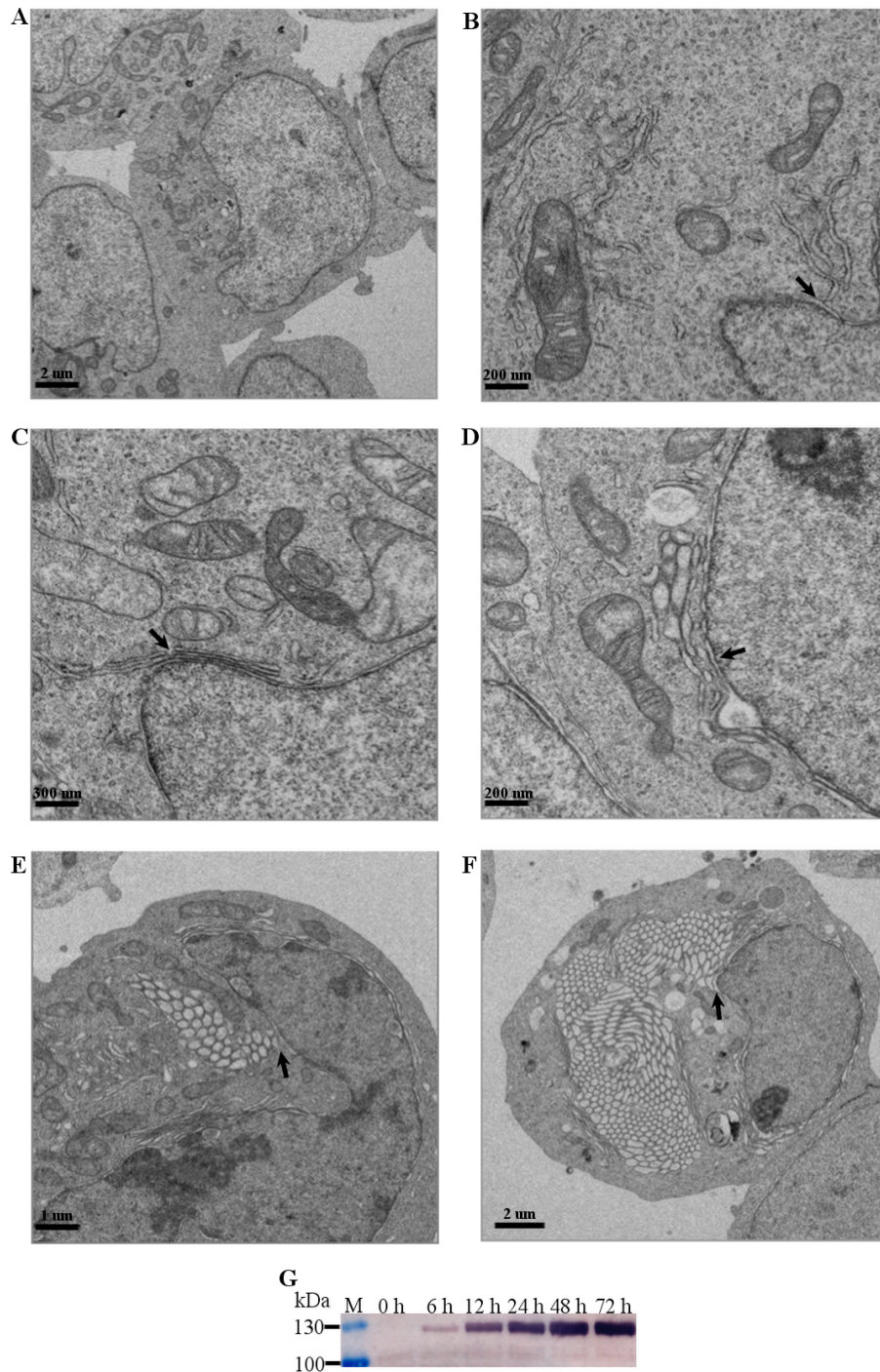


Figure 29: Thin sections of PC-2 expressing GnTII cells at different time points

The morphology of GnTII cells at different time points during PC-2 expression. (A) Before PC-2 expression was induced no membrane stacks were observed inside the cells. (B) 6 h after induction additional membrane formation was observed at the cell nucleus. (C) 12 h after induction multiple membranes were formed building karmellae-like membrane stacks. (D) The membrane stacks started to expand into the cytoplasm 24 h after induction, (E) forming crystalloid ER 48 h after induction and (F) grew until the entire cell was filled 72 h after induction. During the whole time a connection to the cell nucleus was observed (black arrows). (G) The expression of PC-2 was monitored by Western blot analysis; M marker (PageRuler, Thermo Fisher Scientific, Dreieich).

Since it is known that the second C-terminal coiled-coil domain is essential for the interaction of PC-2 with other proteins (Hanaoka *et al*, 2000; Yu *et al*, 2009) this region was deleted and the cellular effect of PC-2 Δ 143 was investigated. As already shown, PC-2 Δ 143 was glycosylated and expressed in a comparable amount to PC-2 in GnTII cells (figure 25). In contrast to PC-2 the expression of PC-2 Δ 143 did not lead to the formation of additional membrane stacks although the mutant is expressed into the ER like the wild type protein (figure 30 A). Additionally, expression times above 72 h did not lead to cell death, indicating that the formation of crystalloid ER is lethal for the cell and not PC-2 itself. Immunogold labelling studies revealed that PC-2 Δ 143 was exclusively located at the plasma membrane (figure 30 B) although the mutant still has the ER retention sequence. Due to the high amount of PC-2 Δ 143 whole-cell patch-clamp studies were performed to determine PC-2 Δ 143 activity. As for PC-2 no PC-2 Δ 143 activity could be detected.

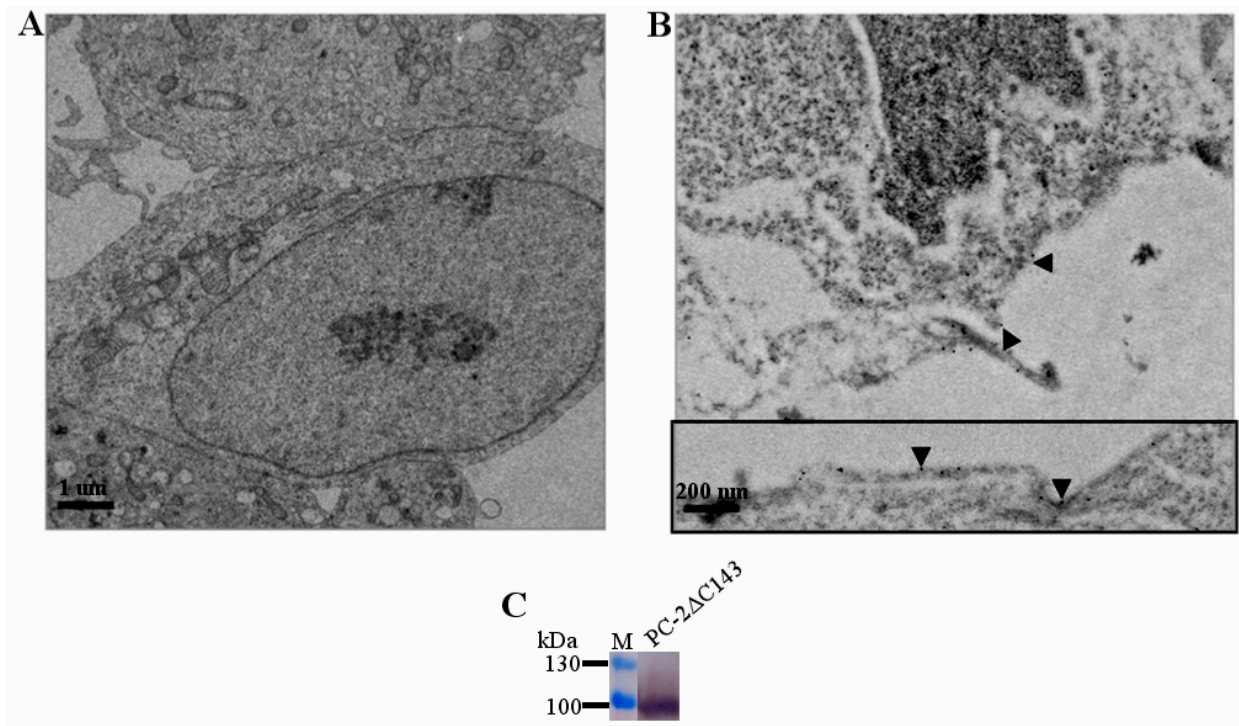


Figure 30: Cellular morphology and localization of PC-2 Δ 143 in GnTII cells

Expression of PC-2 Δ 143 was induced 48 h before cellular morphology was analyzed. (A) The cell morphology did not show any differences compared to not induced cells. (B) Immunogold labelling of PC-2 Δ 143 revealed that it is exclusively found at the plasma membrane (arrowheads point exemplarily to labels visible as small black dots; two different cells are shown). (C) The expression of PC-2 Δ 143 was monitored by Western blot analysis; **M** marker (PageRuler, Thermo Fisher Scientific, Dreieich).

A further truncation of PC-2 Δ 143 to PC-2 Δ 182 resulted in a construct lacking the ER retention signal. Therefore it is expected to be present at the plasma membrane. Strikingly, immunogold labelling of PC-2 Δ 182 showed that this construct was also present in intracellular membranes (figure 31), i.e. in the ER. The remaining of PC-2 Δ 182 in ER membranes may due to an inhibited oligomerization of PC-2 Δ 182 as a result of the truncated cytoplasmatic domain.

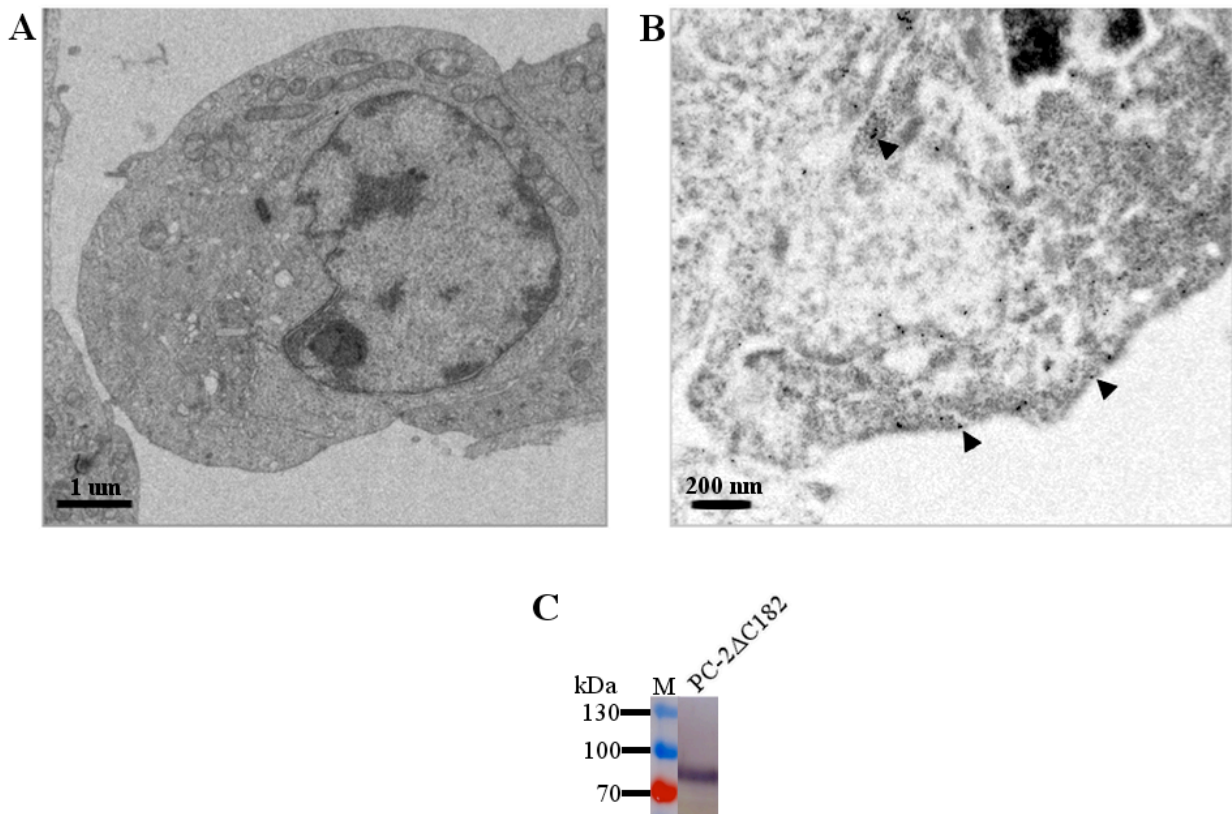


Figure 31: Cellular morphology and localization of PC-2 Δ 182 in GnTII cells

Expression of PC-2 Δ 182 was induced 48 h before cellular morphology was analyzed. (A) Cells did not show any differences compared to the control. (B) Immunogold labelling of PC-2 Δ 182 revealed that it was found at the plasma membrane as well as in intracellular membranes (arrowheads point to representing gold labels). (C) The expression of PC-2 Δ 182 was monitored by Western blot analysis; **M** marker (PageRuler, Thermo Fisher Scientific, Dreieich).

Deletion of the remaining regulatory Ca²⁺ binding motif led to a construct without a C-terminal cytoplasmic domain (figure 24). In 50 % of GnTII cells the expression of PC-2 Δ 273 resulted in the formation of small crystalloid ER patches (figure 32 A). Immunogold labelled PC-2 Δ 273 was found at the plasma membrane as well as in the crystalloid ER (figure 32 B). The

appearance of crystalloid ER during PC-2 Δ 273 expression suggests that the C-terminal coiled-coil domain of PC-2 is not essential for crystalloid formation.

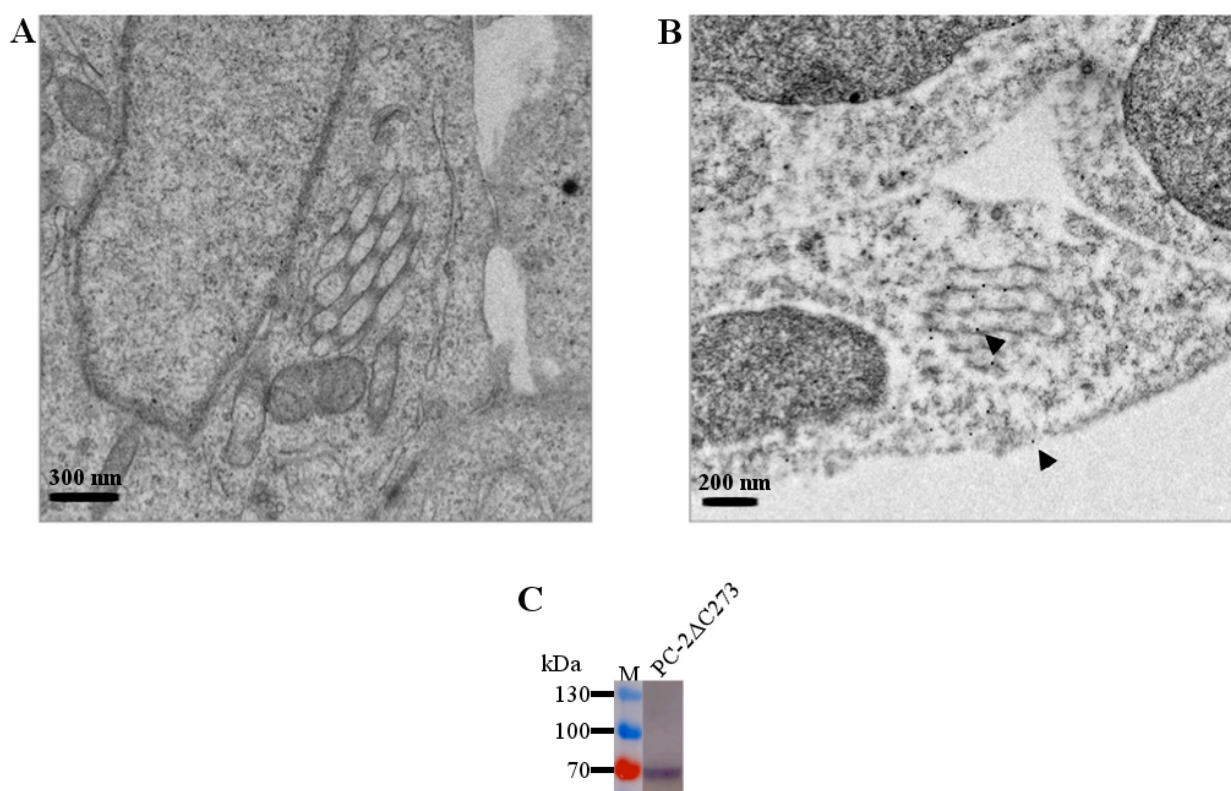


Figure 32: Cellular morphology and localization of PC-2 Δ 273 in GnTII cells

(A) After 48 h of PC-2 Δ 273 expression 50 % of all cells developed small patches of crystalloid ER. (B) Immunogold labelling revealed that PC-2 Δ 273 was located in the crystalloid ER as well as at the plasma membrane (arrowheads). (C) The expression of PC-2 Δ 273 was monitored by Western blot analysis; M marker (PageRuler, Thermo Fisher Scientific, Dreieich).

Taken together, PC-2 and all analysed PC-2 truncation mutants were expressed in GnTII⁻ cells and transported to the plasma membrane. The expression of PC-2 and PC-2 Δ 273 led to the formation of intracellular membrane stacks that were identified as crystalloid ER. Although the C-terminal coiled-coil domain of PC-2 favours the development of crystalloid ER it was shown that this domain is not mandatory for the formation. However, what exactly drives crystalloid ER formation is still an open question. Although all tested constructs were present at the plasma membrane, whole-cell patch-clamp studies did not yet lead to a conclusive result.

3.1.3 Purification, oligomeric state and structure determination of PC-2 expressed in GnTII cells

3.1.3.1 Purification and oligomeric state of PC-2(His₆)

For high-resolution structural investigations, pure and homogenous protein is essential. The common first step of the purification of a membrane protein is its extraction from the lipid bilayer with detergents. To test which detergents solubilise PC-2(His₆) most efficiently, 80 different detergents were tested (figure 33). To compare the efficiency of the detergents, the same batch of membranes was used. Unsolubilised material was removed by centrifugation and 10 µl of the supernatant were applied on an SDS-polyacrylamide gel. Western blot analysis revealed that fos-choline detergents solubilised PC-2(His₆) most efficiently.

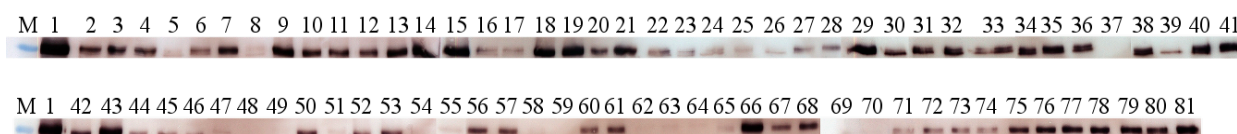


Figure 33: Solubilisation of PC-2(His₆) from GnTII membranes

After solubilisation the amount of solubilised PC-2 was analysed with Western blot analysis. **M** marker (PageRuler, Thermo Fisher Scientific, Dreieich); **1** GnTII membranes before solubilisation; **2** lauryl maltose neopentyl glycol; **3** decyl maltose neopentyl glycol; **4** octyl glucose nepentyl glycol; **5** anapoe-20; **6** anapoe-35; **7** anapoe-58; **8** anapoe-80; **9** anapoe-C₁₀E₆; **10** anapoe-C₁₂E₈; **11** anapoe-C₁₂E₉; **12** anapoe-C₁₂E₁₀; **13** anapoe-C₁₃E₈; **14** anapoe-X-100; **15** anapoe-X-114; **16** anapoe-X-305; **17** anapoe-X-405; **18** anzergernt 3-12; **19** anzergernt 3-14; **20** big CHAPS; **21** big CHAPS deoxy; **22** c-dodecafos; **23** CHAPS; **24** CHAPSO; **25** cyclofos-2; **26** cyclofos-3; **27** cyclofos-4; **28** cyclofos-6; **29** cyclofos-7; **30** cyglu-3; **31** cymal-4; **32** cymal-5; **33** cymal-6; **34** cymal-7; **35** n-decyl-N,N-dimethylglycine; **36** n-decyl-β-D-thiomaltopyranoside; **37** decyl-trimethylammonium chloride; **38** deoxycholic acid; **39** 2,6-dimethyl-4-heptyl-β-D-maltoside; **40** dimethyldecylphosphine oxide; **41** n-dodecyl-N,N-dimethyl-N-oxide; **42** n-dodecyl-N,N-dimethylglycine; **43** n-dodecyl-β-iminodipropionic acid; **44** n-dodecyl-α-D-maltopyranoside; **45** n-dodecyl-β-D-maltopyranoside; **46** n-dodecyl-β-D-thiomaltopyranoside; **47** dodecyltrimethyl-ammonium chloride; **48** fos-choline-iso-9; **49** fos-choline-iso-11; **50** fos-choline-unsat-11-10; **51**-fos-mea-8; **52** fos-mea-10; **53** fosfen 9; **54** n-heptyl-β-D-glucopyranoside; **55** hexadecyl-trimethylammonium chloride; **56** n-nonyl-β-D-maltopyranoside; **57** n-nonyl-β-D-thiomaltopyranoside; **58** nopol-fos; **59** octadecyltrimethyl-lammonium chloride; **60** n-octyl-β-D-glucopyranoside; **61** n-octyl-β-D-thiomaltopyranoside; **62** PMAL-C8; **63** PMAL-C10; **64** 2-propyl-1-pentyl maltopyranoside; **65** sodium cholate; **66** sodium dodecanoyl sarcosine; **67** sucrose monododecanoate; **68** n-tetradecyl-N,N-dimethylamine-N-oxide,

69 n-tetradecyl- β -D-maltopyranoside; **70** tetradecyl-methylammonium chloride; **71** n-undecyl- α -D-maltopyranoside; **72** n-undecyl- β -D-maltopyranoside; **73** n-undecyl- β -D-thiomaltopyranoside; **74** fos-choline-9; **75** fos-choline-10; **76** fos-choline-11; **77** fos-choline-12; **78** fos-choline-13; **79** fos-choline-14; **80** fos-choline-15; **81** fos-choline-16

After PC-2(His₆) was solubilised with fos-choline 14, first purification tests were performed by metal-ion affinity chromatography. However, PC-2(His₆) did not bind to any of the metal-ion affinity materials tested. In a next step a lectin column was used, which specifically binds glycosylated proteins. As for the metal-ion affinity column no binding of PC-2(His₆) to the lectin column was detected. The purification of PC-2(His₆) by ion-exchange chromatography combined with size-exclusion chromatography did not result in satisfying amounts or purity of PC-2(His₆).

In a next step the detergent was exchanged to n-dodecyl- β -D-maltopyranoside (DDM) decreasing the solubilisation efficiency. In DDM PC-2(His₆) did bind to a metal-ion affinity and lectin column, indicating that this binding had been inhibited by fos-choline 14. The elution fractions of the lectin column containing PC-2(His₆) were loaded on a continuous sucrose density gradient (0.7 M to 1.5 M sucrose). The purity of PC-2(His₆) was analysed by SDS-PAGE during the purification procedure (figure 34 A).

The oligomeric state of PC-2(His₆) was analysed by native-PAGE (3-12 % acrylamide) and native-PAGE Western blot. Since all known TRP channels form tetramers the PC-2(His₆) oligomer was expected to have a molecular weight of 460 kDa. However, the native-PAGE revealed a single protein band around 1MDa, about twice the size of what was expected (figure 34 B). A higher migration behaviour in native-PAGE is typical for membrane proteins and is often related to the detergent micelle that keeps the protein in solution. To investigate the stoichiometry of PC-2(His₆) the oligomer was partially disassembled by incubation with 2 % SDS or completely denatured in 2 % SDS and 100 mM DTT. Both samples were loaded on a native-PAGE and analysed by a Western blot (figure 34 B). A total of four bands were obtained indicating that PC-2 is tetrameric.

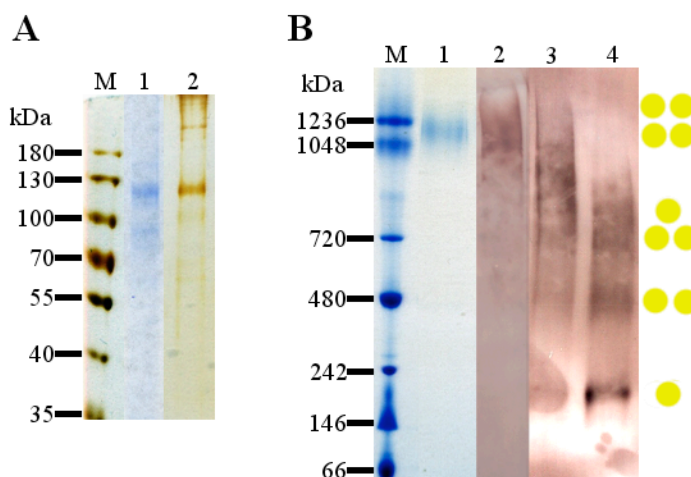


Figure 34: Purification and oligomeric state of PC-2(His₆)

(A) PC-2 was purified with a lectin column followed by a continuous sucrose density gradient (0.7-1.5 M sucrose); **M** marker (PageRuler, Thermo Fisher Scientific, Dreieich); **1** elution of the lectin column; **2** PC-2(His₆) containing fraction of the sucrose density gradient. (B) Native-PAGE and native-PAGE Western blot of the purified PC-2; **M** marker (NativeMark, Thermo Fisher Scientific, Dreieich); **1** native-PAGE of PC-2(His₆) after sucrose density gradient; **2-4** native-PAGE Western blot of PC-2(His₆) after sucrose density gradient (**2** PC-2(His₆), **3** PC-2(His₆) pretreated with 2 % SDS, **4** PC-2(His₆) pretreated with 2 % SDS and 100 mM DTT). Yellow dots on the right indicate the PC-2 oligomer that could be responsible for the band.

For structural analysis purified PC-2 was applied on a carbon coated copper grid, stained with 1 % uranyl acetate and visualized in an electron microscope (EM) operating at 120 kV (CM120, Philips). The recorded micrographs revealed that the purified PC-2(His₆) sample was heterogeneous (figure 35). This heterogeneity was not detectable by SDS-PAGE. However, by comparing negative-stain images of PC-2(His₆) with published micrographs of other TRP channels (Moiseenkova-Bell *et al*, 2008) similar projections of the protein were identified. To increase the content of tetrameric PC-2 the purification protocol was revised.

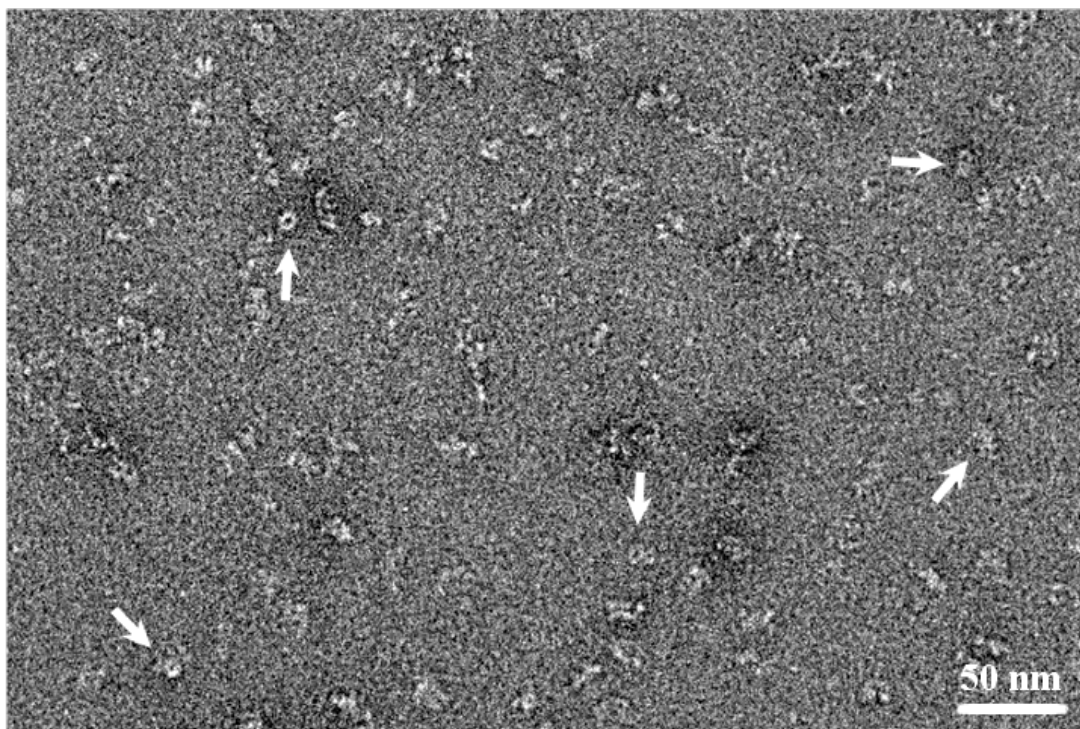


Figure 35: Negative-stain EM of purified PC 2(His₆) in DDM

Purified PC-2(His₆) was applied on a carbon coated copper grid, stained with 1 % uranyl acetate and visualized in an electron microscope (CM120, Philips). Arrows point to particles that appear to be tetrameric PC-2(His₆).

3.1.3.2 Purification of PC-2(StrepII)

The C-terminal His₆-tag was replaced by a StrepII-tag and a stable cell line that expressed PC-2(StrepII) was isolated. The different affinity tag did not change the amount of protein produced in cells. Initial purification trials using a strep-tactin column revealed that PC-2(StrepII) binds to the column even in the presence of fos-choline 14. Accordingly, PC-2(StrepII) was solubilised with 1 % fos-choline 14 and the solubilisate was applied on a strep-tactin column. A strong band around 130 kDa in the elution fractions resulted from the high accumulation of PC-2(StrepII) (figure 36 A). The elution fractions were combined and applied to a size exclusion chromatography using a Superose 6 PC 3.2/300 column (figure 36 B). The size exclusion profile revealed three absorption maxima at 0.9 ml (void volume), 1.17 ml and 1.3 ml. The protein composition in the corresponding fractions was analysed by SDS-PAGE.

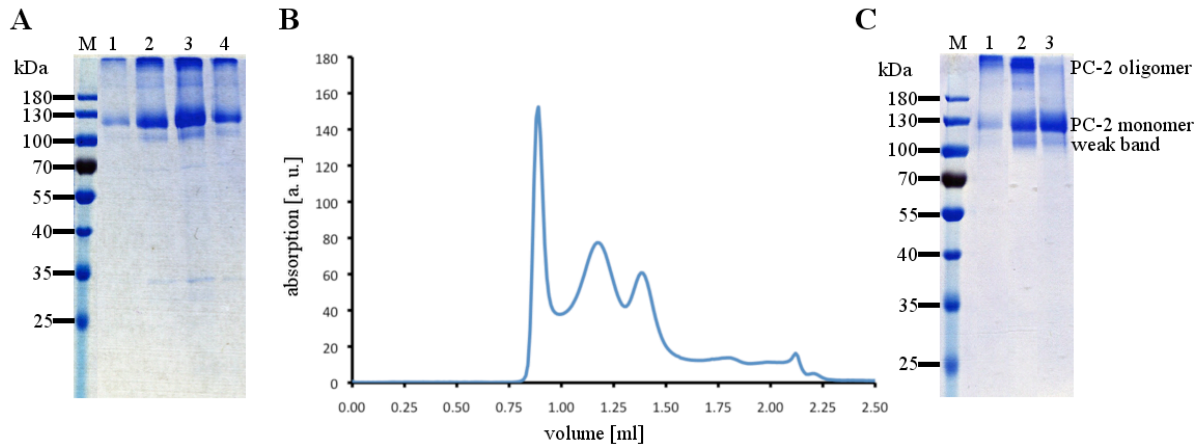


Figure 36: Purification of PC-2(StrepII) in fos-choline 14

(A) PC-2(StrepII) purification using a strep-tactin column; **M** marker (PageRuler, Thermo Fisher Scientific, Dreieich); **1-4** elution of the strep-tactin column. (B) Size exclusion chromatography of purified PC-2(StrepII). Elution of PC-2(StrepII) was monitored at 280 nm resulting in three absorption maxima at 0.9 ml, 1.17 ml and 1.3 ml where 0.9 ml corresponds to the void volume of the used Superose 6 PC 3.2/300 column. (C) SDS-PAGE after size exclusion chromatography; **M** marker (NativeMark, Thermo Fisher Scientific, Dreieich); **1** elution at 0.9 ml; **2** elution at 1.17 ml; **3** elution at 1.3 ml.

At 0.9 ml, aggregated PC-2(StrepII) eluted from the column as almost no protein bands appeared on the SDS gel. The elution fractions with a retention volume of 1.17 ml contained the PC-2(StrepII) oligomer as revealed by SDS-PAGE (figure 36 C). PC-2(StrepII) monomer eluted with a retention volume of 1.3 ml resulting in a single strong band at 130 kDa. However, an additional weak band was observed between 100 - 130 kDa in the elution fractions at 1.17 ml and 1.3 ml. Western blot analysis confirmed that all protein bands correspond to PC-2(StrepII). It is not clear if the weak band resulted from degradation, missing glycosylation or a different folding of PC-2(StrepII), i.e. it may be caused by phosphorylation.

A native-PAGE (4 - 16 % acrylamide) of the elution fraction at 1.17 ml clarified that besides the PC-2(StrepII) oligomer (around 720 kDa) also PC-2(StrepII) monomer (between 242 kDa and 480 kDa) was present in this fraction (figure 37 A). Due to different polyacrylamide concentrations used for native-PAGE, PC2(StrepII) appeared at 720 kDa and PC-2(His₆) at 1 MDa in the native gel.

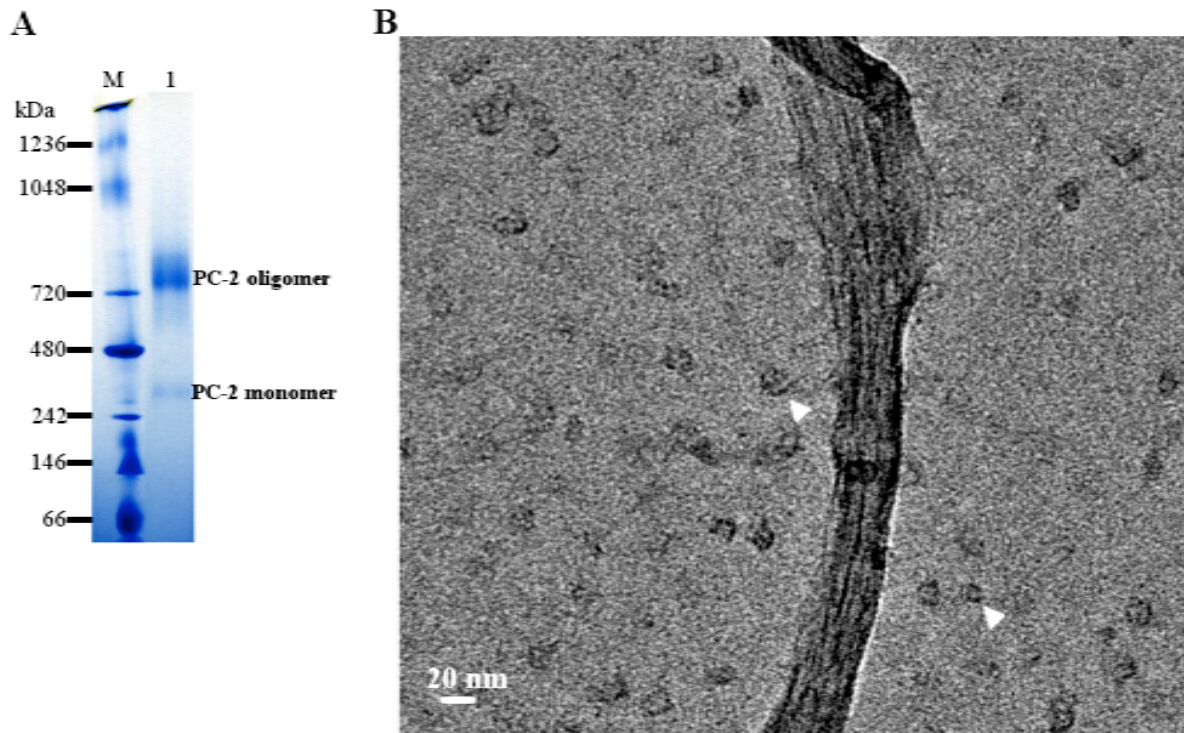


Figure 37: Native-PAGE and negative-stain EM of purified PC-2 in fos-choline 14

(A) PC-2(StrepII) after size exclusion chromatography was applied on a native-PAGE resulting in two bands, around 720 kDa and between 242 kDa and 480 kDa, corresponding to PC-2 oligomer and PC-2 monomer, respectively; **M** marker (NativeMark, Thermo Fisher Scientific, Dreieich) (B) Particles of different size (indicated by white arrowheads) were visible in negative-stain EM (CM120, Philips).

The quality of the elution fraction at 1.17 ml was analysed by negative-stain electron microscopy (EM). Electron micrographs revealed particles of different sizes, which most likely represent PC-2(StrepII) oligomers and monomers. Although different negative-stains (uranyl acetate, uranyl formiate and ammonium molybdate) were tested, PC-2(StrepII) did not stain well in fos-choline 14 (figure 37 B).

Previous studies revealed that membrane proteins can be stained much better if the detergent is exchanged by amphipol A8-35 (Liao *et al*, 2013). Compared to detergents, amphipol A8-35 is a different kind of amphiphatic molecule that binds tightly to the membrane part of proteins, keeping them in solution in the absence of detergents (Tribet *et al*, 1996). Accordingly, fos-choline 14 was replaced by amphipol A8-35. During the exchange of fos-choline 14 to amphipol A8-35, some aggregation of PC-2(StrepII) occurred. To separate oligomeric amphipol-bound PC-2(StrepII) from monomeric and aggregated protein a size exclusion chromatography was performed. The elution profile of PC-2(StrepII) in amphipol A8-35 was shifted towards a

higher molecular mass. Accordingly, the amphipol-bound oligomer of PC-2(StrepII) eluted around 1.04 ml instead of 1.17 ml as previously described for PC-2(StrepII) in fos-choline 14 (figure 37).

The SDS-PAGE of the elution fraction at 1.04 ml revealed that amphipol A8-35 stabilized the PC-2(StrepII) oligomer. The band for the PC-2(StrepII) monomer at 130 kDa was weaker compared to PC-2(StrepII) in fos-choline 14 whereas the bands at high molecular weight (figure 38 A, black arrowheads) were more pronounced. Despite that, a weak band between 100 - 130 kDa was also present (figure 38 A). Strikingly, the native-PAGE of PC-2(StrepII) in amphipol A8-35 revealed two bands at high molecular weight (between 720 - 1048 kDa) that were not visible in DDM or fos-choline 14 before (figure 38 B). The size difference between the oligomers may result from a different oligomeric complex or a different folding of PC-2. The negative-staining of PC-2(StrepII) in amphipol A8-35 worked better compared to PC-2(StrepII) in fos-choline 14 and particles were identified that presumably represent PC-2(StrepII) (figure 38 C, white arrowheads). Nevertheless, negative-stain EM also revealed that the sample was not yet suitable for data collection as it was still too heterogeneous.

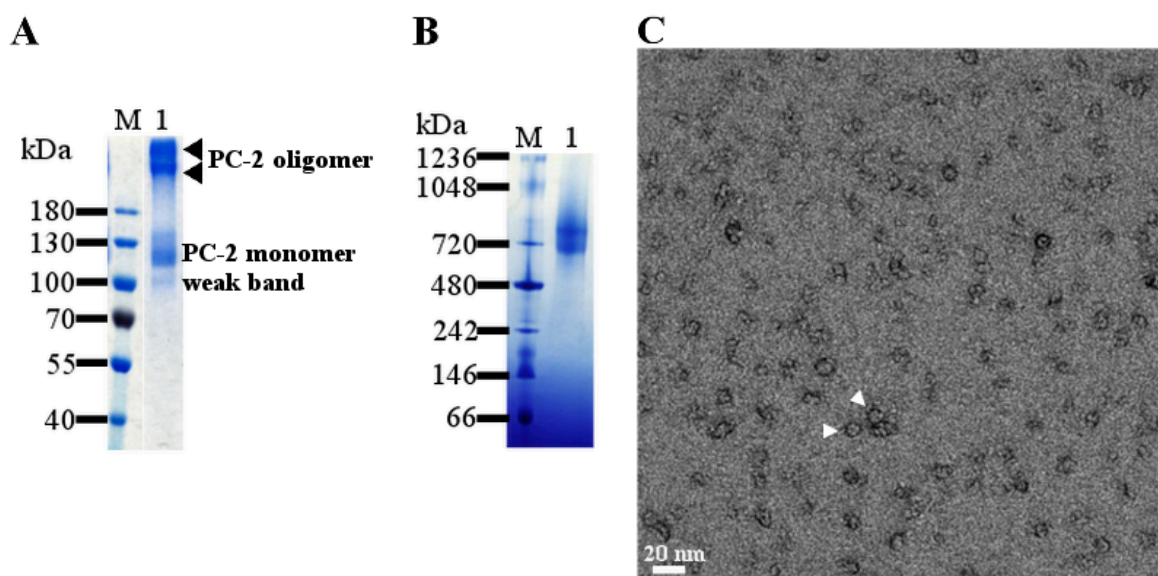


Figure 38: SDS-, native-PAGE and negative-stain EM of PC-2(StrepII) in amphipol A8-35

(A) SDS-PAGE of purified PC-2(StrepII). The strong bands at very high molecular weight indicate that SDS was not able to destroy effectively the oligomeric state of PC-2(StrepII) (black arrowheads); **M** marker (PageRuler, Thermo Fisher Scientific, Dreieich); **1** PC-2(StrepII) (B) Two separated bands were obtained in the native-PAGE representing either two different oligomeric or folding states of PC-2(StrepII); **M** marker (NativeMark, Thermo Fisher Scientific, Dreieich); **1** PC-2(StrepII). (C) Negative-stain EM of PC-2(StrepII) revealed the heterogeneity of the sample. White arrowheads point to particles that may represent correctly assembled PC-2(StrepII) tetramers.

To separate the different states of PC-2(StrepII) that were visible on the native-polyacrylamide gel, electro-elution was performed. Therefore the two bands as well as a band corresponding to the monomer of PC-2(StrepII) were cut out of the gel, homogenized and the protein was eluted over night (figure 39 A). To remove aggregated protein and Coomassie dye eluted with the protein, the samples were filtered through a 0.22 µm cellulose membrane. Clear differences were observed in SDS-PAGE analysis. The proteins eluted from the highest band showed a dominant band at high molecular mass and a weak at 130 kDa (figure 39 B). This indicates that the highest oligomer of PC-2 is SDS stable in amphipol A8-35. Proteins eluted from the second band of the native-polyacrylamid gel resulted in two bands at high molecular weight in the SDS-PAGE next to the monomer at 130 kDa. The electro-elution of PC-2 monomer resulted in a single blurry band around 130 kDa in the SDS-polyacrylamide gel (figure 39 B). However, the amount of intact protein after electro-elution was insufficient for further analysis.

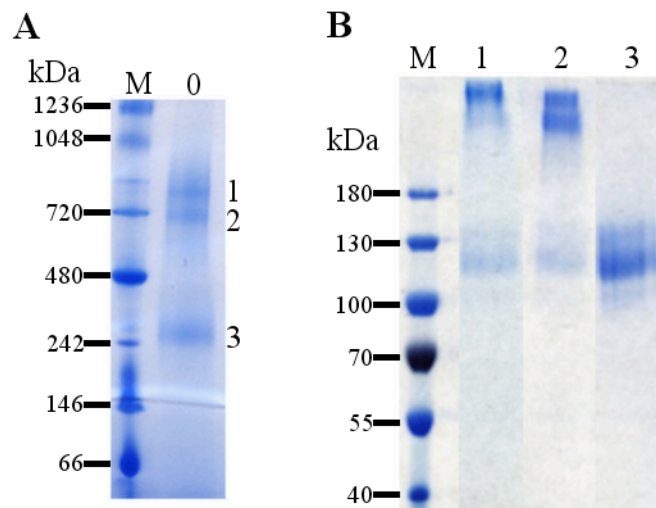


Figure 39: SDS-PAGE after electro-elution of PC-2(StrepII) in amphipol A8-35

(A) Protein bands of a native-PAGE were cut out, homogenized and proteins were electro-eluted; **M** marker (NativeMark, Thermo Fisher Scientific, Dreieich); **0** sample for electro-elution. (B) The eluate was applied on a SDS-PAGE; **M** marker (PageRuler, Thermo Fisher Scientific, Dreieich); **1** proteins eluted from the band with the highest molecular weight between 720 kDa and 1048 kDa; **2** proteins eluted from the band at 720 kDa; **3** proteins eluted from the band around 242 kDa.

Since the purification of PC-2(StrepII) in fos-choline14 and amphipol A8-35 did not lead to enough pure protein, the detergent was changed again and Ca^{2+} was added during the purification. This time 2,2-didecylpropane-1,3-bis- β -D-maltopyranoside (LMNG) was used together with cholesteryl hemisuccinate (CHS) for solubilisation and purification. LMNG has

two hydrophobic tails mimicking the lipid bilayer and thereby stabilizing solubilised membrane proteins better compared to amphiphatic molecules with only one hydrophobic tail. The addition of CHS has an additional stabilizing effect as it was shown for G-protein coupled receptors (Thompson *et al*, 2011). The size exclusion chromatography of PC-2(StrepII) in LMNG and CHS revealed that the entire protein elutes at a retention volume of 1.37 ml (figure 40 A). This indicates that only one type of oligomeric state is present in the sample. For further analysis this sample was frozen immediately on Quantifoil R2/2 grids and visualized by electron cryomicroscopy. In the cryomicrographs single particles with a recognizable shape were identified (figure 40 B).

To visualize PC-2, cryo images were taken at defocus values between 3.0 and 5.0 μm . To increase the signal to noise the lipid and detergent concentration in the buffer has been reduced. PC-2 was incorporated into amphipol A8-35 after purification in LMNG/CHS. The size exclusion chromatogram revealed a sharp monodisperse peak at a retention volume of 1.35 ml, which corresponds to PC-2(StrepII), and a smaller peak at a retention volume of 1.6 ml that contains free amphipol A8-35 micelles (figure 40 C). PC2(StrepII) was frozen on Quantifoil R2/2 grids and analysed by cryo-EM. Electron cryomicrographs were taken with a defocus range of 0.7 - 2.5 μm and in all micrographs single particles were identified (figure 40 D).

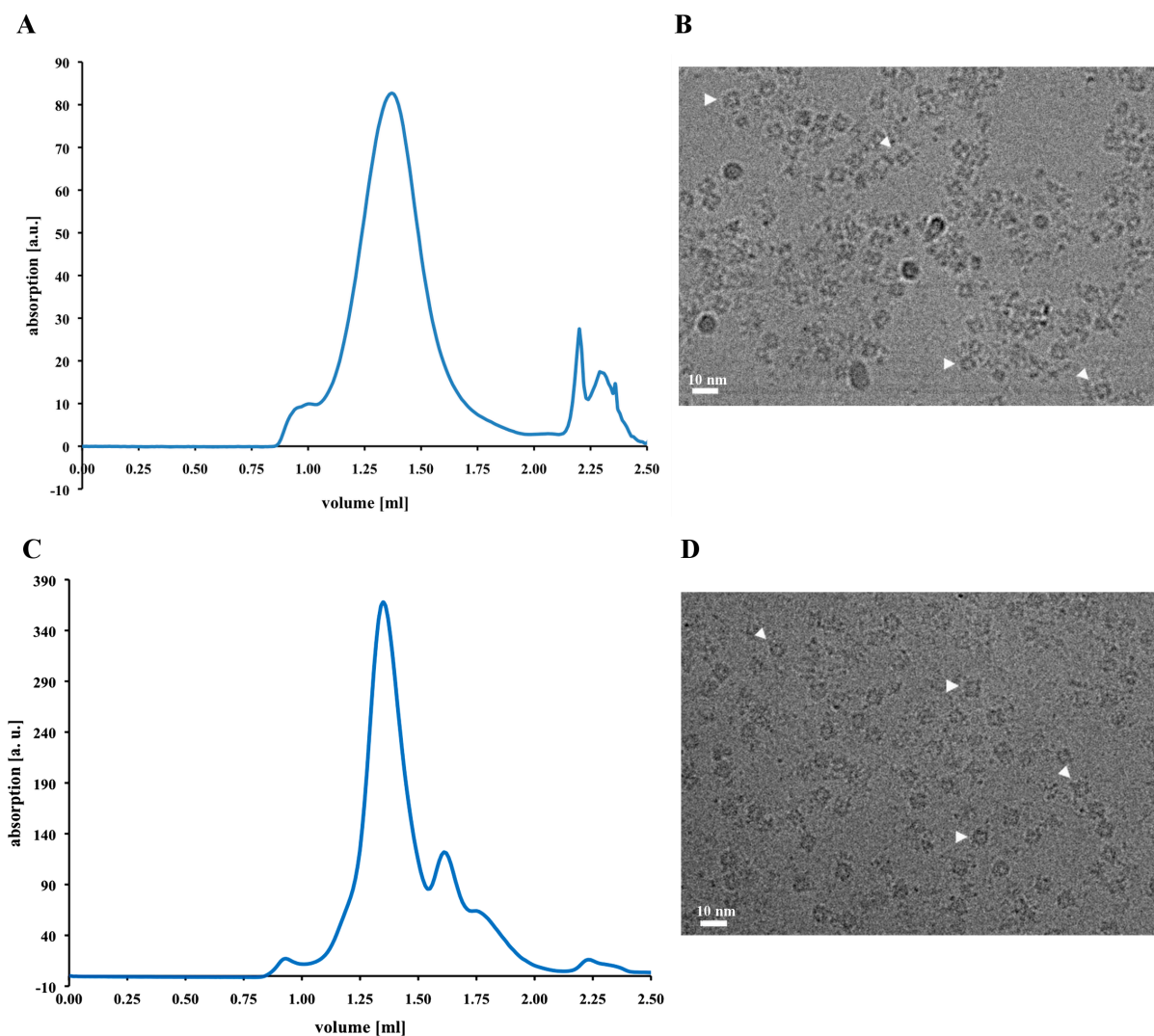


Figure 40: Size exclusion chromatograms and electron cryomicrographs of PC-2(StrepII) in LMNG/CHS and amphipol A8-35

(A) Size exclusion chromatography of PC-2(StrepII) in LMNG/CHS (Superose 6 PC 10/300). PC-2(StrepII) elutes at a retention volume of 1.37 ml. (B) Electron cryomicrograph of PC-2(StrepII) in LMNG/CHS with a defocus of 4.0 μm . (C) Size exclusion chromatography of PC-2(StrepII) in amphipol A8-35 (Superose 6 PC 10/300). PC-2(StrepII) and free amphipol A8-35 micelles elute with a retention volume of 1.35 ml and 1.6 ml, respectively. (D) Electron cryomicrograph of PC-2(StrepII) in amphipol A8-35 with a defocus of 2.5 μm . White arrowheads point to particles corresponding to PC-2(StrepII). Micrographs were taken at a nominal magnification of 30.000x (pixel size of 1.14 \AA).

3.1.3.3 Structure determination of PC-2(StrepII)

For structure determination ~ 120.000 particles from 860 cryomicrographs were selected. These particles were analysed by 2D classification using Relion-1.3. The class averages revealed that

the selected particles were tetrameric PC-2 molecules (figure 41). Interestingly, most of the particles represent the TRP channel viewed from the periplasm (top view). After false-positive particles were removed by 2D classification, a subset of about 50.000 particles was used for a 3D refinement. As initial model the cryo-EM structure of the TRPV1 channel was applied and low passed-filtered to 60 Å. The 3D refinement yielded in a structure with a resolution of 4.6 Å after post-processing (figure 42).

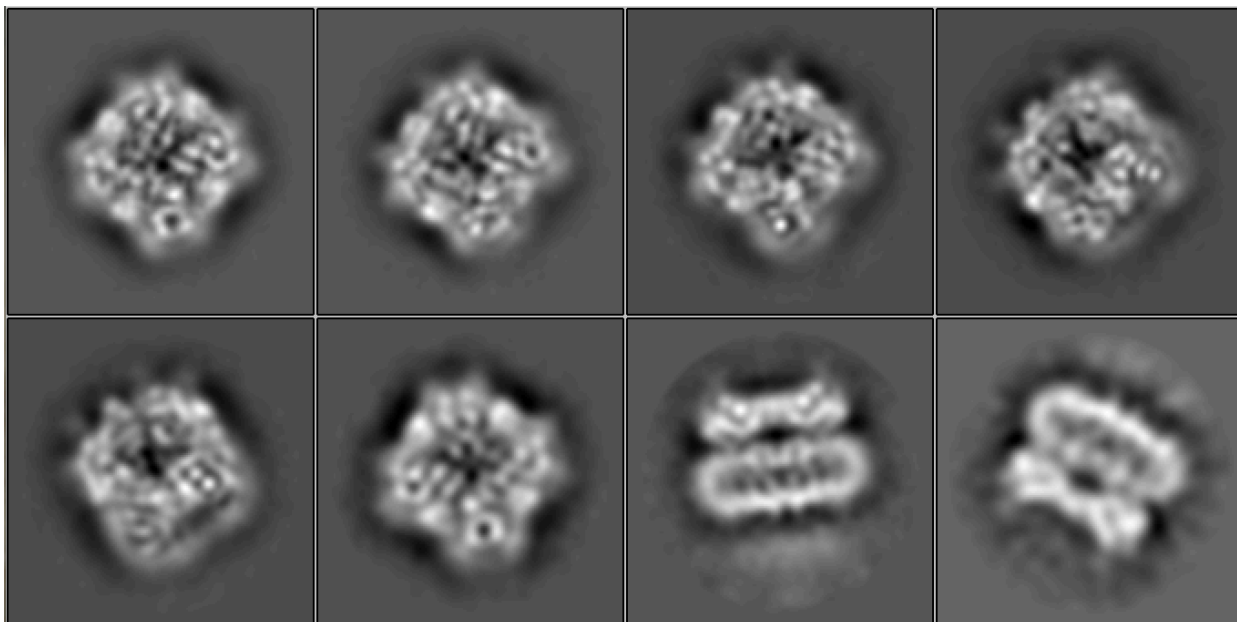


Figure 41: 2D class averages of PC-2

2D class averages show different orientation of PC-2. Except of the last two class-averages, which show side views, all other classes show top views.

3.1.3.4 Cryo-EM structure of PC-2(StrepII)

The structure of PC-2 did not show the soluble cytoplasmic N- and C-terminal domains, although these were present in the full-length protein used for structure determination (figure 42 A, C). This indicates that the N- and C-terminal domains of PC-2 are flexible. Thus about 50 % of the protein is not resolved in the EM structure. Interestingly, details of the extracellular domain formed by loop 1 were identified (figure 42 A, B). The extracellular domain has a size of ~25 kDa and is unique to the TRPP subfamily (figure 43) (Nilius *et al*, 2005).

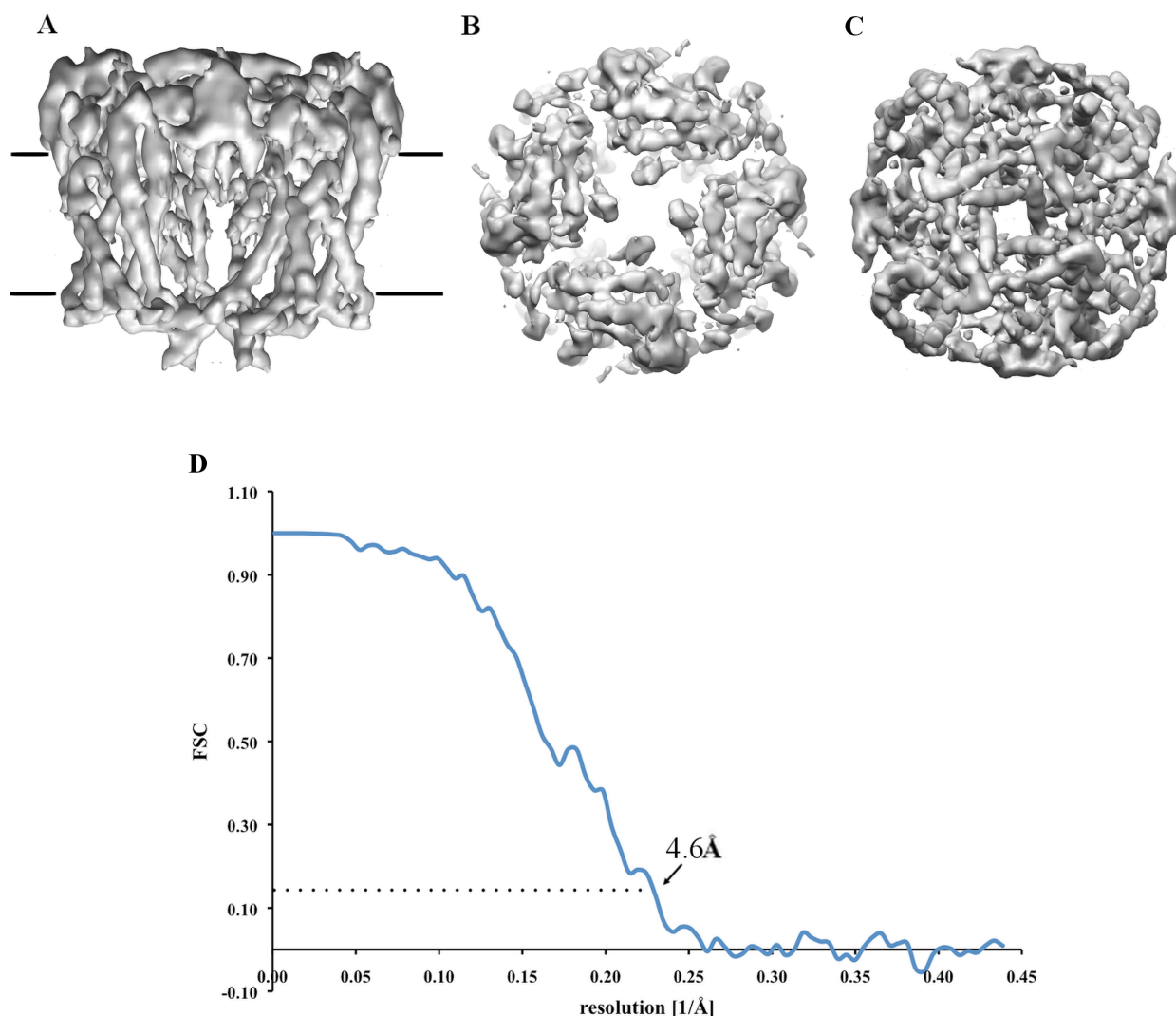


Figure 42: 4.6 Å cryo-EM structure of PC-2

The cryo-EM density of PC-2 viewed (A) along the membrane plane (side view), (B) from the periplasm (top view) and (C) from the cytoplasm (bottom view). The membrane is indicated by black bars. (D) FSC curve of the cryo-EM structure indicating the resolution of 4.6 Å. The gold standard threshold at 0.143 is indicated by the dotted line.

A comparison between the membrane domains of PC-2 with those of the previously determined TRP channels TRPV1 and TRPA1 revealed a similar architecture. As in TRPV1 and TRPA1 TMH 1 - 4 form a scaffold while the pore is built by TMH 5 - 6 (figure 44). In contrast to PC-2 the cytoplasmic domains of TRPV1 and TRPA1 were resolved in the EM structure. Both channels contain N-terminal ankyrin repeat domains, which may have a stabilizing effect. Such domains are lacking in PC-2 (figure 1).

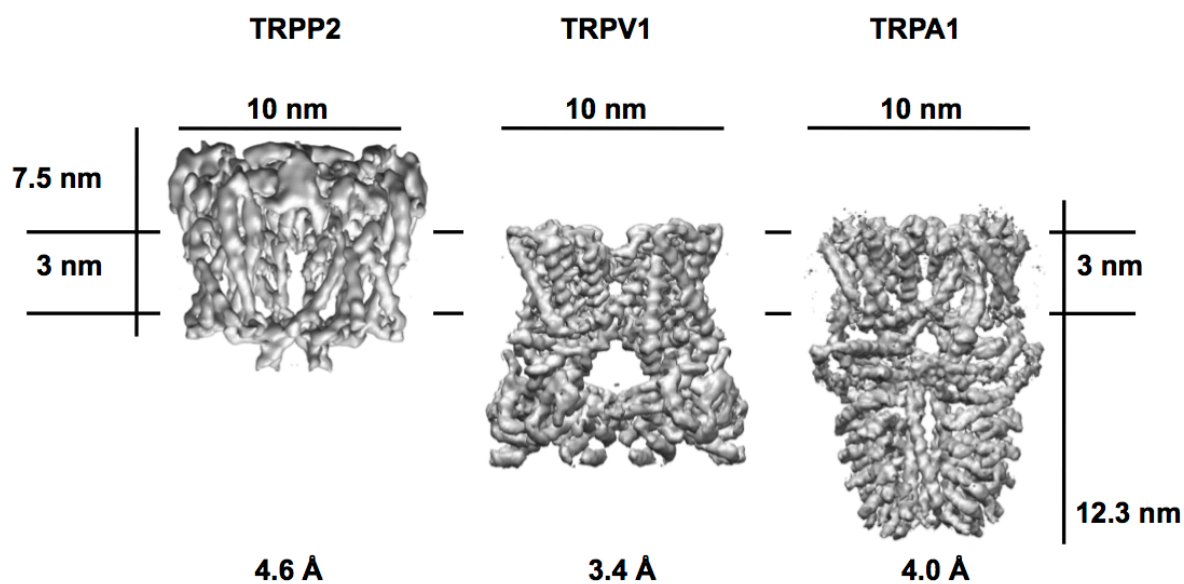


Figure 43: Comparison of cryo-EM structures of PC-2, TRPV1 and TRPA1

A comparison between PC-2, TRV1 and TRPA1 shows that the membrane part of all three TRP channels is conserved while the soluble domains are very different. In contrast to TRPV1 and TRPA1, PC-2 has the long loop 1 forming an ordered extracellular domain.

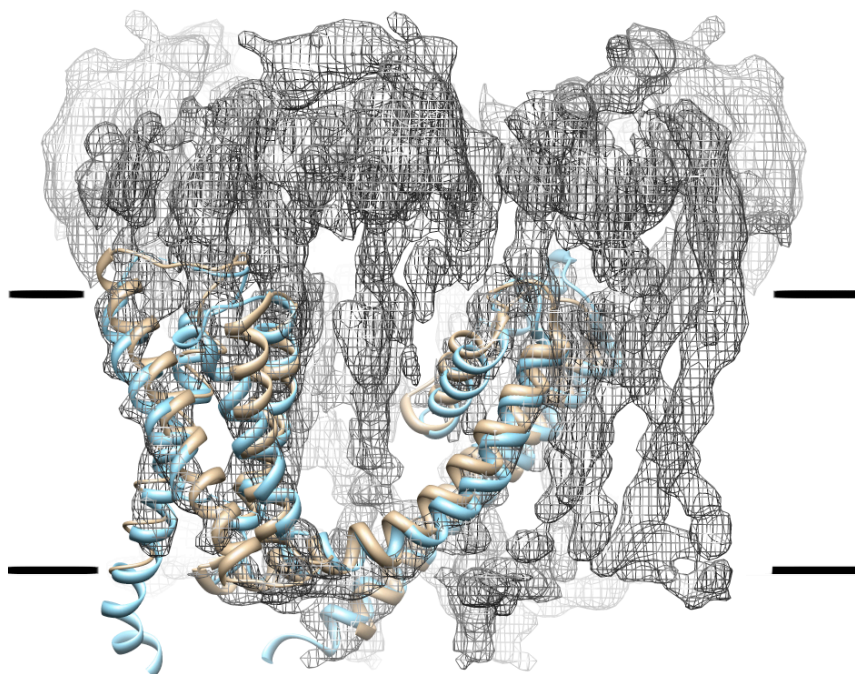


Figure 44: Overlay of the membrane domains of TRPV1, TRPA1 and PC-2

The membrane domains of TRPV1 (gold; pdb 3J5Q) and TRPA1 (blue; pdb 3J9P) were fitted into the cryo-EM structure of PC-2.

To determine the local resolution of the cryo-EM structure it was analysed with ResMap (Kucukelbir *et al*, 2014) revealing that TMH 5 and 6 are better resolved compared to TMH 1 - 4 and loop 1 (figure 45). It is expected that the core of a protein is generally better resolved than the periphery as it forms the centre for particle alignment.

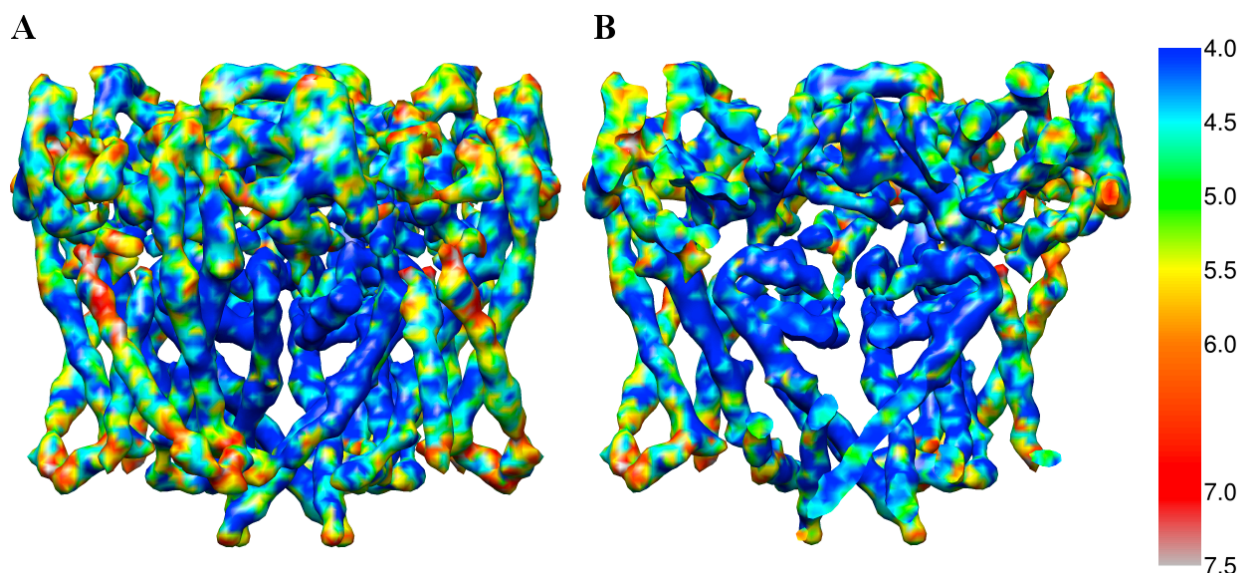


Figure 45: Local resolution of the PC-2 structure

The local resolution of PC-2 was determined by ResMap (Kucukelbir *et al*, 2014) showing that TMH 5 and 6 that form the pore of the channel are better resolved compared to TMH 1 - 4 and the extracellular domain. (A) View of PC-2 along the membrane plane and (B) cut in the middle to highlight the pore region. The structure is coloured corresponding to the local resolution indicated by the rainbow bar on the right. The numbers represent the resolution in angstrom.

Conformation of PC-2

An important question remains if the structure of PC-2 represents the opened or the closed conformation of the protein complex. Functional measurements of PC-2 pointed out that Ca^{2+} stabilises the opened conformation (Vassilev *et al*, 2001). Although the C-terminal calcium-binding EF-hand was not resolved in the EM structure, Ca^{2+} was present during purification and may be bound by the EF-hand. To validate the state of PC-2, the cryo-EM map was superimposed with the cryo-EM map of TRPV1 in the opened and closed state (figure 46). Strikingly, the pore region of the opened TRPV1 channel fits much better into the density of PC-2. This strongly suggests that the structure of PC-2 displays the opened state.

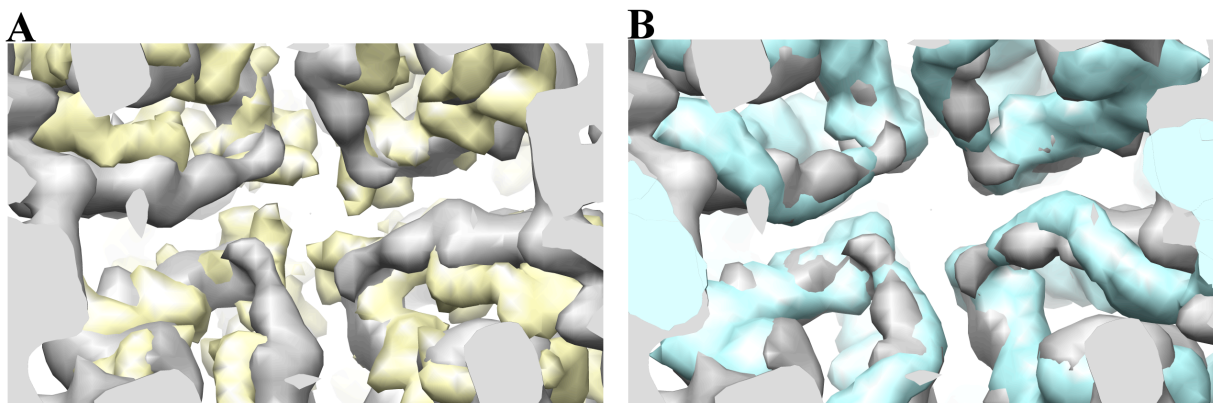


Figure 46: Comparison of the pore region of PC-2 with the closed and opened TRPV1 structure
Fit of the PC-2 pore region (grey) into (A) the closed structure of TRPV1 (yellow; emdb 5778) and (B) the opened conformation of TRPV1 (cyan; emdb 5776).

Extracellular domain of PC-2.

The large extracellular domain of PC-2 is a unique feature of the TRPP channel subfamily. So far no structural information of this domain is available. To get an idea of structural elements present in this domain the amino acid sequence was subjected to several secondary structure prediction programs (figure 47). Based on these programs it is assumed the extracellular domain forms three to six α -helices and six to seven β -strands. However, secondary structure predictions suggested also unordered regions. These regions may be flexible and therefore not visible in the EM density.

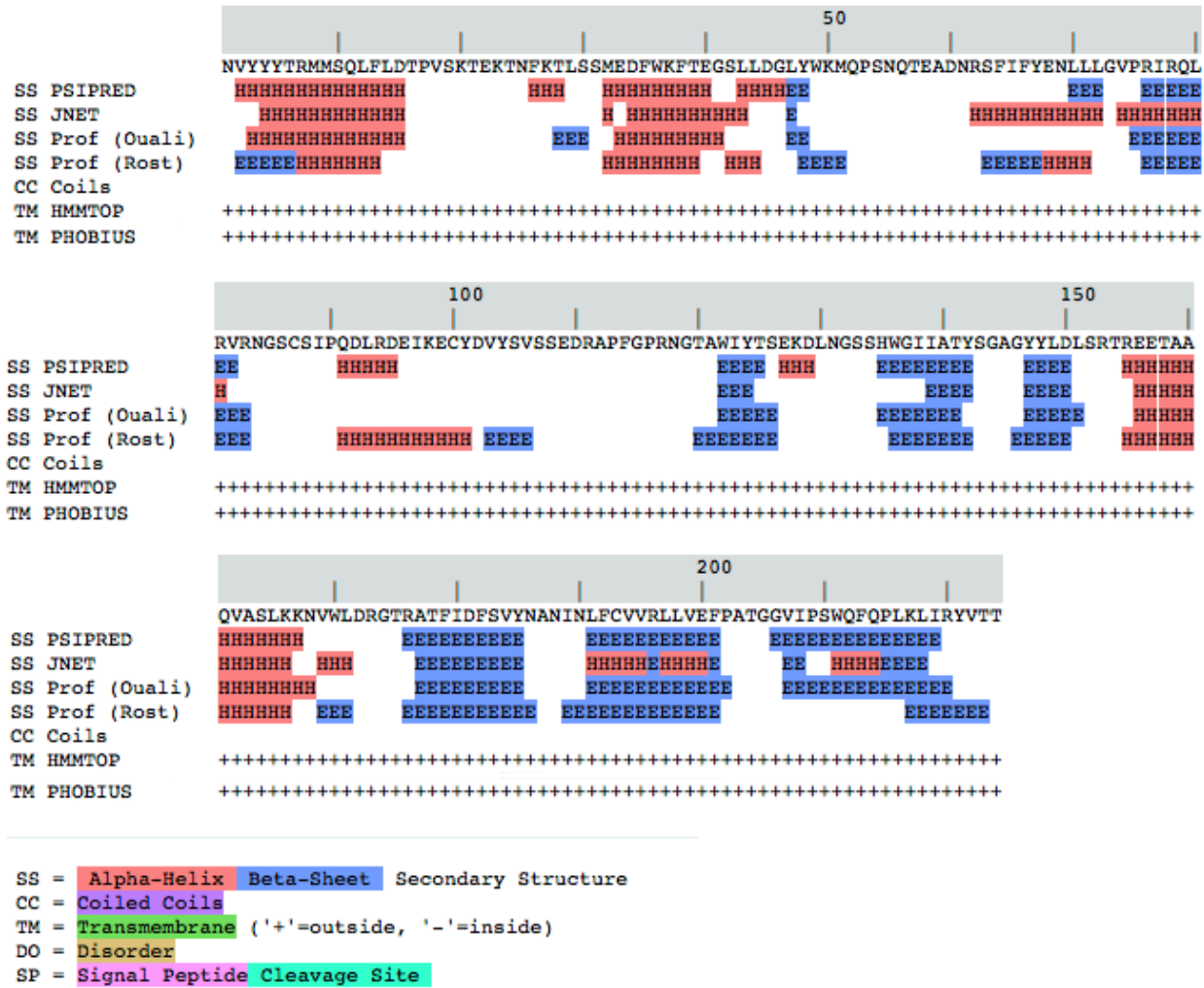


Figure 47: Secondary structure prediction of the extracellular domain

The amino acid sequence of loop 1 was subjected to different secondary structure prediction programs: PSIPRED (Jones, 1999); JNET (Cuff *et al*, 1999); Prof (Ouali) (Ouali *et al*, 2000); Prof (Rost) (Rost, 2001); Coils (Lupas *et al*, 1991); HMMTOP (Tusnady *et al*, 1998) and PHOBIUS (Kall *et al*, 2004).

With the secondary structure prediction in hand, the extracellular density was further examined. Viewed from the periplasm, the top of the channel is formed by two helices located next to each other (figure 48 A). Below these helices a β -sheet of four β -strands is visible. In addition an α -helix is visible which is an extension of TMH 1. Taken together three α -helices and four β -strands are resolved in the EM density. Since three to six helices and six to seven β -strands were predicted it seems that other parts of the extracellular domain are flexible and not resolved in the EM structure. At a resolution better than 4 Å, amino acid side chains are resolved which identify residues in this domain.

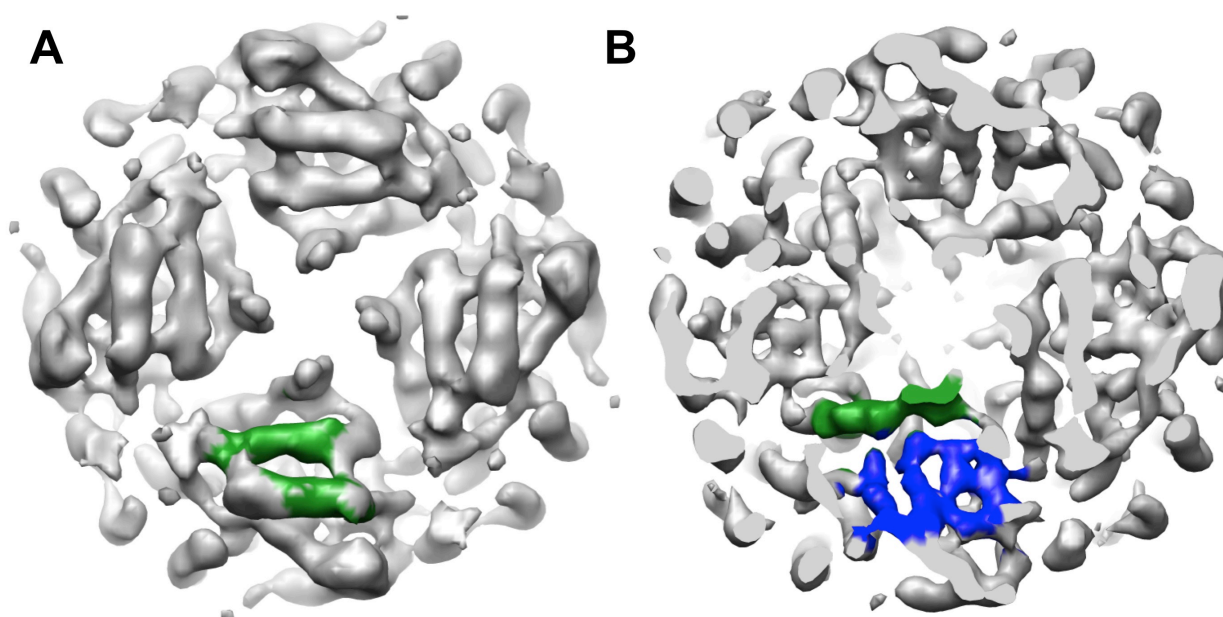


Figure 48: Structural elements of the extracellular domain

The extracellular domain viewed from the periplasm. (A) The top of this domain is formed by two helices located next to each other (green). (B) Below these two helices, four β -strands (blue) and one α -helix (green) that is the elongation of TMH 1 are located.

3.2 Discussion

Polycystin-2 plays a key role in the human genetic disease ADPKD. The lack of therapies treating ADPKD makes the structure of PC-2 an important requisite to understand the proteins function and to develop specific drugs targeting PC-2. The different cellular localization of PC-2 *in vitro* and *in vivo* suggests that PC-2 responds to different cellular stimuli and performs various functions in the cell.

One part of this work was the structural investigation of PC-2. One focus was on the entire protein complex while important soluble domains of the protein were additionally considered. The genes of interest were incorporated into the genome of GnTII⁻ cells, which were used for protein production. The impact of PC-2 and truncation mutants on the cellular morphology was investigated revealing that PC-2 overexpression results in the formation of crystalloid ER. In contrast to previous studies, the activity of PC-2 was not measurable by whole-cell patch-clamp experiments. However, the purification of PC-2 was successful by using a mixture of LMNG and CHS as detergents, which were exchanged by amphipol 8-35 before cryo-EM data collection. Finally the structure of PC-2 was determined to a resolution of 4.6 Å showing that the TRPP subfamily contains structural features that were not observed in the TRPV and TRPA subfamily.

3.2.1 Expression of PC-2 and different PC-2 truncation mutants in GnTII⁻ cells

Analysis of PC-2 related ADPKD patients revealed that disease-inducing mutations are not located in special regions of the protein, they are spread throughout the entire protein (figure 49) (Hateboer *et al*, 2000). Therefore the focus of this study was on the structure determination of full-length PC-2. To obtain sufficient amounts of homogenous glycosylated PC-2, GnTII⁻ cells growing in tissue and solution culture were used for PC-2 expression. GnTII⁻ cells allow an inducible protein expression by having a TetR gene, which is continuously expressed. TetR binds and blocks promoters with a tetracycline response element. In the presence of tetracycline TetR changes its conformation binding tetracycline. In this state the promoter is no longer occupied by TetR, which results in gene transcription. GnTII⁻ cells are an excellent expression system for human membrane proteins as already shown for rhodopsin. The amount of produced rhodopsin was sufficient for 3D crystallization and resulted in a structure containing all post-translational modifications (Standfuss *et al*, 2011).

The drawback of GnTII⁻ cells is that the gene of interest has to be incorporated into the cellular genome for large-scale expression. Otherwise the cells will lose the plasmid during growth. In this work GnTII⁻ cells that have incorporated the gene of interest were selected by single cell

dilution. Most PC-2 constructs were post-translationally modified and expressed in sufficient amounts, indicating a correct and stable protein assembly. The only exceptions were N-terminal truncation mutants, which were not expressed in large amounts. This may result from the fact that the N-terminal amino acids have a huge impact on the half-life of cellular proteins (Bachmair *et al*, 1986) or that the N-terminus is important for proper protein folding.

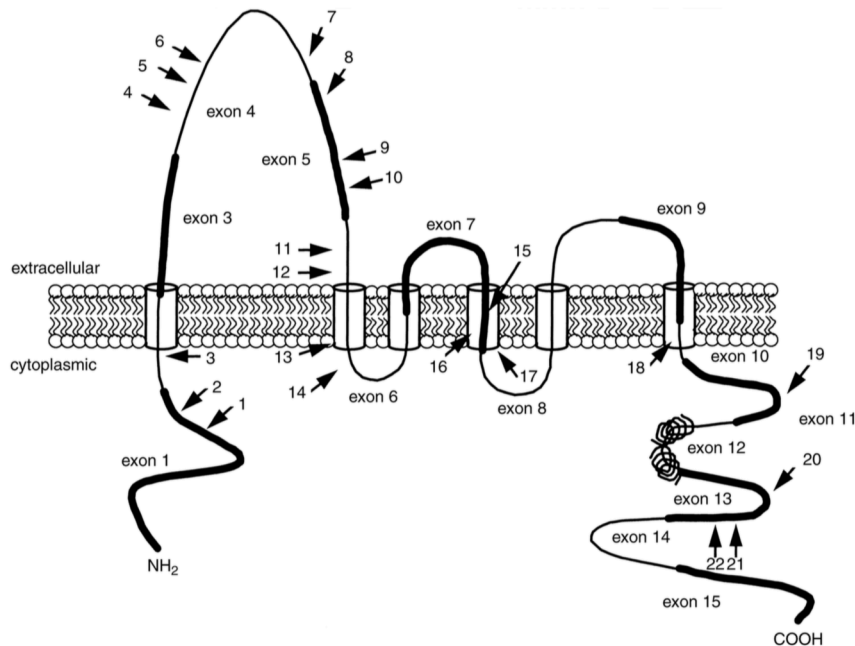


Figure 49: Location of ADPKD related mutations in PC-2

Mutations that cause ADPKD are marked by arrows. The calcium-binding EF hand is highlighted by a helical structure near the C-terminus. Regions encoded by different exons are indicated by alternating thin and thick lines. The figure was taken from (Hateboer *et al*, 2000).

3.2.2 Activity measurements of PC-2 in GnTII cells

Initial laser confocal scanning microscopy studies on PC-2 expressing GnTII cells revealed the plasma membrane localization of PC-2, which is a prerequisite for patch-clamp measurements. However, no activity of PC-2 was detected. A reason may be that PC-2 requires an additional stimulus for activation. This finding is in agreement with the study of Giamarchi *et al*. who measured channel activity only after applying a specific antibody (Giamarchi *et al*, 2010) but contrary to the study of Luo *et al*. who characterized PC-2 without additional stimulus (Luo *et al*, 2003). Our finding that PC-2 is indeed located at the plasma membrane combined with the fact that PC-2 activity was not detected supports that the native PC-2 requires a specific stimulus for

activation. It has been shown that TRP channels are activated by ligands. TRPV1 opens in response to heat, small vanilloid ligands and toxins. A cryo-EM structure in the presence of the vanilloid ligand resiniferatoxin (RTX) and the spider double-knot toxin (DkTx) revealed that these compounds bind to transmembrane helices 5 and 6, which form the pore of the channel. This way the ligands bind to the extracellular region of the channel (figure 50) (Cao *et al*, 2013). In contrast to all other TRP channel subfamilies, TRPP subfamily members have a long first extracellular loop. The function of this loop has not been investigated, but may play a role in PC-2 activation.

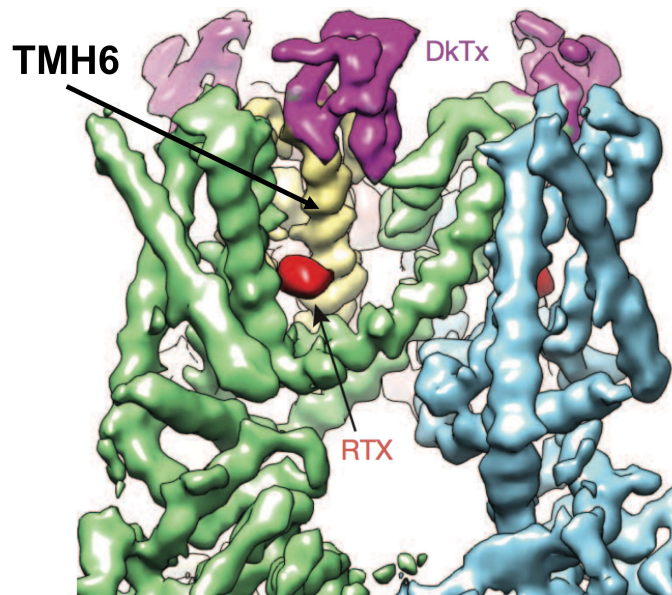


Figure 50: Structure of TRPV1 in complex with the vanilloid ligand resiniferatoxin (RTX) and the spider double-knot toxin (DkTx)

The structure of TRPV1 in the presence of RTX and DkTx shows that activating ligands bind to TMH 5 + 6 that forms the pore of the protein. The figure was modified from (Cao *et al*, 2013).

3.2.3 Crystalloid formation during PC-2 expression in GnTII⁻ cells

Electron microscopy of thin sections of GnTII⁻ cells expressing PC-2 revealed that the cells contain crystalloid ER. The morphology change was clearly connected to PC-2 expression. This result confirms previous studies where the formation of karmellae and whorl ER was likewise linked to PC-2 expression (Giamarchi *et al*, 2010). In contrast to karmellae and whorl ER the formation of crystalloid ER does not occur regularly. Therefore it is still a mystery what drives the formation of crystalloid ER. In general, the overexpression of membrane proteins requires more phospholipids, which is caused by their membrane localization. However, additional

stimuli for membrane biogenesis are essential to result in such a tremendous increase in the ER that finally leads to cell death.

The *in vitro* generation of crystalloid ER has only been described for the overexpression of HMG-CoA reductase in UT-1 cells (Pathak *et al.*, 1986). HMG-CoA reductase is essential during the formation of cardiolipin and therefore it was proposed that formation of crystalloid ER is linked to an overexpression of the lipid cardiolipin (Pathak *et al.*, 1986). In contrast we did not find evidence for the overexpression of HMG-CoA reductase or other proteins involved in ER biogenesis. Recently, an *in vivo* study connected the expression of PC-2 to the repair mechanism of lipid bilayers. Although this study did not conclude that an overexpression of PC-2 led to an increase in cellular phospholipids, it linked PC-2 to the phospholipid biogenesis (Spirli *et al.*, 2015).

The fact that the cytoplasmatic coiled-coil domain, which is known to form strong intermolecular contacts, stabilizes crystalloid ER confirms previous results showing that this domain is essential for the formation of karmellea and whorl ER (Giamarchi *et al.*, 2010). Strikingly, HMG-CoA reductase does not contain such a domain, nor does PC-2 Δ 273, but in both cases crystalloid ER is detected. This indicates that a coiled-coil domain supports the formation of crystalloid ER but it is not mandatory.

Another approach to explain the existence of crystalloid ER is that phospholipids can be stored most efficiently inside cells in form of membrane tubes. But this would not explain why crystalloid ER is found so rarely.

Altogether, the overexpression of a protein that forms strong intermolecular interactions combined with an increase in the phospholipid biogenesis seems to support the formation of crystalloid ER. However, nothing is known about the trigger that causes karmellea instead of whorl or crystalloid ER formation.

3.2.4 Subcellular localization of PC-2 and truncation mutants in GnTI⁻ cells

Immunogold labelling and laser confocal scanning microscopy revealed that PC-2 is not only localized in the ER but also at the plasma membrane. Previous studies showed that the localization of PC-2 differs between cells *in vitro* and *in vivo* (Cai *et al.*, 1999; Gonzalez-Perrett *et al.*, 2001; Koulen *et al.*, 2002; Ong *et al.*, 1999). Since the largest amount of PC-2 was located in the ER it can be assumed that the plasma membrane localization is an artefact caused by the overexpression of PC-2. This would support the hypothesis that PC-2 forms a calcium dependent calcium release channel in the ER (Koulen *et al.*, 2002).

Surprisingly, the deletion of the second coiled-coil domain led to a predominant plasma membrane localization of the protein, although the ER-retention signal formed by aa 787 - 820 was still present. This result showed that PACS-1 and -2 did not recognize the ER retention signal in PC-2 Δ 143. The reason for that may be that without the second coiled-coil domain the C-terminal domain changes its conformation harbouring a fold where the ER retention sequence is not accessible anymore.

The deletion of the ER retention signal led to an increased localization of PC-2 Δ 182 in the ER. While the plasma membrane localization was expected due to the deletion of the ER retention signal, the increase in the ER localization was unexpected. A possible explanation is that the complete C-terminal domain supports protein folding and assembly. If this holds true, a further truncation of the C-terminal domain would increase the time necessary to form stable oligomers. Strikingly, further truncation of the calcium-binding site resulted in formation of small crystalloid ER patches in about 50 % of all cells. In sum, PC-2 Δ 273 was localized equally in the ER and in the plasma membrane. This supports the assumption that the C-terminal domain is indeed important for protein folding and assembly. As a result, truncation mutants require more time for oligomerization in the ER. However, further biochemical studies including stability tests as well as time dependent localization studies for PC-2 Δ 182 and PC-2 Δ 273 in GnTI⁻ cells are necessary to confirm this hypothesis.

3.2.5 Purification and oligomeric state of PC-2

The purification of PC-2(His₆) was performed in different detergents on different affinity columns combined with size exclusion chromatography. The purity of PC-2(His₆) allowed the analysis of the oligomeric state by native-PAGE, which indicated that PC-2(His₆) forms a homotetramer. This is in agreement with previous studies and was expected, since all known TRP channels form tetramers (Ferreira *et al*, 2011; Wu *et al*, 2010). However, the result is contrary to the study of Yu *et al*. who performed the same native PAGE analysis but claimed a trimeric assembly of PC-2. The trimeric assembly supported the finding that the coiled-coil domain of PC-2 crystallized as a trimer (Yu *et al*, 2009). The different oligomeric states of PC-2 after expression in different cell lines are in agreement with the different cellular functions proposed for PC-2. It might be that in the presence of PC-1, PC-2 forms a heterotetramer that is predominantly transported to the primary cilium while it forms a homotetramer in the absence of PC-1 forming a calcium dependent calcium release channel in the ER (Koulen *et al*, 2002; Nauli *et al*, 2003).

The separation of PC-2(StrepII) in amphipol A8-35 by native-PAGE worked much better than the separation of PC-2(StrepII) in detergents. This can be attributed to a different binding behaviour of amphipol A8-35 to PC-2 compared to detergent molecules. In contrast to detergents amphipol A8-35 does not require an excess of unbound amphipol A8-35 molecules in the buffer (Tribet *et al*, 1996). This means that membrane proteins in amphipol A8-35 can be treated like soluble proteins resulting in defined bands in native-PAGE. Surprisingly, the native-PAGE of the purified PC-2(StrepII) complex in amphipol A8-35 revealed two bands above 720 kDa representing either different oligomeric, phosphorylation or folding states of PC-2(StrepII). In the case that the two bands in the native-PAGE result from different oligomeric states it can be concluded that PC-2 homotrimers form a stable intermediate state that can be further oligomerize with other proteins. As already described different oligomeric states of PC-2 are reasonable due to the fact that the protein might be able to form heterotetramers with a stoichiometry of 3:1 (Molland *et al*, 2012; Yu *et al*, 2009; Yu *et al*, 2012) or 2:2 (Kobori *et al*, 2009).

In previous studies an F-type ATPase was purified by native-PAGE and after electro-elution successfully used for 2D crystallization (Poetsch *et al*, 2000). The same approach was used for PC-2(StrepII) after the protein was incorporated in amphipol A8-35. SDS-PAGE analysis revealed that this method worked in principle. However, most of the protein aggregated during electro-elution resulting in an insufficient amount of pure protein for structural investigation.

In a further step the detergent was changed to LMNG/CHS for purification. LMNG is closely related to DDM and has already been used for structure determination (Rollauer *et al*, 2012; White *et al*, 2012). In contrast to DDM LMNG has two instead of one hydrophobic tail and CHS is a cholesterol derivate. Thereby the LMNG/CHS mixture is better mimicking phospholipids compared to other detergents. With this detergent combination the purification of PC-2 yielded in a PC-2 sample that was suitable for further single particle cryo-EM analysis. The exchange of LMNG/CHS with amphipol A8-35 further stabilized PC-2. It seems that PC-2 bound some CHS molecules, which remain bound when the protein was incorporated in amphipol-A8-35. This would explain why PC-2 forms a stable tetramer in amphipol A8-35 after it was purified in LMNG/CHS but not after other detergents like DDM or fos-choline 14.

3.2.6 4.6 Å cryo-EM structure of PC-2

The human TRP channel PC-2 is composed of a regulatory cytoplasmic domain, a membrane domain forming the channel pore and a glycosylated extracellular region. In the cryo-EM structure of PC-2 at a resolution of 4.6 Å only the membrane and extracellular domain were resolved. However, structural investigation of the isolated C-terminal EF-hand and coiled-coil

domain point out that both regions are rigid (Allen *et al*, 2014; Yu *et al*, 2009). The addition of Ca^{2+} during purification should ensure that the EF-hand is in the calcium-bound state. But nevertheless, no cytoplasmic density was obtained in the cryo-EM structure. This points to flexible N- and C-terminal domains of PC-2.

The membrane domain within the TRP channel family is the region with the highest sequence homology (Huang, 2004). Consequently, the membrane domain of PC-2 is very similar to TRPV1, TRPV2 and TRPA1. TMH 1 - 4 form a scaffold at the channel periphery while TMH 5 and 6 of each protomer interact to build the channel pore. The pore of PC-2 was compared with the opened and closed conformation of TRPV1, indicating that PC-2 is in the opened conformation. The opened state of PC-2 would support the finding that Ca^{2+} stabilises the opened state of the channel (Vassilev *et al*, 2001) and is in agreement with the suggestion that PC-2 forms a calcium dependent calcium release channel in the ER (Koulen *et al*, 2002).

The large extracellular domain that is partially resolved in the cryo-EM structure is unique for the TRPP channel subfamily. In the EM density three α -helices and four β -strains are resolved. To get an idea which parts of the extracellular domain are resolved, the sequence of this domain was subjected to the Rosetta protein structure prediction server (Raman *et al*, 2009; Song *et al*, 2013). The program cut the loop into three parts that show similarities of 8 %, 10 % and 13 % to known structures. Two of the structures belong to proteins with unknown function while the last one is a viral protein. The obtained models were placed into the cryo-EM map but none of it fit. However, based on these models α -helices or β -sheets were analysed individually and fitted into the EM map (figure 51). By using only a small fraction of the obtained models almost the entire extracellular domain was covered. This supports that not the entire loop 1 is resolved in the EM structure.

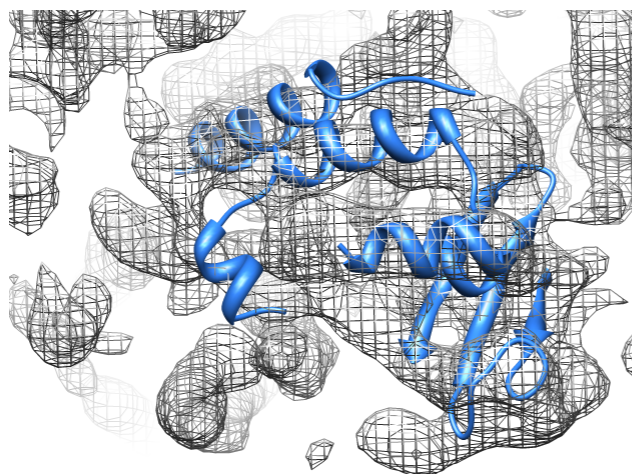


Figure 51: Resolved structural elements of the extracellular domain

In the extracellular domain three α -helices and four β -strands were identified. α -helices and β -sheets of models obtained with the Rosetta protein structure prediction server (Raman *et al*, 2009; Song *et al*, 2013) were fitted separately into the EM density.

The fact that mutations inducing ADPKD are located the extracellular domain indicates that this domain is important for the function of PC-2 (figure 49). The structure of this domain can be used as basis for speculations of its function. It may be that the two helices that point to the extracellular space form a scaffold for regulatory factors that bind to PC-2 when it is present in the primary cilium of kidney epithelia cells. Another aspect may be that the β -sheet that is located below the two α -helices and above the lipid bilayer is involved in the sensing of mechanosensitive stress (Nauli *et al*, 2003). However, both suggestions do not explain why PC-2 is only present in the primary cilium in complex with PC-1.

At the determined resolution of 4.6 Å the membrane helices are better resolved compared to the soluble domain. More micrographs of PC-2 have to be acquired and analysed to increase the resolution. At a resolution below 4 Å an atomic model of PC-2 could be built.

In a further step the structure of this channel should be investigated in the absence of Ca^{2+} , which should result in the closed conformation of PC-2. Having the opened and closed state in hand a mechanism of opening and closing could than be proposed for PC-2.

3.2.7 Summary

In this study G_nT_I cells were successfully used to express PC-2 as well as different truncation mutants of it. The expression of PC-2 was connected to the formation of crystalloid ER. Although the mechanism that causes crystalloid ER is not known, the formation of crystalloid ER seems to depend on proteins that form intermolecular contacts and are connected to phospholipid biogenesis. The sequential truncation of the C-terminal domain of PC-2 changes the cellular localization from the ER to the plasma membrane. The purification of PC-2 was optimized by several steps until PC-2(StrepII) was finally purified in LMNG/CHS, which was exchanged by amphipol A8-35 before PC-2 was analysed by single-particle cryo-EM. Cryo-EM of PC-2 resulted in a 4.6 Å structure. The pore of PC-2 is similar to the opened conformation of the TRPV1 channel, indicating that it is in the opened state. The structure of PC-2 did not show any details of the cytoplasmatic N- and C-terminal domain, but revealed first structural insights of the unique extracellular domain.

4 Cryo-EM structure of BetP from *C. glutamicum*

4.1 Results of the cryo-EM structure determination of BetP

Multiple states of the secondary-active transporter BetP from *C. glutamicum* were trapped in crystal structures making BetP a model system for the molecular description of the alternating access mechanism (Perez *et al*, 2014; Perez *et al*, 2012). However, all X-ray structures of BetP were obtained with an N-terminally truncated, charge-engineered BetP mutant resulting in missing structural information about the N-terminal domain. In addition the C-terminal domain of BetP, which is resolved in X-ray structures, is involved in crystal contacts. Thereby, only limited structural information about the inactive state and the transition into the active state of BetP is known. It is assumed that N- and C-terminal domains undergo conformational changes during activation (Waclawska *et al*, 2015). To obtain structural information about the N- and C-terminal domain of BetP in solution single-particle cryo-EM was performed in this work.

4.1.1 Purification of BetP in amphipol A8-35

Most membrane proteins below 250 kDa that have been investigated by cryo-EM were incorporated in amphipol A8-35 (Bai *et al*, 2015b; Kim *et al*, 2015; Liao *et al*, 2013). Likewise, BetP was embedded into amphipol A8-35 before it was analysed by single-particle cryo-EM. A size exclusion chromatography of BetP in amphipol A8-35 displayed a monodisperse protein sample that elutes with a retention volume of 1.36 ml (figure 52 A). The sample was further analysed by SDS-PAGE and negative-stain EM confirming the monodispersity of BetP (figure 52 B). In the negative-stained EM micrographs different views of BetP were identified and the trimeric assembling of BetP was observed in a top view (figure 53). Subsequently, BetP in amphipol A8-35 was concentrated, plunge-frozen and visualized in a JEOL F3200 electron cryomicroscope.

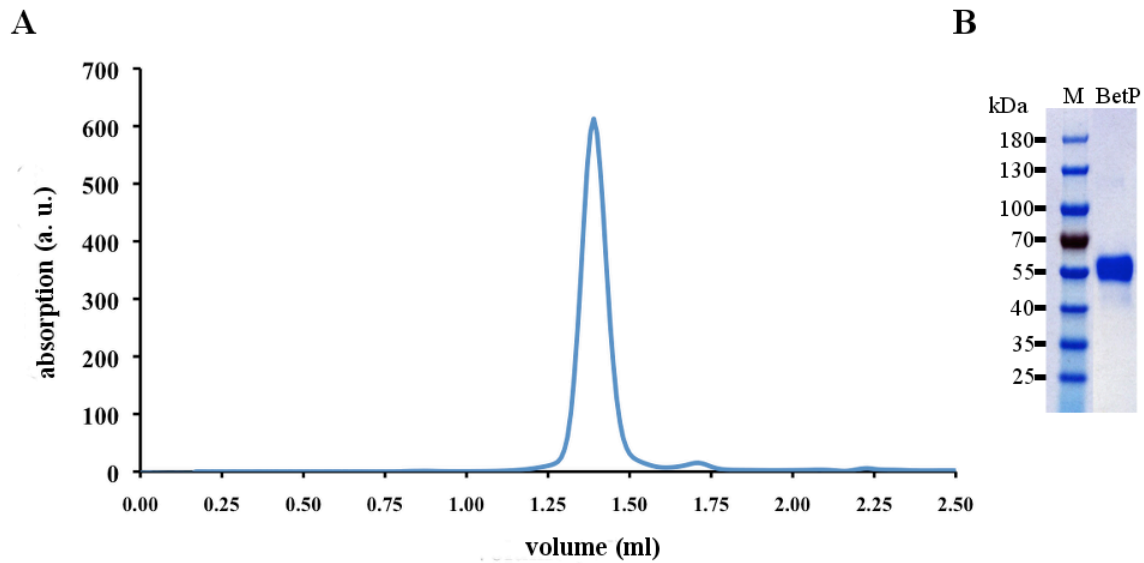


Figure 52: Purification of BetP in amphipol A8-35

(A) Size exclusion chromatography of BetP (Superose 6 PC 10/300). BetP elutes with a retention volume of 1.36 ml. (B) The purified protein was analysed by SDS-PAGE; M marker (PageRuler, Thermo Fisher Scientific, Dreieich).

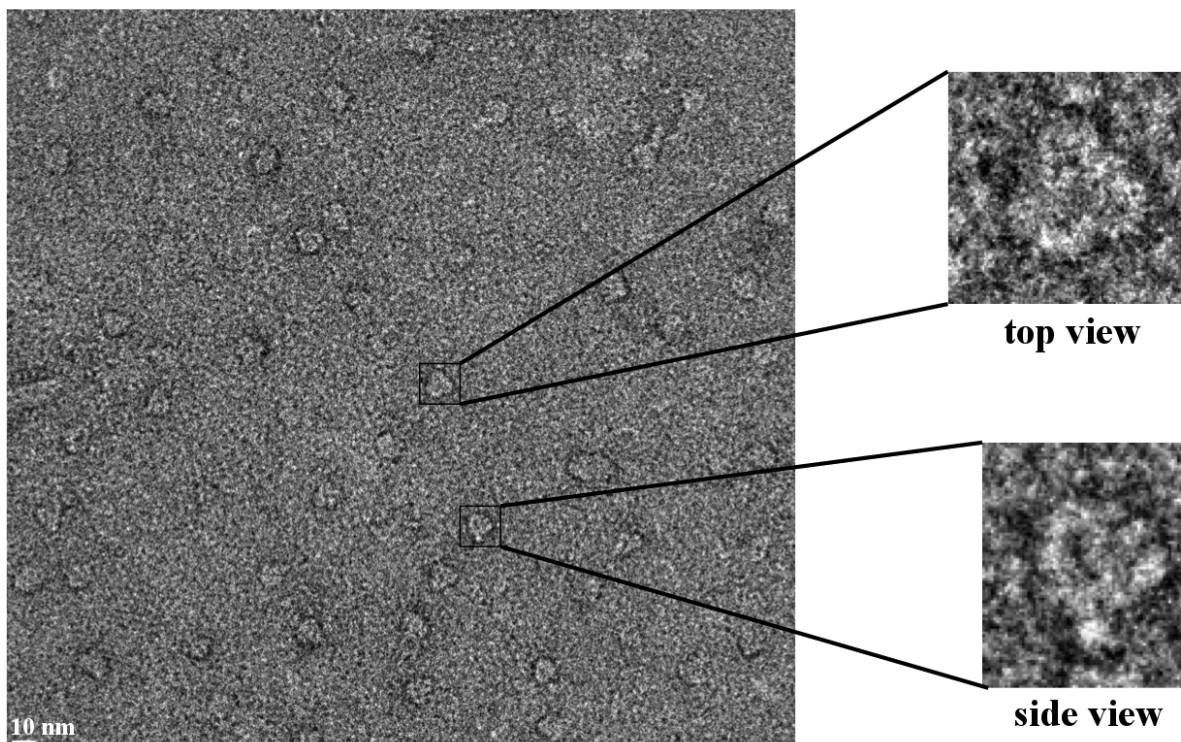


Figure 53: Negative-stain electron micrograph of purified BetP in amphipol A8-35

Purified BetP was applied to a carbon coated copper grid, stained with 1 % uranyl acetate and visualized with an electron microscope (CM120, Philips). A top and side view is enlarged, respectively. In the top view the threefold assembly of BetP is visible.

4.1.2 Single-particle cryo-EM of BetP in amphipol A8-35

4.1.2.1 Cryo-EM of BetP in amphipol A8-35

The total molecular weight of BetP is 196 kDa and therefore it is almost at the size limit for single-particle cryo-EM. However, initial micrographs revealed that single particles were visible representing different views of BetP (figure 54, white arrows).

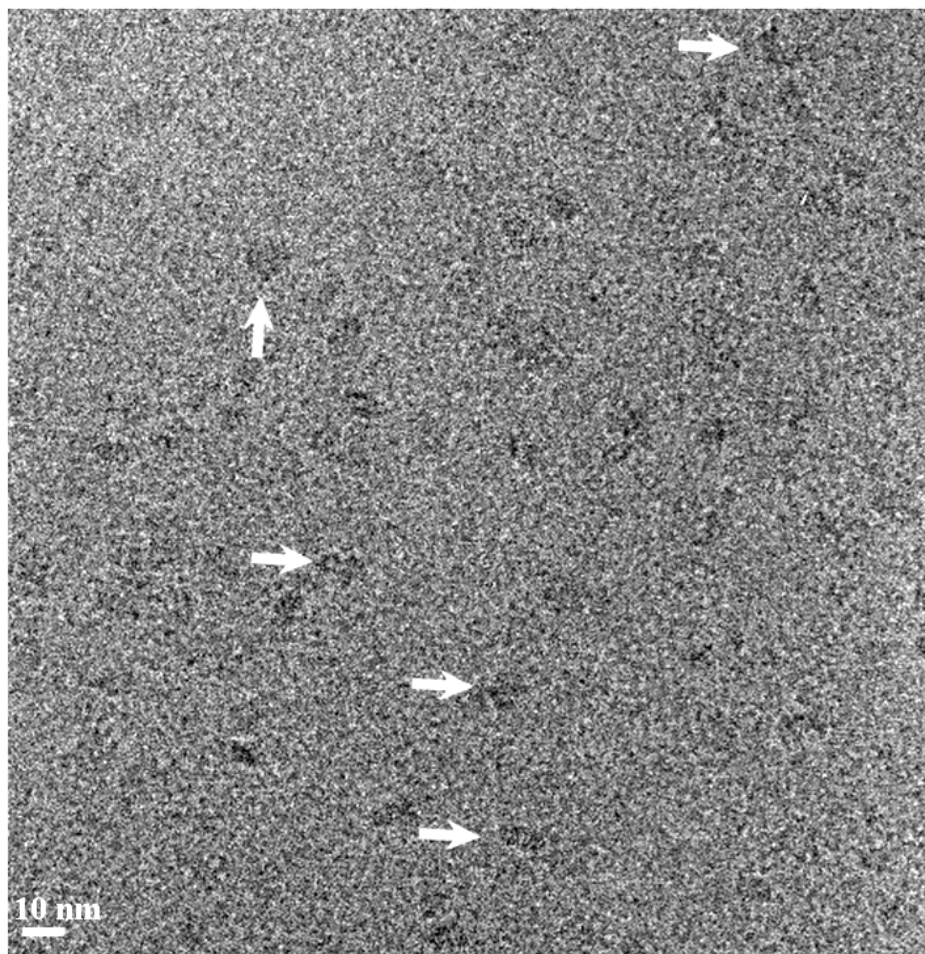


Figure 54: Electron cryomicrograph of purified BetP in amphipol A8-35

An electron cryomicrograph of BetP in amphipol A8-35 recorded at a nominal magnification of 30.000x with a defocus of 2.0 μm . White arrows point to different views of BetP.

In total ~183.000 particles were selected out of ~2150 micrographs. 2D classification clearly identified the selected particles as BetP molecules. In the top and side views, helix features were identified indicated by bright dots or lines (figure 55 A, B). A comparison of the 2D class averages of side views with X-ray structures of BetP revealed that the C-terminal domain

pointing into the cytoplasm in all X-ray structures is missing in the 2D class averages (figure 55 B, C). The absence of the C-termini either implies that they are located very close to the protein or that they are disordered and averaged out during classification.

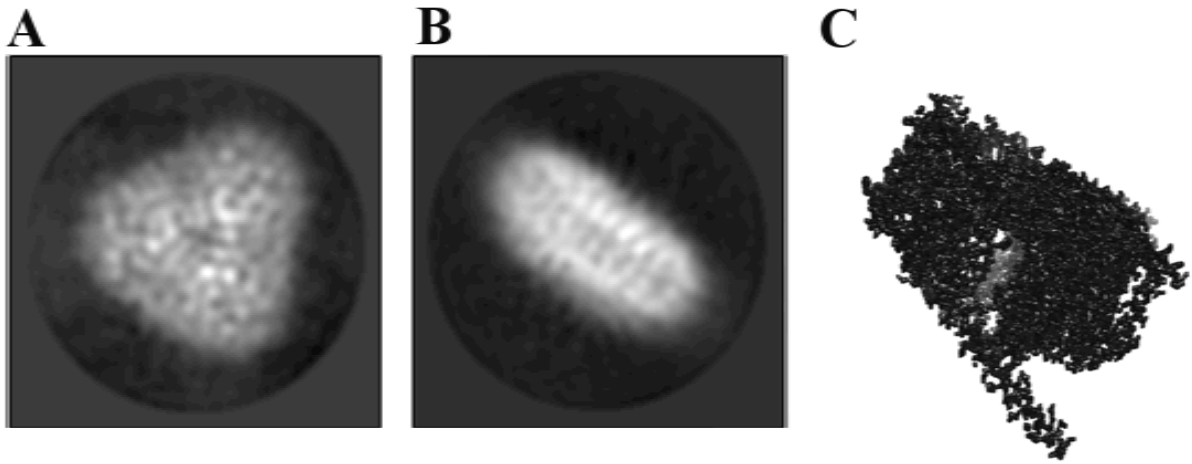


Figure 55: 2D class averages of BetP in amphipol A8-35

2D class averages of BetP show the transporter from (A) the periplasm (top) and (B) viewed along the membrane plane (side). (C) Side view of the BetP X-ray structure (pdb 2WIT) (Ressl *et al*, 2009). The C-terminal domain of the X-ray structure points into the cytoplasm and is not visible in the class average in B.

4.1.2.2 Cryo-EM structure determination of BetP in amphipol A8-35

An initial model with a C-terminally truncated BetP X-ray structure (pdb 2WIT) was created and low-pass filtered to 40 Å. After several rounds of 3D classification, the initial dataset was cleaned from false-positive particles, resulting in a subset of ~19.100 particles. This particle subset was taken as an input for a 3D refinement, resulting in a 6.8 Å structure after particle polishing and post-processing. In the cryo-EM map all twelve α -helices of BetP were identified including the C-terminal domains that were located very close to the membrane surface pointing towards the adjacent protomer (figure 56). The N-terminal domain was not resolved, indicating that it is flexible and averaged out during the 3D refinement.

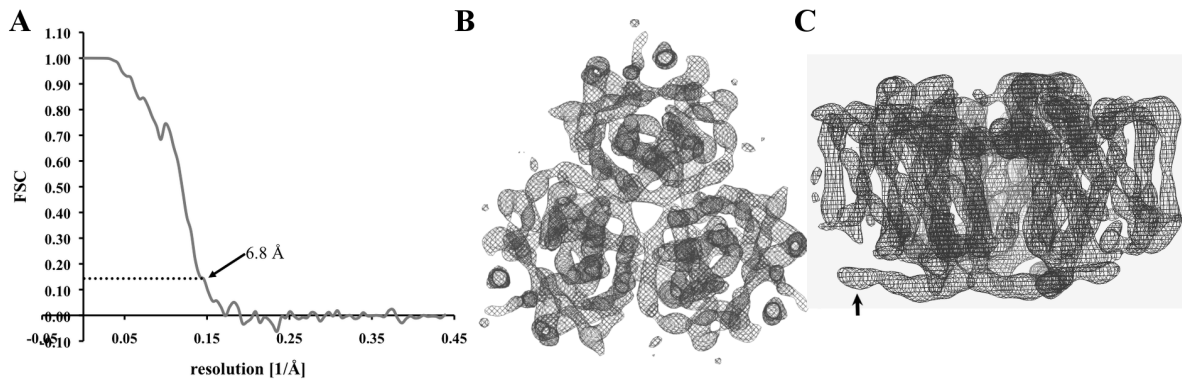


Figure 56: Cryo-EM structure of BetP in amphipol A8 35

(A) FSC curve of the 6.8 Å BetP structure. The 0.143 gold standard threshold is indicated by the dotted line. (B) Top and (C) side view of the cryo-EM density. The black arrow points to one C-terminal helix of BetP.

4.1.2.3 Cryo-EM structure of BetP in amphipol A8-35

The X-ray structure of a BetP monomer was fitted into the cryo-EM map and refined by phenix-real-space refinement (Afonine *et al*, 2012). The refined monomer is in an inward-open state (pdb 4DOJ, protomer C) and was used to generate a BetP trimer. The cryo-EM density revealed the main trimer interaction sites at the residues W101 and F345 similar to the one identified in X-ray structures and by mutagenesis studies (Perez *et al*, 2011) (figure 57).

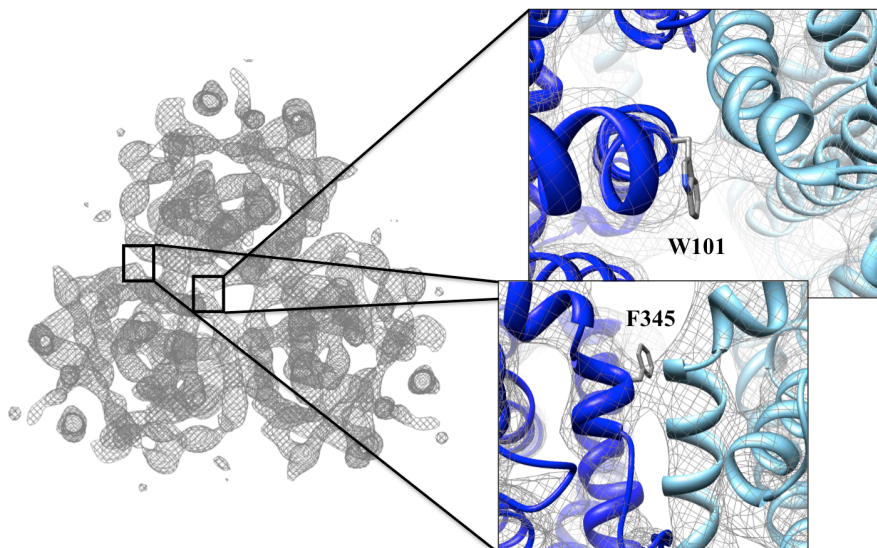


Figure 57: Residues essential for BetP trimerization are visible in the cryo-EM map

In the cryo-EM map two distinct areas were visible where the densities of two monomers are connected. After fitting the refined BetP structure into the cryo-EM density residues F345 and W101 that are essential for BetP trimerization were located in these regions.

4.1.3 Comparison of the cryo-EM and X-ray structure of BetP

A comparison of the X-ray and EM structures revealed three main differences (figure 58). First, the amphiphatic h7 at the trimer interface is shifted up in the cryo-EM structure. In this state h7 is located roughly at the same height as the phospholipid headgroups, while in the X-ray structures h7 plunges deeper into the hydrophobic part of the membrane. The second difference is the position of TMH 6. TMH 6 and TMH 7 form together the cytoplasmic gate and in the cryo-EM structure TMH 6 is shifted in a way that this cytoplasmic gate is more open, representing a new inward-open state. The third and most significant difference is the location of the C-terminal α -helix. This helix is shifted away from the central cavity to the perimeter of the adjacent BetP protomer by a rotation of about 30° (figure 58).

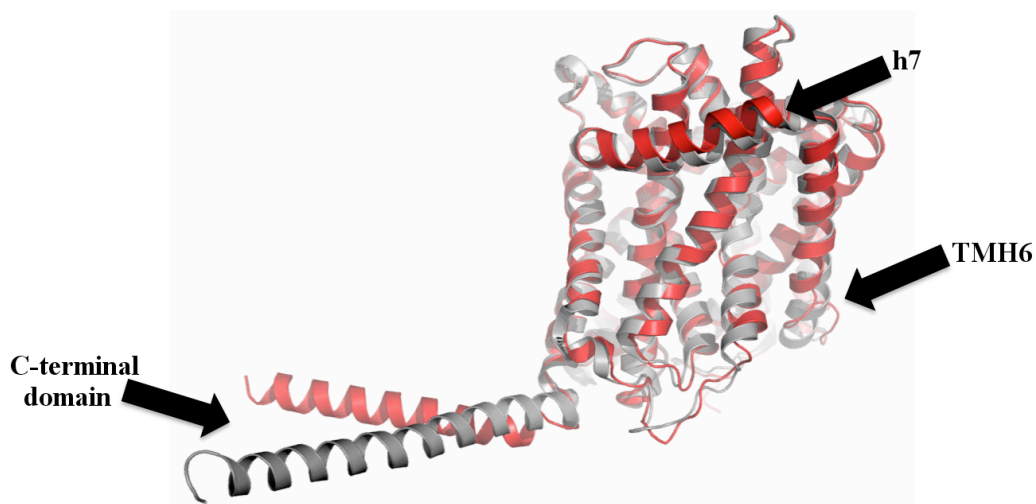


Figure 58: Comparison between the X-ray (grey) and the cryo-EM (red) structure of BetP

Three differences can be seen between the X-ray (pdb 4DOJ) and cryo-EM structure of BetP. The first difference is the position of h7, which is shifted closer to the periplasmic side in the cryo-EM structure. The movement of TMH 6 opens the cytoplasmic gate of BetP in a way that it is more open compared to the inward-open X-ray structure. The most significant difference is observed for the C-terminal domain, which is located at perimeter of the adjacent BetP protomer due to a rotation of about 30° in the cryo-EM structure.

A closer look at the C-terminal domain of the cryo-EM structure revealed that the residues involved in the interaction between the C-terminal domains with an adjacent BetP protomer have changed in comparison to the X-ray structures. R568 now interacts with the negatively charged residue E135 instead of D131 in loop 2 of the adjacent protomer (figure 59 A, B).

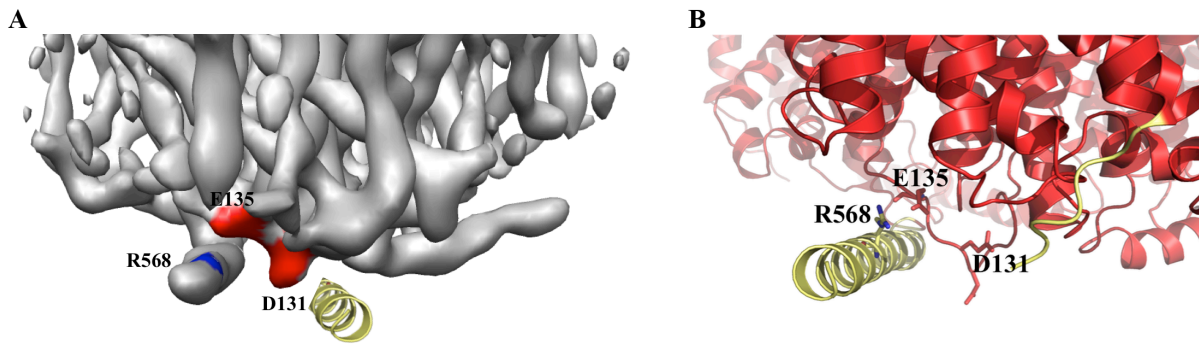


Figure 59: Orientation of the C-terminal α -helix in the cryo-EM structure of BetP

(A) The cryo-EM density shows the reorientation of the C-terminal domain. E135 and D131 are in close proximity to R568. The yellow helix represents the position of the C-terminus in the X-ray structure. (B) In the cryo-EM structure R568 seems to interact with E135 while D131 is not involved in the coordination of the C-terminal domain.

The new position of the C-terminal domain was further compared to the BetP X-ray structure in which five POPG lipids were bound in the central cavity (pdb 4C7R) (Koshy *et al*, 2013). Interestingly, positively charged residues of the C-terminal domain (R554, R558 and R562) of the cryo-EM structure are in the right position to interact with the negatively charged head groups of the bound POPG molecules (figure 60).

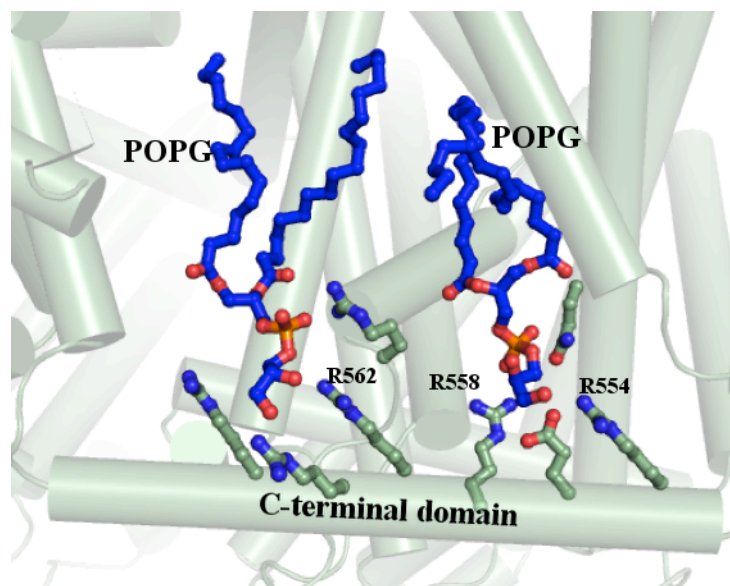


Figure 60: Possible interactions between the C-terminal domain of BetP and POPG molecules

Each C-terminal domain of the cryo-EM structure can interact with POPG molecules bound in the central cavity of BetP via R554, R558 and R562.

BetP is activated during an osmotic upshift due to an increase of K^+ ions combined with a stimulus sensed via the membrane. As no potassium was present in the sample used for cryo-EM data collection, the structure may represent an inactive state of BetP. To obtain the active state, BetP was crystallized in the presence of rubidium chloride, which can mimick potassium ions due to its similar ion radius. Rb^+ shows a strong anomalous signal in the X-ray density. In the BetP structure Rb^+ ions are coordinated by loop 2 and the C-terminal domain (Perez, 2012). This supports that an increase in K^+ ions changes the conformation of the C-terminal domain, thereby activating BetP. In the Rb^+ -bound structure one POPG molecule that is bound in the central cavity of BetP and involved in Rb^+ coordination has been assigned (Perez, 2012).

4.2 Discussion

Previous single-particle analyses of small membrane proteins revealed the advantage of using amphipol A8-35 as amphiphatic molecule for keeping the membrane protein soluble. In these studies it was shown that in amphipol A8-35 the protein is visible in all orientations in cryo- and negative-stain EM (Bai *et al*, 2015b; Kim *et al*, 2015; Liao *et al*, 2013). Therefore amphipol A8-35 seems to support single-particle cryo-EM of small membrane proteins. In addition amphipol A8-35 stabilizes the oligomeric assembly of membrane proteins as shown in this work (see section 2.1.3.2 and 2.2.6).

As for other proteins, the precise selection of the best particles for structure determination was essential for BetP. Finally, 10 % of all picked particles were used for the 3D refinement, resulting in the 6.8 Å structure, which is comparable to other single-particle cryo-EM studies (Bai *et al*, 2015b; Yan *et al*, 2015).

4.2.1 Inward-open state of BetP

Knowledge about the alternating access mechanism in BetP is very detailed, due to the large number of available X-ray structures, supported by biochemical data. This makes BetP one of the best models for the alternating access mechanism in the LeuT-fold superfamily. However, the transition from the inactive to the active state of BetP is still not fully understood. It has been proposed that the C-terminal domain undergoes conformational changes during activation by K⁺ binding (Perez, 2012) and a recent study has shown the importance of the N-terminal domain for BetP activation (Waclawska *et al*, 2015). However, structural information about the inactive state of BetP is still missing, as is structural information on the N-terminal domain, which has been truncated for 3D crystallization. The single-particle cryo-EM structure represents most likely an inactive state of BetP. This would support an activation mechanism of BetP in which the C-terminal domain undergoes a conformational change by binding potassium ions (figure 61). Although full-length BetP was used for single-particle cryo-EM, the N-terminal domain was not resolved, indicating that it is flexible.

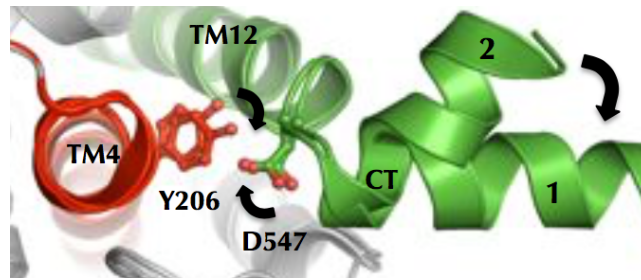


Figure 61: Movement of the C-terminal domain upon K^+ binding

After K^+ binding the C-terminal domain of BetP moves from position 2 to 1, forming a salt bridge between D547 and Y206. The figure was taken from (Perez, 2012).

The cryo-EM structure describes an inward-open state in which the cytoplasmic gate is more opened compared to inward-open X-ray structures (Perez *et al*, 2014; Perez *et al*, 2011; Perez *et al*, 2012). It is assumed that in this state BetP is not able to undergo alternating-access changes. Consequently, the cryo-EM structure is likely to show an inactive-state.

In the inactive state h7 is placed at the position of the head groups of the phospholipid bilayer. In the case of an osmotic shock the physical properties of the membrane change due to an efflux of water. Amphiphatic domains similar to h7 often sense stress. The new position of h7 supports the hypothesis that it responds to a signal perceived via the membrane (Ziegler *et al*, 2010).

The new orientation of the C-terminal α -helix forms a salt bridge between R568 and E135. Arginine residues of the first positively charged cluster in the C-terminal domain (R554, R558 and R562) (Ressl *et al*, 2009) can interact with the negatively charged headgroups of POPG molecules bound in the central cavity (figure 60) (Koshy *et al*, 2013). In this way the POPG molecules form a connection between h7 and the C-terminal domain in both the active and inactive state of BetP, supporting the hypothesis that the POPG molecules are important for signal transmission (Koshy, 2014).

4.2.2 Mechanism of BetP activation

Considering the inactive inward-open as well as active inward-open structures combined with the knowledge about the Rb^+ binding sites, a model for BetP activation can be proposed. The shift from the inactive to the active state is initiated by an increase in the intracellular K^+ concentration. K^+ ions interact with the C-terminal domain of one BetP protomer changing both the interaction to loop 2 as well as to POPG molecules bound in the central cavity (figure 62) (Perez, 2012). In the presence of K^+ one POPG molecule, Q557 of the C-terminal domain and

D131 of the adjacent protomer form a K^+ binding pocket. In this state the salt bridge between R568 and E135 breaks, allowing *BetP* to undergo the alternating access conformational changes.

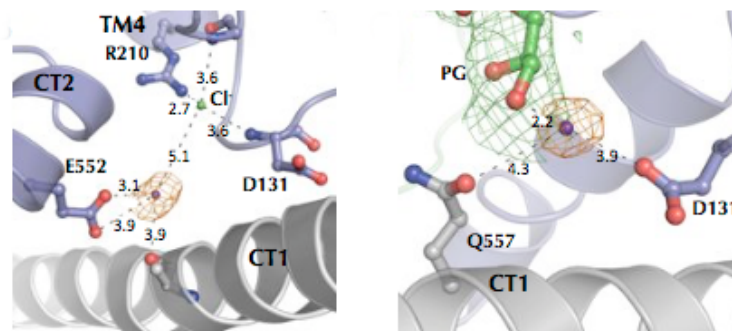


Figure 62: Two possible K^+ binding sites changing the C-terminal interaction network

BetP crystallized in the presence of Rb^+ (purple spheres) revealed possible K^+ binding sites. In two binding sites loop 2 (blue) or a POPG molecule (green) is involved. The figure was taken from (Perez, 2012).

According to this hypothesis, the involvement of the POPG molecule ensures that the potassium signal is transmitted to h7, which then moves slightly into the membrane to stabilize the activated form of *BetP*. This movement also takes place when *BetP* senses the osmotic upshift via changes in the physical properties of the membrane. In this case the POPG molecules transmit the signal to the C-terminal domain, destabilising the inactive inward-open conformation and allowing K^+ to bind.

At this state of the work it would be interesting to investigate the activated state of *BetP* by single-particle cryo-EM. A high-resolution cryo-EM structure of activated *BetP* is necessary to confirm the K^+ binding sites as well as the movement of the C-terminal domain, which were observed in the X-ray structures.

4.2.3 Summary

Although *BetP* is a small membrane protein, single-particle cryo-EM yielded a 6.8 Å structure in which the contact sides essential for the trimeric assembly are clearly visible. This structure represents a new, inactive inward-open state of *BetP*. The cryo-EM structure differs from the X-ray structures in three main points: the shift of h7 closer to the periplasm, the shift of TMH 6 enlarging the cytoplasmic gate and the new orientation of the C-terminal domain, in which R568 is connected to E135 of the adjacent protomer. A comparison of the X-ray and cryo-EM

structures revealed also a possible interaction between the C-terminal domain and POPG molecules bound in the central cavity of the BetP trimer allowing the description of a mechanism for BetP activation. In this mechanism the C-terminal α -helix is connected to the lipid bilayer by ionic interactions in the inactive state. Potassium ions interfere with these interactions, resulting in a movement of the C-terminal domain thereby activating BetP.

5 Structural investigation of the N-type ATPase c-ring from *B. pseudomallei*

5.1 Single-particle cryo-EM of the *B. pseudomallei* N-type ATPase c-ring

Single-particle cryo-EM of the *B. pseudomallei* N-type ATPase c-ring was done in collaboration with Sarah Schulz (group of Dr. Thomas Meier, Department of Structural Biology, MPI of Biophysics Frankfurt; now Prof. and Chair of Structural Biology, Imperial College London, UK), who performed the expression and purification of the complex in amphipol A8-35, DDM, C₁₂E₈ and LDAO, contributed to the data collection and particle picking, calculated a homology model of the N-type ATPase rotor ring and analysed the structure. More detailed information about the data collection, particle picking and 2D classification using Relion-1.3 as well as the resulting structural information can be found in (Schulz, 2015).

5.1.1 2D classification of the rotor ring

In a collaborative project the rotor ring of the *Burkholderia* N-type ATPase was purified in amphipol A8-35, DDM and LDAO and its stoichiometry was determined by 2D classifications using Relion-1.3. This indicated that the rotor ring is composed of 17 c-subunits (Schulz, 2015). Other studies showed that the maximum likelihood algorithm implemented in Relion-1.3 sometimes tends to accumulate particles into the same class even if they belong to different classes (Sorzano *et al*, 2010). Since all known F- and V-type ATPase rotor rings have a stoichiometry between 8 and 15 subunits, the new c₁₇ stoichiometry was further validated by the use of the alternative software packages XMIPP (Marabini *et al*, 1996; Sorzano *et al*, 2004) and EMAN2 (Ludtke *et al*, 1999). Unlike Relion-1.3, these programs classify particles based on different cross correlation algorithms and, like Relion-1.3, they do not require any reference for 2D classification. The top views of the rotor ring in LDAO were transferred into EMAN2, phase-flipped and classified. In the best class average only some features were visible making it difficult to count 17 subunits (figure 63 A). To increase the signal to noise this class average was transferred into IMAGIC (van Heel *et al*, 1996) and rotationally symmetrised applying 8- to 18-fold symmetry. Only the c₁₇ symmetry resulted in a ring where the outer helices were clearly separated from each other (figure 63 B).

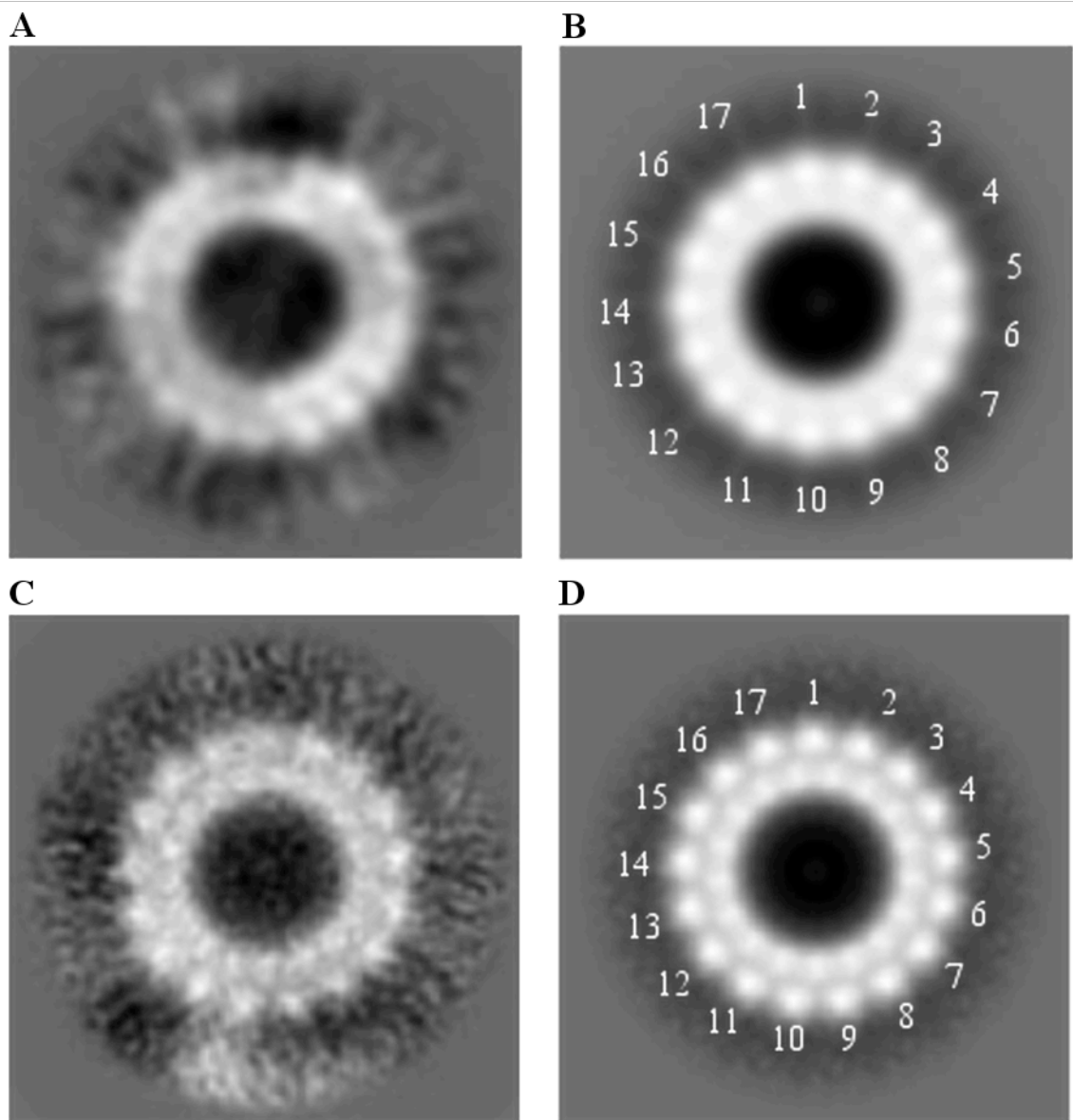


Figure 63: Two-dimensional class averages of the N-type ATPase rotor ring using different software packages (EMAN2, XMIPP and IMAGIC)

(A) Best class average obtained after reference-free 2D classification using EMAN2. (B) The class average of A was transferred into IMAGIC and 17 separated densities were observed after applying rotational 17-fold symmetry. (C) After reference-free 2D classification in XMIPP the best class average showed 17 distinct densities of the outer helices of the rotor ring. (D) 17-fold symmetrisation of C in IMAGIC enhanced the signal and separated the inner ring into 17 punctual densities (highlighted by small white dots).

Further, the phase-flipped top views were imported into XMIPP and classified. The classification algorithm in XMIPP worked better compared to EMAN2 resulting in a class average with 17 distinguishable densities (figure 63 C). The rotational symmetrisation of this class average in

IMAGIC using 8- to 18-fold symmetry resulted in a ring with 34 punctual densities after applying 17-fold symmetry (figure 63 D). Accordingly, the rotational symmetrisation using 8- to 16- and 18-fold symmetry resulted in featureless rings (not shown). The results obtained in EMAN2 and XMIPP confirmed that the N-type ATPase rotor ring is composed of 17 c-subunits. Therefore the N-type ATPase from *B. pseudomallei* increases the number of ions that are required for the production of three ATP molecules from 15 (*S. platensis* c₁₅ ring) to 17.

5.1.2 3D structure determination of the *B. pseudomallei* N-type ATPase rotor ring in different amphiphatic molecules by single-particle cryo-EM

As described in section 1.4, the starting model is crucial for 3D structure determination in a single-particle analysis. This, different starting models were tested. On the one hand crystal structures of rotor rings with different (c-ring) stoichiometries (F-type c₁₅ ring, pdb 2WIE (Pogoryelov *et al*, 2009); F-type c₁₄ ring, pdb 2W5J (Vollmar *et al*, 2009); F-type c₁₃ ring, pdb 2X2V (Preiss *et al*, 2010); V-type k₁₀ ring, pdb 2BL2 (Murata *et al*, 2004)) were applied, as well as an *in silico* model of a c₁₇ ring (Schulz, 2015). On the other hand different starting models were calculated based on manually picked particles in amphipol A8-35 and LDAO using EMAN2 and SIMPLE (Elmlund *et al*, 2012). To investigate the impact of different detergents on single particle cryo-EM structure determination of this small membrane protein complex, datasets of the rotor ring were recorded in amphipol A8-35, DDM, C₁₂E₈ and LDAO (table 17 and 18). The flow chart in figure 64 gives an overview of the processing pathway and starts after particles were selected. The particles were picked automatically in Relion-1.3 but each micrograph was manually verified to delete false-positive and to add false-negative particles. In the next sections, the result for each dataset is reported in detail.

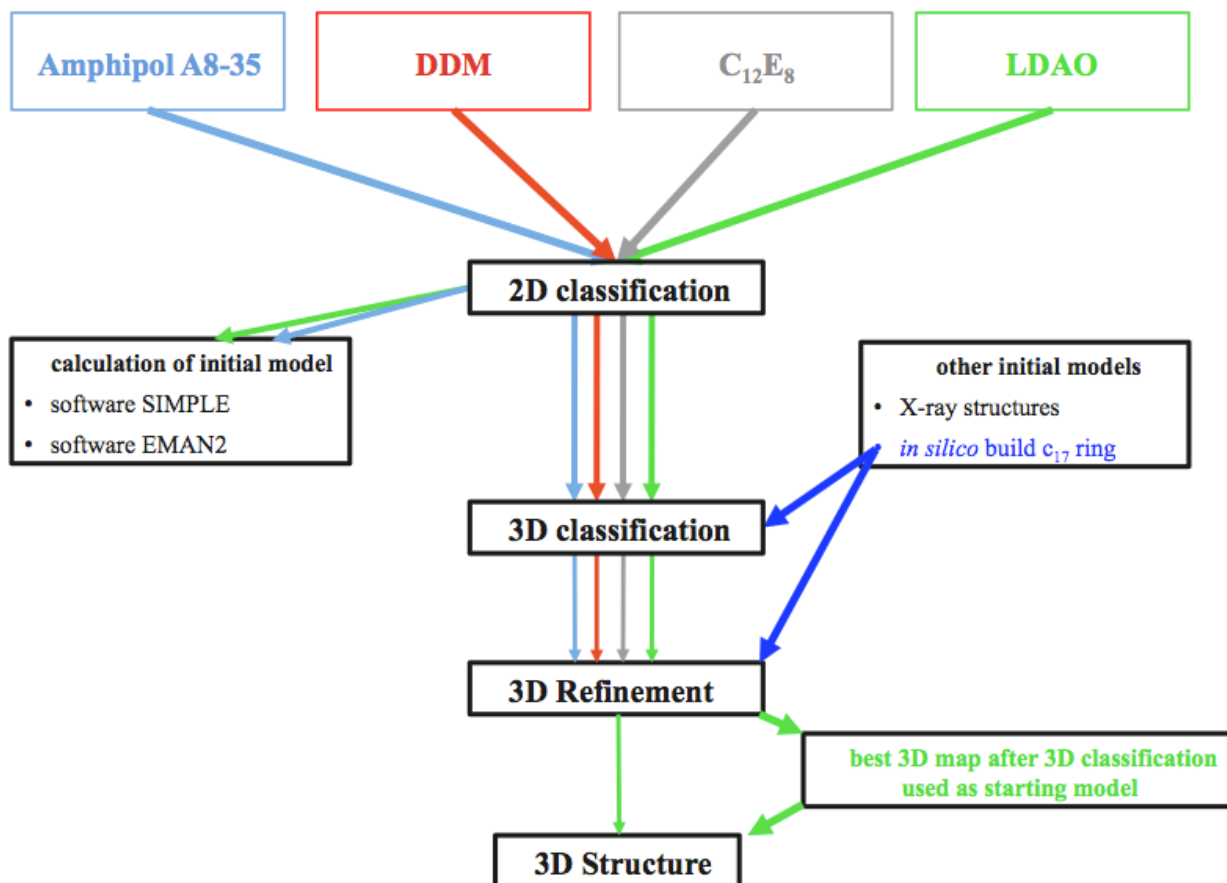


Figure 64: Schematic representation of the processing pathway for each amphiphatic molecule

After particles were selected in Relion-1.3, they were extracted and initially analysed by 2D classification. The particles that contributed to the best class averages were selected and used for further processing. In the case of amphipol A8-35 and LDAO the selected particles were used after 2D classification to calculate initial models using the software EMAN2 and SIMPLE. Different initial models were tested during 3D classification in Relion-1.3. The best result was observed for a c_{17} ring built *in silico*. The particles that contributed to the best 3D class average were selected and used for subsequent 3D refinement. The 3D structure of the rotor ring was finally solved for the rotor ring in LDAO by applying the best 3D class average of the particles in LDAO as starting model for a 3D refinement. The datasets of the rotor ring in different detergents were processed separately.

5.1.2.1 Analysis of the rotor ring in amphipol A8-35

First, a dataset of the rotor ring in amphipol A8-35 containing ~226.000 semiautomatically selected particles was used for structure determination. The remaining false-positive particles were removed by several rounds of 2D and 3D classification. For 3D classification, different starting models were tested, revealing that the c_{17} ring built *in silico* resulted in the best 3D class average containing a subset of about ~60.000 particles. The quality of the particle subset was

analysed by 2D classification before it was used for a 3D refinement in which the c_{17} ring built *in silico* was applied as starting model. The 3D map with a gold standard resolution of 6.4 Å did not contain any helix features (figure 65 A, I), which is unexpected because helices should be visible at a resolution of $\sim 8 - 7$ Å.

The accuracy angles of translation and rotation (described in chapter 1.4), which are calculated for the alignment of selected rotor ring particles in amphipol A8-35 against projections of the applied initial model, reflect that the alignment did not work precisely. The accuracy angle of translation was 4.1° whereas the accuracy angle of rotation was 20° (table 18). This clearly showed that the software did not align the particles of the rotor ring in amphipol A8-35 against the starting model accurately.

As described in chapter 1.4, the user has much more influence during a 3D classification than in a 3D refinement. Therefore a 3D classification was performed in which the particles were aligned against the *in silico* built c_{17} ring. After 30 iteration steps the impact of higher-frequency information was increased and the alignment was stopped after 60 iterations. The resulting accuracy angle of rotation was 2.5° , whereas the accuracy angle of translation was 5.6° (table 18). This indicated that the particles were aligned well resulting in a more detailed 3D map as the outer helices of the rotor ring became visible (figure 65 E). However, the 3D map contained strong symmetrisation artefacts, as the amphipol A8-35 belt was separated into 17 parts. It can be assumed that this 3D map does not show the correct rotor ring structure.

5.1.2.2 Analysis of the rotor ring in DDM

The main difference between amphipol A8-35 and the detergent DDM is that the latter one consists of a dense hydrophilic head group and a hydrophobic tail of a lower density (table 17). The hydrophobic tail of DDM interacts with the membrane part of the protein, shielding it against the aqueous solution. This architecture would increase the protein-to-detergent signal, allowing a better alignment of the particles.

As for the dataset of the rotor ring in amphipol A8-35 the dataset of the c-ring in DDM (~ 76.000 particles) was cleaned from false-positive particles by multiple rounds of 2D and 3D classification resulting in a subset of about ~ 45.000 particles. A subsequent 3D refinement resulted in an 8.3 Å map obtained with the *in silico* built c_{17} ring as starting model. This map showed comparable details like the 3D volume in amphipol A8-35. Again, separated c-subunits were not visible (figure 65 B, I). The accuracy angle of rotation was 18° revealing that the particles in DDM were not properly aligned.

As for amphipol A8-35 the 3D classification algorithm was used to optimize the alignment resulting in an accuracy angle of rotation of 4.8° (table 18). The 3D map was slightly better than the map of the rotor ring in amphipol A8-35. The outer helices were separated but surrounded by a strongly symmetrised detergent belt (figure 65 F), which did not allow determination of the rotor ring structure.

5.1.2.3 Analysis of the rotor ring in $C_{12}E_8$

To further increase the protein-to-detergent signal the rotor ring was purified in $C_{12}E_8$ and subjected to cryo-EM. $C_{12}E_8$ has a similar micelle size to DDM and amphipol A8-35 but a lower density of about 1 g/ml (table 17) (le Maire *et al*, 2000). The density of $C_{12}E_8$ is just slightly higher than that of amorphous ice (0.94 g/ml (Mishima *et al*, 1985)). Given that the phase contrast in EM images of ice embedded specimens arises due to the subtle difference in scattering cross section between ice, protein, and detergent (Schmidt-Krey *et al*, 2011) it is expected that the detergent belt of $C_{12}E_8$ is less visible in cryomicrographs compared to DDM and amphipol A8-35.

The dataset of the rotor ring in $C_{12}E_8$ comprised 740 micrographs with ~ 115.000 particles (table 18). After false-positive particles were removed in the same way as for the rotor ring in DDM and amphipol A8-35, a final subset of ~ 77.000 particles was used for 3D refinements which resulted in a structure with a resolution of 6.6 Å. The accuracy angle of rotation was 17° which indicated poor particle alignment. However, the rotor ring in $C_{12}E_8$ was displayed without a dense detergent belt around it (figure 65 C, I). This shows that the $C_{12}E_8$ belt is indeed less pronounced in the single cryomicrographs compared to DDM and amphipol A8-35.

The 3D classification algorithm was used to improve the particle alignment resulting in accuracy angles of rotation and translation of 5.0° and 2.3° , respectively. In the resulting 3D map, single c-subunits started to separate but the detergent belt still showed symmetrisation artefacts. However, these artefacts were not as strong as in DDM or amphipol A8-35 (figure 65 G), indicating that the detergent density has an impact on structure determination.

5.1.2.4 Analysis of the rotor ring in LDAO

In line with the previous observations and to further increase in the protein-to-detergent signal the rotor ring was analyzed in a detergent with an even lower density and micelle size, namely LDAO (table 17). The final data set of the rotor ring in LDAO comprised 1991 micrographs with ~ 213.000 particles (table 18). Again false-positive particles were removed by 2D and 3D

classification, resulting in a subset of ~47.000 particles. The 3D refinement, in which the c_{17} ring built *in silico* was applied as starting model, resulted in a 6.9 Å structure. As for the 3D refinements in amphipol A8-35, DDM and $C_{12}E_8$, the accuracy angle of rotation was above 10° (table 18) and no helix features were observed in the 3D volume, although the 2D class averages in LDAO show high-resolution details as 34 punctual densities were observed in the top view (5.1.1 and (Schulz, 2015)). In spite of that, the 3D maps looked different: In amphipol A8-35, DDM and $C_{12}E_8$ densities of the detergent belt that surrounded the rotor ring were visible whereas in LDAO the detergent belt was not visible (figure 65 D, I). This result showed that both, the density and the micelle size of a detergent have an impact on structure determination by single particle cryo-EM.

To increase the alignment accuracy the 3D classification algorithm was used resulting in a 3D volume revealing 17 separated hairpins each representing a c-subunit (figure 65 H). The determined 3D class average was applied as initial model for another 3D refinement, resulting in a structure of the rotor ring with a resolution of 6.1 Å (figure 66). The accuracy angles of translation and rotation were 1.48° and 3.9°, respectively, indicating an accurate alignment of the particles for the first time.

Starting again with the model used for structure determination of the rotor ring in LDAO did not improve particle alignment in amphipol A8-35, DDM and $C_{12}E_8$. This means that the application of the correct rotor ring structure as starting model does not increase the particle alignment if the rotor ring is embedded in a detergent with a high density or a large micelle. Thus, it can be concluded that the physical properties of the used detergents were decisive for the structure determination.

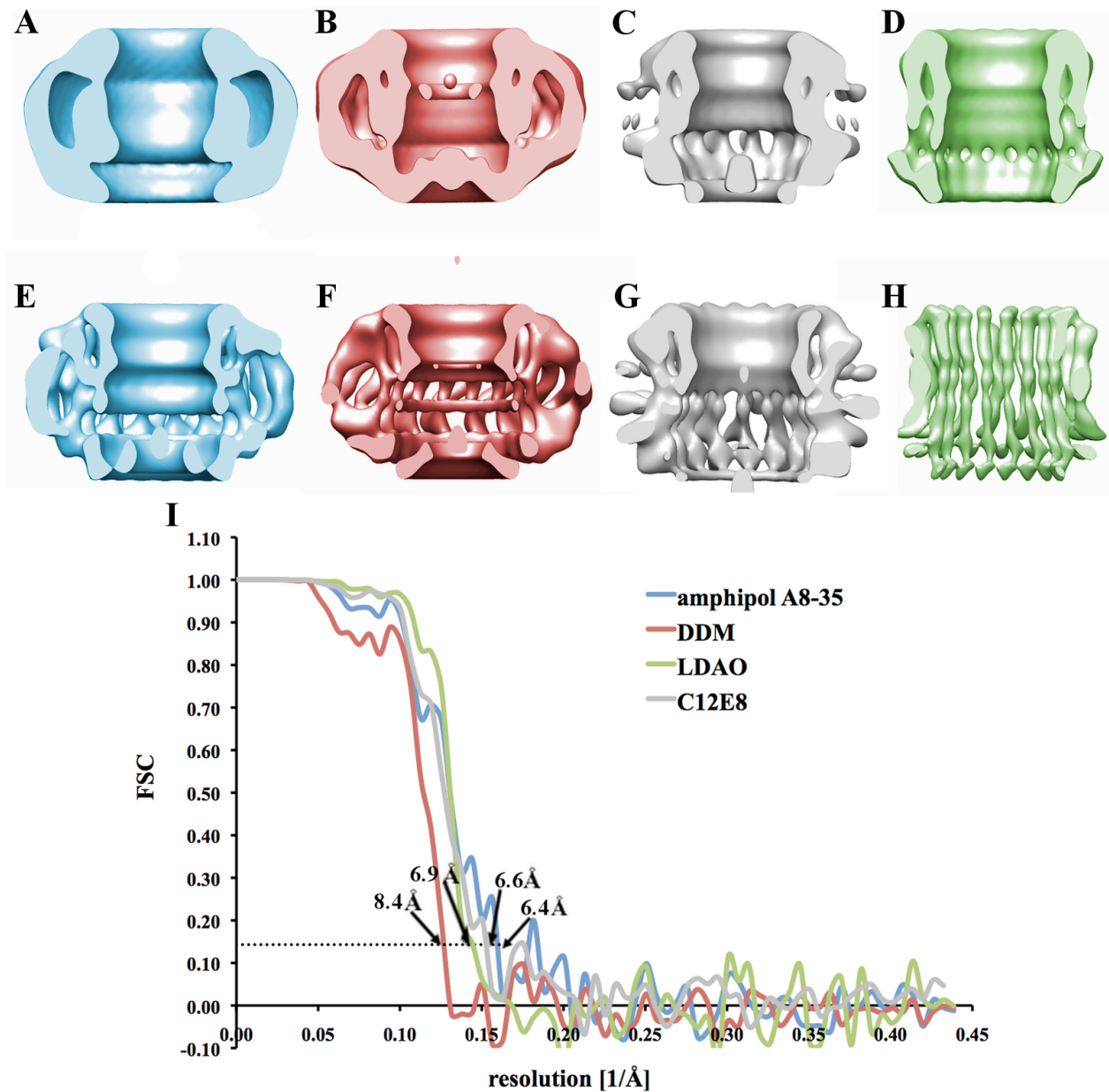


Figure 65: 3D refinements and classifications of the rotor ring in amphipol A8-35, DDM, C₁₂E₈ and LDAO with the corresponding FSC curves

3D cryo-EM maps of the rotor ring after 3D refinement in (A) amphipol A8-35, (B) DDM, (C) C₁₂E₈ and (D) LDAO and after 3D classification in (E) amphipol A8-35, (F) DDM, (G) C₁₂E₈ and (H) LDAO. Well resolved c-subunits were only obtained for the rotor ring in LDAO after 3D classification. (I) The corresponding FSC curves of the 3D refinements in amphipol A8-35, DDM, C₁₂E₈ and LDAO. The gold standard threshold at 0.143 is indicated by the dotted line and the resolution of the four refinements is indicated by arrows.

Table 17: Densities and micelle sizes of amphiphatic molecules compared to the densities of amorphous ice and protein

Amphiphatic molecule	Density [g/ml]	Micelle size [kDa]	Reference
Protein	~1.36		(Fischer <i>et al</i> , 2004)
Amphipol A8-35	1.3-1.19	70	(Tribet <i>et al</i> , 1996)
DDM	1.19	72	(Timmins <i>et al</i> , 1988)
C ₁₂ E ₈	1.04	65	(le Maire <i>et al</i> , 2000)
Amorphous ice	0.94		(Mishima <i>et al</i> , 1985)
LDAO	0.88	17	(Timmins <i>et al</i> , 1988)

Table 18: Summary of single-particle cryo-EM structure determination of the N-type ATPase rotor ring

	Amphipol A8-35	DDM	C ₁₂ E ₈	LDAO
Number of micrographs	2165	1060	740	1991
Number of picked particles	~226.000	~76.000	~115.000	~213.000
Final number of particles	~60.000	~45.000	~77.000	~47.000
Accuracy of translation in 3D classification	5.6°	4.8°	5.0°	3.6°
Accuracy of rotation in 3D classification	2.5°	1.9°	2.6°	1.4°
Accuracy of translation in 3D refinement	4.1°	3.3°	3.2°	1.4°
Accuracy of rotation in 3D refinement	20°	18°	17°	4.0°
Resolution obtained from the FSC curves	6.4 Å	8.3 Å	6.6 Å	6.1 Å

5.1.3 Cryo-EM map of the *B. pseudomallei* N-type ATPase c₁₇ ring

The 6.1 Å cryo-EM map revealed that the N-type ATPase rotor ring consists of 17 single hairpins, each representing a c-subunit. The inner helix of a c-subunit is slightly longer compared to the outer helix that forms an S-like structure. This results in an hour-glass shaped rotor ring (figure 66 A). A similar overall architecture was observed for the F-type ATPase rotor rings from *Ilyobacter tartaricus* (Meier *et al*, 2009; Meier *et al*, 2005) and *Spirulina platensis* (Pogoryelov *et al*, 2009), for example.

To determine the handedness of a protein by EM a random conical tilt study is commonly performed. For this, two micrographs of the same particles are acquired, in one of which the specimen is tilted. Based on the known tilt angle, the relative Euler angles of the particles in the micrographs are known and can be used to calculate a low-resolution model with the correct handedness. However, for this analysis the particle has to show the handedness already at low-resolution. This is not the case for the rotor ring as here the handedness is only visible at higher-resolution, when the loop that connects the inner with the outer helix is resolved. Viewed from the cytoplasm the loop can connect the inner helix with the right or left adjacent outer helix resulting in a right- or left-handed vorticity, respectively. Strikingly, all known c-ring structures of F-type ATPases have a right-handed vorticity when viewed from the F₁ domain. The N-type and F-type ATPase c-rings have a similar architecture and a high sequence homology, expecting that the N-type ATPase c-ring also shows a right-handed vorticity. Therefore a right-handed vorticity was imposed during structure determination. A cytoplasmic view of the rotor ring shows the vorticity and the connection of the inner and outer helices of each c-subunit (figure 66 B).

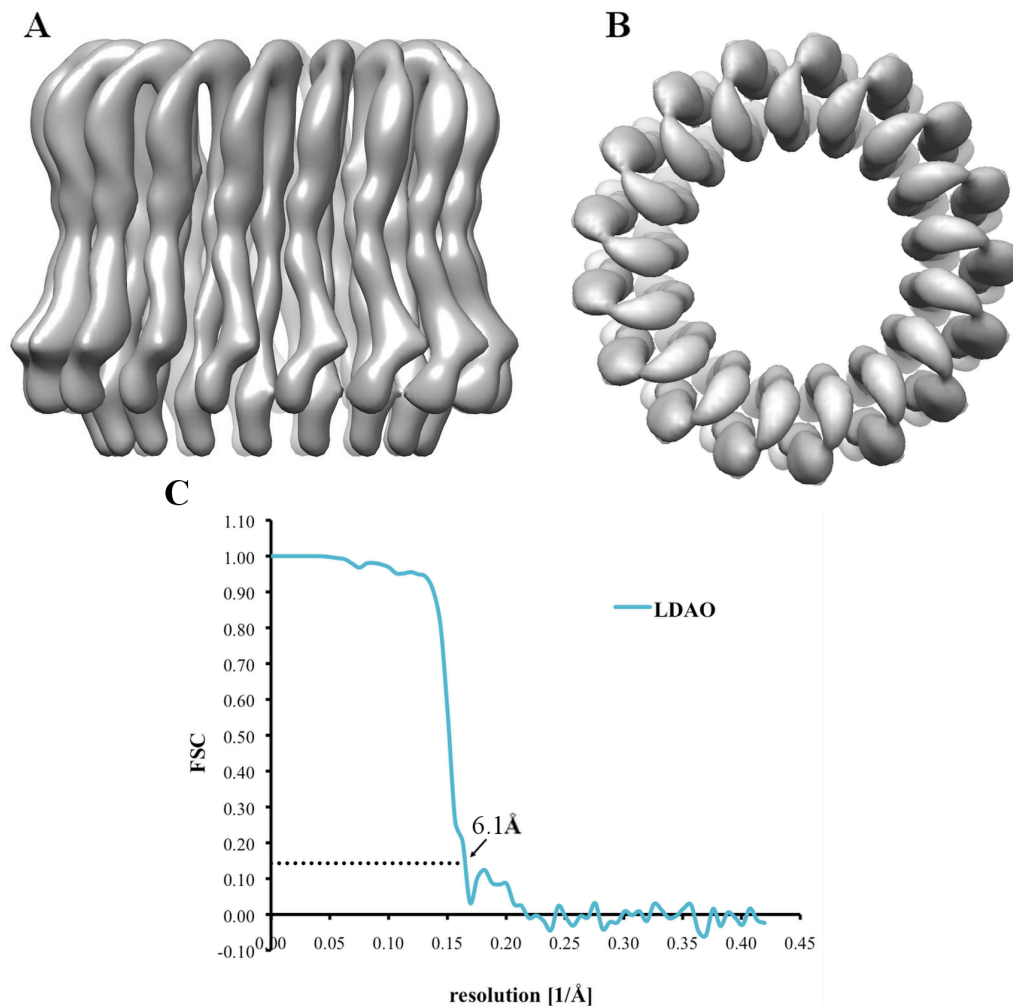


Figure 66: Electron cryomicroscopy map of the N-type ATPase rotor ring

(A) The side view of the rotor ring revealed that the inner helix is slightly longer than the outer helix of each c-subunit. The outer helix has an S-shape resulting in the typical hour-glass shape of rotor rings. (B) The top view of the rotor ring showed the connection of the inner and outer helices as well as the right-handed vorticity. (C) FSC curve of the 3D refinement indicating 6.1 Å resolution (black arrow). The gold standard threshold at 0.143 is indicated by the dotted line.

In a next step a hairpin-like c-subunit based on the primary *B. pseudomallei* c-subunit sequence was built, using the WHATIF homology modelling server (Vriend, 1990) and fitted 17 times into the cryo-EM map using Chimera (Pettersen *et al*, 2004). The c_{17} ring was refined using Phenix (Zwart *et al*, 2008) resulting in a model that fitted accurately into the cryo-EM map (figure 67). The fit was evaluated by the bulky residue F76 in each c-subunit that was placed into the density map (figure 67 A) and by the loop of the rotor ring that is formed by the highly conserved residues RQPE (figure 67 B). The N-type ATPase rotor ring structure revealed a c-ring with a

height and a diameter at the cytoplasmic side of $\sim 65 \text{ \AA}$ and a diameter of $\sim 70 \text{ \AA}$ at the periplasmic side (figure 68 A - C).

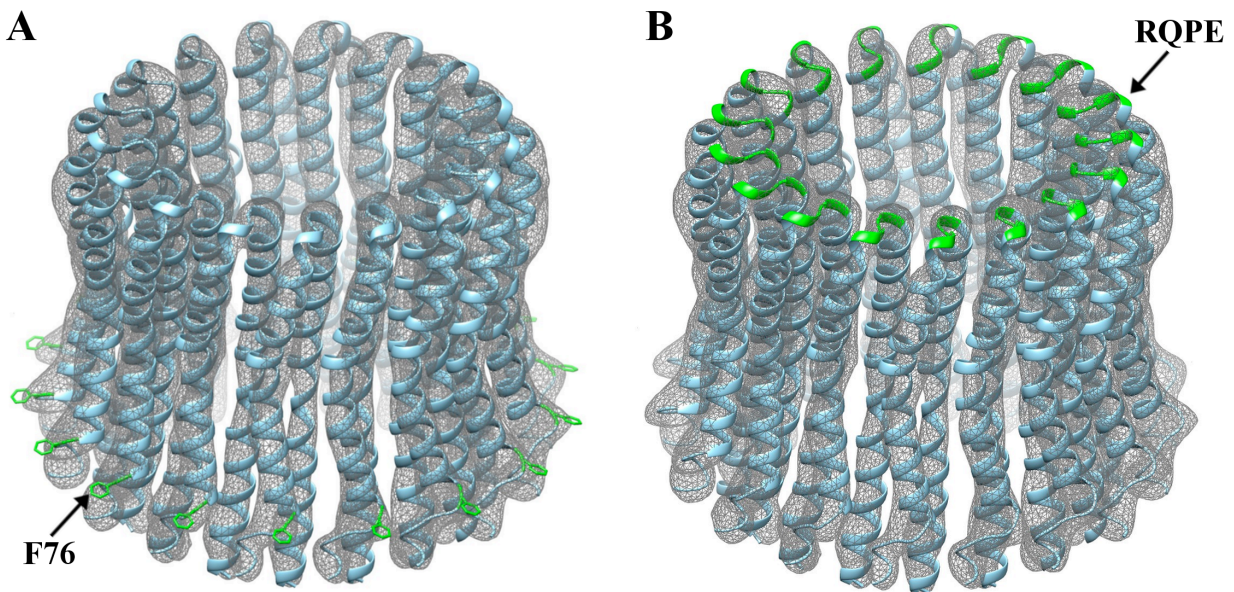


Figure 67: Model of the N-type ATPase rotor ring fitted in the cryo-EM map

The N-type ATPase c-ring model was placed into the cryo-EM map after real-space refinement. (A) F76 (green) of each c-subunit fitted in an extension of the cryo-EM density. (B) The conserved RQPE-motif forms the loop region of the N-type ATPase rotor ring (green).

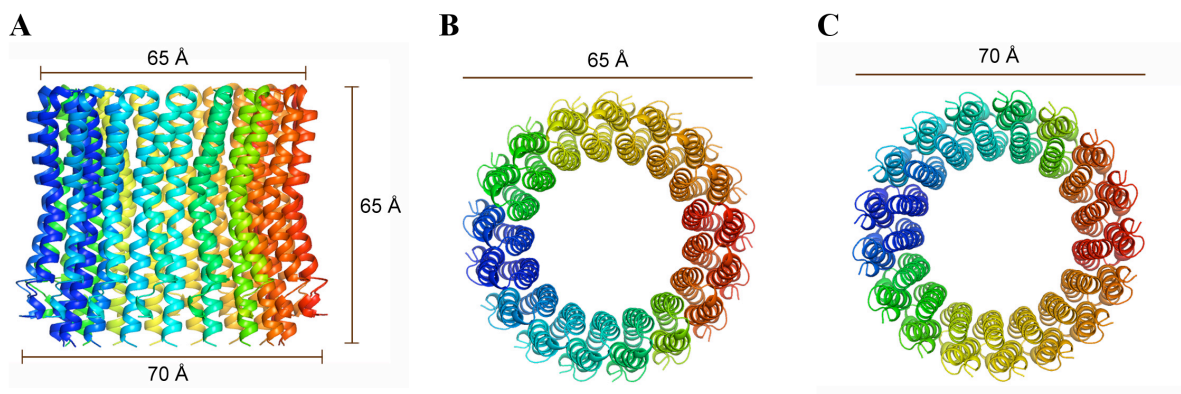


Figure 68: Structure of the N-type ATPase rotor ring

The N-type ATPase c_{17} ring viewed from (A) the side (along the membrane plane), (B) the top (cytoplasm) and (C) the bottom (periplasm). The c_{17} ring has a height of $\sim 65 \text{ \AA}$, a diameter of $\sim 65 \text{ \AA}$ at the cytoplasm and of $\sim 70 \text{ \AA}$ at the periplasm.

5.2 Discussion

The structure determination of small membrane proteins by single-particle cryo-EM has been made possible by a combination of dramatic developments in image recording using direct electron detectors (Li *et al*, 2013) as well as in data processing (Scheres, 2012).

For structure determination the rotor ring of the N-type ATPase was purified in three different detergents (DDM, C₁₂E₈ and LDAO) and amphipol A8-35 and analysed by single-particle cryo-EM. The detergents and amphipol A8-35 differ in their density and micelle size. It was shown that these physical parameters have a decisive impact on the structure determination of this small membrane protein complex by cryo-EM. The rotor ring structure was solved to a resolution of 6.1 Å using LDAO as detergent, showing that the N-type ATPase c-ring is composed of 17 c-subunits, each consisting of a helix hairpin. With 17 c-subunits the N-type ATPase rotor ring has the highest c-ring stoichiometry known so far.

5.2.1 Impact of the detergent on cryo-EM structure determination of the N-type ATPase c-ring

A previous attempt to determine a rotor ring stoichiometry by negative-stain single-particle EM suggested a c₇ ring (Murata *et al*, 2003). A subsequent X-ray structure by the same group revealed that the rotor ring consists of 10 instead of 7 subunits (Murata *et al*, 2004). As the resolution limit of negative-stain EM is ~20 Å (Ohi *et al*, 2004) it is not surprising that the stoichiometry was incorrect.

For electron cryomicroscopy the resolution limit depends on the Nyquist frequency, which is the maximum spatial frequency that can be recovered from an image and corresponds to two times the pixel size. Since the electron cryomicrographs of the N-type ATPase rotor ring were acquired with a pixel size of 1.14 Å, the theoretical resolution limit is 2.28 Å. This means that theoretically each micrograph contains a resolution to 2.28 Å. Therefore it can be assumed that the parameters, which were chosen during data collection, are not a limiting factor for single particle structure determination. Reasons why a protein can not be solved to high-resolution are the limited number of picked particles and protein-specific properties such as flexibility and size. In the case of flexibility all particles are in slightly different conformational states. These conformational states are averaged during a 3D refinement. Therefore protein flexibility generally limits the resolution in single-particle cryo-EM. The size of a protein is important as the number of scattered electrons is proportional to it, which affects the signal-to-noise ratio. Thus, large proteins can be better aligned to a reference than smaller proteins.

The rotor ring of the N-type ATPase has a size of 141 kDa which is about 50 kDa smaller than the human γ -secretase (170 - 230 kDa), which is the smallest membrane protein that was successfully solved to 3.5 Å by single-particle cryo-EM so far (Bai *et al*, 2015b). In contrast to the γ -secretase the rotor ring is composed of 17 identical c-subunits each formed by a hairpin of ~8 kDa. On the one hand this feature is favourable for cryo-EM structure determination, as the calculation speed is increased by applying 17-fold symmetry during a 3D refinement, because the software considers only the asymmetric unit (Cheng *et al*, 2015). On the other hand this means that the software has to align a single hairpin within each projection accurately. To make it even more difficult, the rotor ring is surrounded by a belt of unordered amphiphatic molecules. In sum, the software has to align a ~8 kDa c-subunit of a small particle, which is surrounded by a belt of unordered detergent molecules.

Structure determination of the N-type ATPase rotor ring in different detergents revealed that it is not straightforward to solve its structure by single-particle cryo-EM. In general, features that are visible in 2D class averages have to be resolved in the 3D structure as well. This was the case for the secondary-active transporter BetP from *C. glutamicum* and for the human TRP channel polycystin-2, which were also investigated by this method, as described in chapter 3 and 4 of this thesis. However this was not the case for the rotor ring in amphipol A8-35, DDM or C₁₂E₈. In these amphiphatic molecules c-subunits were visible in the 2D class averages showing the rotor ring viewed along the membrane plane (figure 69 A - C). In DDM the outer helices were additionally separated in the top view class average (figure 69 B). Based on the class averages it was assumed that the structure of the rotor ring can be solved in DDM. Surprisingly, this was not the case even if the later determined N-type ATPase c-ring structure was applied as a starting model. Initial separation of c-subunits in a 3D map was observed for the c-ring in C₁₂E₈, revealing that other factors apart from the protein density are crucial for 3D reconstruction. By comparing the 2D class averages of the c-ring in different amphiphatic molecules, remarkable differences were apparent in the detergent belt that surrounded the c-ring. Whereas in amphipol A8-35 and DDM, a dense belt surrounded the protein complex, this belt started to disappear in C₁₂E₈ and was almost invisible in LDAO. The disappearance of the detergent belt correlates with the detergent density and micelle size (table 17). While amphipol A8-35 has the highest density and micelle size, LDAO has the lowest.

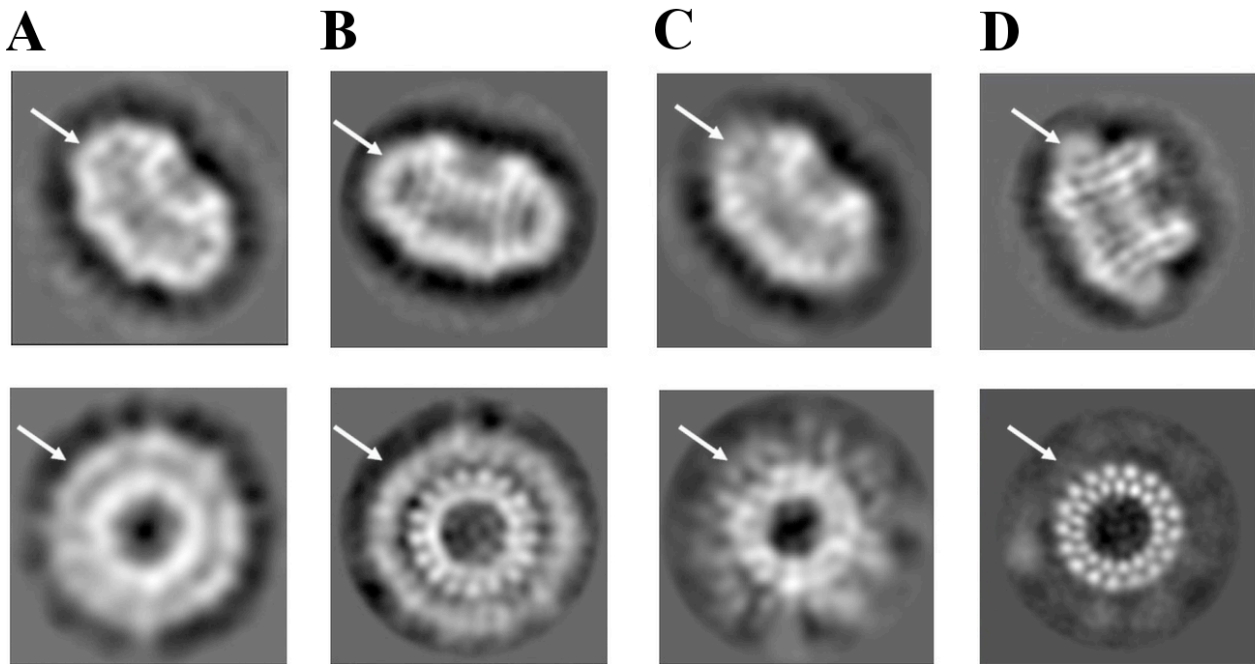


Figure 69: 2D class averages of the N-type ATPase rotor ring in different amphiphatic molecules

2D classifications were performed without full CTF-correction. The best side and top view class averages of the rotor ring in (A) amphipol A8-35, (B) DDM, (C) $C_{12}E_8$ and (D) LDAO are compared. White arrows point to the detergent belt that starts to disappear in $C_{12}E_8$ until it is not visible anymore in the top view of the rotor ring in LDAO.

A comparison of the 3D structures of the rotor ring in the four different amphiphatic molecules in solid mode representation confirmed the observation of the 2D class averages (figure 70). In amphipol A8-35 and DDM a dense belt of detergent surrounded the rotor ring while first details of it became visible when it is surrounded by $C_{12}E_8$. In the case of LDAO the detergent belt was very weak revealing the structure of the rotor ring.

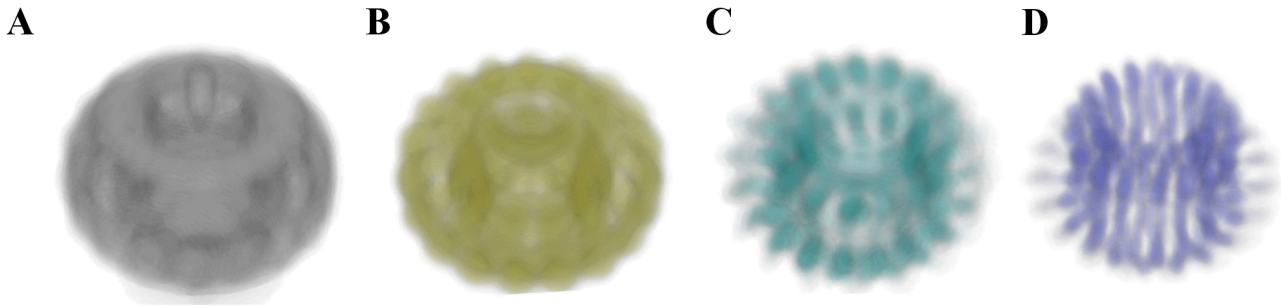


Figure 70: Cryo-EM maps of the rotor ring in different amphiphatic molecules

Solid-mode representation of the rotor ring cryo-EM maps in (A) amphipol A8-35, (B) DDM, (C) $C_{12}E_8$ and (D) LDAO.

It has to be considered that the structure determination of the rotor ring in LDAO was only successful because the small micelle size of LDAO resulted in an asymmetric particle viewed along the membrane plane. This means that the periplasmatic and cytoplasmic site of the particle could be clearly distinguished. In the case of amphipol A8-35 and DDM, higher-resolution information would be necessary to separate the periplasmic from the cytoplasmic side. It would have to be tested if the structure of the rotor ring can also be solved in a detergent that has a small micelle size but a high density like deoxycholic acid or SDS. If this is possible it can be concluded that the micelle size of a detergent has a higher impact on structure determination than its density. However, as many membrane proteins are not stable in SDS, this detergent is not suitable for common structural analysis.

An alternative approach for structure determination of the rotor ring in detergents of high density would be the subtraction of the detergent density in each particle. This approach was used to trap different conformations of the human γ -secretase (Bai *et al.*, 2015a), for example. However, Bai *et al.* subtracted parts of the protein and not the detergent belt. To apply this approach the accurate Euler angles of each particle have to be determined. However, it has to be considered that the removal of detergent in each particle will modify the selected particles *in silico* before they can be used for a 3D refinement. Therefore this approach was not used in this work.

The advantage of changing the amphiphatic molecule instead of modifying the selected particles *in silico* is that there is no risk of introducing user bias. However, this biochemical approach is limited by the possibilities for detergent exchange, as membrane proteins are generally only stable in a small number of detergents. In addition it has to be considered that proteins

surrounded by detergents with a low density and a small micelle size appear smaller and are therefore more difficult to recognize by cryo-EM. This drawback can be bypassed by using an energy filter and slightly higher defocus. The energy filter removes inelastically scattered electrons that contribute to noise. Using a higher defocus increases the contrast of the particles, making it possible to identify them. However, at higher defocus more particles are required to compensate for the defocus-dependent fall-off in resolution.

5.2.2 Impact of the particle number on cryo-EM structure determination of the N-type ATPase rotor ring

A closer look at table 18 shows that the datasets of the rotor ring do not only differ in the amphiphatic molecule used but also in the number of particles. The question remains which impact the particle number has and how many particles would be necessary to obtain a rotor ring structure with a higher-resolution than 4 Å that allows the assignment of side chain residues. It might be also interesting to know if it is possible to solve the structure of the rotor ring in other detergents besides LDAO by just increasing the number of particles.

A comparison of all structures determined by single-particle cryo-EM shows that the larger the protein and the higher its symmetry the fewer particles are needed to obtain a high-resolution structure. However, there is no simple formula, which can be used to calculate the required number of particles to solve a high-resolution structure. But as soon as a reliable structure is obtained, an approximation can be used to calculate the number of particles, which have to be added to increase the resolution by a factor of two. The formula takes into account that to increase the resolution of a 3D structure by the factor of two the information in x, y- and z-direction each has to be increased by the same factor. Accordingly, $2^3 = 8$ times more particles are needed for a 2-fold increase in resolution. This would mean $47.000 \cdot 8 = 376.000$ good particles of the rotor ring should theoretically result in a structure with a resolution of about 3 Å. It has to be considered that the number of initially picked particles has to be increased by the same factor. Therefore $226.000 \cdot 8 = 1.808.000$ rotor ring particles in LDAO would have to be picked to achieve a 3 Å structure which would take ~32 terabyte of storage and months to collect and process the data. For the human γ -secretase, it was shown that the addition of ~1.200.000 particles increased the resolution from 4.5 Å to 3.5 Å, which is in line with the formula given above (Bai *et al.*, 2015b; Lu *et al.*, 2014).

The final number of particles of the rotor ring in different detergents ranges from 45.000 - 77.000. At first sight a difference of 32.000 particles seems to be substantial for structure determination, but it is negligible when compared to the number of particles that would be necessary to improve the resolution significantly. In addition, the final 3D structure of the rotor ring in LDAO was calculated from only 47.000 particles. However, the relative amount of good particles to initially picked particles differs a lot. In amphipol A8-35 and LDAO only a small portion of picked particles (26.5 % and 22 %, respectively) was useful for final structure determination. In contrast in the case of DDM and C₁₂E₈, a much larger percentage of particles (59.2 % and 66.9 %, respectively) was included in the final structure. Most likely the particles were better recognized by the automatic picking procedure in DDM and C₁₂E₈ in comparison to amphipol A8-35 and LDAO.

As mentioned above an increase in the particle number only makes sense if a reliable low-resolution structure of the protein is available. This was not the case for the rotor ring in amphipol A8-35 and DDM. Consequently, it would probably not make sense to increase the particle number of the c-ring in these two detergents, as the detergent density inhibits particle alignment during single-particle structure determination. Therefore it has to be assumed that the rotor ring structure can not be solved in these detergents by single-particle cryo-EM. In the case of C₁₂E₈ single c-subunits started to separate in the 3D refinement (figure 70). Possibly, a larger number of c-ring particles in this detergent could lead to a high-resolution 3D structure. However, as already mentioned the number of particles has to be increased significantly in this case. Thus, the most promising strategy to obtain a high-resolution structure of the rotor ring is further data collection of the c-ring in LDAO.

5.2.3 Rotor ring stoichiometry and biological consequences for the N-type ATPase

N-type ATPases were classified as novel type of rotary ATPases about six years ago (Dibrova *et al*, 2010). Since then only one study was published biochemically describing a Na⁺ dependent ATPase which probably belongs to the N-type ATPases (Soontharapirakkul *et al*, 2010). However, there is still no structure of this complex available. In the present work a structural investigation of the N-type ATPase rotor ring revealed that it is composed of 17 identical c-subunits, each forming a hairpin. The 6.1 Å structure shows that the architecture of the N-type ATPase c-ring is similar to rotor rings of F-type ATPases. This is in line with sequence alignments showing similarities between F-type and N-type ATPase c-subunits (Schulz, 2015). Based on prior structural knowledge about F-type ATPase rotor rings and the cryo-EM map of

the N-type ATPase c-ring, it was possible to model the c-ring at this point. The basis for this was a homology model of the *B. pseudomallei* c-subunit, which was fitted 17 times into the cryo-EM density. A close-up of the highly conserved ion-binding glutamate, E61 in this case, reveals that it is located approximately in the middle of the membrane, at the narrowest part of adjacent c-subunits where the outer helices are sharply kinked (figure 71). The location of the ion-binding site in the middle of the membrane is conserved in all known c-rings. At a resolution of 6.1 Å no conclusions can be drawn about the orientation of amino acid side chains. However, based on the knowledge about the ion-binding site of other c-rings it was proposed that E61 and E28 of one c-subunit and Y66 of the adjacent c-subunit are involved in proton coordination. The proton may be further coordinated by the side chain oxygen of T62 or by the sulphur of M63 of the adjacent c-subunit depending on the orientation of these side chains. In case M63 is involved, T62 might further stabilize the coordination by a polar interaction with M63 (Schulz, 2015).

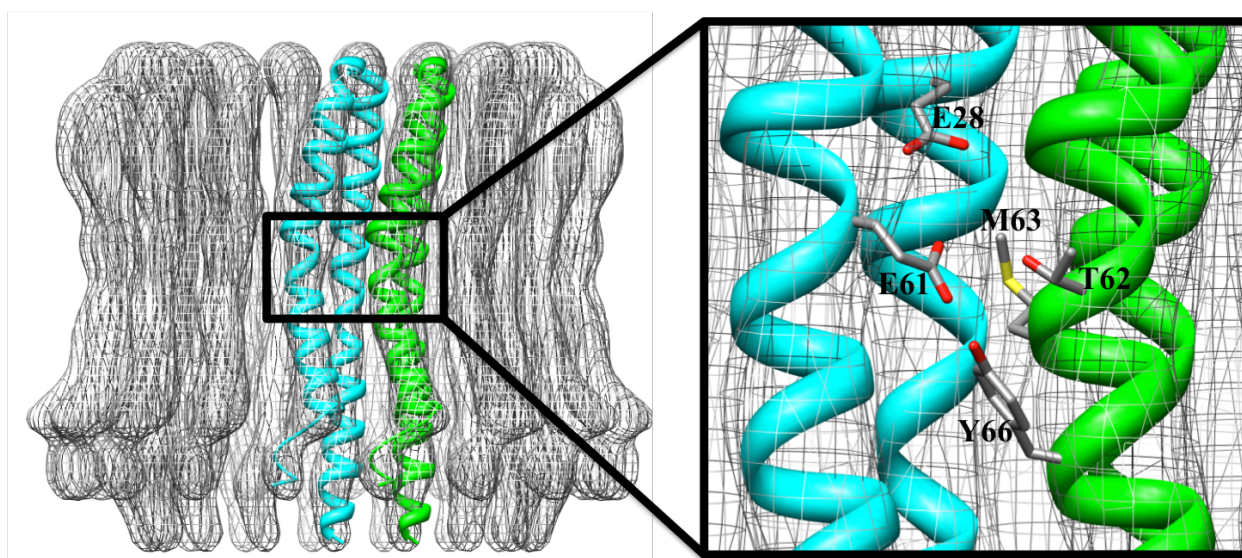


Figure 71: Putative proton binding site of the N-type ATPase rotor ring

The rotor ring structure seen from the membrane plane, with two c-subunits highlighted in cyan and green. A close-up of the conserved ion-binding E61 reveals that it is located at the kink of the outer helix and surrounded by E28 of the same and Y66, T62 and M63 of the adjacent c-subunit. Note that the resolution of the data does not allow side chain orientations. The relative positions of the side chains were inferred from structures of other rotor rings.

A 360° rotation of a F-type ATPase c-ring is coupled to the transport of 8 - 15 ions across the membrane depending on the respective rotor ring stoichiometry. During this rotation three ADP + P_i are converted into three ATP. Depending on the number of transported ions each rotor ring

has a specific ion to ATP ratio. In analogy to the mechanism proposed for the F-type rotary ATPases, an N-type ATPase c_{17} ring would transport 17 ions during the synthesis of three ATP molecules. Conclusively, this ATPase has an ion to ATP ratio of 17/3, which is the highest ratio known so far.

The ion per ATP ratio is directly coupled to the *proton* or *sodium motif force* (pmf/smf). The pmf describes the electrochemical proton gradient across the membrane and is a combination of the proton concentration gradient ΔpH and the electrical gradient $\Delta\psi$. The energy (ΔG), which is available for ATP synthesis under standard conditions, can be calculated by the Nernst equation (Voet D. *et al*, 2010):

$$\Delta G = RT \ln\left(\frac{[H_{in}]}{[H_{out}]}\right) + zF\Delta\Psi$$

(H_{in} = proton concentration inside the cell, H_{out} = proton concentration outside the cell, R = universal gas constant, T = absolute temperature, z = number of moles of electrons transferred, $\Delta\psi$ = electrochemical gradient).

To drive ATP synthesis with a c_8 ring the energy derived from the electrochemical gradient across the membrane has to be equal or higher to the free Gibbs energy of three ATP molecules divided by 8, which is $\frac{3 \cdot 30.5 \text{ kJ/mol}}{8} = 11.4 \text{ kJ/mol}$ (for calculation standard conditions are assumed) (Voet D. *et al*, 2010). Analogous 10.2 kJ/mol, 9.2 kJ/mol, 8.3 kJ/mol, 7.6 kJ/mol, 7.0 kJ/mol, 6.5 kJ/mol, 6.1 kJ/mol and 5.4 kJ/mol are required to drive a c_9 , c_{10} , c_{11} , c_{12} , c_{13} , c_{14} , c_{15} , and c_{17} ring, respectively, one step further. This clearly shows that the N-type ATPase requires less kJ per mol to drive ATP synthesis compared to all known rotary ATPases. Bacteria expressing such an N-type ATPase have a selective advantage against other in an environment that provides only a low electrochemical gradient across the membrane. In an environment with a higher electrochemical gradient rotary ATPases with small ion to ATP ratios are favoured for ATP synthesis, as more ATP molecules can be generated with fewer ions compared to rotary ATPases with higher ion to ATP ratios. The transcription of both, an F-type ATPase with a small rotor ring and an N-type ATPase with a large rotor ring, might be useful for bacteria living in an environment where the electrochemical gradient can drop significantly and requires a long time period to recover.

Alternatively, bacteria might use the N-type ATPase as proton/sodium ion pump. On the first view this looks highly beneficial as the N-type ATPase from *B. pseudomallei* could transport 17

protons during the hydrolysis of three ATP. However, this works only in an environment where protons are pumped against an electrochemical gradient that results in a ΔG of less than 5.4 kJ/mol. As soon as the energy derived from the electrochemical gradient exceeds 5.4 kJ/mol, an ATPase with a c_{17} ring can no longer function as an ion pump. A previous study reported that a Na^+ dependent rotary ATPase which most likely belongs to the N-type ATPase family seems to support growth of a bacterium under high-salt concentrations (Soontharapirakkul *et al*, 2011). Taken into account that this enzyme has to pump sodium ions against a large Na^+ -gradient, the rotor ring of this enzyme presumably has a smaller c-ring stoichiometry compared to the *B. pseudomallei* ATPase.

5.2.4 Summary

The focus of this study was on the 3D structure determination of the N-type ATPase rotor ring from *B. pseudomallei*. The c_{17} stoichiometry of the protein complex was determined by 2D classifications and the structure was solved to 6.1 Å resolution. The cryo-EM map and the similarity between F-type and N-type ATPase rotor rings allowed the generation of an N-type ATPase c-ring model. The analysis of the rotor ring in different amphiphatic molecules revealed their decisive impact for single-particle cryo-EM. Thus, a biochemical approach for successful single-particle cryo-EM of such small membrane protein complexes is the selection of the most appropriate detergent.

6 Conclusions and perspectives

At the beginning of this thesis there was no high-resolution single-particle cryo-EM structure of a small membrane protein. In those days, the structure of the TRPC3 channel was solved to a resolution of only 15 Å with more than 150.000 particles (Mio *et al*, 2007). In the time period of this work the resolution limit of cryo-EM changed dramatically due to the development of direct electron detectors and better software for particle alignment (Kühlbrandt, 2014). Using a high-end electron microscope equipped with a direct electron detector, only the particle number and the intrinsic flexibility of a protein limit the modern single-particle cryo-EM structure determination.

In this work single-particle cryo-EM was used to determine the structure of three different types of membrane proteins. The first project dealt with the human TRP channel polycystin-2 (PC-2), which was expressed in GnTI⁻ cells. The expression of PC-2 resulted in crystalloid ER, a formation that was previously only obtained *in vitro* by the overexpression of HMG-CoA reductase in UT-1 cells. Although it seems that proteins involved in lipid biogenesis as well as proteins that form intracellular interactions seem to support crystalloid formation we are still far away from understanding what triggers the formation of crystalloid versus karmellea and whorl ER.

PC-2 was produced in GnTI⁻ cells and different strategies for protein purification were tested. The use of a StrepII-tag and LMNG/CHS as detergent mixture resulted in a pure protein sample suitable for cryo-EM data acquisition. A dataset of PC-2 in amphipol A8-35 comprising ~860 micrographs and ~120.000 particles was taken and yielded a 4.6 Å structure. The structure of PC-2 displays the open conformation and gives first insights into its extracellular domain.

To gain higher-resolution the dataset of PC-2 has to be increased. With a resolution below 4 Å an atomic model of PC-2 could be build, which would help to understand how specific mutations could cause ADPKD. Further, structure determination of the closed state of PC-2 in the absence of Ca²⁺ would allow understanding how PC-2 changes its conformation. On the basis of the opened and closed state and the knowledge of the residues involved in causing ADPKD, a drug-based treatment can be developed. This would help thousands of people suffering from ADPKD especially because currently kidney transplantation is their only hope of healing.

The structural investigation of the secondary-active transporter BetP by single-particle cryo-EM was the second project of this work. BetP was incorporated into amphipol A8-35 before a cryo-EM dataset was acquired which yielded in a 6.8 Å structure. The cryo-EM structure of BetP showed a new state in which the C-terminal domains are located differently compared to all known X-ray structures in which one of the three C-terminal domains always forms an essential crystal contact. Since no potassium and glycine betaine were present, the cryo-EM map most likely shows an inactive state of BetP. As in the case of the human γ -secretase, the collection of more data would most likely result in a high-resolution structure of BetP (Bai *et al*, 2015b; Lu *et al*, 2014). However, the extensive knowledge of BetP together with the cryo-EM map already allowed the generation of a very detailed model of the inactive state.

Single-particle cryo-EM of BetP in the presence of K^+ is a structural approach to investigate the regulation and activation cycle of the protein. This would reveal the activated structure of BetP in solution and the movement of the C-terminal domain upon activation. It has to be considered that in the presence of K^+ the binding sites of these ions are important. The determination of these sites requires a resolution of about 3.5 Å and thus a very large dataset, comprising approximately 1.500.000 particles.

In the third project of this work, the structure of the N-type ATPase rotor ring was determined. The N-type ATPase c-ring was a suitable membrane protein to investigate the impact of amphiphatic molecules on single-particle cryo-EM structure determination. The choice of the amphiphatic molecule was decisive for structure determination of this small membrane protein complex. The particles were only accurately aligned against projections of a reference if the rotor ring was embedded in a detergent of a low density and small micelle size. By using LDAO as detergent, a 6.1 Å structure of the N-type ATPase c_{17} ring was solved. Based on the c-ring stoichiometry, a possible function of this enzyme was discussed. Although it is not known whether the *B. pseudomallei* N-type ATPase is an ATP synthase or a proton pump, it can be concluded that this enzyme can work efficiently in ATP synthesis in the presence of a low electrochemical gradient.

A single-particle cryo-EM analysis on the entire N-type ATPase would answer many more questions about this type of ATPase such as the number of outer stalks and how ions are transported through the F_o domain.

The limit of single-particle cryo-EM was estimated by Richard Henderson on the basis of theoretical considerations in 1995 (Henderson, 1995). He postulated that it would be possible to

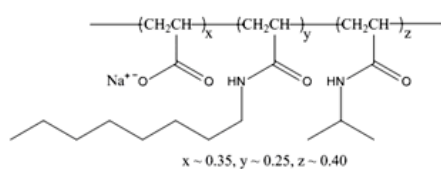
determine an atomic structure of a 100 kDa protein from approximately 10.000 reprojections acquired under ideal conditions. Considering the impact of the detergent it would be interesting to see how many particles would be necessary to obtain the structure of a 100 kDa membrane protein. It has to be mentioned that the technical development of direct electron detectors as well as the software development for single-particle cryo-EM is still ongoing. I assume that the next generation of detectors, which have more pixels and a better quantum efficiency, will enable high-resolution structure determination of proteins with a molecular weight even below 100 kDa by single-particle cryo-EM.

There are already centres for cryo-EM sample freezing and data-collection allowing more scientists access to this method. Combining the new developments in cryo-EM with NMR spectroscopy, the structure of every protein could, theoretically, be investigated in solution without the need of protein crystals. Additionally, the sample amount necessary for cryo-EM is much lower compared to X-ray crystallography and NMR. However, to take advantage of this method the protein has to be expressed and purified in high quality, which is still a challenge for most membrane proteins.

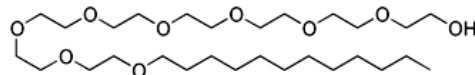
7 Appendix

Table 19: Applied b-factors in cryo-EM structure determination

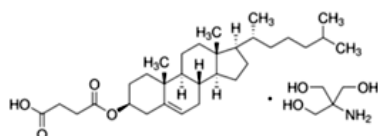
EM structure	b-factor
PC-2	- 312
BetP	- 400
N-type ATPase c-ring	- 207



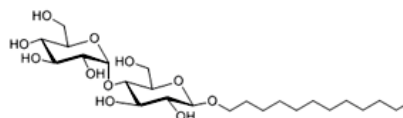
Amphipol A8-35



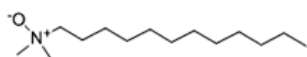
C₁₂E₈



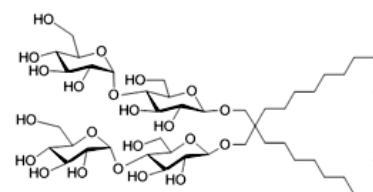
CHS



DDM



LDAO



LMNG

Figure 72: Chemical structures of amphiphatic molecules used in this work for single-particle cryo-EM

8 References

Abrahams JP, Leslie AGW, Lutter R, Walker JE (1994) Structure at 2.8-Angstrom Resolution of F1-ATPase from Bovine Heart-Mitochondria. *Nature* **370**: 621-628

Adachi K, Oiwa K, Nishizaka T, Furuike S, Noji H, Itoh H, Yoshida M, Kinosita K, Jr. (2007) Coupling of rotation and catalysis in F(1)-ATPase revealed by single-molecule imaging and manipulation. *Cell* **130**: 309-321

Afonine PV, Grosse-Kunstleve RW, Echols N, Headd JJ, Moriarty NW, Mustyakimov M, Terwilliger TC, Urzhumtsev A, Zwart PH, Adams PD (2012) Towards automated crystallographic structure refinement with phenix.refine. *Acta Crystallogr D Biol Crystallogr* **68**: 352-367

Aksimentiev A, Balabin IA, Fillingame RH, Schulten K (2004) Insights into the molecular mechanism of rotation in the Fo sector of ATP synthase. *Biophys J* **86**: 1332-1344

Allegretti M, Klusch N, Mills DJ, Vonck J, Kühlbrandt W, Davies KM (2015) Horizontal membrane-intrinsic alpha-helices in the stator a-subunit of an F-type ATP synthase. *Nature* **521**: 237-240

Allen MD, Qamar S, Vadivelu MK, Sandford RN, Bycroft M (2014) A high-resolution structure of the EF-hand domain of human polycystin-2. *Protein Sci* **23**: 1301-1308

Altendorf K, Booth IR, Gralla J, Greie JC, Rosenthal AZ, Wood JM (2009) Osmotic Stress. *Ecosal Plus* **3**

Anderson RG, Orci L, Brown MS, Garcia-Segura LM, Goldstein JL (1983) Ultrastructural analysis of crystalloid endoplasmic reticulum in UT-1 cells and its disappearance in response to cholesterol. *J Cell Sci* **63**: 1-20

Arakawa T, Timasheff SN (1985) The stabilization of proteins by osmolytes. *Biophys J* **47**: 411-414

Bachmair A, Finley D, Varshavsky A (1986) In vivo half-life of a protein is a function of its amino-terminal residue. *Science* **234**: 179-186

Bai XC, Rajendra E, Yang G, Shi Y, S. S (2015a) Sampling the conformational space of the catalytic subunit of human γ -secretase. *bioRxiv*

Bai XC, Yan C, Yang G, Lu P, Ma D, Sun L, Zhou R, Scheres SH, Shi Y (2015b) An atomic structure of human gamma-secretase. *Nature*

Beatrix B, Bendrat K, Rospert S, Buckel W (1990) The biotin-dependent sodium ion pump glutacoyl-CoA decarboxylase from *Fusobacterium nucleatum* (subsp. *nucleatum*). Comparison with the glutacoyl-CoA decarboxylases from gram-positive bacteria. *Arch Microbiol* **154**: 362-369

- Boiangiu CD, Jayamani E, Brugel D, Herrmann G, Kim J, Forzi L, Hedderich R, Vgenopoulou I, Pierik AJ, Steuber J, Buckel W (2005) Sodium ion pumps and hydrogen production in glutamate fermenting anaerobic bacteria. *J Mol Microbiol Biotechnol* **10**: 105-119
- Bolen DW, Baskakov IV (2001) The osmophobic effect: natural selection of a thermodynamic force in protein folding. *J Mol Biol* **310**: 955-963
- Booth IR, Edwards MD, Black S, Schumann U, Miller S (2007) Mechanosensitive channels in bacteria: signs of closure? *Nat Rev Microbiol* **5**: 431-440
- Boyer PD (1993) The binding change mechanism for ATP synthase--some probabilities and possibilities. *Biochim Biophys Acta* **1140**: 215-250
- Bradford MM (1976) A rapid and sensitive method for the quantitation of microgram quantities of protein utilizing the principle of protein-dye binding. *Anal Biochem* **72**: 248-254
- Bycroft M, Bateman A, Clarke J, Hamill SJ, Sandford R, Thomas RL, Chothia C (1999) The structure of a PKD domain from polycystin-1: implications for polycystic kidney disease. *EMBO J* **18**: 297-305
- Cai Y, Maeda Y, Cedzich A, Torres VE, Wu G, Hayashi T, Mochizuki T, Park JH, Witzgall R, Somlo S (1999) Identification and characterization of polycystin-2, the PKD2 gene product. *J Biol Chem* **274**: 28557-28565
- Cantiello HF (2004) Regulation of calcium signaling by polycystin-2. *Am J Physiol Renal Physiol* **286**: F1012-1029
- Cao E, Liao M, Cheng Y, Julius D (2013) TRPV1 structures in distinct conformations reveal activation mechanisms. *Nature* **504**: 113-118
- Catterall WA (2010) Ion channel voltage sensors: structure, function, and pathophysiology. *Neuron* **67**: 915-928
- Cayley S, Record MT, Jr. (2003) Roles of cytoplasmic osmolytes, water, and crowding in the response of Escherichia coli to osmotic stress: biophysical basis of osmoprotection by glycine betaine. *Biochemistry* **42**: 12596-12609
- Chen XZ, Vassilev PM, Basora N, Peng JB, Nomura H, Segal Y, Brown EM, Reeders ST, Hediger MA, Zhou J (1999) Polycystin-L is a calcium-regulated cation channel permeable to calcium ions. *Nature* **401**: 383-386
- Cheng Y, Grigorieff N, Penczek PA, Walz T (2015) A primer to single-particle cryo-electron microscopy. *Cell* **161**: 438-449
- Cingolani G, Duncan TM (2011) Structure of the ATP synthase catalytic complex (F(1)) from Escherichia coli in an autoinhibited conformation. *Nat Struct Mol Biol* **18**: 701-707
- Clapham DE, Julius D, Montell C, Schultz G (2005) International Union of Pharmacology. XLIX. Nomenclature and structure-function relationships of transient receptor potential channels. *Pharmacol Rev* **57**: 427-450

Conover TE, Prairie RL, Racker E (1963) Partial Resolution of the Enzymes Catalyzing Oxidative Phosphorylation. Iii. A New Coupling Factor Required by Submitochondrial Particles Extracted with Phosphatides. *J Biol Chem* **238**: 2831-2837

Cross RL, Muller V (2004) The evolution of A-, F-, and V-type ATP synthases and ATPases: reversals in function and changes in the H⁺/ATP coupling ratio. *Febs Letters* **576**: 1-4

Cuff JA, Barton GJ (1999) Evaluation and improvement of multiple sequence methods for protein secondary structure prediction. *Proteins* **34**: 508-519

Cvetkov TL, Huynh KW, Cohen MR, Moiseenkova-Bell VY (2011) Molecular architecture and subunit organization of TRPA1 ion channel revealed by electron microscopy. *J Biol Chem* **286**: 38168-38176

Dibrova DV, Galperin MY, Mulkidjanian AY (2010) Characterization of the N-ATPase, a distinct, laterally transferred Na⁺-translocating form of the bacterial F-type membrane ATPase. *Bioinformatics* **26**: 1473-1476

Dimroth P, von Ballmoos C, Meier T (2006) Catalytic and mechanical cycles in F-ATP synthases. Fourth in the Cycles Review Series. *EMBO Rep* **7**: 276-282

Dinnibier U, Limpinsel E, Schmid R, Bakker EP (1988) Transient Accumulation of Potassium Glutamate and Its Replacement by Trehalose during Adaptation of Growing-Cells of Escherichia-Coli K-12 to Elevated Sodium-Chloride Concentrations. *Archives of Microbiology* **150**: 348-357

Doyle DA, Morais Cabral J, Pfuetzner RA, Kuo A, Gulbis JM, Cohen SL, Chait BT, MacKinnon R (1998) The structure of the potassium channel: molecular basis of K⁺ conduction and selectivity. *Science* **280**: 69-77

Elmlund D, Elmlund H (2012) SIMPLE: Software for ab initio reconstruction of heterogeneous single-particles. *J Struct Biol* **180**: 420-427

Empadinhas N, da Costa MS (2008) Osmoadaptation mechanisms in prokaryotes: distribution of compatible solutes. *Int Microbiol* **11**: 151-161

Faham S, Watanabe A, Besserer GM, Cascio D, Specht A, Hirayama BA, Wright EM, Abramson J (2008) The crystal structure of a sodium galactose transporter reveals mechanistic insights into Na⁺/sugar symport. *Science* **321**: 810-814

Fang Y, Jayaram H, Shane T, Kolmakova-Partensky L, Wu F, Williams C, Xiong Y, Miller C (2009) Structure of a prokaryotic virtual proton pump at 3.2 Å resolution. *Nature* **460**: 1040-1043

Feniouk BA, Suzuki T, Yoshida M (2006) The role of subunit epsilon in the catalysis and regulation of FOF1-ATP synthase. *Biochim Biophys Acta* **1757**: 326-338

Feniouk BA, Yoshida M (2008) Regulatory mechanisms of proton-translocating F(O)F (1)-ATP synthase. *Results Probl Cell Differ* **45**: 279-308

- Ferreira FM, Oliveira LC, Germino GG, Onuchic JN, Onuchic LF (2011) Macromolecular assembly of polycystin-2 intracytosolic C-terminal domain. *Proc Natl Acad Sci U S A* **108**: 9833-9838
- Fischer H, Polikarpov I, Craievich AF (2004) Average protein density is a molecular-weight-dependent function. *Protein Sci* **13**: 2825-2828
- Forgac M (2007) Vacuolar ATPases: rotary proton pumps in physiology and pathophysiology. *Nat Rev Mol Cell Biol* **8**: 917-929
- Forrest LR, Rudnick G (2009) The rocking bundle: a mechanism for ion-coupled solute flux by symmetrical transporters. *Physiology (Bethesda)* **24**: 377-386
- Forrest LR, Zhang YW, Jacobs MT, Gesmonde J, Xie L, Honig BH, Rudnick G (2008) Mechanism for alternating access in neurotransmitter transporters. *Proc Natl Acad Sci U S A* **105**: 10338-10343
- Frey G, Chen J, Rits-Volloch S, Freeman MM, Zolla-Pazner S, Chen B (2010) Distinct conformational states of HIV-1 gp41 are recognized by neutralizing and non-neutralizing antibodies. *Nat Struct Mol Biol* **17**: 1486-1491
- Fujiwara Y, Minor DL, Jr. (2008) X-ray crystal structure of a TRPM assembly domain reveals an antiparallel four-stranded coiled-coil. *J Mol Biol* **383**: 854-870
- Gallagher AR, Cedzich A, Gretz N, Somlo S, Witzgall R (2000) The polycystic kidney disease protein PKD2 interacts with Hax-1, a protein associated with the actin cytoskeleton. *Proc Natl Acad Sci U S A* **97**: 4017-4022
- Gallagher AR, Hidaka S, Gretz N, Witzgall R (2002) Molecular basis of autosomal-dominant polycystic kidney disease. *Cell Mol Life Sci* **59**: 682-693
- Gallagher AR, Hoffmann S, Brown N, Cedzich A, Meruvu S, Podlich D, Feng Y, Konecke V, de Vries U, Hammes HP, Gretz N, Witzgall R (2006) A truncated polycystin-2 protein causes polycystic kidney disease and retinal degeneration in transgenic rats. *J Am Soc Nephrol* **17**: 2719-2730
- Geng L, Okuhara D, Yu Z, Tian X, Cai Y, Shibasaki S, Somlo S (2006) Polycystin-2 traffics to cilia independently of polycystin-1 by using an N-terminal RVxP motif. *J Cell Sci* **119**: 1383-1395
- Giamarchi A, Feng S, Rodat-Despoix L, Xu Y, Bubenshchikova E, Newby LJ, Hao J, Gaudioso C, Crest M, Lupas AN, Honore E, Williamson MP, Obara T, Ong AC, Delmas P (2010) A polycystin-2 (TRPP2) dimerization domain essential for the function of heteromeric polycystin complexes. *EMBO J* **29**: 1176-1191
- Girvin ME, Rastogi VK, Abildgaard F, Markley JL, Fillingame RH (1998) Solution structure of the transmembrane H⁺-transporting subunit c of the F1F0 ATP synthase. *Biochemistry* **37**: 8817-8824

- Gonzalez-Perrett S, Kim K, Ibarra C, Damiano AE, Zotta E, Batelli M, Harris PC, Reisin IL, Arnaut MA, Cantiello HF (2001) Polycystin-2, the protein mutated in autosomal dominant polycystic kidney disease (ADPKD), is a Ca²⁺-permeable nonselective cation channel. *Proc Natl Acad Sci U S A* **98**: 1182-1187
- Hanaoka K, Qian F, Boletta A, Bhunia AK, Piontek K, Tsiokas L, Sukhatme VP, Guggino WB, Germino GG (2000) Co-assembly of polycystin-1 and -2 produces unique cation-permeable currents. *Nature* **408**: 990-994
- Harris PC (1999) Autosomal dominant polycystic kidney disease: clues to pathogenesis. *Hum Mol Genet* **8**: 1861-1866
- Hateboer N, Veldhuisen B, Peters D, Breuning MH, San-Millan JL, Bogdanova N, Coto E, van Dijk MA, Afzal AR, Jeffery S, Saggarr-Malik AK, Torra R, Dimitrakov D, Martinez I, de Castro SS, Krawczak M, Ravine D (2000) Location of mutations within the PKD2 gene influences clinical outcome. *Kidney Int* **57**: 1444-1451
- Hayashi T, Mochizuki T, Reynolds DM, Wu G, Cai Y, Somlo S (1997) Characterization of the exon structure of the polycystic kidney disease 2 gene (PKD2). *Genomics* **44**: 131-136
- Hellmich UA, Gaudet R (2014) Structural biology of TRP channels. *Handb Exp Pharmacol* **223**: 963-990
- Henderson R (1995) The potential and limitations of neutrons, electrons and X-rays for atomic resolution microscopy of unstained biological molecules. *Q Rev Biophys* **28**: 171-193
- Henderson R, Sali A, Baker ML, Carragher B, Devkota B, Downing KH, Egelman EH, Feng Z, Frank J, Grigorieff N, Jiang W, Ludtke SJ, Medalia O, Penczek PA, Rosenthal PB, Rossmann MG, Schmid MF, Schroder GF, Steven AC, Stokes DL, Westbrook JD, Wriggers W, Yang H, Young J, Berman HM, Chiu W, Kleywegt GJ, Lawson CL (2012) Outcome of the first electron microscopy validation task force meeting. *Structure* **20**: 205-214
- Hidaka S, Konecke V, Osten L, Witzgall R (2004) PIGEA-14, a novel coiled-coil protein affecting the intracellular distribution of polycystin-2. *J Biol Chem* **279**: 35009-35016
- Hilario E, Gogarten JP (1998) The prokaryote-to-eukaryote transition reflected in the evolution of the V/F/A-ATPase catalytic and proteolipid subunits. *J Mol Evol* **46**: 703-715
- Hoenderop JG, van der Kemp AW, Hartog A, van Os CH, Willems PH, Bindels RJ (1999) The epithelial calcium channel, ECaC, is activated by hyperpolarization and regulated by cytosolic calcium. *Biochem Biophys Res Commun* **261**: 488-492
- Hoffmeister H, Babinger K, Gurster S, Cedzich A, Meese C, Schadendorf K, Osten L, de Vries U, Rasclé A, Witzgall R (2011a) Polycystin-2 takes different routes to the somatic and ciliary plasma membrane. *J Cell Biol* **192**: 631-645
- Hoffmeister H, Gallagher AR, Rasclé A, Witzgall R (2011b) The human polycystin-2 protein represents an integral membrane protein with six membrane-spanning domains and intracellular N- and C-termini. *Biochem J* **433**: 285-294

- Huang CL (2004) The transient receptor potential superfamily of ion channels. *J Am Soc Nephrol* **15**: 1690-1699
- Hunte C, Screpanti E, Venturi M, Rimon A, Padan E, Michel H (2005) Structure of a Na⁺/H⁺ antiporter and insights into mechanism of action and regulation by pH. *Nature* **435**: 1197-1202
- Inada H, Procko E, Sotomayor M, Gaudet R (2012) Structural and biochemical consequences of disease-causing mutations in the ankyrin repeat domain of the human TRPV4 channel. *Biochemistry* **51**: 6195-6206
- Itoh H, Takahashi A, Adachi K, Noji H, Yasuda R, Yoshida M, Kinoshita K (2004) Mechanically driven ATP synthesis by F1-ATPase. *Nature* **427**: 465-468
- Jardetzky O (1966) Simple allosteric model for membrane pumps. *Nature* **211**: 969-970
- Jin X, Touhey J, Gaudet R (2006) Structure of the N-terminal ankyrin repeat domain of the TRPV2 ion channel. *J Biol Chem* **281**: 25006-25010
- Johansen MB, Kiemer L, Brunak S (2006) Analysis and prediction of mammalian protein glycation. *Glycobiology* **16**: 844-853
- Jones DT (1999) Protein secondary structure prediction based on position-specific scoring matrices. *J Mol Biol* **292**: 195-202
- Junge W, Lill H, Engelbrecht S (1997) ATP synthase: an electrochemical transducer with rotatory mechanics. *Trends Biochem Sci* **22**: 420-423
- Kagawa Y, Racker E (1966) Partial resolution of the enzymes catalyzing oxidative phosphorylation. X. Correlation of morphology and function in submitochondrial particles. *J Biol Chem* **241**: 2475-2482
- Kall L, Krogh A, Sonnhammer EL (2004) A combined transmembrane topology and signal peptide prediction method. *J Mol Biol* **338**: 1027-1036
- Kempf B, Bremer E (1998) Uptake and synthesis of compatible solutes as microbial stress responses to high-osmolality environments. *Arch Microbiol* **170**: 319-330
- Khafizov K, Staritzbichler R, Stamm M, Forrest LR (2010) A study of the evolution of inverted-topology repeats from LeuT-fold transporters using AlignMe. *Biochemistry* **49**: 10702-10713
- Kim J, Wu S, Tomasiak TM, Mergel C, Winter MB, Stiller SB, Robles-Colmanares Y, Stroud RM, Tampe R, Craik CS, Cheng Y (2015) Subnanometre-resolution electron cryomicroscopy structure of a heterodimeric ABC exporter. *Nature* **517**: 396-400
- Kobori T, Smith GD, Sandford R, Edwardson JM (2009) The transient receptor potential channels TRPP2 and TRPC1 form a heterotetramer with a 2:2 stoichiometry and an alternating subunit arrangement. *J Biol Chem* **284**: 35507-35513

- Koshy C (2014) Insights into the functional and regulatory mechanisms of the osmoregulated Na⁺/glycine betaine symporter BetP from *Corynebacterium glutamicum*: A structural and computational study. . Biochemistry, Goethe University, Frankfurt
- Koshy C, Schweikhard ES, Gartner RM, Perez C, Yildiz O, Ziegler C (2013) Structural evidence for functional lipid interactions in the betaine transporter BetP. *EMBO J* **32**: 3096-3105
- Kottgen M, Benzing T, Simmen T, Tauber R, Buchholz B, Feliciangeli S, Huber TB, Schermer B, Kramer-Zucker A, Hopker K, Simmen KC, Tschucke CC, Sandford R, Kim E, Thomas G, Walz G (2005) Trafficking of TRPP2 by PACS proteins represents a novel mechanism of ion channel regulation. *EMBO J* **24**: 705-716
- Koulen P, Cai Y, Geng L, Maeda Y, Nishimura S, Witzgall R, Ehrlich BE, Somlo S (2002) Polycystin-2 is an intracellular calcium release channel. *Nat Cell Biol* **4**: 191-197
- Kramer R (2009) Osmosensing and osmosignaling in *Corynebacterium glutamicum*. *Amino Acids* **37**: 487-497
- Krishnamurthy H, Piscitelli CL, Gouaux E (2009) Unlocking the molecular secrets of sodium-coupled transporters. *Nature* **459**: 347-355
- Kucukelbir A, Sigworth FJ, Tagare HD (2014) Quantifying the local resolution of cryo-EM density maps. *Nat Methods* **11**: 63-65
- Kühlbrandt W (2014) Biochemistry. The resolution revolution. *Science* **343**: 1443-1444
- Laemmli UK (1970) Cleavage of structural proteins during the assembly of the head of bacteriophage T4. *Nature* **227**: 680-685
- Landoure G, Zdebik AA, Martinez TL, Burnett BG, Stanescu HC, Inada H, Shi Y, Taye AA, Kong L, Munns CH, Choo SS, Phelps CB, Paudel R, Houlden H, Ludlow CL, Caterina MJ, Gaudet R, Kleta R, Fischbeck KH, Sumner CJ (2010) Mutations in TRPV4 cause Charcot-Marie-Tooth disease type 2C. *Nat Genet* **42**: 170-174
- Lau SY, Procko E, Gaudet R (2012) Distinct properties of Ca²⁺-calmodulin binding to N- and C-terminal regulatory regions of the TRPV1 channel. *J Gen Physiol* **140**: 541-555
- le Maire M, Champeil P, Moller JV (2000) Interaction of membrane proteins and lipids with solubilizing detergents. *Biochim Biophys Acta* **1508**: 86-111
- Li Q, Liu Y, Zhao W, Chen XZ (2002) The calcium-binding EF-hand in polycystin-L is not a domain for channel activation and ensuing inactivation. *FEBS Lett* **516**: 270-278
- Li X, Mooney P, Zheng S, Booth CR, Braunfeld MB, Gubbens S, Agard DA, Cheng Y (2013) Electron counting and beam-induced motion correction enable near-atomic-resolution single-particle cryo-EM. *Nat Methods* **10**: 584-590
- Liao M, Cao E, Julius D, Cheng Y (2013) Structure of the TRPV1 ion channel determined by electron cryo-microscopy. *Nature* **504**: 107-112

- Lishko PV, Procko E, Jin X, Phelps CB, Gaudet R (2007) The ankyrin repeats of TRPV1 bind multiple ligands and modulate channel sensitivity. *Neuron* **54**: 905-918
- Liu Y, Li Q, Tan M, Zhang YY, Karpinski E, Zhou J, Chen XZ (2002) Modulation of the human polycystin-L channel by voltage and divalent cations. *FEBS Lett* **525**: 71-76
- Long SB, Campbell EB, Mackinnon R (2005) Crystal structure of a mammalian voltage-dependent Shaker family K⁺ channel. *Science* **309**: 897-903
- Lu P, Bai XC, Ma D, Xie T, Yan C, Sun L, Yang G, Zhao Y, Zhou R, Scheres SH, Shi Y (2014) Three-dimensional structure of human gamma-secretase. *Nature* **512**: 166-170
- Ludtke SJ, Baldwin PR, Chiu W (1999) EMAN: semiautomated software for high-resolution single-particle reconstructions. *J Struct Biol* **128**: 82-97
- Luo Y, Vassilev PM, Li X, Kawanabe Y, Zhou J (2003) Native polycystin 2 functions as a plasma membrane Ca²⁺-permeable cation channel in renal epithelia. *Mol Cell Biol* **23**: 2600-2607
- Lupas A, Van Dyke M, Stock J (1991) Predicting coiled coils from protein sequences. *Science* **252**: 1162-1164
- Marabini R, Masegosa IM, San Martin MC, Marco S, Fernandez JJ, de la Fraga LG, Vaquerizo C, Carazo JM (1996) Xmipp: An Image Processing Package for Electron Microscopy. *J Struct Biol* **116**: 237-240
- Martinez JR, Grantham JJ (1995) Polycystic kidney disease: etiology, pathogenesis, and treatment. *Dis Mon* **41**: 693-765
- Maruyama Y, Ogura T, Mio K, Kiyonaka S, Kato K, Mori Y, Sato C (2007) Three-dimensional reconstruction using transmission electron microscopy reveals a swollen, bell-shaped structure of transient receptor potential melastatin type 2 cation channel. *J Biol Chem* **282**: 36961-36970
- McCleverty CJ, Koesema E, Patapoutian A, Lesley SA, Kreusch A (2006) Crystal structure of the human TRPV2 channel ankyrin repeat domain. *Protein Sci* **15**: 2201-2206
- Meier T, Dimroth P (2002) Intersubunit bridging by for the unusual stability Na⁺ ions as a rationale of the c-rings of Na⁺-translocating F1F0 ATP synthases. *Embo Reports* **3**: 1094-1098
- Meier T, Faraldo-Gómez JD, Börsch M (2011) ATP Synthase – A Paradigmatic Molecular Machine. In *Molecular Machines in Biology*, Frank J (ed), pp 208-238. Cambridge University Press
- Meier T, Krah A, Bond PJ, Pogoryelov D, Diederichs K, Faraldo-Gomez JD (2009) Complete ion-coordination structure in the rotor ring of Na⁺-dependent F-ATP synthases. *J Mol Biol* **391**: 498-507
- Meier T, Polzer P, Diederichs K, Welte W, Dimroth P (2005) Structure of the rotor ring of F-Type Na⁺-ATPase from *Ilyobacter tartaricus*. *Science* **308**: 659-662

- Mesmin B, Drin G, Levi S, Rawet M, Cassel D, Bigay J, Antonny B (2007) Two lipid-packing sensor motifs contribute to the sensitivity of ArfGAP1 to membrane curvature. *Biochemistry* **46**: 1779-1790
- Mindell JA, Grigorieff N (2003) Accurate determination of local defocus and specimen tilt in electron microscopy. *J Struct Biol* **142**: 334-347
- Mio K, Ogura T, Kiyonaka S, Hiroaki Y, Tanimura Y, Fujiyoshi Y, Mori Y, Sato C (2007) The TRPC3 channel has a large internal chamber surrounded by signal sensing antennas. *J Mol Biol* **367**: 373-383
- Mishima O, Calvert LD, Whalley E (1985) An apparent first-order transition between two amorphous phases of ice induced by pressure. *Nature* **314**, 76-78
- Mitome N, Ono S, Sato H, Suzuki T, Sone N, Yoshida M (2010) Essential arginine residue of the F(o)-a subunit in F(o)F(1)-ATP synthase has a role to prevent the proton shortcut without c-ring rotation in the F(o) proton channel. *Biochem J* **430**: 171-177
- Mizutani K, Yamamoto M, Suzuki K, Yamato I, Kakinuma Y, Shirouzu M, Walker JE, Yokoyama S, Iwata S, Murata T (2011) Structure of the rotor ring modified with N,N'-dicyclohexylcarbodiimide of the Na⁺-transporting vacuolar ATPase. *P Natl Acad Sci USA* **108**: 13474-13479
- Mochizuki T, Wu G, Hayashi T, Xenophontos SL, Veldhuisen B, Saris JJ, Reynolds DM, Cai Y, Gabow PA, Pierides A, Kimberling WJ, Breuning MH, Deltas CC, Peters DJ, Somlo S (1996) PKD2, a gene for polycystic kidney disease that encodes an integral membrane protein. *Science* **272**: 1339-1342
- Moiseenkova-Bell VY, Stanciu LA, Serysheva, II, Tobe BJ, Wensel TG (2008) Structure of TRPV1 channel revealed by electron cryomicroscopy. *Proc Natl Acad Sci U S A* **105**: 7451-7455
- Molland KL, Paul LN, Yernool DA (2012) Crystal structure and characterization of coiled-coil domain of the transient receptor potential channel PKD2L1. *Biochim Biophys Acta* **1824**: 413-421
- Morbach S, Kramer R (2005) Structure and function of the betaine uptake system BetP of *Corynebacterium glutamicum*: strategies to sense osmotic and chill stress. *J Mol Microbiol Biotechnol* **10**: 143-153
- Muench SP, Trinick J, Harrison MA (2011) Structural divergence of the rotary ATPases. *Q Rev Biophys* **44**: 311-356
- Muller V (2004) An exceptional variability in the motor of archael A1A0 ATPases: from multimeric to monomeric rotors comprising 6-13 ion binding sites. *J Bioenerg Biomembr* **36**: 115-125
- Mullis KB, Faloona FA (1987) Specific synthesis of DNA in vitro via a polymerase-catalyzed chain reaction. *Methods Enzymol* **155**: 335-350

- Murata T, Arechaga I, Fearnley IM, Kakinuma Y, Yamato I, Walker JE (2003) The membrane domain of the Na⁺-motive V-ATPase from *Enterococcus hirae* contains a heptameric rotor. *J Biol Chem* **278**: 21162-21167
- Murata T, Yamato I, Kakinuma Y, Leslie AGW, Walker JE (2004) Crystal structure at 2.1 angstrom resolution of the membrane rotor domain of the V-type NA(+)-ATPase from *enterococcus hirae*. *Bba-Bioenergetics* **1658**: 116-116
- Nauli SM, Alenghat FJ, Luo Y, Williams E, Vassilev P, Li X, Elia AE, Lu W, Brown EM, Quinn SJ, Ingber DE, Zhou J (2003) Polycystins 1 and 2 mediate mechanosensation in the primary cilium of kidney cells. *Nat Genet* **33**: 129-137
- Nesterenko MV, Tilley M, Upton SJ (1994) A simple modification of Blum's silver stain method allows for 30 minute detection of proteins in polyacrylamide gels. *J Biochem Biophys Methods* **28**: 239-242
- Nilius B, Prenen J, Hoenderop JG, Vennekens R, Hoefs S, Weidema AF, Droogmans G, Bindels RJ (2002) Fast and slow inactivation kinetics of the Ca²⁺ channels ECaC1 and ECaC2 (TRPV5 and TRPV6). Role of the intracellular loop located between transmembrane segments 2 and 3. *J Biol Chem* **277**: 30852-30858
- Nilius B, Voets T, Peters J (2005) TRP channels in disease. *Sci STKE* **2005**: re8
- Obermuller N, Gallagher AR, Cai Y, Gassler N, Gretz N, Somlo S, Witzgall R (1999) The rat pkd2 protein assumes distinct subcellular distributions in different organs. *Am J Physiol* **277**: F914-925
- Ohi M, Li Y, Cheng Y, Walz T (2004) Negative Staining and Image Classification - Powerful Tools in Modern Electron Microscopy. *Biol Proced Online* **6**: 23-34
- Okazaki K, Takada S (2011) Structural comparison of F1-ATPase: interplay among enzyme structures, catalysis, and rotations. *Structure* **19**: 588-598
- Oldham ML, Hite RK, Steffen AM, Damko E, Li Z, Walz T, Chen J (2016) A mechanism of viral immune evasion revealed by cryo-EM analysis of the TAP transporter. *Nature* **529**: 537-540
- Ong AC, Ward CJ, Butler RJ, Biddolph S, Bowker C, Torra R, Pei Y, Harris PC (1999) Coordinate expression of the autosomal dominant polycystic kidney disease proteins, polycystin-2 and polycystin-1, in normal and cystic tissue. *Am J Pathol* **154**: 1721-1729
- Orlova EV, Saibil HR (2011) Structural analysis of macromolecular assemblies by electron microscopy. *Chem Rev* **111**: 7710-7748
- Ott V, Koch J, Spate K, Morbach S, Kramer R (2008) Regulatory properties and interaction of the C- and N-terminal domains of BetP, an osmoregulated betaine transporter from *Corynebacterium glutamicum*. *Biochemistry* **47**: 12208-12218
- Ouali M, King RD (2000) Cascaded multiple classifiers for secondary structure prediction. *Protein Sci* **9**: 1162-1176

- Ozcan N, Kramer R, Morbach S (2005) Chill activation of compatible solute transporters in *Corynebacterium glutamicum* at the level of transport activity. *J Bacteriol* **187**: 4752-4759
- Park SH, Zhu PP, Parker RL, Blackstone C (2010) Hereditary spastic paraplegia proteins REEP1, spastin, and atlastin-1 coordinate microtubule interactions with the tubular ER network. *J Clin Invest* **120**: 1097-1110
- Pathak RK, Luskey KL, Anderson RG (1986) Biogenesis of the crystalloid endoplasmic reticulum in UT-1 cells: evidence that newly formed endoplasmic reticulum emerges from the nuclear envelope. *J Cell Biol* **102**: 2158-2168
- Paulsen CE, Armache JP, Gao Y, Cheng Y, Julius D (2015) Structure of the TRPA1 ion channel suggests regulatory mechanisms. *Nature* **520**: 511-517
- Penczek PA (2010) Resolution measures in molecular electron microscopy. *Methods Enzymol* **482**: 73-100
- Penczek PA, Grassucci RA, Frank J (1994) The Ribosome at Improved Resolution - New Techniques for Merging and Orientation Refinement in 3d Cryoelectron Microscopy of Biological Particles. *Ultramicroscopy* **53**: 251-270
- Penefsky HS, Pullman ME, Datta A, Racker E (1960) Partial resolution of the enzymes catalyzing oxidative phosphorylation. II. Participation of a soluble adenosine tolphosphatase in oxidative phosphorylation. *J Biol Chem* **235**: 3330-3336
- Perez C (2012) Structural and functional studies on the osmoregulated trimeric Na⁺/betaine symporter BetP from *Corynebacterium glutamicum*., Biochemistry, Goethe University, Frankfurt
- Perez C, Faust B, Mehdipour AR, Francesconi KA, Forrest LR, Ziegler C (2014) Substrate-bound outward-open state of the betaine transporter BetP provides insights into Na⁺ coupling. *Nat Commun* **5**: 4231
- Perez C, Khafizov K, Forrest LR, Kramer R, Ziegler C (2011) The role of trimerization in the osmoregulated betaine transporter BetP. *EMBO Rep* **12**: 804-810
- Perez C, Koshy C, Yildiz O, Ziegler C (2012) Alternating-access mechanism in conformationally asymmetric trimers of the betaine transporter BetP. *Nature* **490**: 126-130
- Peter H, Burkovski A, Kramer R (1996) Isolation, characterization, and expression of the *Corynebacterium glutamicum* betP gene, encoding the transport system for the compatible solute glycine betaine. *J Bacteriol* **178**: 5229-5234
- Peter H, Burkovski A, Kramer R (1998) Osmo-sensing by N- and C-terminal extensions of the glycine betaine uptake system BetP of *Corynebacterium glutamicum*. *J Biol Chem* **273**: 2567-2574
- Peters DJ, Sandkuijl LA (1992) Genetic heterogeneity of polycystic kidney disease in Europe. *Contrib Nephrol* **97**: 128-139

- Petri ET, Celic A, Kennedy SD, Ehrlich BE, Boggon TJ, Hodsdon ME (2010) Structure of the EF-hand domain of polycystin-2 suggests a mechanism for Ca²⁺-dependent regulation of polycystin-2 channel activity. *Proc Natl Acad Sci U S A* **107**: 9176-9181
- Pettersen EF, Goddard TD, Huang CC, Couch GS, Greenblatt DM, Meng EC, Ferrin TE (2004) UCSF Chimera--a visualization system for exploratory research and analysis. *J Comput Chem* **25**: 1605-1612
- Phelps CB, Huang RJ, Lishko PV, Wang RR, Gaudet R (2008) Structural analyses of the ankyrin repeat domain of TRPV6 and related TRPV ion channels. *Biochemistry* **47**: 2476-2484
- Poetsch A, Neff D, Seelert H, Schagger H, Dencher NA (2000) Dye removal, catalytic activity and 2D crystallization of chloroplast H(+)-ATP synthase purified by blue native electrophoresis. *Biochim Biophys Acta* **1466**: 339-349
- Pogoryelov D, Krah A, Langer JD, Yildiz O, Faraldo-Gomez JD, Meier T (2010) Microscopic rotary mechanism of ion translocation in the F(o) complex of ATP synthases. *Nat Chem Biol* **6**: 891-899
- Pogoryelov D, Reichen C, Klyszejko AL, Brunisholz R, Muller DJ, Dimroth P, Meier T (2007) The oligomeric state of c rings from cyanobacterial F-ATP synthases varies from 13 to 15. *Journal of Bacteriology* **189**: 5895-5902
- Pogoryelov D, Yildiz O, Faraldo-Gomez JD, Meier T (2009) High-resolution structure of the rotor ring of a proton-dependent ATP synthase. *Nat Struct Mol Biol* **16**: 1068-1073
- Preiss L, Langer JD, Hicks DB, Liu J, Yildiz O, Krulwich TA, Meier T (2014) The c-ring ion binding site of the ATP synthase from *Bacillus pseudofirmus* OF4 is adapted to alkaliphilic lifestyle. *Mol Microbiol* **92**: 973-984
- Preiss L, Langer JD, Yildiz O, Eckhardt-Strelau L, Guillemont JEG, Koul A, Meier T (2015) Structure of the mycobacterial ATP synthase Fo rotor ring in complex with the anti-TB drug bedaquiline. *Sci Adv* **1** (4)
- Preiss L, Yildiz O, Hicks DB, Krulwich TA, Meier T (2010) A new type of proton coordination in an F(1)F(o)-ATP synthase rotor ring. *PLoS Biol* **8**: e1000443
- Pullman ME, Penefsky HS, Datta A, Racker E (1960) Partial resolution of the enzymes catalyzing oxidative phosphorylation. I. Purification and properties of soluble dinitrophenol-stimulated adenosine triphosphatase. *J Biol Chem* **235**: 3322-3329
- Qian F, Germino FJ, Cai Y, Zhang X, Somlo S, Germino GG (1997a) PKD1 interacts with PKD2 through a probable coiled-coil domain. *Nat Genet* **16**: 179-183
- Qian F, Germino GG (1997b) "Mistakes happen": somatic mutation and disease. *Am J Hum Genet* **61**: 1000-1005
- Raman S, Vernon R, Thompson J, Tyka M, Sadreyev R, Pei J, Kim D, Kellogg E, DiMaio F, Lange O, Kinch L, Sheffler W, Kim BH, Das R, Grishin NV, Baker D (2009) Structure prediction for CASP8 with all-atom refinement using Rosetta. *Proteins* **77 Suppl 9**: 89-99

- Record MT, Jr., Courtenay ES, Cayley DS, Guttman HJ (1998) Responses of *E. coli* to osmotic stress: large changes in amounts of cytoplasmic solutes and water. *Trends Biochem Sci* **23**: 143-148
- Rees DM, Montgomery MG, Leslie AG, Walker JE (2012) Structural evidence of a new catalytic intermediate in the pathway of ATP hydrolysis by F1-ATPase from bovine heart mitochondria. *Proc Natl Acad Sci U S A* **109**: 11139-11143
- Reeves PJ, Callewaert N, Contreras R, Khorana HG (2002a) Structure and function in rhodopsin: high-level expression of rhodopsin with restricted and homogeneous N-glycosylation by a tetracycline-inducible N-acetylglucosaminyltransferase I-negative HEK293S stable mammalian cell line. *Proc Natl Acad Sci U S A* **99**: 13419-13424
- Reeves PJ, Kim JM, Khorana HG (2002b) Structure and function in rhodopsin: a tetracycline-inducible system in stable mammalian cell lines for high-level expression of opsin mutants. *Proc Natl Acad Sci U S A* **99**: 13413-13418
- Reeves PJ, Thurmond RL, Khorana HG (1996) Structure and function in rhodopsin: high level expression of a synthetic bovine opsin gene and its mutants in stable mammalian cell lines. *Proc Natl Acad Sci U S A* **93**: 11487-11492
- Ressl S, Terwisscha van Scheltinga AC, Vonnrhein C, Ott V, Ziegler C (2009) Molecular basis of transport and regulation in the Na(+)/betaine symporter BetP. *Nature* **458**: 47-52
- Rollauer SE, Tarry MJ, Graham JE, Jaaskelainen M, Jager F, Johnson S, Krehenbrink M, Liu SM, Lukey MJ, Marcoux J, McDowell MA, Rodriguez F, Roversi P, Stansfeld PJ, Robinson CV, Sansom MS, Palmer T, Hogbom M, Berks BC, Lea SM (2012) Structure of the TatC core of the twin-arginine protein transport system. *Nature* **492**: 210-214
- Roscoe JM, Brissenden JE, Williams EA, Chery AL, Silverman M (1993) Autosomal dominant polycystic kidney disease in Toronto. *Kidney Int* **44**: 1101-1108
- Rosenthal PB, Henderson R (2003) Optimal determination of particle orientation, absolute hand, and contrast loss in single-particle electron cryomicroscopy. *J Mol Biol* **333**: 721-745
- Rost B (2001) Review: protein secondary structure prediction continues to rise. *J Struct Biol* **134**: 204-218
- Rothman JE, Fine RE (1980) Coated vesicles transport newly synthesized membrane glycoproteins from endoplasmic reticulum to plasma membrane in two successive stages. *Proc Natl Acad Sci U S A* **77**: 780-784
- Rubenhagen R, Morbach S, Kramer R (2001) The osmoreactive betaine carrier BetP from *Corynebacterium glutamicum* is a sensor for cytoplasmic K⁺. *EMBO J* **20**: 5412-5420
- Rubenhagen R, Ronsch H, Jung H, Kramer R, Morbach S (2000) Osmosensor and osmoregulator properties of the betaine carrier BetP from *Corynebacterium glutamicum* in proteoliposomes. *J Biol Chem* **275**: 735-741

- Saier MH, Jr. (2000) A functional-phylogenetic classification system for transmembrane solute transporters. *Microbiol Mol Biol Rev* **64**: 354-411
- Scheffers MS, Le H, van der Bent P, Leonhard W, Prins F, Spruit L, Breuning MH, de Heer E, Peters DJ (2002) Distinct subcellular expression of endogenous polycystin-2 in the plasma membrane and Golgi apparatus of MDCK cells. *Hum Mol Genet* **11**: 59-67
- Scheres SH (2012) RELION: implementation of a Bayesian approach to cryo-EM structure determination. *J Struct Biol* **180**: 519-530
- Schiller D, Ott V, Kramer R, Morbach S (2006) Influence of membrane composition on osmosensing by the betaine carrier BetP from *Corynebacterium glutamicum*. *J Biol Chem* **281**: 7737-7746
- Schmidt-Krey I, Rubinstein JL (2011) Electron cryomicroscopy of membrane proteins: specimen preparation for two-dimensional crystals and single particles. *Micron* **42**: 107-116
- Schulz S. (2015) Structural and functional characterization of the rotor rings from a *Fusobacterium* F- type and a *Burkholderia* N-type rotary ATPase. In University G (ed.). University library Frankfurt am Main.
- Schulze S, Koster S, Geldmacher U, Terwisscha van Scheltinga AC, Kühlbrandt W (2010) Structural basis of Na(+)-independent and cooperative substrate/product antiport in CaiT. *Nature* **467**: 233-236
- Schumann FH, Hoffmeister H, Schmidt M, Bader R, Besl E, Witzgall R, Kalbitzer HR (2009) NMR-assignments of a cytosolic domain of the C-terminus of polycystin-2. *Biomol NMR Assign* **3**: 141-144
- Shi DJ, Ye S, Cao X, Zhang R, Wang K (2013) Crystal structure of the N-terminal ankyrin repeat domain of TRPV3 reveals unique conformation of finger 3 loop critical for channel function. *Protein Cell* **4**: 942-950
- Shibata Y, Voss C, Rist JM, Hu J, Rapoport TA, Prinz WA, Voeltz GK (2008) The reticulon and DP1/Yop1p proteins form immobile oligomers in the tubular endoplasmic reticulum. *J Biol Chem* **283**: 18892-18904
- Shigematsu H, Sokabe T, Danev R, Tominaga M, Nagayama K (2010) A 3.5-nm structure of rat TRPV4 cation channel revealed by Zernike phase-contrast cryoelectron microscopy. *J Biol Chem* **285**: 11210-11218
- Shimamura T, Weyand S, Beckstein O, Rutherford NG, Hadden JM, Sharples D, Sansom MS, Iwata S, Henderson PJ, Cameron AD (2010) Molecular basis of alternating access membrane transport by the sodium-hydantoin transporter Mhp1. *Science* **328**: 470-473
- Song Y, DiMaio F, Wang RY, Kim D, Miles C, Brunette T, Thompson J, Baker D (2013) High-resolution comparative modeling with RosettaCM. *Structure* **21**: 1735-1742

- Soontharapirakkul K, Incharoensakdi A (2010) Na⁺-stimulated ATPase of alkaliphilic halotolerant cyanobacterium *Aphanothece halophytica* translocates Na⁺ into proteoliposomes via Na⁺ uniport mechanism. *BMC Biochem* **11**: 30
- Soontharapirakkul K, Promden W, Yamada N, Kageyama H, Incharoensakdi A, Iwamoto-Kihara A, Takabe T (2011) Halotolerant cyanobacterium *Aphanothece halophytica* contains an Na⁺-dependent F1F0-ATP synthase with a potential role in salt-stress tolerance. *J Biol Chem* **286**: 10169-10176
- Sorzano CO, Bilbao-Castro JR, Shkolnisky Y, Alcorlo M, Melero R, Caffarena-Fernandez G, Li M, Xu G, Marabini R, Carazo JM (2010) A clustering approach to multireference alignment of single-particle projections in electron microscopy. *J Struct Biol* **171**: 197-206
- Sorzano CO, Marabini R, Velazquez-Muriel J, Bilbao-Castro JR, Scheres SH, Carazo JM, Pascual-Montano A (2004) XMIPP: a new generation of an open-source image processing package for electron microscopy. *J Struct Biol* **148**: 194-204
- Spirli C, Villani A, Mariotti V, Fabris L, Fiorotto R, Strazzabosco M (2015) Posttranslational regulation of polycystin-2 protein expression as a novel mechanism of cholangiocyte reaction and repair from biliary damage. *Hepatology*
- Standfuss J, Edwards PC, D'Antona A, Fransen M, Xie G, Oprian DD, Schertler GF (2011) The structural basis of agonist-induced activation in constitutively active rhodopsin. *Nature* **471**: 656-660
- Steger R, Weinand M, Kramer R, Morbach S (2004) LcoP, an osmoregulated betaine/ectoine uptake system from *Corynebacterium glutamicum*. *FEBS Lett* **573**: 155-160
- Stewart AG, Sobti M, Harvey RP, Stock D (2013) Rotary ATPases: models, machine elements and technical specifications. *Bioarchitecture* **3**: 2-12
- Stock D, Leslie AGW, Walker JE (1999) Molecular architecture of the rotary motor in ATP synthase. *Science* **286**: 1700-1705
- Street TO, Krukenberg KA, Rosgen J, Bolen DW, Agard DA (2010) Osmolyte-induced conformational changes in the Hsp90 molecular chaperone. *Protein Sci* **19**: 57-65
- Streets AJ, Moon DJ, Kane ME, Obara T, Ong AC (2006) Identification of an N-terminal glycogen synthase kinase 3 phosphorylation site which regulates the functional localization of polycystin-2 in vivo and in vitro. *Hum Mol Genet* **15**: 1465-1473
- Studier FW (2005) Protein production by auto-induction in high density shaking cultures. *Protein Expr Purif* **41**: 207-234
- Sutters M (2006) The pathogenesis of autosomal dominant polycystic kidney disease. *Nephron Exp Nephrol* **103**: e149-155
- Symersky J, Pagadala V, Osowski D, Krah A, Meier T, Faraldo-Gomez JD, Mueller DM (2012) Structure of the c(10) ring of the yeast mitochondrial ATP synthase in the open conformation. *Nat Struct Mol Biol* **19**: 485-491, S481

- Szallasi A, Cortright DN, Blum CA, Eid SR (2007) The vanilloid receptor TRPV1: 10 years from channel cloning to antagonist proof-of-concept. *Nat Rev Drug Discov* **6**: 357-372
- Szallasi A, Sheta M (2012) Targeting TRPV1 for pain relief: limits, losers and laurels. *Expert Opin Investig Drugs* **21**: 1351-1369
- Thompson AA, Liu JJ, Chun E, Wacker D, Wu HX, Cherezov V, Stevens RC (2011) GPCR stabilization using the bicelle-like architecture of mixed sterol-detergent micelles. *Methods* **55**: 310-317
- Thuman-Commike PA (2001) Single particle macromolecular structure determination via electron microscopy. *FEBS Lett* **505**: 199-205
- Timmins PA, M. L, H.U. W, T. W, W. W (1988) α physical characterization of some detergents of potential use for membrane protein crystallization. *FEBS Letters* **238**: 361-368
- Toei M, Gerle C, Nakano M, Tani K, Gyobu N, Tamakoshi M, Sone N, Yoshida M, Fujiyoshi Y, Mitsuoka K, Yokoyama K (2007) Dodecamer rotor ring defines H⁺/ATP ratio for ATP synthesis of prokaryotic V-ATPase from *Thermus thermophilus*. *Proc Natl Acad Sci U S A* **104**: 20256-20261
- Torra R, Badenas C, Darnell A, Nicolau C, Volpini V, Revert L, Estivill X (1996) Linkage, clinical features, and prognosis of autosomal dominant polycystic kidney disease types 1 and 2. *J Am Soc Nephrol* **7**: 2142-2151
- Tribet C, Audebert R, Popot JL (1996) Amphipols: polymers that keep membrane proteins soluble in aqueous solutions. *Proc Natl Acad Sci U S A* **93**: 15047-15050
- Tsiokas L, Kim E, Arnould T, Sukhatme VP, Walz G (1997) Homo- and heterodimeric interactions between the gene products of PKD1 and PKD2. *Proc Natl Acad Sci U S A* **94**: 6965-6970
- Tusnady GE, Simon I (1998) Principles governing amino acid composition of integral membrane proteins: application to topology prediction. *J Mol Biol* **283**: 489-506
- van Heel M, Gowen B, Matadeen R, Orlova EV, Finn R, Pape T, Cohen D, Stark H, Schmidt R, Schatz M, Patwardhan A (2000) Single-particle electron cryo-microscopy: towards atomic resolution. *Q Rev Biophys* **33**: 307-369
- van Heel M, Harauz G, Orlova EV, Schmidt R, Schatz M (1996) A new generation of the IMAGIC image processing system. *J Struct Biol* **116**: 17-24
- Vassilev PM, Guo L, Chen XZ, Segal Y, Peng JB, Basora N, Babakhanlou H, Cruger G, Kanazirska M, Ye C, Brown EM, Hediger MA, Zhou J (2001) Polycystin-2 is a novel cation channel implicated in defective intracellular Ca(2+) homeostasis in polycystic kidney disease. *Biochem Biophys Res Commun* **282**: 341-350
- Veldhuisen B, Saris JJ, de Haij S, Hayashi T, Reynolds DM, Mochizuki T, Elles R, Fossdal R, Bogdanova N, van Dijk MA, Coto E, Ravine D, Norby S, Verellen-Dumoulin C, Breuning MH,

- Somlo S, Peters DJ (1997) A spectrum of mutations in the second gene for autosomal dominant polycystic kidney disease (PKD2). *Am J Hum Genet* **61**: 547-555
- Vik SB, Antonio BJ (1994) A mechanism of proton translocation by F1F0 ATP synthases suggested by double mutants of the a subunit. *J Biol Chem* **269**: 30364-30369
- Voet D., G. VJ (2010) *Biochemistry*, Vol. 4th Edition: Wiley.
- Vollmar M, Schlieper D, Winn M, Buchner C, Groth G (2009) Structure of the c14 rotor ring of the proton translocating chloroplast ATP synthase. *J Biol Chem* **284**: 18228-18235
- von Ballmoos C, Wiedenmann A, Dimroth P (2009) Essentials for ATP synthesis by F1F0 ATP synthases. *Annu Rev Biochem* **78**: 649-672
- Vriend G (1990) What If - a Molecular Modeling and Drug Design Program. *J Mol Graphics* **8**: 52-&
- Waclawska I, Ziegler C (2015) Regulatory role of charged clusters in the N-terminal domain of BetP from *Corynebacterium glutamicum*. *Biological Chemistry* **396**: 1117-1126
- Walker JE (2013) The ATP synthase: the understood, the uncertain and the unknown. *Biochem Soc Trans* **41**: 1-16
- Watt IN, Montgomery MG, Runswick MJ, Leslie AG, Walker JE (2010) Bioenergetic cost of making an adenosine triphosphate molecule in animal mitochondria. *Proc Natl Acad Sci U S A* **107**: 16823-16827
- Whatmore AM, Chudek JA, Reed RH (1990) The effects of osmotic upshock on the intracellular solute pools of *Bacillus subtilis*. *J Gen Microbiol* **136**: 2527-2535
- White JF, Noinaj N, Shibata Y, Love J, Kloss B, Xu F, Gvozdenovic-Jeremic J, Shah P, Shiloach J, Tate CG, Grisshammer R (2012) Structure of the agonist-bound neurotensin receptor. *Nature* **490**: 508-513
- Wilkens S, Rodgers A, Ogilvie I, Capaldi RA (1997) Structure and arrangement of the delta subunit in the *E. coli* ATP synthase (ECF1F0). *Biophys Chem* **68**: 95-102
- Wittig I, Braun HP, Schagger H (2006) Blue native PAGE. *Nat Protoc* **1**: 418-428
- Witzgall R (2005) Polycystin-2--an intracellular or plasma membrane channel? *Naunyn Schmiedebergs Arch Pharmacol* **371**: 342-347
- Wolf A, Kramer R, Morbach S (2003) Three pathways for trehalose metabolism in *Corynebacterium glutamicum* ATCC13032 and their significance in response to osmotic stress. *Mol Microbiol* **49**: 1119-1134
- Wong W, Bai XC, Brown A, Fernandez IS, Hanssen E, Condrón M, Tan YH, Baum J, Scheres SH (2014) Cryo-EM structure of the *Plasmodium falciparum* 80S ribosome bound to the anti-protozoan drug emetine. *Elife* **3**

- Wood JM (1999) Osmosensing by bacteria: signals and membrane-based sensors. *Microbiol Mol Biol Rev* **63**: 230-262
- Wright R, Keller G, Gould SJ, Subramani S, Rine J (1990) Cell-type control of membrane biogenesis induced by HMG-CoA reductase. *New Biol* **2**: 915-921
- Wu G, D'Agati V, Cai Y, Markowitz G, Park JH, Reynolds DM, Maeda Y, Le TC, Hou H, Jr., Kucherlapati R, Edelmann W, Somlo S (1998) Somatic inactivation of Pkd2 results in polycystic kidney disease. *Cell* **93**: 177-188
- Wu LJ, Sweet TB, Clapham DE (2010) International Union of Basic and Clinical Pharmacology. LXXVI. Current progress in the mammalian TRP ion channel family. *Pharmacol Rev* **62**: 381-404
- Yagi H, Kajiwarra N, Tanaka H, Tsukihara T, Kato-Yamada Y, Yoshida M, Akutsu H (2007) Structures of the thermophilic F1-ATPase epsilon subunit suggesting ATP-regulated arm motion of its C-terminal domain in F1. *Proc Natl Acad Sci U S A* **104**: 11233-11238
- Yamaguchi H, Matsushita M, Nairn AC, Kuriyan J (2001) Crystal structure of the atypical protein kinase domain of a TRP channel with phosphotransferase activity. *Mol Cell* **7**: 1047-1057
- Yamamoto A, Masaki R, Tashiro Y (1996) Formation of crystalloid endoplasmic reticulum in COS cells upon overexpression of microsomal aldehyde dehydrogenase by cDNA transfection. *J Cell Sci* **109 (Pt 7)**: 1727-1738
- Yamashita A, Singh SK, Kawate T, Jin Y, Gouaux E (2005) Crystal structure of a bacterial homologue of Na⁺/Cl⁻-dependent neurotransmitter transporters. *Nature* **437**: 215-223
- Yan Z, Bai XC, Yan C, Wu J, Li Z, Xie T, Peng W, Yin CC, Li X, Scheres SH, Shi Y, Yan N (2015) Structure of the rabbit ryanodine receptor RyR1 at near-atomic resolution. *Nature* **517**: 50-55
- Yoder BK, Hou X, Guay-Woodford LM (2002) The polycystic kidney disease proteins, polycystin-1, polycystin-2, polaris, and cystin, are co-localized in renal cilia. *J Am Soc Nephrol* **13**: 2508-2516
- Yu Y, Ulbrich MH, Li MH, Buraei Z, Chen XZ, Ong AC, Tong L, Isacoff EY, Yang J (2009) Structural and molecular basis of the assembly of the TRPP2/PKD1 complex. *Proc Natl Acad Sci U S A* **106**: 11558-11563
- Yu Y, Ulbrich MH, Li MH, Dobbins S, Zhang WK, Tong L, Isacoff EY, Yang J (2012) Molecular mechanism of the assembly of an acid-sensing receptor ion channel complex. *Nat Commun* **3**: 1252
- Zhao JH, Benlekbir S, Rubinstein JL (2015) Electron cryomicroscopy observation of rotational states in a eukaryotic V-ATPase. *Nature* **521**: 241-+

Zhou A, Rohou A, Schep DG, Bason JV, Montgomery MG, Walker JE, Grigorieff N, Rubinstein JL (2015) Structure and conformational states of the bovine mitochondrial ATP synthase by cryo-EM. *Elife* **4**

Ziegler C, Bremer E, Kramer R (2010) The BCCT family of carriers: from physiology to crystal structure. *Mol Microbiol* **78**: 13-34

Zubcevic L, Herzik MA, Jr., Chung BC, Liu Z, Lander GC, Lee SY (2016) Cryo-electron microscopy structure of the TRPV2 ion channel. *Nat Struct Mol Biol* **23**: 180-186

Zwart PH, Afonine PV, Grosse-Kunstleve RW, Hung LW, Ioerger TR, McCoy AJ, McKee E, Moriarty NW, Read RJ, Sacchettini JC, Sauter NK, Storoni LC, Terwilliger TC, Adams PD (2008) Automated structure solution with the PHENIX suite. *Methods Mol Biol* **426**: 419-435

9 Acknowledgement

Ich bedanke mich bei Prof. Christine Ziegler für die Betreuung meiner Doktorarbeit und die Möglichkeit diese in ihrem Labor durchzuführen. Dein großes Vertrauen hat es mir ermöglicht, meinen wissenschaftlichen Interessen im Rahmen dieser Arbeit nachzugehen. Du hast mir die Freiheit gegeben in Kollaborationen zusätzliche Projekte zu bearbeiten, sodass ich mich mit vielfältigen biologischen Themengebieten befassen konnte.

Ich bedanke mich bei Prof. Werner Kühlbrandt für die Möglichkeit meine Arbeit in seiner Abteilung für Strukturbiologie durchführen zu können. Die einmalige Ausstattung im Bereich der Kryo-Elektronenmikroskopie machte es erst möglich die Ergebnisse während meiner Arbeit zu produzieren. Ich danke dir für deine Unterstützung und die regelmäßigen Messzeiten an den Mikroskopen.

Prof. Thomas Meier danke ich für die Kollaboration, den Rückhalt und die Möglichkeit an der N-Typ ATPase zu arbeiten. Ich danke dir für die vielen wertvollen Ratschläge, die du mir während meiner Arbeit gegeben hast.

Prof. Clemens Glaubitz danke ich für die Übernahme der universitären Betreuung meiner Doktorarbeit.

Prof. Ralph Witzgall danke ich für die Messzeiten an dem konfokalen Laser-Scanning-Mikroskop.

Ich bedanke mich bei Dr. Sarah Schulz für die hervorragende Zusammenarbeit. Vielen Dank für deine Geduld, die vielen Stunden der Datenaufnahme und für die vielen tausend Partikel, die du gepickt hast. Deine positive Einstellung und deine kontinuierliche Unterstützung haben dieses Projekt erfolgreich gemacht.

I thank Edoardo D’Imprima for all the useful discussions about single-particle cryo-EM, your friendship and your willingness to help. It was fun working with you.

I thank Deryck Mills for the excellent support at the electron microscopes and that you showed me how to use them independently.

I thank Dr. Janet Vonck for all the useful advices about single-particle EM.

Ich bedanke mich bei Friederike Joos für die großartige Zusammenarbeit und die vielen Dünnschnitte und Gefrierbrüche, die meine Arbeit enorm bereichern.

Ich bedanke mich bei allen aktuellen und ehemaligen Mitgliedern unseres Labors - Katrin Rhode, Dr. Rebecca Richter, Izabela Waclawska, Susann Kaltwasser, Dr. Eva Schweikhard, Dr. Caroline Koshy, Dr. Camillo Perez und Ulrike Geldmacher. Ihr wart immer hilfsbereit und habt ein angenehmes Arbeitsumfeld geschaffen.

Ich bedanke mich bei Marvin Gläsner für die Unterstützung während seiner Masterarbeit und bei allen Mitgliedern aus der Gruppe von Prof. Christine Ziegler in Regensburg, besonders Dr. Sylvia Sanctis für die Unterstützung bei der Analyse der PC-2 Struktur.

Ich danke Monika Hobrack für die Unterstützung bei organisatorischen Angelegenheiten.

Zum Schluss danke ich meinen Freunden und meiner Familie, die mich während dieser Zeit besonders unterstützt haben.

10 Curriculum vitae

Martin Wilkes

Born: august, 8th 1985 in Siegen, Germany

Address: Oberurseler Str. 9
61440 Oberursel
Germany

Education:

05/2011 – 05/2016 **PhD thesis at the Max-Planck-Institute of Biophysics Frankfurt/M.**
Department of Structural Biology, group of Prof. Dr. Christine Ziegler

10/2006 - 04/2011 **Studies of Biochemistry at the Goethe-University Frankfurt/M.**

10/2005-06/2006 **Military service**
SKA-IMZBW, Sankt Augustin, Germany

09/1996 - 07/2005 **Albert-Einstein-Gymnasium Sankt Augustin, Germany**

Fellowships:

10/2011- 09/2013 Chemiefonds Fellowship

03/2009- 04/2011 Fellowship of the German National Academic Foundation